Holism for Target Recognition in Synthetic Aperture Radar Imagery

by

© Khalid El-Darymli

B.Sc., M.Sc.

A thesis submitted to the
School of Graduate Studies
in partial fulfillment of the
requirements for the degree of
Doctor of Philosophy

Faculty of Engineering and Applied Science
Memorial University of Newfoundland

January 2015

St. John's, Newfoundland

I dedicate this thesis to my family,
my wife, Necmiye Erdöl, and our beloved daughter, Firdaus,
for their constant support and unconditional love.
I love you all dearly.

"The whole is greater than the sum of its parts."
~Aristotle (384 BC – 322 BC)

"Behind every atom of this world hides an infinite universe."
~Rumi (1207 – 1273)

"A man should look for what is, and not for what he thinks should be."
~Albert Einstein (1879 – 1955)

Abstract

Reductionism and holism are two worldviews that underlie the fields of linear and nonlinear signal processing, respectively. In the reductionist worldview, deviation from linearity is seen as a noise that warrants removal. In the holistic worldview, the system is viewed as a whole that cannot be fully understood solely in terms of its constituent parts. Conventional radar resolution theory is a direct application of the reductionist view. Consequently, analysis of single-channel synthetic aperture radar imagery for automatic target recognition (SAR-ATR) has traditionally been based on linear techniques associated with the image intensity while the phase content is ignored. The insufficiency of the linear system theory to extended targets has been empirically observed in the literature.

This thesis consists of a development of novel tools that exploit the nonlinear phenomenon in focused single-channel SAR imagery and application of these tools to the SAR-ATR problem. A systematic procedure to infer the statistical significance of the nonlinear dynamics is introduced. Furthermore, two novel frameworks for feature extraction from complex-valued SAR imagery are presented. The first framework is solely based on the often ignored phase content, and it is built on techniques from the fields of complex-valued and directional statistics. The second framework utilizes complex-valued SAR imagery and provides for exploiting nonlinear and nonstationary signal analysis methods based on the Poincaré and Hilbert views for nonlinear phenomena. Using real-world SAR datasets, the overall results confirm the statistical significance of the nonlinear effect for the case of extended targets. Furthermore, when the complex-valued SAR image is detected, the nonlinear dynamics are found to be obliterated or greatly altered. The efficacy of the frameworks developed is clearly demonstrated.

Acknowledgments

Pursuing this Ph.D. has been a truly life-changing experience for me, and it would not have been possible without the guidance and enormous support that I received from many people.

I would like to express my deepest gratitude to my advisors: Dr. Peter McGuire, Mr. Desmond Power, Prof. Dr. Cecilia Moloney and Prof. Dr. Eric W. Gill. Four of them provided me with constructive criticism, encouragement and necessary pressure at different phases of this research work. I am extremely thankful to Peter who introduced me to the fascinating field of synthetic aperture radar (SAR), and who believed in my ability to contribute to this field. The guidance I received from Peter was instrumental, and it helped me immensely in defining the research topic. Peter has treated me as a good friend, and his door was always open for discussions and friendly conversations. Mr. Power has provided me with a real-world insight, and his comments contributed distinctly to the development of this research. Dr. Moloney has always offered invaluable support and feedback that made the accomplishment of this thesis attainable. I am especially indebted to Dr. Gill for his priceless support and encouragement. Dr. Gill's feedback did not only contribute to the betterment of this research but also it added eminently to my own personal development. Dr. Gill always unconsciously demonstrated that expertise and humility are not mutually exclusive attributes.

I graciously acknowledge Dr. Leonard Lye, the Associate Dean of Graduate Studies, for introducing me to my advisors at C-CORE. If not for him, my Ph.D. could have been significantly delayed.

I would like to thank all the members of the High Frequency Radar Ocean Surface Applications (HF-ROSA) group at the Faculty of Engineering and Applied Science, Memorial University, led by Dr. Gill and Dr. Weimin Huang. By allowing me to join their biweekly meetings, I have developed an interdisciplinary insight which is

crucial for the advancement of my career. Also, I acknowledge C-CORE and all the staff members for the facilities and support they provided throughout the course of my Ph.D. Furthermore, I am thankful to Dr. Paris Vachon from Defence R&D Canada (DRDC Ottawa) who provided advice and oversight to the project team for the last five years.

Defence R&D Canada is duly acknowledged for providing the Radarsat-2 Spotlight imagery through a project entitled Virtual SAR Constellation (VSC) funded by the Canadian Space Agency Government Research Initiatives Program. RADARSAT is an official mark of the Canadian Space Agency (CSA). CMC Microsystems is kindly acknowledged for the provision of products and services that facilitated this research, including an vector network analyzer and an RF signal generator.

Financial support from the Research and Development Corporation (RDC) of Newfoundland and Labrador, the Atlantic Innovation Fund (AIF) of the Atlantic Canada Opportunities Agency, the School of Graduate Studies at Memorial University, and the Natural Sciences and Engineering Research Council of Canada (NSERC) is gratefully acknowledged. Without this support, it would not have been possible to pursue this thesis on a full-time basis.

And finally, thank you to my family for believing in me. To Necmiye Erdöl, who has been by my side throughout this Ph.D., living every single minute of it. And to our darling Firdaus for being such a good little baby that past three years. You both make it all worthwhile and because of you it was possible for me to complete what I started.

Contents

List of Tables

List of Figures

Nomenclature

α	significance level, *p. 79*
η	slow time, *p. 4*
η_c	beam center in the azimuth direction, *p. 4*
γ	kernel parameter, *p. 211*
$\hat{\mu}$	sample mean, *p. 209*
$\hat{\sigma}$	sample standard deviation, *p. 209*
λ	shape parameter of WCGSM PDF, *p. 189*
$\mathbb{K}$	Boltzmann constant, *p. 60*
$\mathbb{R}$	real number, *p. 210*
BRPI	polar representation of BRPI, *p. 190*
$\mathbf{W}$	normal vector to the hyperplane, *p. 211*
$\mathbf{z}_t$	surrogate signal, *p. 76*
$\mathcal{H}_0$	null hypothesis, *p. 76*
$\mathcal{H}_{1,NC}$	alternative hypothesis for noncircularity, *p. 147*
$\mathcal{H}_1$	alternative hypothesis, *p. 79*
μ	population mean, *p. 209*
ω_i	target class i, *p. 211*
$\otimes$	convolution, *p. 4*
Φ	phase chip, *p. 143*

$\phi(.)$	higher dimensional space function, *p. 211*
Ψ	pseudo-covariance, *p. 145*
ψ	phase change in the received pulse, *p. 4*
σ	radar cross section, *p. 60*
σ_o	backscatter coefficient, *p. 4*
sup	supremum, *p. 79*
τ	fast time, *p. 4*
θ	projection angle, *p. 81*
$\triangle A$	theoretical azimuth resolution, *p. 60*
$\triangle R$	theoretical slant-range resolution, *p. 59*
$\underline{\phi}$	location parameter of WCGSM PDF, *p. 189*
$\underline{\sigma}$	population standard deviation, *p. 209*
$\underline{c}$	speed of light in a vacuum, *p. 58*
$\underline{h}$	static instantaneous transform, *p. 76*
$\underline{m}$	total number of IMFs, *p. 197*
εM	electromagnetic, *p. 39*
$\xi^{\omega_i \omega_j}$	a non-negative slack variable which measures the degree of misclassification of the data, *p. 211*
B	chirp width, *p. 4*
b	number of bins, *p. 78*
$b_{DQ}(.)$	instantaneous magnitude for $H_{DQ}(.)$, *p. 197*
$b_{GZC}(.)$	zero-crossing amplitude of a local whole wave, *p. 198*
BL	baseline, *p. 164*
C	penalty or regularization parameter for SVM classifier, *p. 211*

$c(.,.)$ complex-valued SAR chip, *p. 143*

CDN combined degree of nonlinearity, *p. 199*

DN degree of nonlinearity, *p. 199*

$E\{.\}$ expectation, *p. 146*

$F(.)$ fluctuation, *p. 201*

f_{avg} average frequency, *p. 198*

f_{BL} baseline feature, *p. 164*

f_b beat frequency, *p. 58*

f_d Doppler shift, *p. 58*

f_{IF} intrawave frequency, *p. 198*

f_I oscillation frequency, *p. 199*

f_k convolution kernel, *p. 144*

f_{max} maximum frequency, *p. 57*

f_{min} minimum frequency, *p. 57*

f_{NL} nonlinear feature, *p. 207*

F_N receiver noise factor, *p. 60*

f_o center frequency, *p. 57*

f_{Ph} phase feature, *p. 205*

$fu_{iq}(.,.)$ furud'ed 2-D representation, *p. 85*

$Fu_{iq}(.)$ furud'ed 1-D representation, *p. 85*

G antenna gain, *p. 60*

$g(\tau,\eta)$ ground reflectivity, *p. 4*

$g^{\omega_i\omega_j}(.)$ decision or predictor function, *p. 212*

$h(\tau,\eta)$ impulse response, *p. 4*

H_c	entropy for the encoded sequence, p. 200
$H_{DQ}(.)$	Hilbert spectrum based on the DQ method, p. 197
$h_{DQ}(.)$	unwrapped instantaneous phase for $H_{DQ}(.)$, p. 197
$i(.,.)$ or $I(.,.)$	real-part, p. 143
$IF_{DQ}(.)$	instantaneous frequency for $H_{DQ}(.)$, p. 197
$IF_{GZC}(.)$	instantaneous frequency based on the GZC method, p. 198
$IQ(.)$	bivariate 1-D representation, p. 85
JSD_N	normalized Jensen-Shannon divergence, p. 150
K	number of target classes, p. 210
K_r	frequency modulation rate of the range pulse, p. 4
L	length of the antenna, p. 60
l	number of possible permutation patterns, p. 200
L_s	general loss factor, p. 60
M	magnitude-detected chip, p. 164
N	number of surrogates, p. 78
$n(\tau, \eta)$	noise component, p. 4
n_+	number of positive instances, p. 212
n_-	number of negative instances, p. 212
N_{dB}	noise floor in dB, p. 60
NL	nonlinear, p. 207
O	order induced by the dispersive scatterer, p. 5
p or P	power-detected chip, p. 164
$P_{r,\text{dB}}$	received power for a range profile in dB, p. 60
P_t	peak transmit power, p. 60

Ph	phase, *p. 205*
$q(.,.)$ or $Q(.,.)$	imaginary-part, *p. 143*
$R_\theta(.)$	Radon transform, *p. 81*
T_N	effective noise temperature, *p. 60*
v	velocity of moving target, *p. 58*
$vM(\mu_{vM}, \kappa)$	von Mises distribution with location parameter μ_{vM} and concentration parameter κ, *p. 137*
$w_a(\eta)$	two-way azimuth beam pattern, *p. 4*
$WC(\mu_{wc}, \rho)$	wrapped Cauchy distribution with location parameter μ_{wc} and scale parameter ρ, *p. 137*
$WCGSM\left(\underline{\phi}, \lambda\right)$	wrapped complex Gaussian scale mixture with shape parameter $\underline{\phi}$ and location parameter λ, *p. 137*
$x_{BB}(\tau, \eta)$	baseband backscatter, *p. 3*
1-D	one dimensional, *p. 68*
2-D	two dimensional, *p. 68*
3-D	three dimensional, *p. 38*
ωKA	omega-K algorithm, *p. 56*
ADC	analog-to-digital converter, *p. 57*
AI	artificial intelligence, *p. 33*
AM	amplitude modulation, *p. 4*
arg	argument, *p. 143*
ATR	automatic target recognition, *p. 1*
B	sweep bandwidth, *p. 57*
BP	band-pass, *p. 33*
BRPI	binary relative phase image, *p. 143*

CA-CFAR	cell-averaging CFAR, *p. 31*
CAD	computer-aided design, *p. 38*
CDF	cumulative distribution function, *p. 79*
CFAR	constant false alarm rate, *p. 30*
CGSM	complex Gaussian scale mixture, *p. 151*
CLT	central limit theorem, *p. 2*
COTS	commercial off-the-shelf , *p. 9*
CR	corner reflector, *p. 88*
CSA	Canada Space Agency, *p. 245*
CTD	coherent target decomposition, *p. 239*
CV	complex-valued, *p. 122*
DARPA	Defense Advanced Research Projects Agency, *p. 246*
DFA	detrended fluctuation analysis, *p. 183*
DQ	direct quadrature, *p. 197*
DWT	discrete wavelet transform, *p. 31*
EBH	equiprobable bin histogram, *p. 77*
EDF	empirical distribution function, *p. 79*
EDH	equidistant histogram, *p. 77*
EEMD	ensemble EMD, *p. 126*
EMD	empirical mode decomposition, *p. 70*
EOC(s)	extended operating condition(s), *p. 37*
ET	extended target, *p. 88*
FIR	finite impulse response, *p. 33*
FM	frequency modulation, *p. 4*

FOA focus-of-attention, *p. 28*

GCLT generalized central limit theorem, *p. 2*

GGD generalized Gaussian distribution, *p. 70*

GLRT generalized likelihood ratio test, *p. 42*

GOCA-CFAR greatest of CA-CFAR, *p. 31*

GR Gaussianity rejected, *p. 106*

GSM Gaussian scale mixture, *p. 70*

GZC generalized zero-crossing, *p. 197*

H horizontal, *p. 201*

HF high frequency, *p. 238*

HHT Hilbert-Huang transform, *p. 3*

HLC high level classificatoin/classifier, *p. 2*

iAAFT iterative amplitude adjusted Fourier transform, *p. 76*

IMF intrinsic mode function, *p. 122*

IQR interquartile range, *p. 183*

ITD incoherent target decomposition, *p. 239*

JS or JSD Jensen-Shannon divergence, *p. 189*

KB knowledge-based, *p. 34*

KDE kernel density estimation, *p. 31*

KS Kolmogorov-Smirnov, *p. 79*

LANTRIN Low Altitude Navigation and Targeting Infrared, *p. 27*

LFM linear frequency modulation, *p. 1*

LFMCW linear frequency modulated continuous wave, *p. 56*

LIBSVM a library for support vector machines, *p. 167*

LLC low level classification/classifier, *p. 1*

LPF low pass filter, *p. 57*

LSI linear space invariant, *p. 11*

LTI linear time invariant, *p. 11*

LUT look-up table, *p. 43*

MDA Macdonald Dettwiler and Associates, *p. 245*

MI mutual information, *p. 77*

MIT Massachusetts Institute of Technology, *p. 37*

MLE maximum likelihood estimation, *p. 42*

MSTAR Moving and Stationary Target Acquisition and Recognition, *p. 246*

MVUE minimum variance unbiased estimator, *p. 97*

nICA nonlinear independent component analysis, *p. 70*

OCs operating conditions, *p. 1*

OS-CFAR order statistics CFAR, *p. 31*

PCA principal component analysis, *p. 70*

PCB printed circuit board, *p. 61*

PD probability of detection, *p. 29*

PDF probability density function, *p. 42*

PE permutation entropy, *p. 183*

PFA probability of false alarm, *p. 29*

PM phase modulation, *p. 122*

PMF probability mass function, *p. 77*

POSP principle of stationary phase, *p. 5*

PPMC Pearson product-moment correlation, *p. 77*

PR	pattern recognition, *p. 34*
R	slant range, *p. 58*
RBF	radial basis function, *p. 211*
RCS	radar cross section, *p. 29*
RF	radio frequency, *p. 60*
ROI(s)	regions(s) of interest, *p. 29*
RS-2	Radarsat-2, *p. 88*
SAS	synthetic aperture sonar, *p. 69*
SAU	synthetic aperture ultrasound, *p. 183*
SDMS	Sensor and Data Management System, *p. 246*
sgn	sign function, *p. 212*
SLC	single look complex, *p. 12*
SNL	Sandia National Laboratory, *p. 246*
SNR	signal to noise ratio, *p. 60*
SOC(s)	standard operating condition(s), *p. 45*
SOCA-CFAR	smallest of CA-CFAR, *p. 31*
std	standard deviation, *p. 199*
SVM	support vector machine, *p. 163*
T	time delay, *p. 58*
TCM	target coherency matrix, *p. 239*
TF	target-free, *p. 88*
V	vertical, *p. 201*
VCO	voltage controlled oscillator, *p. 56*
VNA	vector network analyzer, *p. 9*

VSC Virtual SAR Constellation, *p. 245*

WMF weighted myriad filter, *p. 70*

WP(s) work package(s), *p. 6*

1. Introduction

1.1. Background

The development of modern high resolution synthetic aperture radar (SAR) was led by three key innovations [1, 2]. First, pulse compression enabled radars to resolve closely spaced targets in range. The most widely used pulse compression technique is linear frequency modulation (LFM), which was introduced in the early 1950s. Second, in 1951, it was possible to resolve closely spaced targets in angular position relative to the antenna beam center of side looking airborne radars. This was achieved through Doppler filtering which was pioneered by Carl Wiley of Goodyear Aircraft Corporation. Finally, high resolution SAR was enabled through the advent of a technique to synthesize a long aperture for storing the magnitude and phase of successive radar returns along the platform trajectory. The integration of these innovations led to the formation of the first focused SAR image at the university of Michigan in 1957.

Automatic target recognition (ATR) deals with the use of computer processing capabilities to infer the classes of targets (i.e., objects of interest) in the sensory data, and to characterize the desired operating conditions (OCs). ATR technology originated in the military but today it is of a paramount importance to both the military and civilian applications [3]. In the literature, there is a wide range of ATR applications varying from recognizing a pre-known signature in homogeneous clutter to recognizing the source of the signature that varies considerably with pose and configuration and is located in a highly heterogeneous and probably occluded scene [4].

SAR images are not amenable for interpretation by the most sophisticated ATR systems, let alone the trained eye [5]. In order to handle the SAR imagery in a divide-and-conquer approach, an end-to-end ATR system for SAR imagery (SAR-ATR) is typically multistaged. The front-end stage in the processing chain is known as the detector. The intermediate stage is known as the low-level classifier (LLC). Finally,

the back-end stage is referred to as the high-level classifier (HLC) [6–12]. In this research, attention is focused on single-channel SAR (i.e., single polarization) imagery. A description of the SAR datasets used in this thesis is provided in Appendix A.

1.2. Motivations

The underpinning philosophy for science in general, and the field of signal processing in particular, is based on either one of two multidisciplinary worldviews: reductionism (also known as Newtonianism) and holism [13–15]. In the reductionist worldview, a complex system is assumed to be simply the superposition of its parts, and its analysis is reduced to the analysis of its individual components. Although this view may not seem to explicitly dismiss the existence of the so-called emergence phenomenon (i.e., multiplicity due to interactions between the individual components), it is implicit that the emergence phenomenon can be captured by the constituent processes. On the contrary, in the holistic worldview, the system is viewed as a whole that cannot be fully understood solely in terms of its constituent parts. This principle was succinctly summarized twenty-four centuries ago by Aristotle in Metaphysics: "The whole is greater than the sum of its parts" [15].

Reductionism and holism set the philosophical foundations of linear and nonlinear signal processing, respectively [13, 15]. In linear system theory [16], the reductionist view, in which the signal is decomposed into fragments that are analyzed individually, is applied verbatim. The analysis result for the whole signal is obtained from proper scaling (i.e., homogeneity property) and addition of the fragments (i.e., superposition property). For this process to hold, the central limit theorem (CLT) is invoked. Hence, in this approach, it is implicit that the signal samples are drawn from a distribution possessing a finite variance [17]. Accordingly, the linear system theory views deviation from linearity as a noise that warrants removal. For example, the Fourier view, the heart of linear system theory, assumes a first-order fundamental oscillation and bounding higher order harmonics. Despite its mathematical soundness, this view does not correspond to physical reality [18].

When the underlying random processes are nonlinear, advantages of the holistic approach should be apparent. Statistically, nonlinear signal processing is motivated by the generalized central limit theorem (GCLT) which holds that the variance of the

underlying random variables is infinite [19]. The Poincaré view [18, 20] is one such important view for nonlinear signal processing, which sets the foundations for chaos theory. The Hilbert view [18] is another salient view which was popularized after the advent of the Hilbert-Huang transform (HHT) [21], an important advancement in adaptive nonlinear and nonstationary signal processing.

Conventional radar resolution theory, which is a resolution theory of point targets [22], is a direct application of the reductionist view. Thus, analysis of the single-channel SAR image has traditionally been based on linear techniques associated with the image intensity while the phase content is ignored. The conclusion, based on the empirical observation that man-made targets produce dispersive scattering, that linear theory cannot adequately deal with extended targets has been reported in the literature [23–25]. In effect, dispersive scattering induces a nonlinear phase modulation in the radar return signal which causes a mismatch in the correlator's output. This phenomenon is preserved in the complex-valued image rather than the detected one.

Research efforts into nonlinear scattering effects can be broadly classified into two branches: (1) development of methods which seek to explicitly exploit the nonlinear phenomenon, and (2) development of techniques to harness the nonlinear dynamics embedded in the data generated by the linear signal processing methods. The research work presented in this thesis is concerned with the second branch, as it is applied to the focused *single-channel* complex-valued SAR image.

1.3. Origin of the Nonlinear Phenomenon in SAR Imagery

The baseband backscatter x_{BB} from a single point target, output from the quadrature demodulator and downlinked to the SAR processor, is known as the phase history or the raw data and is given by [22]

$$\begin{aligned} x_{BB}(\tau,\eta) = A\exp(j\psi)\Bigg\{ & w_r\left(\tau - 2\frac{R(\eta)}{c}\right) w_a(\eta-\eta_c) \\ & \exp\left(-j4\pi f_o \frac{R(\eta)}{c}\right)\exp\left(j\pi K_r\left(\tau - 2\frac{R(\eta)}{c}\right)^2\right)\Bigg\}. \end{aligned} \tag{1.1}$$

Here, A is the backscatter coefficient (i.e., σ_o), ψ is a phase change in the received pulse due to the scattering process from a surface, $j = \sqrt{-1}$, τ is the fast time, η is the slow time, $w_r(\tau) = \text{rect}(\tau/T_r)$ is the transmitted pulse envelope, T_r is the pulse duration, $R(\eta)$ is the distance between the radar and the point target, $\underline{c}$ is the speed of light in a vacuum, $w_a(\eta)$ is the two-way azimuth beam pattern, η_c is the beam center in the azimuth direction, f_o is the center frequency, and K_r is the frequency modulation (FM) rate of the range pulse. The SAR raw signal $x_{BB}(\tau, \eta)$ is conventionally modeled as

$$x_{BB}(\tau, \eta) = g(\tau, \eta) \otimes h(\tau, \eta) + n(\tau, \eta), \tag{1.2}$$

where $\otimes$ denotes convolution, $g(\tau, \eta)$ is the ground reflectivity, $h(\tau, \eta)$ is the impulse response of the SAR, and $n(\tau, \eta)$ is a noise component mainly due to the front-end receiver.

The SAR processor solves for $g(\tau, \eta)$. Following conventional radar resolution theory, $h(\tau, \eta)$, bounded by the curly brackets in Eq. 1.1, is an impulse response of a point target. For a given reflector within the radar illumination time, ψ is assumed to be constant [22]. For the case of an extended target, this assumption is adopted verbatim. Hence, such a target is modeled as the linear combination of its point reflectors. However, the assumption of constant ψ is violated in the presence of dispersive scattering from cavity-like reflectors, typical in stationary and moving man-made (extended) targets such as vehicles and airplanes. These reflectors trap the incident wave before it is backscattered, thus, inducing a phase modulation. The problem arises when the phase modulation is nonlinear. Besides the phase modulation, this phenomenon also introduces amplitude modulation (AM) [23–25]. Thus, the backscatter term in Eq. 1.1 is rewritten

$$s(\tau(f_\tau), \eta) = A(\tau(f_\tau), \eta) \exp(j\psi(\tau(f_\tau), \eta)), \tag{1.3}$$

where $\tau(f_\tau)$ is the time delay due to the phase modulation, and f_τ indicates a frequency which varies across the spectral width of the chirp, B. In Eq. 1.3, it is emphasized that the magnitude and phase of the backscatter is frequency dependent. While the

amplitude modulation is a linear process, this is often not the case for the phase modulation. Indeed, based on the principle of stationary phase (POSP), the time delay induced by a dispersive scatterer is

$$\tau\left(f_\tau\right) \propto \frac{\mathrm{d}}{\mathrm{d}f}\left(f_\tau\right)^O, \tag{1.4}$$

where O is the order induced by the dispersive scatterer. For $O \in \{0, 1, 2\}$, the phase modulation is linear, and its effect is either translation or smearing of the response in the correlation filter. Another reason for the smearing of the response is the variable Doppler processing used for motion compensation. However, for $O \notin \{0, 1, 2\}$, the phase center possesses a nonlinear delay which introduces spurious effects in the correlator's output. This phenomenon is referred to as 'sideband responses', and the information about it is preserved in the complex-valued image but not in the detected one. Furthermore, in the presence of an extended target, it is empirically observed that this effect dominates the focused SAR imagery [23–25]. The sideband responses are radically different from the range and Doppler sidelobes. One of the reasons for this is that they are among the strongest responses. Secondly, unlike the range and the Doppler sidelobes, they are not restricted to the range and cross range gates. Thirdly, they are distributed over an area far larger than that occupied by the target. As stressed in [23–25], these sideband responses cannot be suppressed by weighting methods because they are target generated. Clearly, the nonlinear phase modulation violates the conventional radar resolution theory.

1.4. Research Objective(s)

The primary objective of this research is the *development of novel tools that take advantage of the nonlinear phenomenon in focused single-channel SAR imagery*, and *to apply the developed tools to the problem of SAR-ATR*. The specific objectives of this research are the following: *first*ly, to ascertain the status quo in SAR-ATR; *second*ly, to develop a low-level understanding of the SAR data as well as the various factors that impact the SAR image; and *finally*, to design novel *features*, inherently specific to SAR imagery, suitable for use in SAR-ATR.

1.5. Research Methodology

In order to achieve the objective of this research, our research methodology was built on four bottom-up research problems ordered as follows. Firstly, a review for the state-of-the-art in SAR-ATR was conducted. This aimed at determining the status quo in the field and defining a way forward. Secondly, the design and implementation of an operational SAR system was undertaken. This provided for a firsthand understanding of the various factors that impact the SAR image. Thirdly, examination and development of methods for nonlinear and complex-valued statistical signal processing for SAR imagery were conducted. This offered an in-depth study of the inherent statistical characteristics of the SAR data and provided tools to take advantage of these statistics. Fourthly, a target recognition system for single-channel SAR imagery was designed. This allowed for interrelating and applying the findings obtained previously to the SAR-ATR problem. Accordingly, the efficacy of the method(s) developed was gauged.

To facilitate the development of the research work proposed in this thesis, five work packages (WPs) were developed with specific tasks and sub-tasks. Under each WP, listed below are the main problems underpinning the development of the research along with the proposed solutions and methodology to tackle these problems, and the overall contributions to the body of knowledge in this field.

1.5.1. WP1000: Review for the State-of-the-Art in SAR-ATR

1.5.1.1. Problem Statement

SAR-ATR is a difficult and diverse problem that continues to receive increasing attention from researchers around the globe. As is evidenced in the overwhelming number of research articles published on the subject in the open literature, there is a lack of a unified framework for this topic. That is, different researchers tend to approach the topic from different perspectives. This makes it challenging to relate the various research findings and to grasp the relationship between these various approaches.

1.5.1.2. Solution and Methodology

The development of a review for the state-of-the-art pertinent to the end-to-end SAR-ATR system involved more than a literature review. Rather, this review work offered an umbrella under which the various research activities in the field are broadly probed and taxonomized. Thus, here, we proposed relevant taxonomies, identified and summarized the underpinnings of the methods surveyed, pinpointed advantages, shortcomings and challenges, and proposed relevant evaluation criteria for existing systems along with a benchmarking scheme for a new system design. The ultimate goal was to produce a review article(s) suitable for publication in relevant reputable venues. To achieve this goal, the following sub-tasks were defined:

WP1100: Development of a literature review for target detection in SAR imagery. This sub-task was devoted to a literature review on the front-end stage in the SAR-ATR processing chain.

WP1200: Development of a literature review for target classification in SAR imagery. This sub-task was devoted to a literature review on the intermediate (i.e., LLC) and the back-end (i.e., HLC) stages in the SAR-ATR processing chain.

WP1300: Development of an analysis for the status quo in SAR-ATR. This sub-task aimed to provide analysis and interpretation for the constituents of the SAR-ATR system both on the individual stage-level as well as for the end-to-end perspective.

WP1400: Production of a state-of-the-art review article(s) to disseminate results. This sub-task was devoted to encapsulating our findings in research article(s) suitable for publication in reputable venues on the subject.

1.5.1.3. Contribution(s) to the Body of Knowledge

The primary outcome from WP1000 is the development of in-depth review works that offer analysis of the state-of-the-art in SAR-ATR. These review works provided a roadmap that encapsulated the past and present of the subject along with a hint on the future.

1.5.1.4. Overall Progress

WP1000 was completed. Two review articles were authored. The first article is pertinent to the front-end stage in the SAR-ATR processing chain. This article has already been published in the Journal of Applied Remote Sensing. Please see [**J-1-WP1000**] under Sect. 1.6. The second article is a book chapter which encompasses a review for the intermediate and back-end stages in the SAR-ATR processing chain along with a perspective for the end-to-end system. Please refer to [**B-1-WP1000**] under Sect. 1.6. A synopsis of these review works is presented as part of a literature review under Chapter 2.

1.5.2. WP2000: Design and Implementation of an Operational SAR System

1.5.2.1. Problem Statement

The lowest-level SAR data commercially and/or publicly available is that output from the SAR processor (i.e., focused). The lack of phase history implies that extreme limitations are imposed on the end-user (particularly, the researcher) which can be summarized in two main aspects. Firstly, having only the focused output means that a lack of practical knowledge for the various low-level factors that impact the focused SAR image, such as the effect the SAR processor intrinsically has on the raw data. This firsthand knowledge is important for developing an in-depth understanding of the focused SAR image which is instrumental, for example, in developing novel ATR tool(s) specifically tailored to SAR imagery. Secondly, the restriction imposes an inability to apply relevant algorithms in the phase-domain (prior to focusing), for example, to experiment with and develop relevant techniques such as compressive sensing [26], video SAR [27], various SAR focusing algorithms [22, 28], and detection and classification of targets in the phase-domain [29, 30]. Such topics cannot be properly researched without unrestricted access to the SAR phase history.

1.5.2.2. Solution and Methodology

To circumvent the phase history problem it was proposed to design and build an operational and cost-effective SAR system. This entailed designing both the hardware

and the required SAR processor (i.e., focusing algorithm). Commercial off-the-shelf (COTS) items were used as applicable. While a small dataset based on the designed SAR system was developed, the ultimate goal here was not to develop a dataset compatible with those available for use in this thesis. Developing such dataset is a time-consuming task beyond the scope of this thesis. However, throughout this exercise it was expected to develop an in-depth understanding for the SAR phase history, the SAR processor, and the impact of focusing on the SAR phase history, among other issues. Further, additional applications of this exercise were expected to extend beyond the scope of this thesis. To achieve our SAR system design and implementation, the following sub-tasks were defined:

WP2100: Setting of the design objective(s) and option(s). This sub-task aimed at defining the design objective of our SAR system for the purpose of this thesis work. Primarily, the design offers a low-power SAR system that provided hands-on demonstration of the SAR imaging process, both on the low-level and the high-level. Various design options were researched. Ideally, a design option that enabled achieving our objective with minimum hardware cost and man-hours was chosen.

WP2200: Definition of design requirements and budget. This sub-task was undertaken in order to define the design requirements, in terms of both the hardware and software, for the design option identified in WP2100. On the hardware design level, specific interrelated design parameters such as resolution, center frequency, bandwidth and transmit power, among others, needed to be specified. Then, specific hardware items were either purchased (i.e., COTS) or built, if found possible and more affordable. These items include: radio frequency (RF) components, passive components, active components, transmit and receive antennas, and analog-to-digital converter (ADC), among others. On the software design level, a suitable SAR digital signal processor was appropriately adopted.

WP2300: Building of the system hardware. This sub-task translated the SAR hardware design plan in WP2200 into action. A suitable printed circuit board (PCB) was built and populated. The overall hardware of the SAR system was integrated together. A suitable vector network analyzer (VNA) was sought to characterize the system's performance.

WP2400: Building of the system software. In this sub-task, the SAR digital signal processor, researched in WP2200, for focusing the SAR phase history into a SAR image, was implemented.

WP2500: Examination of SAR phase history, and producing focused SAR imagery for a limited number of targets. Under this sub-task, a limited number of targets was imaged using our SAR system. This fulfilled the objective of the SAR system designed for this thesis.

WP2600: Production of research article(s) and dissemination of the results. This sub-task aimed at encapsulating our SAR system design experience in one or more research articles for publication in relevant venue(s) on the subject.

1.5.2.3. Contribution(s) to the Body of Knowledge

The primary outcome of WP2000 was to provide a low-cost facility for hands-on examination of the phase history, the SAR processor, and various factors (i.e., both low-level and high-level) that impact the SAR image. This provided for examining the value of the phase history for direct use in SAR-ATR. Furthermore, this paved the way for an in-depth understanding of the SAR image. Thus, specific features and a SAR-ATR system that take advantage of the inherent characteristics of the SAR data were able to be developed.

1.5.2.4. Overall Progress

The completed work alluded to under WP2000 resulted in the description of the design and implementation of the operational SAR system being disseminated in a research article. Please refer to [**C-1-WP2000**] under Sect. 1.6. This paper is presented in Chapter 3.

1.5.3. WP3000: Development of Methods for Nonlinear and Complex-Valued Statistical Signal Processing for SAR-ATR

1.5.3.1. Problem Statement I: Nonlinear Statistical Signal Processing for SAR-ATR

An assumption of linearity underpins most commonly used algorithms for SAR-ATR. Indeed, the single-channel SAR image is often implicitly assumed to be linear. The main reason for this assumption is the general desire to use foundational radar resolution theory, which is a resolution theory of point targets [22, 28]. In the literature, there are two definitions of linearity considered [31–34]: (1) the definition of a strictly linear signal, and (2) the commonly adopted definition of a linear signal. In the former, the signal is assumed to be generated by a linear time invariant (LTI) or a linear space invariant (LSI) system with a white Gaussian noise. The definition of the latter is similar to the former but in the latter the magnitude distribution is allowed to deviate from the Gaussian distribution. This implies that the strictly defined linear signal is allowed to be characterized by a nonlinear observation function. Thus, the use of linear digital signal processing methods on the latter is justified in the literature. The main reason for the popularity of the linear signal processing techniques is their rich and well-defined linear system theory and simplicity of implementation. However, if the SAR data is proven to be nonlinear, significant gains from applying relevant nonlinear techniques to the SAR-ATR problem are to be anticipated [19]. This is because nonlinear methods allow for exploiting the nonlinear statistics often ignored by common linear signal processing methods.

1.5.3.2. Solution and Methodology for Problem Statement I

While the SAR sensor is often characterized in the literature as a linear system [22, 28], this does not guarantee that the focused image output from the SAR processor is linear. Furthermore, with the advent of high resolution radars, the insufficiency of the standard radar resolution theory to extended targets has been reported in the literature [23–25]. This was based on the empirical observation that man-made targets induce a nonlinear phase modulation in the radar return signal due to so-called dispersive scattering. It is observed that much of the information about this phenomenon is preserved in the complex-valued SAR image rather than the detected one. Accordingly,

it is important to research and define a suitable method for characterizing the linearity/nonlinearity of the SAR image. If images are found to be nonlinear, the usage of suitable nonlinear signal processing methods is strongly justified. Primarily, nonlinear techniques are expected to achieve advantages both for detection and classification of targets in SAR imagery. To achieve our goal, the following sub-tasks were defined:

WP3100: Investigation of the linearity/nonlinearity of the SAR data. This sub-task aimed at researching suitable method(s) for characterizing the statistical significance for linearity/nonlinearity in the SAR data. Then, the complex-valued SAR image was examined for linearity/nonlinearity. Finally, the effect of detection on linearity/nonlinearity in the SAR data was investigated.

WP3300: Development of suitable nonlinear method(s) for characterizing the SAR data. This sub-task was contingent upon WP3100. When found nonlinear, suitable methods to exploit this characteristic in SAR imagery were researched and properly developed. Further, results from this sub-task were utilized in WP4000 described under Sect. 1.5.4.

1.5.3.3. Problem Statement II: Complex-Valued Statistical Signal Processing for SAR-ATR

In most SAR-ATR works published in the literature utilizing single look complex (SLC) SAR imagery, and particularly for single polarization, the phase content is entirely discarded. A common belief among researchers in the field is that the phase is random and uniformly distributed (i.e., in the range $(-\pi, \pi]$), and, thus, is useless. Subsequently, either the detected magnitude image, intensity image, or a radiometrically calibrated relative is exclusively used. This is often (implicitly) justified by the hypotheses of the so-called fully-developed speckle model [35, 36], built on standard radar resolution theory, which as already noted is not strictly applicable to high resolution SAR imagery. Another relevant problem is the underlying (and often implicit) assumption for circularity (also known as propriety) [12, 37, 38]. The assumption of circularity means that the complex-valued SAR image has a probability distribution that is invariant under rotation in the complex plane. It also implies that the complex-valued SAR image is uncorrelated with its complex-conjugate. Accordingly, discarding the phase

content in single-channel SAR imagery implies that all the foregoing assumptions are satisfied, otherwise, important information about the targets in the complex-valued SAR imagery is lost.

1.5.3.4. Solution and Methodology for Problem Statement II

To address the issues identified under Sect. 1.5.3.3, the following tasks were outlined. Firstly, proper tools to examine the circularity in complex-valued SAR imagery were identified. Secondly, suitable methods(s) for the characterization and statistical modeling of complex-valued SAR imagery were developed. As discussed under WP4000 (see Sect. 1.5.4) these method(s) were properly exploited in the form of features. To achieve our goal, the following sub-tasks were defined:

WP3200: Investigation of the non-circularity (also known as impropriety) of the complex-valued SAR data. This sub-task aimed at researching the literature for suitable tools to characterize the complex-valued statistics in SAR imagery. Then, these tools were applied to complex-valued SAR imagery.

WP3400: Development of suitable method(s) for characterization and statistical modeling of complex-valued SAR data. This sub-task was contingent upon WP3200. Suitable tools that exploit the complex-valued statistics in SAR imagery were designed. More specifically, statistical model(s) for the phase and/or the complex-valued SAR image were developed. Furthermore, features that exploit the complex-valued statistics in SAR imagery were identified. The results from this sub-task were utilized under WP4000 in Sect. 1.5.4.

WP3500: Production of research article(s) and dissemination of the results. The overall findings under WP3000 were encapsulated in research article(s) suitable for dissemination in relevant venue(s) on the subject.

1.5.3.5. Contribution(s) to the Body of Knowledge

WP3000 provides an in-depth understanding of the SAR data in terms of nonlinearity and complex-valued statistics. This leads to an informed choice and development of

suitable tools for target detection and target classification in SAR imagery as encapsulated in WP4000 below. Furthermore, WP3000 provided for the development of features that account for the intrinsic statistical characteristics specific to SAR imagery.

1.5.3.6. Overall Progress

The completion of WP3000 resulted in an in-depth analysis of the nonlinearity and the noncircularity in complex-valued SAR imagery. Moreover, the effect of detection on the nonlinear statistics in the SAR image has been studied. In the presence of extended targets, it is found that the SAR image is intrinsically nonlinear. Furthermore, a method for characterizing the phase content in complex-valued SAR imagery was developed. Upon applying the developed method, it was found that in the presence of extended targets, the complex-valued SAR image is inherently noncircular. Additionally, statistical model for the characteristic phase image was derived. Finally, a comprehensive set of novel features that take advantage of the complex-valued and the noncircular statistics has been devised. Our results are disseminated in multiple research articles as follows (see Sect. 1.6). Firstly, the effect of detection on the spatial resolution in complex-valued SAR imagery was studied in [**J-2-WP3000**] and [**C-3-WP3000**]. Secondly, the statistical significance for the nonlinear dynamics in complex-valued SAR imagery, and the effect of detection on the nonlinearity were investigated in [**J-2-WP3000**], [**C-4-WP3000**] and [**C-5-WP3000**]. Finally, circularity/noncircularity, phase characterization and modeling were presented in [**J-4-WP3/4000**], [**C-6-WP3000**], [**C-7-WP3000**], and [**C-8-WP3/4000**]. In this thesis, [**J-2-WP3000**], [**C-8-WP3/4000**] and [**J-4-WP3/4000**] are presented in Chapter 4, Chapter 5 and Chapter 6, respectively.

1.5.4. WP4000: Application to Target Recognition in SAR Imagery

1.5.4.1. Problem Statement

SAR-ATR is a multidisciplinary field. In order to design a successful SAR-ATR system, not only an in-depth understanding of the intrinsic characteristics of the SAR

image is required but also a comprehension of the state-of-the-art pertaining to pattern classification (in the SAR-ATR context) is entailed. The knowledge and tools accumulated from earlier WPs need to be translated into a practical SAR-ATR system. This provides for applying the knowledge acquired and demonstrating the value of the newly developed features in SAR-ATR.

1.5.4.2. Solution and Methodology

To address the problem statement highlighted above, our aim was to develop an HLC classifier for target recognition in SAR imagery. For the sake of manageability, our attention in this thesis was restricted to the HLC stage in the SAR-ATR processing chain. However, the techniques developed may be applicable or extendable to both the front-end and the intermediate stages of the SAR-ATR system. The HLC classifier was solely based on nonlinear, complex-valued and phase-based features. Multiple instances for the HLC classifier based on different combinations of features were investigated. Comparison with standard baseline features based on the detected image was also considered. The performance of the HLC classifiers developed were properly assessed and compared. To achieve our goal, the following sub-tasks were defined:

WP4100: Development of baseline features. A suitable set of standard features based on the detected SAR image were defined and extracted. These features were used to train a suitable feature-based classifier. The classification accuracy of this classifier was used for comparison with our novel features.

WP4200: Development of nonlinear and phase-based features Under this subtask, two sets of features were developed. Firstly, nonlinear features based solely on the complex-valued SAR image were constructed. The purpose for this set of features was to utilize the nonlinear dynamics in complex-valued SAR imagery. Suitable methods for feature extraction utilizing nonlinear and nonstationary signal processing methods were researched. Furthermore, methods motivated by chaos theory were also investigated. Secondly, features based solely on the phase image were extracted. These features were used to take advantage of the characteristic phase image as well as the phase model developed under WP3000 in Sect. 1.5.3.4.

WP4400: Development and assessment of HLC classifiers. This sub-task aimed at properly assessing the performance of the features developed under WP4100 and WP4200. Primarily, multiple instances of a multi-class support vector machine (SVM) classifier [39] were utilized. SVM was chosen mainly because it is a powerful method for feature-based classification, and it was found to offer excellent performance for our SAR dataset. In the first instance, a classifier based on the baseline features was constructed. Additional SVM classifier instances based on the nonlinear and the phase features were also developed. Furthermore, other instances of the SVM classifier utilizing different combinations of the preceding features were examined and compared. Classification accuracy for each classifier was presented in terms of a confusion matrix. The statistical significance for the various features was computed, and was used to rank and select the features accordingly.

WP4400: Production of research article(s) and dissemination of the results. The overall findings under WP4000 were encapsulated in multiple research articles and disseminated in relevant venue(s) on the subject.

1.5.4.3. Contribution(s) to the Body of Knowledge

The ultimate outcome of this research was to apply the knowledge, tools and algorithms developed to construct new features for target recognition in SAR imagery. Various novel features that exploit the often ignored nonlinear dynamics in complex-valued SAR imagery were developed. Furthermore, additional set of features solely based on the often discarded phase image were presented. The statistical significance of these new features was clearly demonstrated on the SAR dataset available for this research work.

1.5.4.4. Overall Progress

WP4000 was completed. For the case of extended targets, the importance of the nonlinear dynamics for target recognition in complex-valued SAR imagery was clearly demonstrated. Furthermore, the statistical significance for the information carried in the phase image was confirmed. Our overall findings were disseminated in multiple research articles as follows (see Sect. 1.6). Firstly, a method for estimating the

nonlinear order of the scatterers in complex-valued SAR imagery was introduced in [**C-8-WP3/4000**]. These nonlinear scatterers serve as important features for target recognition in SAR imagery. Secondly, the statistical significance for various solely phase-based features was presented in [**J-4-WP3/4000**]. Finally, our overall major research findings were provided in [**J-5-WP4000**]. In that paper, multiple comparisons and assessments of different features was detailed. In this thesis, [**J-5-WP4000**] is presented in Chapter 7.

1.5.5. WP5000: Thesis Writing

This final WP is devoted to thesis writing. Given the publication-oriented style through which our research work has been conducted, the manuscript-based thesis format has been followed. The research papers chosen for incorporation into this dissertation are summarized in Sect. 1.7.

1.6. Publications

Our overall research findings are contained in the following research articles:

- **Book Chapter**

  [**B-1-WP1000**] **K. El-Darymli**, P. McGuire, E. W. Gill, D. Power, and C. Moloney, *Automatic Target Recognition in SAR Imagery (SAR-ATR): A State-of-the-Art Review,* 2015 *[To be submitted*].

- **Journal Papers**

  [**J-1-WP1000**] **K. El-Darymli**, P. McGuire, D. Power, and C. Moloney, "Target detection in synthetic aperture radar imagery: a state-of-the-art survey," *Journal of Applied Remote Sensing*, vol. 7, no. 1, 2013. Available: http://dx.doi.org/10.1117/1.JRS.7.071598

  [**J-2-WP3000**] **K. El-Darymli**, P. McGuire, E. W. Gill, D. Power, and C. Moloney, "Effect of detection on spatial resolution in synthetic aperture radar imagery and mitigation through upsampling," *Journal of Applied Remote Sensing*, vol. 8, no. 1, 2014. Available: http://d x.doi.org/10.1117/1.JRS.8.083601

[**J-3-WP3000**] **K. El-Darymli**, E. W. Gill, P. McGuire, D. Power, and C. Moloney, "Unscrambling nonlinear dynamics in synthetic aperture radar imagery," 2015 *[Under Review]*.

[**J-4-WP3/4000**] **K. El-Darymli**, P. McGuire, E. W. Gill, D. Power, and C. Moloney, "Characterization and statistical modeling of phase in single-channel synthetic aperture radar imagery," *Aerospace and Electronic Systems, IEEE Transactions on,* 2015 *[Accepted]*.

[**J-5-WP4000**] **K. El-Darymli**, P. McGuire, E. W. Gill, D. Power, and C. Moloney, "Holism for target classification in synthetic aperture radar imagery," 2015 *[Under Review]*.

- **Conference Papers**

[**C-1-WP2000**] **K. El-Darymli**, C. Moloney, E. W. Gill, P. McGuire, and D. Power, "Design and implementation of a low-power synthetic aperture radar," in *International Geoscience and Remote Sensing Symposium (IGARSS'14), IEEE, Quebec, Canada,* 2014. [Online]. Available: http://dx.doi.org/10.1109/IGARSS.2014.69466184

[**C-2-WP3000**] **K. El-Darymli**, P. Mcguire, E. W. Gill, D. Power, and C. Moloney, "Understanding the significance of radiometric calibration for synthetic aperture radar imagery," in *Electrical and Computer Engineering (CCECE), 2014 IEEE 27th Canadian Conference on.* Toronto, Canada, 2014, pp. 1-6. Available: http://dx.doi.org /10.1109/CCECE.2014.6901104

[**C-3-WP3000**] **K. El-Darymli**, P. McGuire, D. Power, and C. Moloney, "An algorithm for upsampling spotlight SAR imagery: a Radarsat-2 SLC perspective," in *Algorithms for Synthetic Aperture Radar Imagery XX,* vol. 8746. Baltimore, USA: SPIE, 2013, pp. 874 607–874 607–9. Available: http://dx.doi.org/10.1117/12.2011151

[**C-4-WP3000**] **K. El-Darymli**, P. Mcguire, D. Power, and C. Moloney, "Nonlinearity in synthetic aperture radar imagery," in *Newfoundland Electrical and Computer Engineering Conference (NECEC'13)*, St. John's, Newfoundland, 2013. [Wally Read Best Student Paper Award].

[**C-5-WP3000**] **K. El-Darymli**, C. Moloney, E. W. Gill, P. McGuire, and D. Power, "Nonlinearity and the effect of detection on single-channel synthetic aperture radar imagery," in *OCEANS'14 MTS /IEEE,* Taipei, Taiwan, 2014. Available: http://dx.doi.org/10.1109/OCEANS-TAIPEI.2014.6964493

[**C-6-WP3000**] **K. El-Darymli**, P. McGuire, D. Power, and C. Moloney, "Rethinking the Phase in Single-Channel SAR Imagery," *IEEE 14th International Radar Symposium (IRS)* 2013, Dresden, Germany. Available: http://bit.ly/1or0pdo

[**C-7-WP3000**] **K. El-Darymli**, C. Moloney, E. W. Gill, P. McGuire, and D. Power, "On circularity/noncircularity in single-channel synthetic aperture radar imagery," in *OCEANS'14 MTS/IEEE,* St. John's, Canada, 2014. Available: http://dx.doi.org/10.1109/OCEANS.2014.7003163

[**C-8-WP3/4000**] **K. El-Darymli**, C. Moloney, E. W. Gill, P. McGuire, and D. Power, "Recognition of nonlinear dispersive scattering in SAR imagery," in *IEEE IGARSS/CSRS'14,* Quebec, Canada, 2014. Available: http://dx.doi.org/10.1109/IGARSS.2014.6947548

1.7. Organization of the Dissertation

The remainder of this dissertation is organized as follows.

Chapter 2: Literature Review This chapter offers a synopsis of two state-of-the-art review articles for automatic target recognition in SAR imagery (SAR-ATR) taken from [**B-1-WP1000**] and [**J-1-WP1000**]. Firstly, ATR in the SAR context is introduced. Secondly, the target detection module of the front-end stage is considered. Thirdly, the target classification module of the intermediate and the back-end stages is addressed. Taxonomy for the major methods under each module is proposed. Further, a brief description pertaining to the architecture of each taxon is offered. Additionally, representative examples from the literature are provided.

Chapter 3: Design and Implementation of a Low-Power Synthetic Aperture Radar This chapter is for the research article [**C-1-WP2000**]. It reports on the design and implementation of a high-resolution low-power SAR. Our system utilizes the linear frequency-modulated continuous wave (LFMCW) concept, and it operates in the S-band. The generic architecture for our design is presented along with a description of the digital SAR processor. Finally, for demonstration purposes, a focused SAR image for a ground-truthed target is provided.

Chapter 4: Unscrambling Nonlinear Dynamics in Synthetic Aperture Radar Imagery This chapter is for the research article [**J-3-WP3000**]. In analyzing single-channel SAR imagery, three interrelated questions often arise. Firstly, should one use the detected or the complex-valued image? Secondly, what is the 'best' statistical model? Thirdly, what constitute the 'best' signal processing methods? This chapter addresses these questions from the overarching perspective of the generalized central limit theorem, which underpins nonlinear signal processing. A novel procedure for characterizing the nonlinear dynamics in SAR imagery is proposed. To apply the procedure, three complementary 1-D abstractions for a 2-D SAR chip[1] are introduced. Our analysis is demonstrated on real-world datasets from multiple SAR sensors. The nonlinear dynamics are found to be resolution-dependent. As the SAR chip is detected, nonlinear effects are found to be obliterated (i.e., for magnitude-detection) or altered (i.e., for power-detection). In the presence of extended targets (i.e., nonlinear scatterers), it is recommended to use the complex-valued chip rather than the detected one. Further, to exploit the embedded nonlinear statistics, it is advised to utilize relevant nonlinear signal analysis techniques.

Chapter 5: Recognition of Nonlinear Dispersive Scattering in Synthetic Aperture Radar Imagery Imagery This chapter is for the research article [**C-8-WP3/4000**]. It presents a new insight into the nonlinear dynamics in SAR imagery. For extended targets, the conventional radar resolution theory is violated due to the nonlinear phase modulation induced by the dispersive scatterers. A novel algorithm motivated by the Hilbert view for nonlinear phenomena is introduced. Our algorithm may be used to not only detect the dispersive scatterers but also to estimate the nonlinear order of the

[1]The term *chip* is used to refer to a smaller image, for a particular target or clutter, extracted from a bigger scene.

phase modulation. Our results are demonstrated on a representative real-world target chip.

Chapter 6: Characterization and Statistical Modeling of Phase in Single-Channel Synthetic Aperture Radar Imagery This chapter is for the research article [**J-4-WP3/4000**]. Traditionally, the phase content in single-channel synthetic aperture radar (SAR) imagery is discarded. This practice is justified by the conventional radar resolution theory, which is a theory strictly relevant to point targets. The advent of high-resolution radars permits small targets previously considered to be points to be now treated as extended targets, in which case this theory is not strictly applicable. With this in mind, this chapter offers a new insight into the relevance of phase in single-channel SAR imagery. The proposed approach builds on techniques from the fields of complex-valued and directional statistics. In doing so, three main contributions are presented, the first being a novel method for characterizing the phase content. Secondly, a new statistical model for the phase is considered, and then a set of fifteen solely-phase-based features are discussed. Our results are demonstrated on real-world SAR datasets for ground-truthed targets. The statistical significance of the information carried in the phase is clearly demonstrated. Furthermore, if applied to a dataset with higher resolution, the proposed techniques are expected to achieve even higher performance.

Chapter 7: Holism for Target Classification in Synthetic Aperture Radar Imagery This chapter is for the research article [**J-5-WP4000**]. Reductionism and holism are two worldviews underlying the fields of linear and nonlinear signal processing, respectively. The conventional radar resolution theory is motivated by the former view, and it is violated due to nonlinear phase modulation induced by the dispersive scattering typically associated with extended targets. Motivated by the latter view, this chapter offers a new insight into the process of feature extraction for target recognition applications in single-channel SAR imagery. Two novel frameworks for feature extraction are presented. The first framework is based solely on the often-ignored phase chip. The second framework uses the complex-valued 2-D SAR chip after it is transformed into a 1-D vector. This transformation provides for the utilization of various nonlinear and nonstationary time series analysis methods. Some representative nonlinear features based on these two frameworks are introduced. Further, for comparison pur-

poses, baseline features from the power-detected chip are also considered. Multiple instances of an eight-class SVM classifier are designed based on combinations of feature sets extracted from the public-domain MSTAR dataset. A classification accuracy of 93.4186% is achieved for the combination of the phase and 1-D based nonlinear features. This is in comparison to 73.6269% for the baseline features. Because the nonlinear phenomenon is resolution-dependent, our proposed approach is expected to achieve even greater accuracy for SAR sensors with higher resolution.

Chapter 8: Summary This is a concluding chapter summarizing the main lessons learned from this research work and wraps-up the dissertation. Also, suggestions for future work are provided.

1.8. Co-Authorship Statement

Mr. Khalid El-Darymli (thesis author) is the main author for all papers pertaining to this research work including those presented in Chapters 2 to 7. Other co-authors are: Dr. Peter McGuire (thesis supervisor), Mr. Desmond Power (thesis co-supervisor), Prof. Dr. Cecilia Moloney (thesis co-supervisor), and Prof. Dr. Eric W. Gill (thesis co-supervisor). Dr. McGuire is a Senior Project Engineer with C-CORE. He is also cross-appointed with the Faculty of Engineering and Applied Science at Memorial University of Newfoundland. Mr. Power is the Vice President for the department of Remote Sensing at C-CORE. Dr. Moloney is a Professor of Electrical and Computer Engineering with the Faculty of Engineering and Applied Science at Memorial University of Newfoundland. Dr. Gill is a Professor of Electrical Engineering with the Faculty of Engineering and Applied Science at Memorial University of Newfoundland.

The candidate was responsible for the conception and development of the ideas contained in each research paper. Programming for the techniques developed and data analysis were performed by the candidate, as were all duties associated with the preparation of each manuscript. Dr. McGuire, Mr. Power, Dr. Moloney and Dr. Gill critically reviewed the research manuscripts and suggested minor revisions.

Bibliography

[1] C. Jackson and J. Apel, *SAR marine user manual*, National Oceanic and Atmospheric Administeration (NOAA), 2004. [Online]. Available: http://www.sarusersmanual.com 1

[2] A. Love, "In memory of Carl A. Wiley," *Antennas and Propagation Society Newsletter, IEEE*, vol. 27, no. 3, pp. 17–18, 1985. [Online]. Available: http://dx.doi.org/10.1109/MAP.1985.27810 1

[3] M. Roth, "Survey of neural network technology for automatic target recognition," *Neural Networks, IEEE Transactions on*, vol. 1, no. 1, pp. 28–43, 1990. [Online]. Available: http://dx.doi.org/10.1109/72.80203 1

[4] D. Dudgeon, "ATR performance modeling and estimation," *Digital Signal Processing*, vol. 10, no. 4, pp. 269–285, 2000. [Online]. Available: http://dx.doi.org/10.1006/dspr.2000.0375 1

[5] M. Koch, M. Moya, L. Hostetler, and R. Fogler, "Cueing, feature discovery, and one-class learning for synthetic aperture radar automatic target recognition," *Neural Networks*, vol. 8, no. 7-8, pp. 1081–1102, 1995. [Online]. Available: http://tinyurl.com/mpyb9zk 1

[6] H. Chiang and R. Moses, "ATR performance prediction using attributed scattering features," in *Proc. of SPIE, Algorithms for Synthetic Aperture Radar Imagery VI*, vol. 3721, no. 785, 1999. [Online]. Available: http://dx.doi.org/10.1117/12.357693 2

[7] T. Cooke, "Detection and classification of objects in synthetic aperture radar imagery," Tech. Rep. DSTO-RR-0305, 2006. [Online]. Available: http://tinyurl.com/orx668d

[8] D. Kreithen, S. Halversen, and G. Owirka, "Discriminating targets from clutter," *The Lincoln Laboratory Journal*, vol. 6, no. 1, pp. 25–52, 1993. [Online]. Available: http://tinyurl.com/o3h2srf

[9] L. Novak, G. Owirka, W. Brower, and A. Weaver, "The automatic target-recognition system in SAIP," *Lincoln Laboratory Journal*, vol. 10, no. 2, pp. 187–202, 1997. [Online]. Available: http://tinyurl.com/q8o8f3x

[10] L. Novak, G. Owirka, and W. Brower, "An efficient multi-target SAR ATR algorithm," in *Signals, Systems and Computers, the Thirty-Second IEEE Asilomar Conference on*, vol. 1, 1998, pp. 3–13. [Online]. Available: http://dx.doi.org/10.1109/ACSSC.1998.750815

[11] N. Sandirasegaram, "Spot SAR ATR using wavelet features and neural network classifier," Defence Research and Development Canada Ottawa, Ontario, Tech. Rep. DRDC-TM-2005-154), 2005. [Online]. Available: http://pubs.drdc.gc.ca/PDFS/unc89/p524497.pdf

[12] J. Schroeder, "Automatic target detection and recognition using synthetic aperture radar imagery," in *Proc. of the 2002 Workshop on the Applications of Radio Science (WARS02) Conference*, 2002. [Online]. Available: http://tinyurl.com/oy5npsa 2

[13] A. Scott, "Reductionism revisited," *Journal of Consciousness Studies*, vol. 11, no. 2, pp. 51–68, 2004. [Online]. Available: http://www.ingentaconnect.com/content/imp/jcs/2004/00000011/00000002/art00004 2

[14] S. Y. Auyang, *Foundations of complex-system theories: in economics, evolutionary biology, and statistical physics*. Cambridge: UK: Cambridge University Press, 1999.

[15] A. Scott, Ed., *Encyclopedia of nonlinear science*. New York, NY: Routledge, Taylor & Francis Group, 2005. 2

[16] A. V. Oppenheim, *Discrete-Time Signal Processing*, 3rd ed. Upper Saddle River: NJ: Prentice-Hall, 2009. 2

[17] J. Rice, *Mathematical Statistics and Data Analysis*. Belmont, CA: Duxbury Press, 1995. 2

[18] N. Huang, Z. Shen, and S. Long, "A new view of nonlinear water waves: the Hilbert spectrum," *Annual Review of Fluid Mechanics*, vol. 31, no. 1, pp. 417–457, 1999. [Online]. Available: http://dx.doi.org/10.1146/annurev.fluid.31.1.417 2, 3

[19] G. R. Arce, *Nonlinear signal processing: a statistical approach.* Hoboken, NJ: Wiley-Interscience, 2004. 3, 11

[20] S. H. Strogatz, *Nonlinear dynamics and chaos (with applications to physics, biology, chemistry and engineering.* New York, NY: Perseus Publishing, 1994. 3

[21] N. Huang, Z. Shen, S. Long, M. Wu, H. Shih, Q. Zheng, N.-C. Yen, C. Tung, and H. Liu, "The empirical mode decomposition and the Hilbert spectrum for nonlinear and non-stationary time series analysis," *Proceedings of the Royal Society of London. Series A: Mathematical, Physical and Engineering Sciences*, vol. 454, no. 1971, pp. 903–995, 1998. [Online]. Available: http://dx.doi.org/10.1098/rspa.1998.0193 3

[22] I. Cumming and F. Wong, *Digital Processing of Synthetic Aperture Radar Data.* Norwood, MA: Artech House, 2005. 3, 4, 8, 11

[23] A. Rihaczek and S. Hershkowitz, "Man-made target backscattering behavior: Applicability of conventional radar resolution theory," *IEEE Transactions on Aerospace and Electronic Systems*, vol. 32, no. 2, pp. 809–824, 1996. [Online]. Available: http://dx.doi.org/10.1109/7.489523 3, 4, 5, 11

[24] ——, *Radar Resolution and Complex-Image Analysis.* Norwood, MA: Artech House, 1996.

[25] ——, *Theory and Practice of Radar Target Identification.* Norwood, MA: Artech House, 2000. 3, 4, 5, 11

[26] R. Baraniuk, E. Candes, R. Nowak, and M. Vetterli, "Compressive sampling [from the guest editors]," *Signal Processing Magazine, IEEE*, vol. 25, no. 2, pp. 12–13, 2008. [Online]. Available: http://dx.doi.org/10.1109/MSP.2008.915557 8

[27] DARPA. (2013) Video SAR (ViSAR). [Online]. Available: http://tinyurl.com/cpev5dv 8

[28] W. Carrara, R. Goodman, and R. Majewski, *Spotlight Synthetic Aperture Radar: Signal Processing Algorithms.* Artech House, 1995. 8, 11

[29] M. Friend, "Combat identification with synthetic aperture radar, out-of-library identification, and non-declarations," Ph.D. dissertation, Air Force Institute of Technology, 2007. 8

[30] T. Albrecht, "Optimization framework for a multiple classifier system with

non-registered targets," *Journal of Defense Modeling and Simulation*, vol. 5, no. 1, pp. 61–81, 2007. [Online]. Available: http://dx.doi.org/10.1177/154851290800500104 8

[31] T. Gautama, D. P. Mandic, and M. M. V. Hulle, "Signal nonlinearity in fMRI: A comparison between BOLD and MION," *IEEE Trans. Med. Imaging*, vol. 22, no. 5, pp. 636–644, 2003. [Online]. Available: http://dx.doi.org/10.1109/TMI.2003.812248 11

[32] ——, "The delay vector variance method for detecting determinism and nonlinearity in time series," *Physica D: Nonlinear Phenomena*, vol. 190, no. 3-4, pp. 167–176, 2004. [Online]. Available: http://dx.doi.org/10.1016/j.physd.2003.11.001

[33] R. G. Andrzejak, K. Lehnertz, F. Mormann, C. Rieke, P. David, and C. E. Elger, "Indications of nonlinear deterministic and finite-dimensional structures in time series of brain electrical activity: Dependence on recording region and brain state," *Physical Review E - Statistical, Nonlinear, and Soft Matter Physics*, vol. 64, no. 6I, pp. 061 907/1–061 907/8, 2001. [Online]. Available: http://dx.doi.org/10.1103/PhysRevE.64.061907

[34] T. Schreiber and A. Schmitz, "Surrogate time series," *Physica D: Nonlinear Phenomena*, vol. 142, no. 3-4, pp. 346–382, 2000. [Online]. Available: http://dx.doi.org/10.1016/S0167-2789(00)00043-9 11

[35] J. C. Dainty, *Laser Speckle and Related Phenomena*. Springer-Verlag, 1984. 12

[36] H. Maitre, Ed., *Processing of Synthetic Aperture Radar Images*. Hoboken, NJ: ISTE and Wiley, 2008. 12

[37] T. Adali and S. Haykin, *Adaptive Signal Processing*. Hoboken, NJ: Wiley, 2010. 12

[38] P. J. Schreier and L. L. Scharf, *Statistical signal processing of complex-valued data the theory of improper and noncircular signals*. Cambridge, UK: Cambridge University Press, 2010. 12

[39] R. Duda, P. Hart, and D. Stork, *Pattern classification*. New York: John Wiley and Sons, 2001. 16

2. Literature Review

2.1. Overview

This chapter offers a synopsis of two reviews of the state-of-the-art for automatic target recognition in SAR imagery (SAR-ATR) from [1, 2]. Firstly, ATR in the SAR context is introduced. Secondly, the target detection module of the front-end stage is considered. Thirdly, the target classification module of the intermediate and the back-end stages is addressed. Taxonomy for the major methods under each module is proposed. Further, a brief description pertaining to the architecture of each taxon is offered. Additionally, representative examples from the literature are provided.

2.2. Automatic Target Recognition in the SAR Context (SAR-ATR)

Automatic target recognition (ATR) deals with the information output from one (or more) sensor(s) aimed at a scene of interest. ATR generally refers to the use of computer processing capabilities to infer the classes of the targets in the sensory data, and to (optionally) characterize some attributes of interest such as articulation, orientation, occlusion, sub-class and so on, without human intervention. The term ATR originated in the military in the early 1980s under the Low Altitude Navigation and Targeting Infrared for Night (LANTRIN) program [3]. Today, ATR technology is important to both military and civilian applications. The ATR problem is a part of the general broad problem of machine vision, namely, *how can computers be configured to do what we humans do efficiently and naturally?*

Target, clutter and noise are three terms of military origin associated with ATR and are dependent on the application of interest. In the case of SAR imagery, a target

refers to an object of interest in the imaged scene. Clutter refers to either man-made (e.g., building, vehicles, etc.) or natural objects (e.g., trees, topological features, etc.) which tend to dominate the imaged scene. Noise refers to imperfections in the SAR image which are result of electronic noise in the SAR sensor as well as computational inaccuracies introduced by the SAR signal processor. In the literature, there is a spectrum of ATR problems ranging from classifying a pre-known signature in a well-characterized clutter to recognizing the source of signature that varies greatly with pose and state, and is located in a highly complex and probably an occluded scene [4].

The general structure of an end-to-end SAR-ATR system as reported in the literature is depicted in Fig. 2.1. To counter the prohibitive amounts of processing pertaining to the input SAR imagery, the strategy is to divide-and-conquer. Accordingly, SAR-ATR processing is split into three distinctive stages: detection (also known as prescreening), low-level classification (LLC, also known as discrimination), and high-level classification (HLC) [5–13]. The first two stages together are commonly known as the focus-of-attention (FOA) module.

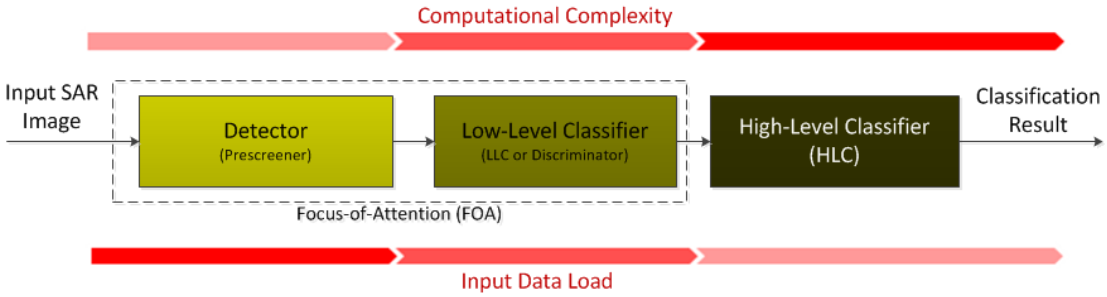

Figure 2.1: General structure for an end-to-end SAR-ATR system.

As the input SAR data progresses throughout the SAR-ATR processing chain, the data load is reduced. The HLC stage deals with SAR data that have relatively lower computational load. On the contrary, the computational complexity of the SAR-ATR chain increases as the SAR data progresses from the front-end stage toward the back-end stage. In the next sections, the three blocks depicted in Fig. 2.1 are briefly reviewed. The front-end stage is reviewed in Sect. 2.3. The intermediate and the back-end stages are reviewed in Sect. 2.4.

Central to the three stages in the SAR-ATR processing chain are the features. Features are heuristic measurable attributes of the individual objects being observed in the

SAR image. In order for the SAR-ATR algorithm to be successful, features pertaining to each stage should be discriminating and independent. Thus, the choice of particular feature(s), as well as the design of a particular stage in the SAR-ATR processing chain. entails an in-depth understanding of the SAR image.

2.3. The Detection Module (Front-End Stage)

Under this section a synopsis for the front-end stage in the SAR-ATR processing chain is presented. Firstly, a taxonomy for the various target detection methods is proposed. Then, a classification for the various detection approaches that fall under the proposed taxa is introduced. Finally, this section is ended with concluding remarks. An in-depth review for the state-of-the-art pertinent to the detection module can be found in our review article published in the Journal of Applied Remote Sensing [1].

2.3.1. Taxonomy and Architecture of the Detection Approaches

The detection module takes the entire SAR image and identifies the regions(s) of interest (ROI(s)). Ultimately, the detected regions in the SAR image are passed to the next stage in the SAR-ATR chain for further analysis. The goodness of any detection module is typically judged based upon three aspects of significance: computational complexity, probability of detection (PD), and false alarm rate (also known as probability of false alarm, PFA). The detection module should enjoy a low computational complexity such that it operates in real-time or near-real-time. This is in contrast to the succeeding stages in the SAR-ATR chain which are relatively more computationally expensive. Further, a good detection module should provide a means to refine detections, reduce clutter false alarms, and pass ROIs. Thus, such a detection method should exhibit a reasonable PFA and acceptable PD. We broadly taxonomize the target detection algorithms reported in the open literature into three major taxa: single-feature-based, multi-feature-based and expert-system-oriented. This taxonomy is depicted in Fig. 2.2.

The single-feature-based taxon bases the detection in the SAR image on a single feature, typically the brightness in the pixel intensity, which is proportional to the radar cross section (RCS). There exist various methods in the literature that fall under

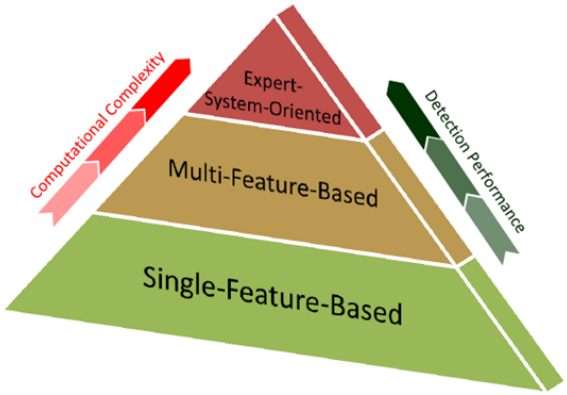

Figure 2.2: Taxonomy of target detection methods for SAR imagery.

this taxon. The single-feature-based approach is placed at the base of the pyramid in Fig. 2.2 because it is the most common and widely used in the literature. Further, the single-feature-based approach is the building block for the other two taxa.

The multi-feature-based taxon bases the detection decision on a fusion of two or more features extracted from the input SAR image. Besides the RCS, additional features that can be inferred and fused include multi-resolution RCS (i.e., features extracted from the intensity image after it is analyzed with mulch-resolution technique such as the continuous wavelet transform) and fractal dimension, among others. Obviously, the multi-feature-based taxon builds on the previous taxon and is expected to provide relatively improved detection performance along with fewer false alarms. Multiple methods in the literature fall under this taxon.

Finally, the expert-system-oriented taxon is the most sophisticated. It extends the two aforementioned taxa and utilizes a multi-stage (two or more stages) artificial intelligence (AI) approach that bases the detection process in the SAR image on exploitation of prior knowledge about the imaged scene, clutter and/or target(s). Prior knowledge is exploited through various means such as: image segmentation, scene maps, previously gathered data, etc. As the sophistication of the detection taxon increases, the complexity-performance trade-off arises. Caution should be exercised when opting for a certain approach in order to carefully balance this trade-off.

Based on the aforementioned taxonomy, we broadly classify the various target detection schemes and relevant methods reported in the literature in Fig. 2.3. Primarily, under the single-feature-based taxon, the sliding window constant false alarm rate (CFAR-based) sub-taxon is the most popular. There exist three perspectives through

which the various CFAR methods can be viewed. First, based on the specifications of the sliding window: there is fixed-size vs. adaptive as well as square-shaped vs. non-square-shaped [14, 15]. Second, based on the method used to implement the CFAR technique, there are various strategies, of which the most commonly applied are cell-averaging CFAR (CA-CFAR) [16–18], smallest of CA-CFAR (SOCA-CFAR) [19], greatest of CA-CFAR (GOCA-CFAR) [20], and order statistics CFAR (OS-CFAR) [21], among others. Third, based on the method used to estimate the threshold (for a desired PFA) in the boundary ring, and/or the approach utilized for estimating the target signature (for a desired PD), two parametric and non-parametric sub-classes emerge.

Under the parametric sub-class, two approaches are recognized: only background modeling (e.g., Weibull distribution [22, 23], K-distribution [24], alpha-stable distribution [25, 26], or beta-prime (β') distribution [27], among other models), and background and target modeling [28, 29]. A choice of the parametric model that best represents the SAR data in use has to be made among the various parametric models. Unlike the parametric approach, the non-parametric approach [30, 31] does not assume any form for the background/target model(s). Rather, it directly infers an approximate model from the training data. One such method that performs model inference is the kernel-density-estimation (KDE) [32]. Less popular non-CFAR-based methods [33], such as those relying on a coherence image [34], represent the other sub-taxon of single-feature-based methods. The single-feature-based taxon has the limitation that it bases the detection decision solely on the RCS, and, thus, can become overwhelmed in regions in the SAR image where there is heterogeneous clutter and/or a high density of targets. Methods under the multi-feature-based taxon are implemented in an attempt to circumvent this drawback through basing the detection decision on a fusion of two or more features. Obviously, this taxon can utilize a suitable method among those presented under the single-feature-based taxon, and incorporate additional features besides RCS such as: multi-resolution RCS analysis, fractal dimension [9, 35]. Multi-resolution methods can be either space-scale-based or space-frequency-based. Prime examples of methods utilize space-scale features are those based on the wavelet-transform including the discrete wavelet transform (DWT) [36] and the continuous wavelet transform (CWT) [37].

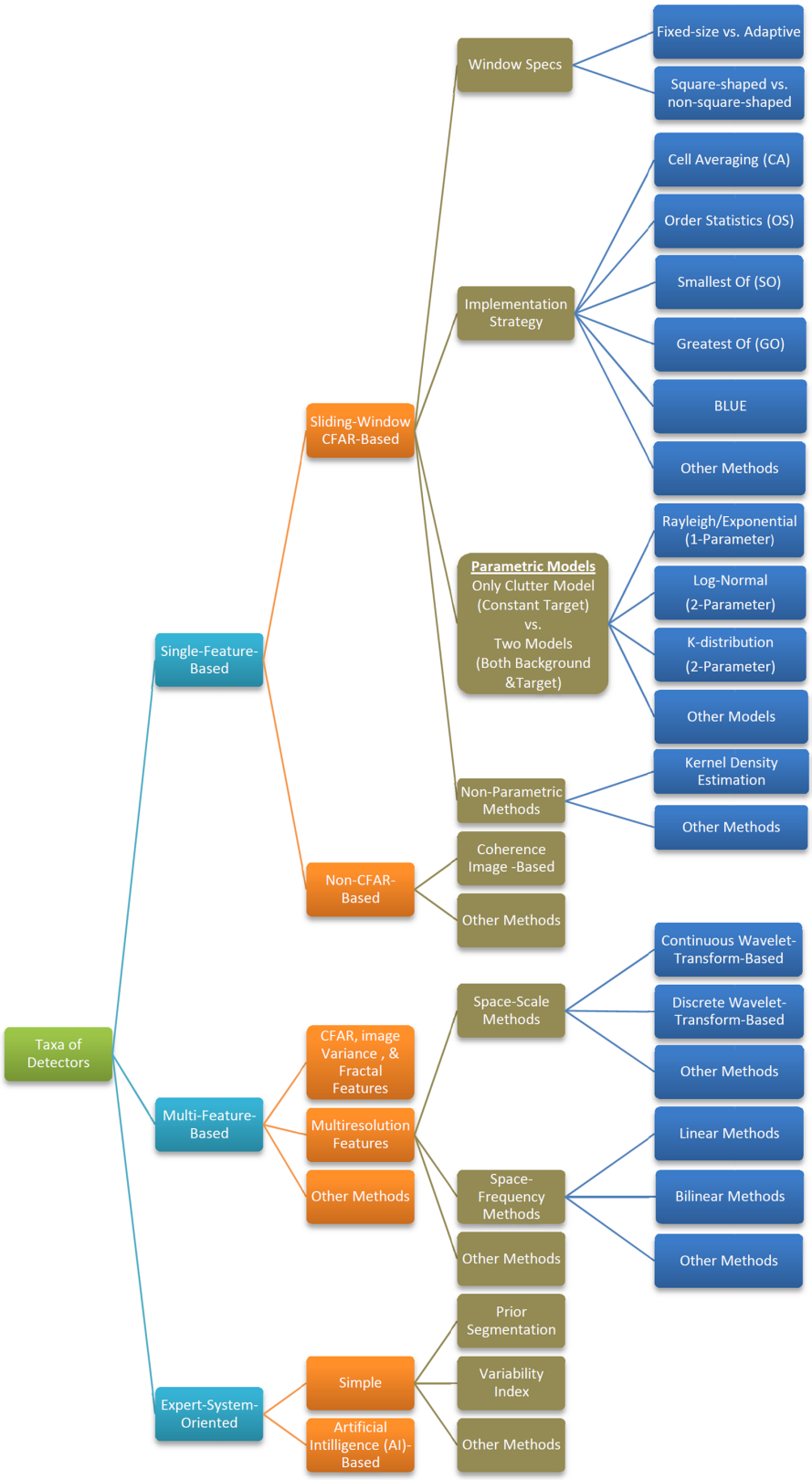

Figure 2.3: Major taxa and classes for implementing the target detection module.

Prime examples of methods that utilizing time-frequency features include linear time-frequency methods such as the Gabor transform and the S-transform [38]; and bilinear (also known as quadratic) time-frequency methods such as Cohen's class distributions (e.g., Wigner distribution, Wigner-Ville distribution, pseudo-Wigner-Ville distribution, etc.) [39, 40]. Finally, a more robust taxon is the expert-system-oriented approach which incorporates intelligence into the process to guide the decision making [41]. In its simplest form, detection decisions can be guided by a structure map of the imaged scene generated from properly segmenting the SAR image [42]. Further, methods of AI can be appropriately integrated to achieve near-optimal context utilization [43–45].

2.3.2. Remarks

The following remarks are drawn based on our review of the state-of-the-art for the detection module.

- The SAR image is typically available as a level-1 processed product (i.e., output from the SAR processor) in a complex-valued form.
- The common practice in the radar community is to detect this image (i.e., to convert it to a real-valued image through magnitude-detection or, more commonly, power-detection), and to input it to a suitable target detection algorithm. In this process, the phase content is entirely discarded.
- There is a wide range of options for implementing the target detection module. Due to its relative ease of implementation, variations of the CFAR approach are amongst the most popular.
- The target detection process is often based on the RCS and a statistical model for the clutter. These are the features often used in the target detection module.
- From a signal processing perspective, it can be easily shown that CFAR is a finite impulse response (FIR) band-pass (BP) filter [1].
- From a statistical pattern recognition perspective, it can be easily shown that CFAR is an anomaly detector one-class classifier - i.e., a Euclidean distance classifier and a quadratic discriminant with a missing term for one-parameter and two-parameter CFAR, respectively [1].

- Finally, no matter how good the target detection method, the detection performance is highly dependent on the features fed to the detector.

2.4. The Classification Module (Intermediate and Back-End Stages)

Under this section, a synopsis of the intermediate and back-end stages in the SAR-ATR processing chain is presented. First, the various methods pertaining to classification in SAR-ATR are broadly taxonomized. Second, a concise description for the main methods and relevant architectures under each taxon is introduced. An in-depth analysis for the target classification module can be found in our state-of-the art review book chapter [2].

2.4.1. Taxonomy and Architecture of the Classification Approaches

While the front-end stage in the SAR-ATR system identifies ROI(s) in the input SAR image, the subsequent two stages are concerned with LLC and HLC classifications. A suitable classifier is required in each of these two stages. Given its position in the SAR-ATR processing chain, the LLC stage, as compared to the HLC stage, typically utilizes a relatively simple classifier when compared to the HLC stage. ATR algorithms may be broadly taxonomized into two distinctive taxa based on their implementation approach: pattern recognition (PR) and knowledge-based (KB) [46] approaches. The latter also goes by other names including AI-based, expert system, rule-based and model-based approach. In the context of SAR-ATR, we refer to the methods that solely rely on feature vectors (and also representative templates being a kind of feature vectors) as being feature-based, and the methods that incorporate intelligence into the design as a model-based. These two taxa for SAR-ATR are distinguished by the motivation of the feature generation technique utilized and whether the system training is classifier-oriented or target-model-oriented.

A careful examination of the literature pertinent to SAR-ATR reveals a third taxon of methods fitting between the feature-based and the model-based taxa. We refer to

this taxon as being semi-model-based. What distinguishes this taxon from the earlier two taxa is that, although it solely relies on features, it incorporates intelligence into the SAR-ATR system design. For an end-to-end SAR-ATR system, the feature-based taxon is extensively used in the literature for both LLC and HLC classifications. The semi-model-based and model-based taxa are primarily used for HLC classification. Fig. 2.4 depicts the three taxa proposed.

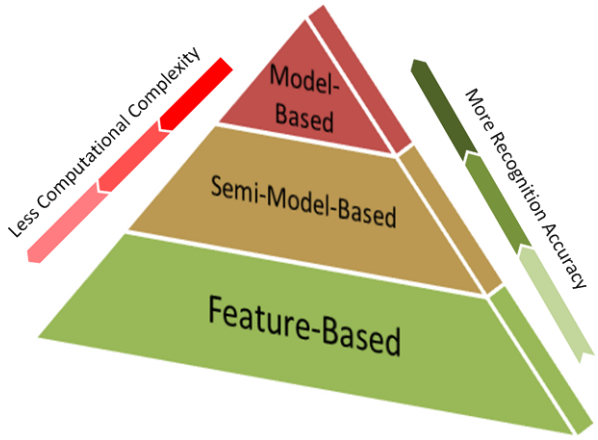

Figure 2.4: Taxonomy of SAR-ATR approaches.

The feature-based taxon is placed at the base of the pyramid because it is the most common in the literature. As one ascends from the base to the top of the pyramid, a better recognition performance is expected to be attained. Conversely, as one descends from the top to the base of the pyramid, the computational complexity of the SAR-ATR system declines. These are design tradeoffs that need to be appropriately accounted for.

In the next subsections, we provide a brief description for each taxon. Typically, regardless of the taxon in question, there are two phases involved, namely, offline classifier training (i.e., for the feature-based taxon), or offline model construction/training (i.e., for the model-based and the semi-model-based taxa, respectively), and online prediction and classification. The feature-based and model-based taxa are presented Sect. 2.4.1.1 and Sect. 2.4.1.2, respectively. The semi-model-based taxon is introduced in Sect. 2.4.1.3. The issues addressed under each subsection include: generic description, architecture(s), major challenges, advantages and disadvantages.

2.4.1.1. Feature-Based Taxon

The feature-based taxon is a pattern recognition approach that solely relies on features to represent the target. These features can be either image target templates or feature vectors extracted from the target(s) of interest (i.e., the SAR target chips). The feature-based approach assumes that the features of targets from different classes lie in separable regions of the multidimensional feature space, while features from the same class cluster together. The process of recognition in the feature-based approach involves two distinctive phases, namely, an offline classifier training and online classification.

The classifier training phase is performed entirely offline as depicted in Fig. 2.5. One needs to have an extensive set of target chips pertaining to all the targets of interest. From the target chips, features of choice are extracted and properly preprocessed. Then, these features are used to train the classifier of choice.

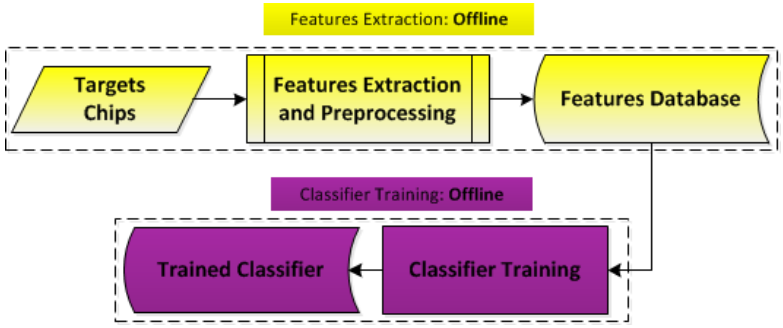

Figure 2.5: Classifier training for the feature-based approach.

In the classification phase, features are extracted online from the input SAR chip to be classified, and fed to the previously trained classifier as depicted in Fig. 2.6. Obviously, the classification result relies on the choice of the training features and their uniqueness in abstracting the target(s) of interest.

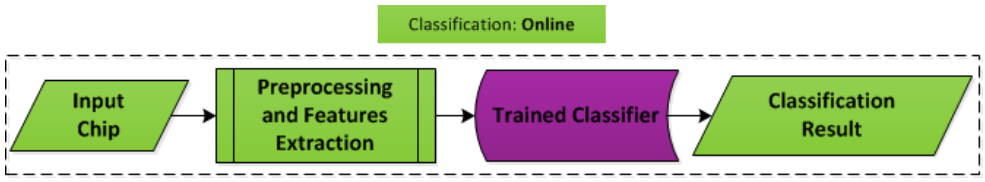

Figure 2.6: Classification in the feature-based approach.

Various methods pertaining to the feature-based approach can be found in classical statistical pattern recognition texts [30, 31]. Further, a state-of-the-art review for the SAR-ATR systems that utilize this taxon can be found in our work in [2]. While this method is the most common in the literature, it may be overwhelmed when faced with (substantial) variations in the input chip signature (i.e., extracted features) due to factors such as clutter heterogeneity or extended operating condition(s) (EOC(s)). Thus, the major drawback of this method is that it has a limited knowledge, and almost no intelligence and reasoning capability to learn from the dynamic environment and to adapt to it.

2.4.1.2. Model-Based Taxon

Unlike the feature-based taxon, the model-based taxon handles the recognition problem in a bottom-up fashion. In other words, the recognition process in the model-based approach begins with a simple feature extraction operation from the input SAR chip. Then, the extracted features are compared against feature hypotheses derived on-the-fly from offline pre-designed models of the targets of interest and the SAR sensor. Typically, there exists one such model per each target of interest. By contrast, the feature-based taxon incorporates a top-down approach in that it attempts to capture the multiple aspects of the target variations and represent them in the form of features, which are subsequently used to produce a trained classifier. Actually, the debate on the preference of the bottom-up approach over the top-down approach originated in the field of computer vision. Professor Rodney A. Brooks of Massachusetts Institute of Technology (MIT) showcased the superiority of the bottom-up approach in relation to the top-down approach through explaining that such system design should focus on actions and behavior rather than representation and function [47]. The first model-based system for target recognition, referred to as ACRONYM , was introduced by R. A. Brooks in the early 1980s [48].

The model-based approach seeks to combat the major challenges of the feature-based approach through incorporating prior knowledge into the design. Thus, the model-based approach utilizes some of the techniques used in the feature-based approach and builds on them. Model-based approaches represent a spectrum of attempts

steered towards the characterization of the physical structure of the target classes of interest. Typically the model-based approach is comprised of an offline target-model construction and an online prediction and classification. These two phases resemble the feature-based approach but there are two major differences. First, the offline model-construction is a major task in the model-based approach which focuses on building a holistic and generic physical model for any target of interest. This is dissimilar to the feature-based approach where, in this phase, a classifier of choice is merely trained based on an ad hoc selection of training target features. Second, unlike the feature-based approach where the online classification is merely based on extracting certain features from the input SAR chip and determining where the extracted features fit in the feature space of the offline-trained classifier(s), the model-based approach hypothesizes relevant attributes in the input SAR chip, and, based on these attributes, it produces certain predictions on-the-fly from the offline-constructed target-model. The online classifier then looks for the hypothesis prediction that yields close resemblance to the input SAR chip.

Multiple methods pertaining to the offline target-model construction are reported in the literature. Regardless of the method used for target-model construction, the online classification phase for all methods has similar structure with a few minor differences. Next, we summarize some of the major methods reported in the open literature for the offline target-model construction. This is followed by a description of the online prediction and classification process.

In the first target-model construction method [49–54], only a 3-D CAD model for each target of interest is designed offline and stored in the system's database. This process is depicted in Fig. 2.7. These 3-D CAD models are used for online prediction and classification in the second phase.

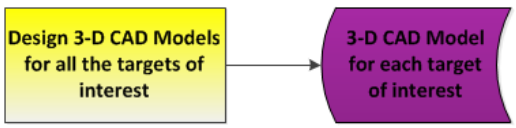

Figure 2.7: First model-based method for the offline target-model construction.

In the second method [55, 56], similar to the first, 3-D CAD models are designed for all targets of interest. Then, a so-called global scattering center model is generated for

each target of interest using a suitable electromagnetic (εM) prediction tool. These 3-D global scattering center models are stored offline in the training database and used for the online prediction and classification phase. The process of offline target-model construction is depicted in Fig. 2.8.

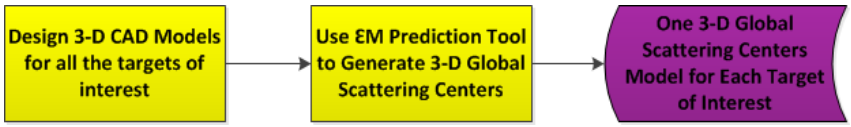

Figure 2.8: Second model-based method for the offline target-model construction.

In the third method [57], similar to the first, a 3-D CAD model for each target of interest is designed offline. An εM prediction tool is used to generate 2-D target templates at uniformly sampled azimuth angles. Then, for each template, a dictionary of invariant histograms is generated. These 2-D target templates and corresponding dictionaries are stored offline in the target-model database. This database is used during the online prediction and classification phase. The process of offline model construction is depicted in Fig. 2.9.

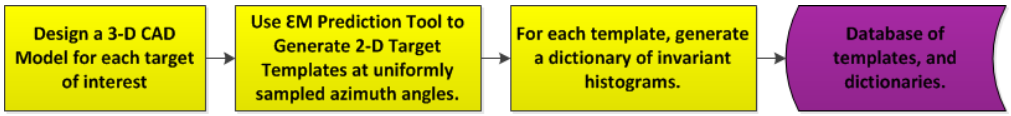

Figure 2.9: Third model-based method for the offline target-model construction.

In the fourth method [58, 59], unlike the previous three methods, no CAD models are utilized. Rather, for each target of interest, a set of target chips that covers the span of the azimuth angles from 0^{o} to 360^{o} is required. Scattering centers are extracted from each chip. These scattering centers are used to produce a 3-D target model comprised of a number of N primitives each of which is characterized by a canonical primitive type, a 3-D location of the primitive, and a set of continuous-valued descriptors. This process is summarized in Fig. 2.10. These 3-D target models are stored offline in the target-model database and invoked on-the-fly during the online classification phase.

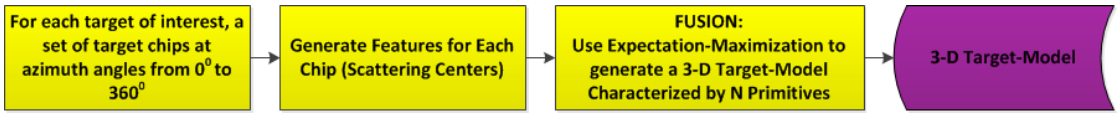

Figure 2.10: Fourth model-based method for the offline target-model construction.

In the next phase, online prediction and classification are performed. This is depicted in Fig. 2.11. Two distinctive sub-stages are executed in parallel. In the first sub-stage, pertinent features are extracted from the input SAR chip and fed to the hypothesis verification unit. In the second sub-stage, pertinent parameters are extracted from the input SAR chip and fed to the hypothesis generation unit. Depending on the method used for model construction (i.e., method 1 through method 4), the functionality of the hypothesis generation unit may vary from retrieving an εM prediction tool (i.e., to generate prediction hypotheses based on the extracted parameters from the input SAR chip) to simply retrieving relevant entries in the target-model database and characterizing these entries based on the extracted parameters from the input chip. This process is often referred to as indexing.

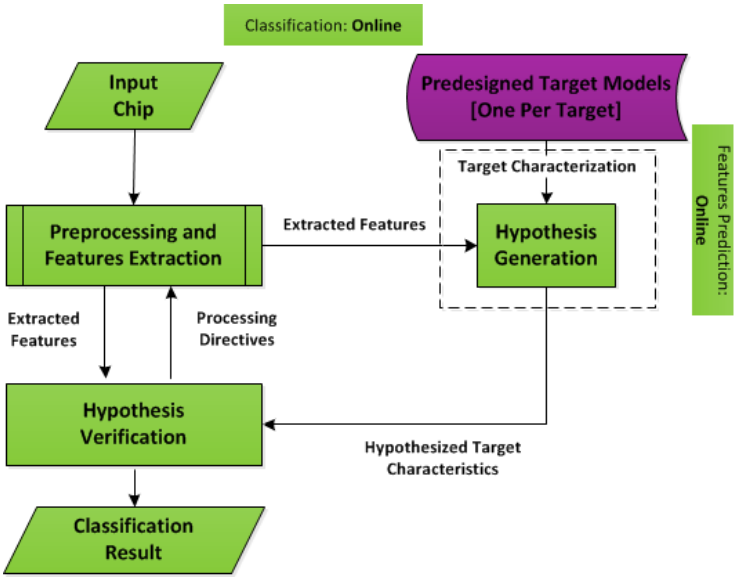

Figure 2.11: The online model-based prediction and classification.

The output from the hypothesis generation unit is a set of arbitrary feature-vector predictions pertinent to various target classes, poses and the EOCs of interest. All the predicted feature hypotheses are fed to the hypothesis verification unit. Finally,

the classification of an input chip is performed by searching over the hypothesis space for the set of possible combinations of target class, pose and relevant EOCs (if any) that yield a predicted observation close to the actual observation. The feature-vector prediction that scores the highest match, normally within some predefined threshold constraint, is chosen. Being a function of the target-class, pose and relevant EOC(s), matched features reflect the recognized target and its corresponding pose and EOC(s). The pre-designed threshold constraint is often used to reject non-target confusers so that no forced recognition is allowed.

From the earlier description it is obvious that regardless of the method used for the target-model construction, the generic structure of the online model-based prediction and classification phase is similar for all methods. For the four methods, the hypothesis generation unit is used to hypothesize feature predictions that are fed to the hypothesis verification unit for feature matching that yields a classification result. However, depending on the target modeling method utilized, additional operations may need to be incorporated into the hypothesis generation unit as described earlier. It should be highlighted that while methods 1, 2 and 4 for target-model construction yield 3-D target-models, method 3 yields a 2-D target-model that presumably handles the 3-D space. This makes method 3 cumbersome when compared to the other three methods. However, the challenge of the model-based method is that the identification, design and incorporation of pertinent knowledge are major tasks that introduce additional complexity to the SAR-ATR system. Thus, there always exists a trade-off between system complexity and performance that needs to be carefully accounted for in the target-model design process.

2.4.1.3. Semi-Model-Based Taxon

There is a class of approaches to the SAR-ATR problem that are neither strictly feature-based nor explicitly model-based. It differs from the feature-based approach in that it does not solely rely on an ad hoc selection of feature vectors for the offline classifier training, and thus, it is not strictly classifier-oriented. It deviates from the model-based approach in that it does not tightly follow the online classification regime prescribed in the previous subsection. We refer to the approaches that are neither feature-based nor model-based as a semi-model-based. This taxon of SAR-ATR loosely fits between the feature-based and the model-based approaches that were described

earlier. In this subsection, we describe two such methods from the literature to depict the spectrum of these techniques. For each method, we first describe the major steps in the offline target-model training. We use the term, target-model training to distinguish this approach from the target-model construction process utilized in the model-based approach. This is followed by a few details on the online classification process.

In the first method [60–64], an extensive set of target chips that covers the span of uniformly sampled azimuth angles from 0^o to 360^o is utilized. After certain preprocessing, the variance for each target chip is estimated. The variances for the various target chips are stored in the model database as a function of the target class and pose angles. The process of offline model training is depicted in Fig. 2.12. There exists one such target-model for each target of interest. These variances are utilized during the online classification phase.

Figure 2.12: First semi-model-based method for the offline model-training.

In the online classification phase, a complex Gaussian probability density function (PDF) is utilized. Note that a suitable PDF model other than the Gaussian can also be used. The PDF model is parametrized by the pixel values of the preprocessed input test chip as well as the target-model variances drawn from the database of variances pertaining to the different targets and corresponding pose angles that were constructed offline. A generalized likelihood ratio test (GLRT) is used to search for the variance value that maximizes the likelihood test. Provided that the GLRT test exceeds some predetermined threshold, the variance value that achieves the highest score over all other variances is chosen. The corresponding parameters of the chosen variance (i.e., target class and pose) represent the classification result. If the threshold of the GLRT is found to be less than the pre-determined threshold over all the variances space, the input SAR chip is declared as a non-target confuser. The online classification process pertaining to three-target classes is depicted in Fig. 2.13.

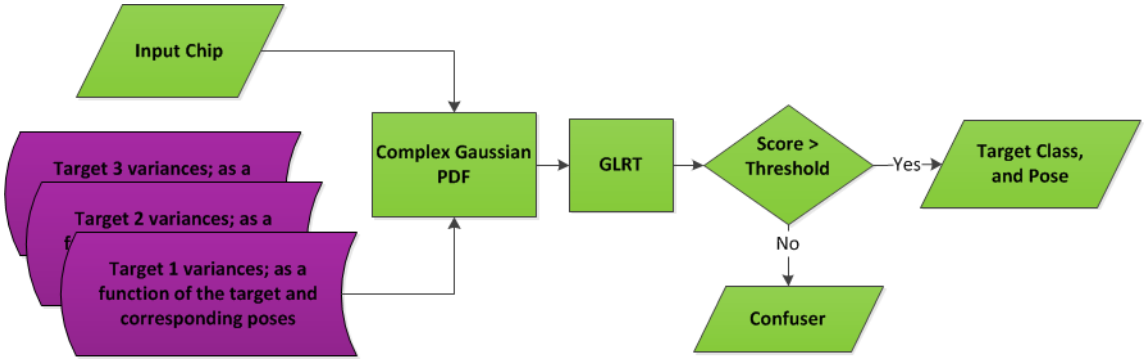

Figure 2.13: First semi-model-based method for the online classification phase. In this example, only three targets of interest are depicted.

In the second method [65–74], similar to the first, an extensive set of SAR target chips at uniformly sampled azimuth angles from 0° to 360° is required. For each chip, the N strongest scattering centers are sought (i.e., these are from $p = 1$ to N), and their pixel values S, along with the corresponding range location R and cross-range location C, are determined. This yields a triple (R, C, S). Such triples are arranged in a descending order based on the pixel value S. Then, an origin pair $(R_o,\ C_o)$ is chosen from the N pairs (R, C). Further, dR and dC are calculated as

$$dR = R_p - R_o,\ \ dC = C_p - C_o. \tag{2.1}$$

Accordingly, a look-up table (LUT) is constructed where its $(x,\ y)$ addresses are $(dR,\ dC)$, and its corresponding entries are (Object Class, R_o, S_o, S_p). This process is repeated N times, and, in each time, a unique origin $(R_o,\ P_o)$ is chosen from the tuple $(R,\ C)$ for $p = 1$ to N. The results are stored in the LUT table. There is one such LUT table for each target-class of interest. The process of LUT table construction is depicted in Fig. 2.14. In the online classification phase, similar features as those described above for the offline phase are extracted and arranged in a descending order based on the pixel value S. Then, the distances DR and DC are calculated as

$$DR = dR - 1 : dR + 1,\ \text{and}\ DC = dC - 1 : dC + 1. \tag{2.2}$$

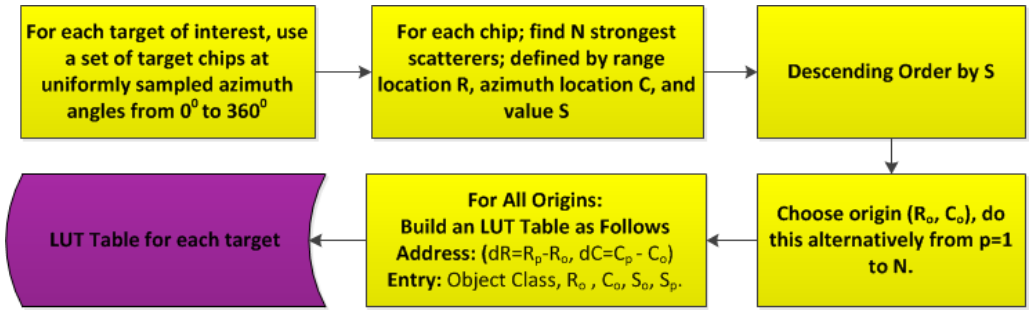

Figure 2.14: Second semi-model-based method for the offline model-training.

Next, a weighted vote is defined. Moreover, transition and magnitude limits are introduced. These limits serve as thresholds to reject non-target confusers. Then, a search is performed over all the pre-constructed LUT tables pertaining to the target-classes of interest. The search result that achieves the highest score over all the LUT tables is declared provided that it exceeds the abovementioned thresholds. Corresponding entries in the relevant LUT table represent the target-class and its respective pose. This process is depicted in Fig. 2.15 for three target-models (i.e., three LUT tables).

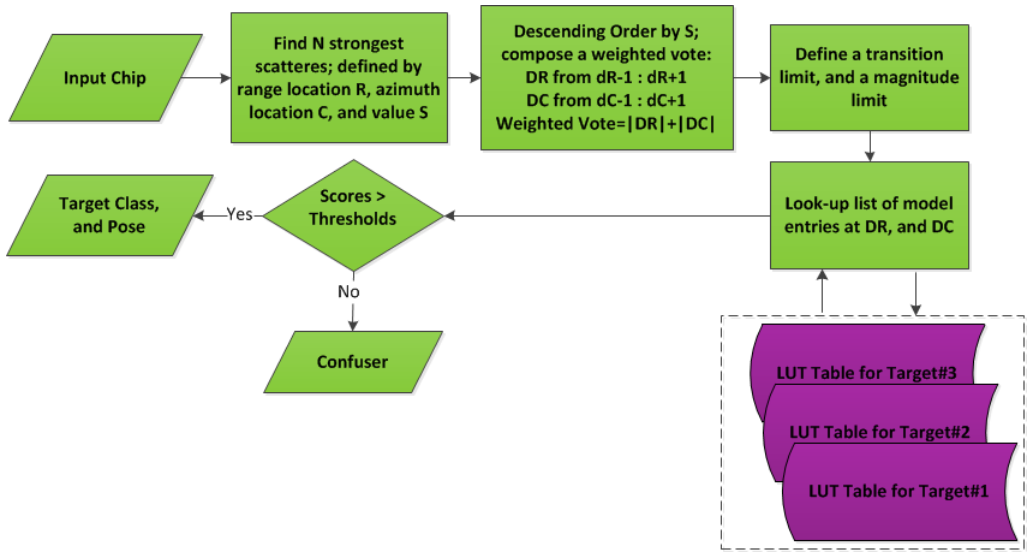

Figure 2.15: Second semi-model-based method for the online classification. In this example, only three targets of interest are depicted.

2.5. Conclusions

An end-to-end SAR-ATR system is comprised of three stages: front-end (i.e., detector), intermediate (i.e., LLC classifier) and back-end (i.e., HLC classifier). Important points to note are the following. Firstly, most works published in the literature exclusively utilize the detected SAR image (i.e., magnitude or intensity) while the phase content pertinent to the complex-valued SAR image is entirely discarded. Secondly, despite the apparent superiority of the model-based taxon (for HLC classification) in comparison to the other two taxa, this superiority is conditional upon the target model of choice and its design feasibility. Indeed, unlike optical imagery, this is a much bigger challenge in the case of SAR imagery (i.e., for radar signals in general). A detailed account for the reasons of the combinatorial explosion of the SAR target signature and characterization of the operating conditions for SAR imagery into standard operating conditions (SOCs) and extended operating conditions (EOCs) can be found in our review article on the topic [2]. A summary of these reasons is provided in Appendix B.

Bibliography

[1] K. El-Darymli, P. McGuire, D. Power, and C. Moloney, "Target detection in synthetic aperture radar imagery: a state-of-the-art survey," *J. Appl. Remote Sens*, vol. 7, no. 1, 2013. [Online]. Available: http://dx.doi.org/10.1117/1.JRS.7.071598 27, 29, 33

[2] K. El-Darymli, P. McGurie, E. W. Gill, D. Power, and C. Moloney, "Automatic target recognition in SAR imagery (SAR-ATR): A state-of-the-art review," *[To be submitted]*, 2015. 27, 34, 37, 45

[3] M. Roth, "Survey of neural network technology for automatic target recognition," *Neural Networks, IEEE Transactions on*, vol. 1, no. 1, pp. 28–43, 1990. [Online]. Available: http://dx.doi.org/10.1109/72.80203 27

[4] D. Dudgeon, "ATR performance modeling and estimation," *Digital Signal Processing*, vol. 10, no. 4, pp. 269–285, 2000. [Online]. Available: http://dx.doi.org/10.1006/dspr.2000.0375 28

[5] H. Chiang and R. Moses, "ATR performance prediction using attributed scattering features," in *Proc. of SPIE, Algorithms for Synthetic Aperture Radar Imagery VI*, vol. 3721, no. 785, 1999. [Online]. Available: http://dx.doi.org/10.1117/12.357693 28

[6] T. Cooke, "Detection and classification of objects in synthetic aperture radar imagery," Tech. Rep. DSTO-RR-0305, 2006. [Online]. Available: http://tinyurl.com/orx668d

[7] D. Kreithen, S. Halversen, and G. Owirka, "Discriminating targets from clutter," *The Lincoln Laboratory Journal*, vol. 6, no. 1, pp. 25–52, 1993. [Online]. Available: http://tinyurl.com/o3h2srf

[8] S. D. Halversen, "Calculating the orientation of a rectangular target in SAR imagery," in *Aerospace and Electronics Conference, NAECON 1992, Proceedings*

of the IEEE, 1992. [Online]. Available: http://dx.doi.org/10.1109/NAECON.1992.220611

[9] L. Kaplan, R. Murenzi, and K. Namuduri, "Extended fractal feature for first-stage SAR target detection," in *Proc. SPIE, Algorithms for Synthetic Aperture Radar Imagery VI*, vol. 3721, 1999, pp. 35–46. [Online]. Available: http://dx.doi.org/10.1117/12.357684 31

[10] L. Novak, G. Owirka, W. Brower, and A. Weaver, "The automatic target-recognition system in SAIP," *Lincoln Laboratory Journal*, vol. 10, no. 2, pp. 187–202, 1997. [Online]. Available: http://tinyurl.com/q8o8f3x

[11] L. Novak, G. Owirka, and W. Brower, "An efficient multi-target SAR ATR algorithm," in *Signals, Systems and Computers, the Thirty-Second IEEE Asilomar Conference on*, vol. 1, 1998, pp. 3–13. [Online]. Available: http://dx.doi.org/10.1109/ACSSC.1998.750815

[12] N. Sandirasegaram, "Spot SAR ATR using wavelet features and neural network classifier," Defence Research and Development Canada Ottawa, Ontario, Tech. Rep. DRDC-TM-2005-154), 2005. [Online]. Available: http://pubs.drdc.gc.ca/PDFS/unc89/p524497.pdf

[13] J. Schroeder, "Automatic target detection and recognition using synthetic aperture radar imagery," in *Proc. of the 2002 Workshop on the Applications of Radio Science (WARS02) Conference*, 2002. [Online]. Available: http://tinyurl.com/oy5npsa 28

[14] J. C. Principe, A. Radisavljevic, M. Kim, J. F. III, M. Hiett, and L. M. Novak, "Target prescreening based on 2D gamma kernels," in *Proceedings of the SPIE-The International Society for Optical Engineering,Algorithms for Synthetic Aperture Radar Imagery II*, vol. 2487, 1995, pp. 251–258. [Online]. Available: http://dx.doi.org/10.1117/12.210842 31

[15] J. C. Principe, M. Kim, and M. F. III, "Target discrimination in synthetic aperture radar using artificial neural networks," *Image Processing, IEEE Transactions on*, vol. 7, no. 8, pp. 1136–1149, 1998. [Online]. Available: http://dx.doi.org/10.1109/83.704307 31

[16] H. Finn and R. Johnson, "Adaptive detection mode with threshold control as a function of spatial sampled clutter level estimates," *RCA REVIEW*, pp. 414–464, 1968. 31

[17] R. Viswanathan, *Handbook of Statistics*. Amsterdam, The Netherlands: Elsevier, 1998, vol. 17, ch. Order statistics application to CFAR radar target detection, pp. 643–671.

[18] H. You, G. Jian, P. Yingning, and L. Dajin, "A new CFAR detector based on ordered statistics and cell averaging," in *CIE International Conference, IEEE*, 1996, pp. 106–108. [Online]. Available: http://dx.doi.org/10.1109/ICR.1996.573783 31

[19] G. V. Trunk, "Range resolution of targets using automatic detectors," *Aerospace and Electronic Systems, IEEE Transactions on*, vol. 14, no. 5, pp. 750–755, 1978. [Online]. Available: http://dx.doi.org/10.1109/TAES.1978.308625 31

[20] M. Richards, *Fundamentals of radar signal processing*. New York, NY: McGraw-Hill Education, 2005. 31

[21] H. Rohling, "Radar CFAR thresholding in clutter and multiple target situations," *Aerospace and Electronic Systems, IEEE Transactions on*, vol. 19, no. 4, pp. 608–621, 1983. [Online]. Available: http://dx.doi.org/10.1109/TAES.1983.309350 31

[22] M. di Bisceglie and C. Galdi, "CFAR detection of extended objects in high-resolution SAR images," *Geoscience and Remote Sensing, IEEE Transactions on*, vol. 43, no. 4, pp. 833–843, 2005. [Online]. Available: http://dx.doi.org/10.1109/TGRS.2004.843190 31

[23] M. D. Bisceglie and C. Galdi, "Cfar detection of extended objects in high resolution sar images," in *Geoscience and Remote Sensing Symposium, IEEE IGARSS*, vol. 6, 2001. [Online]. Available: http://dx.doi.org/10.1109/IGARSS.2001.978126 31

[24] S. Kuttikkad and R. Chellappa, "Non-Gaussian CFAR techniques for target detection in high resolution SAR images," in *Image Processing ICIP-94, IEEE International Conference*, vol. 1, 1994, pp. 910–914. [Online]. Available: http://dx.doi.org/10.1109/ICIP.1994.413444 31

[25] M. Liao, C. Wang, Y. Wang, and L. Jiang, "Using SAR images to detect ships from sea clutter," *Geoscience and Remote Sensing Letters, IEEE*, vol. 5, no. 2, pp. 194–198, 2008. [Online]. Available: http://dx.doi.org/10.1109/LGRS.2008.915593 31

[26] J. Xu, W. Han, X. feng He, and R. xi Chen, "Small target detection in

SAR image using the alpha-stable distribution model," in *Image Analysis and Signal Processing (IASP), IEEE International Conference on*, 2010, pp. 64–68. [Online]. Available: http://dx.doi.org/10.1109/IASP.2010.5476160 31

[27] I. I. Salazar, "Detection schemes for synthetic-aperture radar imagery based on a beta prime statistical model," Ph.D. dissertation, The University of New Mexico, 1999. 31

[28] R. Gan and J. Wang, "Distribution-based CFAR detectors in SAR images," *Journal of Systems Engineering and Electronics*, vol. 17, no. 4, pp. 717–721, 2006. [Online]. Available: http://dx.doi.org/10.1016/S1004-4132(07)60004-8 31

[29] G. Rong-bing and W. Jian-Guo, "Distribution-based CFAR detection in SAR images," in *Geoscience and Remote Sensing Symposium (IGARSS), IEEE International*, vol. 3, 2005, pp. 1753–1756. [Online]. Available: http://dx.doi.org/10.1109/IGARSS.2005.1526342 31

[30] R. Duda, P. Hart, and D. Stork, *Pattern classification*. New York, NY: John Wiley and Sons, 2001. 31, 37

[31] C. Bishop, *Pattern recognition and machine learning (information science and statistics)*. Secaucus, NJ: Springer-Verlag, 2006. 31, 37

[32] G. Gao, "A Parzen-window-kernel-based CFAR algorithm for ship detection in SAR images," *Geoscience and Remote Sensing Letters, IEEE*, vol. 8, no. 3, pp. 557–561, 2011. [Online]. Available: http://dx.doi.org/10.1109/LGRS.2010.2090492 31

[33] D. Howard, S. Roberts, and R. Brankin, "Target detection in SAR imagery by genetic programming," *Adv. Eng. Software*, vol. 30, no. 5, pp. 303–311, 1999. [Online]. Available: http://dx.doi.org/10.1016/S0965-9978(98)00093-3 31

[34] K. Ouchi, S. Tamaki, H. Yaguchi, and M. Iehara, "Ship detection based on coherence images derived from cross correlation of multilook SAR images," *Geoscience and Remote Sensing Letters, IEEE*, vol. 1, no. 3, pp. 184–187, 2004. [Online]. Available: http://dx.doi.org/10.1109/LGRS.2004.827462 31

[35] L. M. Kaplan, "Improved SAR target detection via extended fractal features," *Aerospace and Electronic Systems, IEEE Transactions on*, vol. 37, no. 2, pp. 436–451, 2001. [Online]. Available: http://dx.doi.org/10.1109/LGRS.2005.845033 31

[36] M. Tello, C. Lopez-Martinez, and J. J. Mallorqui, "A novel algorithm for ship detection in SAR imagery based on the wavelet transform," *Geoscience and Remote Sensing Letters, IEEE*, vol. 2, no. 2, pp. 201–205, 2005. [Online]. Available: http://dx.doi.org/10.1109/LGRS.2005.845033 31

[37] J.-P. Antoine, R. Murenzi, P. Vandergheynst, and S. T. Ali, *Two-dimensional wavelets and their relatives*. Cambridge, UK: Cambridge University Press, 2004. 31

[38] T. Tao, Z. Peng, C. Yang, F. Wei, and L. Liu, *Electrical Engineering and Control: Lecture Notes in Electrical Engineering*. Elsevier, 2011, vol. 2, ch. Targets detection in SAR image used coherence analysis based on S-transform, pp. 1–9. [Online]. Available: http://dx.doi.org/10.1007/978-3-642-21765-4_1 33

[39] S. Haykin and T. Bhattacharya, "Wigner-Ville distribution: an important functional block for radar target detection in clutter," in *Signals, Systems and Computers, the IEEE Twenty-Eighth Asilomar Conference on*, 1994, pp. 68–72. [Online]. Available: http://dx.doi.org/10.1109/ACSSC.1994.471419 33

[40] V. C. Chen and H. Ling, *Time-frequency transforms for radar imaging and signal analysis*. Norwood, MA: Artech House Publishers, 2002. 33

[41] G. Gao, L. Liu, L. Zhao, G. Shi, and G. Kuang, "An adaptive and fast CFAR algorithm based on automatic censoring for target detection in high-resolution SAR images," *Geoscience and Remote Sensing, IEEE Transactions on*, vol. 47, no. 6, pp. 1685–1697, 2009. [Online]. Available: http://dx.doi.org/10.1109/TGRS.2008.2006504 33

[42] I. McConnell and C. Oliver, "Segmentation-based target detection in SAR," in *SAR Image Analysis, Modelling and Techniques II, Vol. Proceedings of SPIE*, vol. 3869, 1999. [Online]. Available: http://dx.doi.org/10.1117/12.373158 33

[43] G. T. Capraro, G. B. Berdan, R. A. Liuzzi, and M. C. Wicks, "Artificial intelligence and sensor fusion," in *Integration of Knowledge Intensive Multi-Agent Systems, IEEE International Conference on*, 2003, pp. 591–595. [Online]. Available: http://dx.doi.org/10.1109/KIMAS.2003.1245106 33

[44] M. C. Wicks, J. William J. Baldygo, and R. D. Brown, "Expert system constant false alarm rate (CFAR) processor," US Patent US5 499 030, 1996. [Online]. Available: http://www.google.com/patents/US5499030

[45] W. Baldygo, R. Brown, M. Wicks, P. Antonik, G. Capraro, and L. Hennington,

"Artificial intelligence applications to constant false alarm rate (CFAR) processing," in *Radar Conference, IEEE*, 1993, pp. 275–280. [Online]. Available: http://dx.doi.org/10.1109/NRC.1993.270451 33

[46] B. Bhanu, "Automatic target recognition: State of the art survey," *Aerospace and Electronic Systems, IEEE Transactions on*, vol. 22, no. 4, pp. 364–379, 1986. [Online]. Available: http://dx.doi.org/10.1109/TAES.1986.310772 34

[47] M. Dennis. (2012, 3) Rodney Allen Brooks (Australian-American scientist). [Online]. Available: http://www.britannica.com/EBchecked/topic/745412/Rodney-Allen-Brooks 37

[48] R. Brooks, *Model-based computer vision*. Ann Arbor, MI: UMI Research Press, 1984. 37

[49] L. Potter and R. Moses, "Attributed scattering centers for SAR ATR," *Image Processing, IEEE Transactions on*, vol. 6, no. 1, pp. 79–91, 1997. [Online]. Available: http://dx.doi.org/10.1109/83.552098 38

[50] H. Chiang, R. Moses, and W. Irving, "Performance estimation of model-based automatic target recognition using attributed scattering center features," in *Image Analysis and Processing, IEEE International Conference on*, 1999, pp. 303–308. [Online]. Available: http://dx.doi.org/10.1109/ICIAP.1999.797612

[51] R. Moses, L. Potter, and I. Gupta, "Feature extraction using attributed scattering center models for model-based automatic target recognition," Air Force Research Laboratory, Tech. Rep. AFRL/WS-06-0079, 2005. [Online]. Available: http://tinyurl.com/q9acecy

[52] Y. Akyildiz and R. Moses, "Scattering center model for SAR imagery," in *SAR Image Analysis, Modeling, and Techniques II*, vol. 3869, 1999, pp. 76–85. [Online]. Available: http://dx.doi.org/10.1117/12.373151

[53] M. Koets and R. Moses, "Feature extraction using attributed scattering center models on SAR imagery," in *Proc. of SPIE, Algorithms for Synthetic Aperture Radar Imagery VI*, vol. 3721, 1999. [Online]. Available: http://dx.doi.org/10.1117/12.357628

[54] R. Moses. (2014) Publications list. [Online]. Available: http://tinyurl.com/pxzc8ba 38

[55] Z. Jianxiong, S. Zhiguang, C. Xiao, and F. Qiang, "Automatic target recognition

of SAR images based on global scattering center model," *Geoscience and Remote Sensing, IEEE Transactions on*, vol. 49, no. 10, pp. 3713–3729, 2011. [Online]. Available: http://dx.doi.org/10.1109/TGRS.2011.2162526 38

[56] Z. Jianxiong, Z. Hongzhong, S. Zhiguang, and F. Qiang, "Global scattering center model extraction of radar targets based on wideband measurements," *Antennas and Propagation, IEEE Transactions on*, vol. 56, no. 7, pp. 2051–2060, 2008. [Online]. Available: http://dx.doi.org/10.1109/TAP.2008.924698 38

[57] K. Ikeuchi, M. Wheeler, T. Yamazaki, and T. Shakunaga, "Model-based SAR ATR system," in *Proc. of SPIE, Algorithms for Synthetic Aperture Radar Imagery III*, 1996, pp. 376–387. [Online]. Available: http://dx.doi.org/10.1117/12.242040 39

[58] J. Richards, A. Willsky, and J. Fisher, "Expectation-maximization approach to target model generation from multiple synthetic aperture radar images," *Optical Engineering*, vol. 41, no. 1, pp. 150–166, 2002. [Online]. Available: http://dx.doi.org/10.1117/1.1417493 39

[59] J. Richards, J. Fisher, and A. Willsky, "Target model generation from multiple SAR images," in *Proc. of SPIE, Algorithm for SAR Imagery VI*, vol. 3721. SPIE, 2000. [Online]. Available: http://dx.doi.org/10.1117/12.357675 39

[60] M. DeVore, J. Osullivan, S. Anand, and N. Schmid, "Probabilistic approach to model extraction from training data," in *Proc. of SPIE, Algorithms for Synthetic Aperture Radar Imagery VIII*, vol. 4382. SPIE, 2001, pp. 358–366. [Online]. Available: http://dx.doi.org/10.1117/12.438229 42

[61] M. Devore and J. Osullivan, "Target-centered models and information-theoretic segmentation for automatic target recognition," *Multidimensional Systems and Signal Processing*, vol. 14, no. 1-3, pp. 139–159, 2003. [Online]. Available: http://dx.doi.org/10.1023/A:1022277209974

[62] J. Osullivan, M. DeVore, V. Kedia, and M. Miller, "SAR ATR performance using a conditionally gaussian model," *Aerospace and Electronic Systems, IEEE Transactions on*, vol. 37, no. 1, pp. 91–108, 2001. [Online]. Available: http://dx.doi.org/10.1109/7.913670

[63] M. DeVore. (2013) Personal web page. [Online]. Available: http://tinyurl.com/qj5w9qv

[64] ——, "Recognition performance from synthetic aperture radar imagery subject

to system constraints," Ph.D. dissertation, the Sever Institute of Washington University, 2001. [Online]. Available: http://tinyurl.com/ptehalw 42

[65] Visualization and I. S. L. (VISLab). (2013) Publications. [Online]. Available: http://vislab.ee.ucr.edu/PUBLICATIONS 43

[66] B. Bhanu and G. Jones, "Recognizing target variants and articulations in synthetic aperture radar images," *Optical Engineering*, vol. 39, no. 3, pp. 712–723, 2000. [Online]. Available: http://dx.doi.org/10.1117/1.602418

[67] B. Bhanu, G. J. III, and J. Ahn, "Recognizing articulated objects and object articulation in SAR images," in *Proc. SPIE, Algorithms for Synthetic Aperture Radar Imagery V*, vol. 3370, 1998. [Online]. Available: http://dx.doi.org/10.1117/12.321852

[68] B. Bhanu and G. J. III, "Exploiting azimuthal variance of scatterers for multiple-look SAR recognition," in *Proc. of SPIE, Algorithms for Synthetic Aperture Radar Imagery IX*, vol. 4727, 2002, pp. 290–298. [Online]. Available: http://dx.doi.org/10.1117/12.478686

[69] B. Bhanu and G. Jones, *Computer Vision Beyond the Visible Spectrum, Advances in Pattern Recognition*. London, UK: Springer-Verlag, 2005, ch. Methods for Improving the Performance of an SAR Recognition System, pp. 36–69. [Online]. Available: http://dx.doi.org/10.1007/1-84628-065-6_2

[70] B. Bhanu, Y. Lin, G. Jones, and J. Peng, "Adaptive target recognition," *Machine Vision and Applications*, vol. 11, no. 6, pp. 289–299, 2000. [Online]. Available: http://dx.doi.org/10.1007/s001380050113

[71] M. Boshra and B. Bhanu, "Predicting an upper bound on SAR ATR performance," *Aerospace and Electronic Systems, IEEE Transactions on*, vol. 37, no. 3, pp. 876–888, 2001. [Online]. Available: http://dx.doi.org/10.1109/7.953243

[72] G. J. III and B. Bhanu, "Recognizing occluded objects in SAR images," *Aerospace and Electronic Systems, IEEE Transactions on*, vol. 37, no. 1, pp. 316–328, 2001. [Online]. Available: http://dx.doi.org/10.1109/7.913694

[73] J. Yi, B. Bhanu, and M. Li, "Target indexing in SAR images using scattering centers and the hausdorff distance," *Pattern Recognition Letters*, vol. 17, no. 11, pp. 1191–1198, 1996. [Online]. Available: http://tinyurl.com/nvynxff

[74] B. Bhanu, "Learning integrated visual database for image exploitation," California Univ Riverside Center for Research in Intelligent Systems, Tech. Rep. CRIS-AFOSR-RPT-02, 2002. [Online]. Available: http://tinyurl.com/pzk8h2q43

3. Design and Implementation of a Low-Power Synthetic Aperture Radar

3.1. Overview

This chapter reports on the design and implementation of a high-resolution low-power synthetic aperture radar (SAR). Our system utilizes the linear frequency-modulated continuous wave (LFMCW) concept, and it operates in the S-band. The generic architecture for our design is presented along with a description of the digital SAR processor. Finally, for demonstration purposes, a focused SAR image for a ground-truthed target is provided.

3.2. Introduction

As an active sensor, synthetic aperture radar (SAR) is a valuable tool for various military and civilian applications. Today, commercial SAR sensors, such as spaceborne Radarsat-2, produce SAR imagery on the order of one metre resolution and finer [1]. Further, some (limited) public-domain high-resolution SAR datasets, such from airborne MSTAR [2], are also available. Additionally, ground-based SAR sensors such as FastGBSAR can be purchased [3]. Thus, one may wonder at the value of building one's own SAR sensor.

Indeed, besides the costly price for acquiring SAR images or sensors, a major challenge to the end-user is the restricted access to the phase history. This imposes extreme limitations on the researcher which can be summarized in two main aspects. Firstly,

a lack of practical knowledge for the various low-level factors that impact the focused SAR image, such as the effect the SAR processor intrinsically has on the raw data. This firsthand knowledge is important for developing an in-depth understanding of the focused SAR image which is instrumental, for example, in developing novel automatic target recognition (ATR) tool(s) specifically tailored to SAR imagery. Secondly, the restriction imposes an inability to apply relevant algorithms in the phase-domain (prior to focusing), for example, to experiment with and develop relevant techniques such as compressive sensing [4], video SAR [5], various SAR focusing algorithms [6, 7], and detection and classification of targets in the phase-domain [8, 9], to name a few. Such topics cannot be properly researched without unrestricted access to the SAR phase history.

Various SAR sensor designs are reported in the open literature [10–12]. Our SAR offers an extension of the design concept originally reported in [13]. The remainder of this chapter is organized as follows. In Sect. 3.3, our system architecture is presented along with a brief description for the concept of operation. General description for the omega-K algorithm (ωKA) used to focus the phase history is given in Sect. 3.4. In Sect. 3.5, a focused SAR image for a ground-truthed target is provided. Conclusions are provided in Sect. 3.6.

3.3. System Architecture

As depicted in Fig. 3.1, our SAR design is based on the concept of linear frequency modulated continuous wave (LFMCW) radar. The LFMCW architecture is chosen because it is relatively simple and cost effective. The analog signal generator produces both a modulating signal input to the voltage controlled oscillator (VCO) to produce an LFMCW chirp and a synchronization signal needed by the digital SAR processor to properly focus the phase history.

The parameters of the modulating signal are chosen to fulfill the desired design requirements. The output from the VCO is amplified using a suitable power amplifier. Then, two identical copies of the amplified LFMCW chirp are produced by the power splitter. One of the these two copies is sent to the transmitter antenna while the other copy is sent to the mixer. This architecture provides for an easy implementation of a heterodyne receiver which down-converts the received backscatter signal from a

pass-band frequency to a baseband frequency through a proper multiplication process [14, 15].

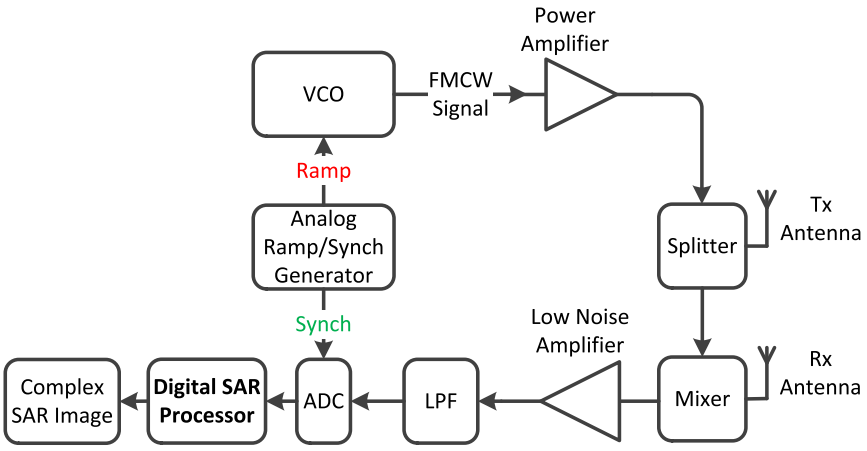

Figure 3.1: Architecture for an end-to-end LFMCW SAR system.

The down-converted baseband analog signal is low-pass filtered (LPF) in accordance with the specifications of the analog-to-digital converter (ADC) being used. The filtering operation is critical as it is designed to prevent aliasing in the sampled signal. The output from the ADC is the SAR phase history of interest. Finally, the SAR image can be appropriately focused through processing both the SAR phase history and the reference synchronization signal generated by the analog signal generator. The SAR processing is performed through using a suitable SAR image formation algorithm [6, 7].

The LFMCW concept is straightforward to explain [16–18]. In our design we utilize a triangular modulating waveform. This is depicted by a solid green line in Fig. 3.2a. The modulating waveform is used to sweep the VCO between f_{min} and f_{max}, so that the sweep bandwidth is given by

$$B = f_{max} - f_{min}. \tag{3.1}$$

with B having a center frequency of f_o. The triangular waveform enables an upsweep and downsweep for a total modulation time period of T_m. The backscatter signal has

a time delay T in reference to the transmitted signal which is related to the range R to the target by

$$T = \frac{2R}{\underline{c}}. \tag{3.2}$$

This form assumes a monostatic configuration where $\underline{c}$ is the speed of light in a vacuum. For a moving target with velocity v, a Doppler shift f_d is produced as

$$f_d = \frac{2v}{\lambda_r}, \tag{3.3}$$

where λ_r is the wavelength of the transmitted radar wave. During an upsweep, the rate of change in the transmitted frequency is given by

$$\frac{df}{dt} = \frac{2B}{T_m}. \tag{3.4}$$

Hence, the change in the transmitted frequency for a time delay T prior to reception is given by

$$df = \frac{2B}{T_m}T. \tag{3.5}$$

Thus, the beat frequency for an upsweep (and downsweep) can be obtained by substituting Eq. 3.2 into Eq. 3.5 and accounting for the Doppler shift from Eq. 3.3, as follows

$$f_b^{\pm} = \frac{4B}{\underline{c}T_m}R \mp f_d. \tag{3.6}$$

Fig. 3.2b shows f_b^+ and f_b^- for the triangular waveform as seen at the mixer's output. This configuration allows for calculating the speed of a moving target, which is given

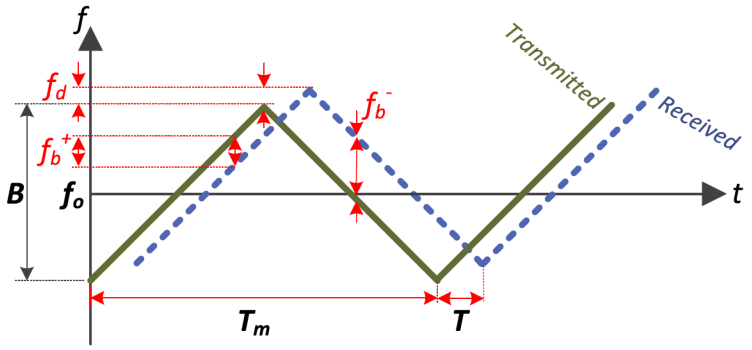

(a) Linear change in frequency vs. time for the transmitted LFMCW signal (solid green) and the backscatter signal (dashed blue).

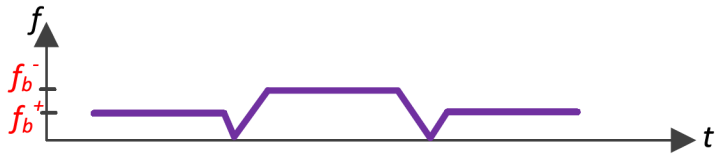

(b) Beat frequency at the mixer's output.

Figure 3.2: Illustration for the LFMCW concept.

by

$$v = \frac{\lambda_r}{2}\frac{f_b^- - f_b^+}{2}. \tag{3.7}$$

It also provides for avoiding ambiguities and separating the slant-range-induced frequency term (of interest in this chapter) embedded in the beat frequency as seen in

$$R = \frac{cT_m}{4B}\frac{f_b^+ + f_b^-}{2}. \tag{3.8}$$

The slant-range theoretical resolution of the LFMCW radar is

$$\triangle R \approx \frac{c}{2B}. \tag{3.9}$$

The backscatter data is collected as the side-looking LFMCW radar is moved in the cross-range direction. The so-called *synthetic aperture* concept is inspired by that of the phased array antenna but instead of having a large number of physical antenna elements, SAR uses one antenna in conjunction with the different positions of the along-track movement to emulate the phased array effect. The theoretical azimuth resolution of the strip-mode SAR is [6]

$$\triangle A \approx \frac{L}{2}, \tag{3.10}$$

where L is the length of the antenna in the azimuth direction. This shows that unlike real aperture radar, the azimuth resolution of SAR improves for smaller L [6]. An important design parameter is the signal to noise ratio (SNR). Assuming a point target, the SNR of a monostatic radar for a single range profile is given by [19]

$$SNR_{\text{dB}} = 10\log_{10}\left(\frac{P_r}{N}\right) = \left\{10\log_{10}\left(\frac{P_t G^2 \lambda_r^2 \sigma}{(4\pi)^3 R^4 L_s}\right)\right\} - \left[10\log_{10}\left(\mathbb{K} T_N F_N B\right)\right], \tag{3.11}$$

where the curly brackets represent the received signal power for a range profile (i.e., $P_{r,\text{dB}}$), the square brackets represent the noise floor (i.e., N_{dB}), P_r is the power at the output of the receiver in watts, N is the total noise power at the output of the receiver, P_t is the peak transmit power in watts, G is the antenna gain, λ_r is the radar operating frequency wavelength in metres, σ is the nonfluctuating target radar cross section in m^2, R is the range to the target, L_s is a general loss factor that accounts for both system and propagation losses, $\mathbb{K}$ is the Boltzmann constant, T_N is the effective noise temperature, F_N is the receiver noise factor, and B is the LFMCW chirp bandwidth. It is often assumed in the literature that $T_s = T_N F_N = 290$ Kelvin, and $L_s = 14$ dB. The chirp bandwidth considered in this study is 221 MHz.

Eq. 3.11 is used to characterize the performance of our LFMCW radar in Fig. 3.3. Table 3.1 lists the main parameters chosen in our SAR system design. These parameters were mainly chosen due to the availability of cost-effective hardware. A PCB board was built for this design. Fig. 3.4 depicts the radio frequency (RF) circuitry

and the PCB board[1]. Further, two identical PCB antennas were built[2]. The Smith chart for one of the antennas is given in Fig. 3.5. The H-plane and E-plane radiation patterns for this antenna are depicted in Fig. 3.6. Relevant antenna parameters are given in Table 3.1.

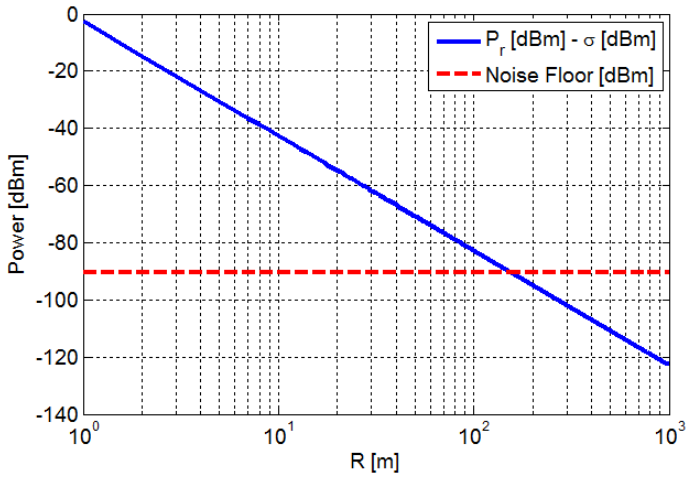

Figure 3.3: Performance of our LFMCW radar. The received power (P_r) is normalized by the radar cross section (σ).

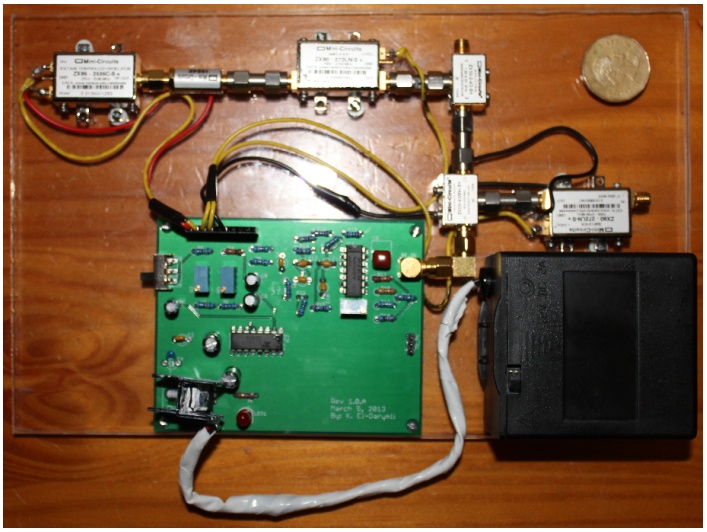

Figure 3.4: Circuitry for our SAR (DAQ unit is not shown).

[1]The device used for data acquisition is provided in Appendix C.
[2]A picture for the antennas is shown in Appendix D.

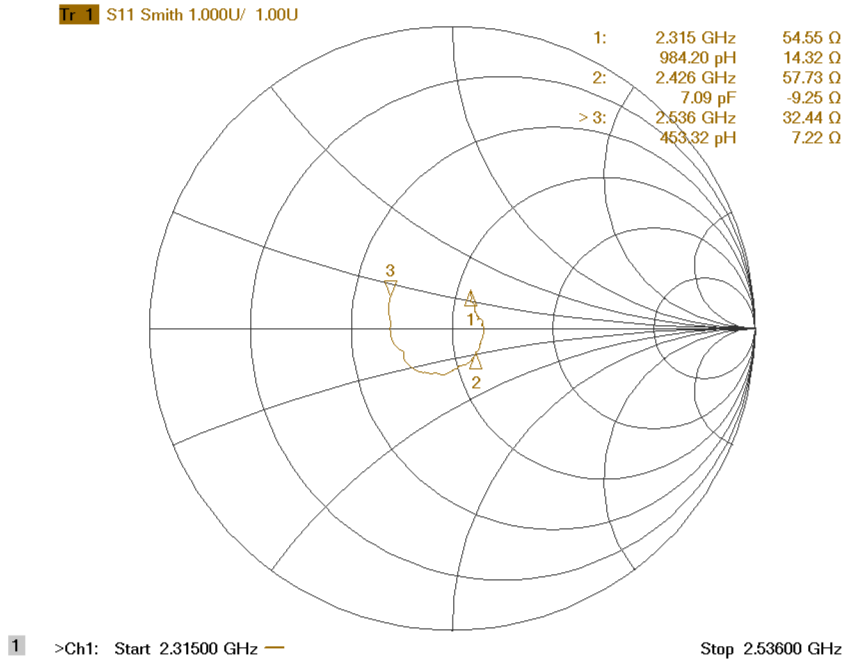

Figure 3.5: Smith chart for one of the antennas used in this study.

Table 3.1: Design parameters for our SAR system.

Design Parameter	Value
f_{min}	2.315 GHz
f_{max}	2.536 GHz
f_o	2.4255 GHz
B	221 MHz
T_m	40 ms
Sampling Frequency	96 kHz
Sampling Resolution	24 bits
Output Power	18.5 dBm (=70.8 mW)
Theoretical $\triangle R$	0.678733 m
Far Range, R_{max}	500 m (Extendable)
Antenna Vertical 3-dB Beamwidth	16.5^o
Antenna Horizontal 3-dB Beamwidth	15.5^o
Antenna VSWR	1.7:1
Antenna Gain	22 dBi
Antenna Front to Back Ratio	>36 dB

3.4. SAR Image Focusing

The range profiles output from the ADC are real-valued. Various operations are performed on these profiles in the digital SAR processor (see Fig. 3.7) to produce the focused complex-valued image. First, with the help of the synchronization signal, the range profiles are properly parsed and converted to a 2-D matrix with each row containing the range profiles for a particular cross-range location in the imaged scene. Second, the range profiles are converted to an analytic signal through quadrature demodulation. Other preprocessing operations can be performed at this stage including motion compensation, calibration, etc. Then, the phase history is focused through utilizing a suitable SAR image formation algorithm. We use the ωKA algorithm due to its simplicity and suitability for the imaging geometry considered in this study [6, 7].

Detailed explanation for the operations performed by the ωKA algorithm can be found in [6, 7]. The main operations performed by the ωKA algorithm are shown in Fig. 3.7. The output from the ωKA algorithm is the focused complex-valued SAR image.

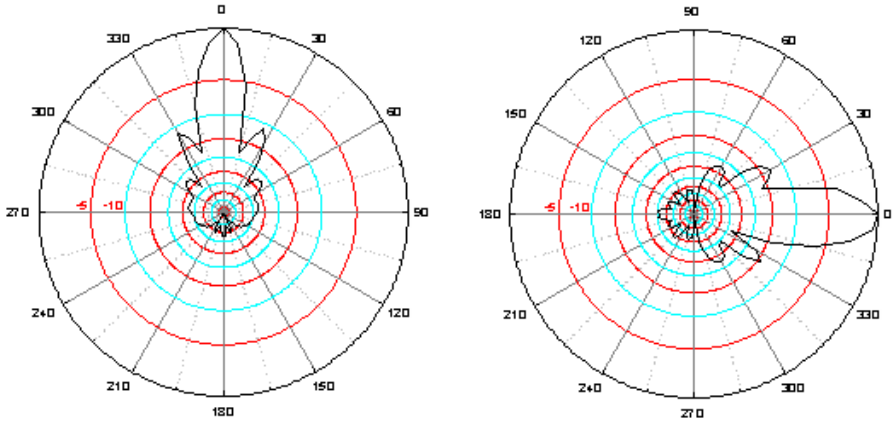

(a) H-plane radiation pattern. **(b)** E-plane radiation pattern.

Figure 3.6: H-plane and E-plane radiation patterns for the antenna.

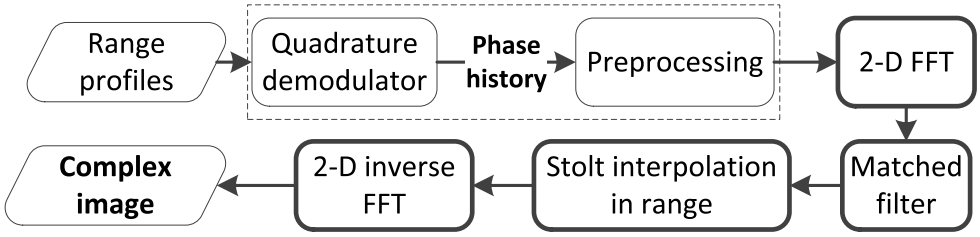

Figure 3.7: Digital SAR processor with the ωKA algorithm.

(a) Ground-truth with the magnitude-detected SAR image superimposed.

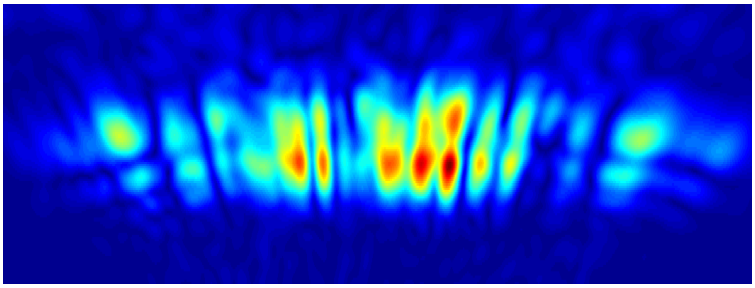

(b) Magnitude-detected SAR image.

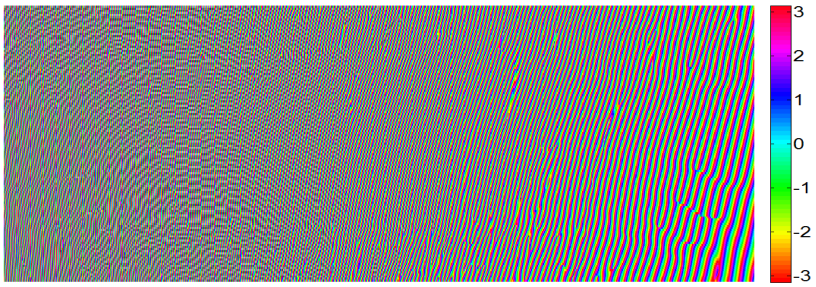

(c) Phase SAR image.

Figure 3.8: Focused image produced by our SAR.

3.5. An Illustrative Example

To demonstrate the applicability of our SAR system, a vehicle target is considered. The SAR sensor is placed at a suitable distance facing the vehicle's side, shown in Fig. 3.8a, and it is systematically moved from right to left. The focused magnitude-detected SAR image is shown superimposed on the ground-truth photograph in Fig. 3.8a, and it is shown separately in Fig. 3.8b. The corresponding phase image is shown in Fig. 3.8c. As depicted in Fig. 3.8b, the scattering centers of the imaged target are well-defined. Given the high-resolution of the SAR sensor, the phase image in Fig. 3.8c exhibits some interesting patterns relevant to the imaged target.

3.6. Conclusions

This chapter has reported on a design and implementation for a low-power S-band SAR. The main advantage of a researcher building their own SAR, besides being cost effective, is the unrestricted access to the phase history. This provides for investigating a plethora of relevant applications. The overall architecture for our system is presented along with a brief description for the concept of operation. The ωKA algorithm is used to focus the phase history, and to produce a complex-valued SAR image for a ground-truthed target. For the future, this design may be extended to a higher center frequency, such as the W-band, with a much higher bandwidth.

Bibliography

[1] MacDonald, Dettwiler and Associated Ltd. Radarsat-2 pricing information. [Online]. Available: http://gs.mdacorporation.com/SatelliteData/Radarsat2/Price.aspx 55

[2] T. Ross, J. Bradley, L. Hudson, and M. O'Connor, "SAR ATR: so what's the problem? an MSTAR perspective," *Proc. SPIE 3721, Algorithms for Synthetic Aperture Radar Imagery VI*, no. 662, 8 1999. [Online]. Available: http://dx.doi.org/10.1117/12.357681 55

[3] MeataSensing. (2013) FastGBSAR. [Online]. Available: http://www.metasensing.com/ 55

[4] R. Baraniuk, E. Candes, R. Nowak, and M. Vetterli, "Compressive sampling [from the guest editors]," *Signal Processing Magazine, IEEE*, vol. 25, no. 2, pp. 12–13, 2008. [Online]. Available: http://dx.doi.org/10.1109/MSP.2008.915557 56

[5] DARPA. (2013) Video SAR (ViSAR). [Online]. Available: https://www.fbo.gov/index?s=opportunity&mode=form&id=0b7df5c5ced08a7396338247b0601f38&tab=core&_cview=1 56

[6] I. Cumming and F. Wong., *Digital Processing of Synthetic Aperture Radar Data*. Norwood, MA: Artech House, 2005. 56, 57, 60, 63

[7] W. Carrara, R. Goodman, and R. Majewski, *Spotlight Synthetic Aperture Radar: Signal Processing Algorithms*. Norwood, MA: Artech House, 1995. 56, 57, 63

[8] M. Friend, "Combat identification with synthetic aperture radar, out-of-library identification, and non-declarations," Ph.D. dissertation, Air Force Institute of Technology, 2007. 56

[9] T. Albrecht, "Optimization framework for a multiple classifier system with non-registered targets," *Journal of Defense Modeling and Simulation*, vol. 5,

no. 1, pp. 61–81, 2007. [Online]. Available: http://dms.sagepub.com/content/5/1/61.abstract 56

[10] M. Edwards, D. Madsen, C. Stringham, A. Margulis, B. Wicks, and D. Long, "microASAR: A small, robust LFM-CW SAR for operation on uavs and small aircraft," vol. 5. Geoscience and Remote Sensing Symposium, IEEE International, July 2008, pp. 514–517. [Online]. Available: http://dx.doi.org/10.1109/IGARSS.2008.4780142 56

[11] R. Saldana and F. Martinez, "Design of a millimetre synthetic aperture radar (SAR) onboard UAV's." Electronics, Circuits and Systems, ICECS, 14th IEEE International Conference on, Dec 2007, pp. 1–5. [Online]. Available: http://dx.doi.org/10.1109/ICECS.2007.4510916

[12] M. Jensen, D. Arnold, and D. Crockett, "Microwave engineering design laboratories: C-band rail SAR and doppler radar systems," vol. 1. Antennas and Propagation Society International Symposium, IEEE, July 1999, pp. 82–85. [Online]. Available: http://dx.doi.org/10.1109/APS.1999.789088 56

[13] G. Charvat, A. Fenn, and B. Perry, "The MIT IAP radar course: Build a small radar system capable of sensing range, doppler, and synthetic aperture (SAR) imaging," in *2012*. Radar Conference (RADAR), IEEE, May, pp. 138–144. [Online]. Available: http://dx.doi.org/10.1109/RADAR.2012.6212126 56

[14] J. Laskar, B. Matinpour, and S. Chakraborty, *Modern Receiver Front-Ends: Systems, Circuits, and Integration*. Hoboken, NJ: Wiley-Interscience, 2004. 57

[15] D. Shaeffer and T. Lee, *The Design and Implementation of Low-Power CMOS Radio Receivers*. Boston: Springer, 1999. 57

[16] M. Skolnik, *Introduction to Radar Systems*. Boston: McGrawHill, 2001. 57

[17] ——, *Radar Handbook*. New York, NY: McGrawHill, 1990.

[18] J. Eaves and K. Edward, Eds., *Principles of Modern Radar*. New York, NY: Van Nostrand Reinhold, 1987, vol. 197. 57

[19] M. Richards, *Fundamentals of Radar Signal Processing*. New York, NY: Tata McGraw-Hill Education, 2005. 60

4. Unscrambling Nonlinear Dynamics in Synthetic Aperture Radar Imagery

4.1. Overview

In analyzing single-channel synthetic aperture radar (SAR) imagery, three interrelated questions often arise. Firstly, should one use the detected or the complex-valued image? Secondly, what is the 'best' statistical model? Thirdly, what constitute the 'best' signal processing methods? This chapter addresses these questions from the overarching perspective of the generalized central limit theorem, which underpins nonlinear signal processing. A novel procedure for characterizing the nonlinear dynamics in SAR imagery is proposed. To apply the procedure, three complementary 1-D abstractions for a 2-D SAR chip are introduced. Our analysis is demonstrated on real-world datasets from multiple SAR sensors. The nonlinear dynamics are found to be resolution-dependent. As the SAR chip is detected, nonlinear effects are found to be obliterated (i.e., for magnitude-detection) or altered (i.e., for power-detection). In the presence of extended targets (i.e., nonlinear scatterers), it is recommended to use the complex-valued chip rather than the detected one. Further, to exploit the embedded nonlinear statistics, it is advised to utilize relevant nonlinear signal analysis techniques.

4.2. Introduction

Although we live in an inherently nonlinear world, conventional signal processing is built on linear system theory. This theory treats deviation from linearity as noise that warrants removal. Much of the original interest in nonlinear phenomena arose from the

study of deterministic chaos, and subsequent research has branched into an analysis of nonlinearity in general [1–3]. Nonlinear-based research efforts can be broadly classified into two main branches: (1) the development of novel methods that seek to explicitly exploit the nonlinear phenomenon, and (2) the advancement of techniques that permit the harnessing of nonlinear dynamics (i.e., so-called nonlinear artifacts) retained in the signal after application of common linear signal processing methods. This chapter, concerned with the second branch, is exclusively aimed at the focused *single-channel* complex-valued synthetic aperture radar (SAR) image outputs from SAR processors.

In SAR and its relatives, such as synthetic aperture sonar (SAS), the signal processor focuses 1-D range profiles into a complex-valued image. The underlying assumption which underpins signal processing theory in general, and its application to SAR imagery in particular, is linearity. Indeed, the SAR image is often implicitly assumed to be linear. This is a consequence of the conventional resolution theory of point targets [4]. Consequently, most of the interest in analyzing the focused single-channel SAR image has traditionally been based on techniques motivated by linear system theory. As a result, many such linear techniques are associated with the detected SAR image (i.e., image intensity) while the phase content is entirely ignored. With the advent of high-resolution remote sensors, the insufficiency of this theory as applied to both stationary and moving extended targets has been reported in the literature [5–7]. This conclusion is based on the empirical observation that extended targets, such as vehicles and airplanes, produce dispersive scattering from cavity-like reflectors. In effect, this induces a nonlinear phase modulation in the radar return signal which causes a mismatch in the correlator's output. This phenomenon is referred to as 'sideband responses', and much of the information about it is preserved in the complex-valued image rather than the detected one.

In the signal processing literature, there are two definitions of linearity considered [8–13]: one is the definition of a strictly linear signal, and the other is the commonly adopted definition of a linear signal. In the former, the signal is assumed to be generated by a linear time invariant (LTI) or a linear space invariant (LSI) system with a white Gaussian noise. The commonly adopted definition differs from the former in that the magnitude distribution is allowed to deviate from the Gaussian distribution. This implies that the strictly defined linear signal is allowed to be characterized by a nonlinear observation function, thereby justifying the use of linear signal processing

methods on the latter. The main reason for the popularity of linear signal processing techniques is their rich and well-defined linear system theory and simplicity of implementation. However, if the SAR data is proven to be nonlinear, significant gains are to be anticipated from applying relevant nonlinear techniques. This is because the nonlinear methods provide for the exploitation of the nonlinear statistics ignored by the common linear signal processing methods. While the SAR sensor is often modeled in the literature as a linear system [4], this does not guarantee that the focused complex-valued image output from the SAR processor is linear, as explained earlier [5–7].

Although our discussion here is presented in the context of automatic target recognition in SAR imagery (SAR-ATR), which includes both detection and classification, it is straightforward to generalize this discussion to any relevant context. In the detection stage, popular linear statistical models include the Gaussian, exponential, Rayleigh, Gamma, and Weibull distributions, etc. [14]. All these linear models implicitly assume the underlying (superimposed) random variables to have a finite variance. Hence, such models are all motivated by the central limit theorem (CLT). On the contrary, nonlinear statistical models are built on the premises that the underlying random variables possess an infinite variance; thus, such models are justified by the generalized central limit theorem (GCLT). Examples of nonlinear statistical models include the generalized Gaussian distribution (GGD) [13], the complex GGD [15], the symmetric α-stable ($S\alpha S$) distribution [13], the Gaussian scale mixture (GSM) [16], and the wrapped complex Gaussian scale mixture (WCGSM) [17], etc.

In the classification stage, suitable signal processing methods are often used to extract and/or select useful features from the SAR data. These features are used for classifier training and testing. Feature generation methods can be broadly classified into linear and nonlinear which are motivated by the CLT theorem and the GCLT theorem, respectively. Among others, popular linear signal processing methods include the Fourier [18, 19], wavelet [20], Radon transforms [20, 21], and principal component analysis (PCA) [22], while nonlinear signal processing methods similarly include the empirical mode decomposition (EMD) [23, 24], Hilbert-Huang transform (HHT) [23, 25, 26], nonlinear independent component analysis (nICA) [27], and the weighted myriad filter (WMF) [13]. While many linear signal processing methods are designed to preserve the nonlinear statistics (i.e., in the linearly transformed signal, when the

nonlinear statistics are present in the original signal), features generated solely based on the linear statistics will be blind to the nonlinear dynamics.

Based on the preceding discussion, it is clear that a proper understanding of the inherent nature of the SAR data in terms of linearity and nonlinearity will not only allow for an informed choice pertaining to the most suitable statistical models and signal processing methods, but also will provide for the extraction of as much information as possible from the SAR data. The novel contributions presented in this chapter may be summarized as follows

- A procedure for empirically demonstrating the inapplicability of the CLT theorem and the applicability of the GCLT theorem to extended targets in SAR imagery, and the interrelationship with the spatial resolution of the SAR sensor (see Sect. 4.3.2 and Sect. 4.8.1),
- A method for linearly transforming the real-valued SAR chip from 2-D to 1-D space (see Sect. 4.5.2),
- A method for linearly transforming the complex-valued SAR chip, in terms of the bivariate statistics, from 2-D to 1-D space (see Sect. 4.5.3),
- A method for linearly transforming the complex-valued SAR chip, in terms of the complex-valued statistics, from 2-D to 1-D space (see Sect. 4.5.4), and
- A procedure for detecting and characterizing the statistical significance of nonlinearity in SAR imagery (see Sect. 4.6).

Throughout this chapter, the term *SAR* is used to inclusively imply all other signals that possess similar properties. Moreover, the term *high-resolution* is used to nominally refer to a sensor with a spatial resolution greater than the size of the imaged target (i.e., extended target) [28]. Further, the term *chip* is used to refer to a smaller image, for a particular target or clutter, extracted from a bigger scene. Finally, in the present context the term *non-Gaussian* is used synonymously with *nonlinear*.

The remainder of this chapter is organized as follows. In Sect. 4.3, the underlying motivations for this study are presented. In Sect. 4.4, the topic of nonlinearity detection in SAR imagery through resampling and hypothesis testing is approached. In Sect. 4.5, a procedure for linear transformation of the real-valued, as well as the complex-valued, SAR chip from 2-D to 1-D space is proposed. In Sect. 4.6, a procedure for testing the statistical significance of nonlinearity in SAR imagery is outlined. In Sect. 4.7,

the overall SAR datasets used in this study are introduced. In Sect. 4.8, results are discussed. Finally, a conclusion appears in Sect. 4.9.

4.3. Motivations

In motivating this study, Sect. 4.3.1 suggests an answer to the question: *why is nonlinear signal processing necessary for SAR image analysis?* This is followed in Sect. 4.3.2 by a discussion on the central limit theorem (CLT) and the generalized central limit theorem (GCLT), in the context of SAR imagery. Demonstrative examples complementary to this section are provided under Sect. 4.8.1.

4.3.1. Why Nonlinear Signal Processing?

Nonlinear signal processing offers significant advantages over traditional linear signal processing in applications where the underlying random processes are non-Gaussian in nature and/or when the system acting on the signal of interest is inherently nonlinear [13, 15]. Given that the SAR sensor is often modeled as a linear system [4], the former case is of interest here. It is important to precisely explain what is meant by linearity and nonlinearity. The following definitions are used in the literature to characterize the signal's linearity/nonlinearity [8–12]:

4.3.1.1. Definition of Strictly Linear Signal

a signal generated by a linear time invariant (LTI) or a linear space invariant (LSI) system with a white Gaussian noise.

4.3.1.2. Commonly Adopted Definition of Linear Signal

similar to the aforementioned definition but the magnitude distribution is allowed to deviate from the Gaussian distribution. This implies that, the strictly defined linear signal is allowed to be characterized by a nonlinear observation function.

4.3.1.3. Definition of Nonlinear Signal

any signal that does not fulfill the definition of either the strictly linear signal or the commonly adopted definition of linear signal.

While much of the original interest in nonlinear phenomena arose from the study of deterministic chaos, subsequent research has branched into an analysis of nonlinearities generally [1–3]. In the remote sensing community, this motivated the development of new techniques that are deliberately designed to excite nonlinear scattering in the imaged object, and to properly harness it using suitable nonlinear signal processing methods [29]. One of the most interesting recent studies on the superiority of nonlinear signal processing for sonar is that reported in [29, 30]. In that study, it is empirically demonstrated that while conventional linear signal processing is not able to distinguish the targets from the bubble clutter, nonlinear signal processing inspired by dolphin-like sonar pulses can both detect and classify such targets. In [29, 31], the extension of this technique allowed the development of a new radar which relies on the excitation of nonlinearities in the imaged scene. Nonlinear signal processing was used to differentiate between linear and nonlinear scatterers, thus, improving the target recognition performance of the radar.

4.3.2. Central Limit Theorem (CLT), Generalized Central Limit Theorem (GCLT), and SAR Imagery

It is intuitive to approach the abovementioned definitions of linearity and nonlinearity from the perspective of the CLT and the GCLT theorems, respectively. In Cases (Sect. 4.3.1.1) and (Sect. 4.3.1.2) above, the signal is assumed to be linear. For the two cases, this implies that the superposition principle (i.e., additivity and homogeneity) either *strictly* or *approximately* hold, respectively [18, 19, 32]. This is a consequence of the CLT theorem. The classical CLT theorem states that the properly normed sum of a set of independent and identically distributed (iid) random variables, *each with a finite variance*, will tend to Gaussian as the number of variables increases [33]. In Case (Sect. 4.3.1.1), the CLT is *strictly* applicable which means that the statistical distribution of the signal can be strictly modeled as Gaussian. However, in many real-world systems the assumption of the strict Gaussianity is impractical. In Case (Sect. 4.3.1.2), although a distribution other than (strict) Gaussian can be used to model the (magni-

tude or power-detected) signal, the applicability of the CLT theorem is still assumed. This is because such distributions (e.g., exponential, Rayleigh, Weibull, etc. [14]), implicitly assume that the random variables they model possess a finite variance. This implies that they lie in the *domain-of-attraction* of the Gaussian distribution (i.e., are asymptotically Gaussian). It transpires that this is the case for any statistical distribution that employs the assumption of finite variance in the random variables modeled. Here, we demonstrate the applicability of this idea to SAR imagery.

In order for Case (Sect. 4.3.1.1) to be applicable to SAR imagery, it is required that the complex-valued speckle (i.e., $Y = Y_I + jY_Q$; imaginary unit $j = \sqrt{-1}$, subscripts I and Q denote the real and imaginary parts, respectively), which is modeled as a multiplicative noise, be bivariate Gaussian (i.e., Y_I is strictly Gaussian and Y_Q is strictly Gaussian). Assuming a homogeneous clutter and a single-look SAR processing, the complex-valued backscatter X is constant (i.e., C). Thus, the statistical multiplicative model of the complex-valued SAR image including speckle (i.e., $Z = X\,Y = Z_I + jZ_Q$) is bivariate Gaussian (i.e., $Z = C\,(Y_I + jY_Q)$). This implies that the power-detected SAR image $\left(\text{i.e., } Z_P = Z_I^2 + Z_Q^2\right)$ is exponentially distributed. Further, the magnitude-detected SAR image $\left(\text{i.e., } Z_M = \sqrt{Z_I^2 + Z_Q^2}\right)$ follows Rayleigh distribution. Hence, the phase image follows a uniform distribution. This makes the assumption of linearity strictly applicable. For Case (Sect. 4.3.1.2), the assumption that the distribution of the complex-valued Y strictly abides by the bivariate Gaussian is replaced with the properties that Y follows the Gamma distribution and the square-root Gamma distribution, respectively, in the power-domain and the magnitude-domain. It may be noted that the exponential distribution, mentioned earlier under Case (Sect. 4.3.1.1), is a special case of the Gamma distribution. Further, the assumption of constant X is replaced with a particular statistical model in the power or the magnitude domain but not in the complex-valued domain. For example, one of the generic distributions used for modeling the SAR image in the magnitude-domain is the G-distribution. The G-distribution uses the square-root of the generalized inverse Gaussian distribution to model $X_M = \sqrt{X_I^2 + X_Q^2}$ for both homogeneous and heterogeneous backgrounds. The speckle model in the power or the magnitude domain, still follows the Gamma distribution and the square-root Gamma distribution, respectively. Some other popular statistical distributions such as the G^o-distribution and the K-distribution are special cases of the G-distribution. This shows the scope of Case (Sect. 4.3.1.2) in the context

of SAR imagery. It is clear that in all these cases the distribution of the magnitude-detected or the power-detected SAR image is allowed to deviate from the Gaussian distribution, in order for the non-strict assumption of linearity to hold. It is interesting to note that the implicit assumption here is that all these distributions are in the domain-of-attraction of the Gaussian distribution. Further, in all such statistical models, the complex-valued statistics are entirely ignored due to the assumption that the phase follows a uniform distribution. A detailed explanation on the interrelation between these statistical models for SAR imagery is found in Sect. 5.2 in [14].

In Case (Sect. 4.3.1.3), due to the *infinite variance* of the signal's distribution (i.e., when the signal is sampled from a population with an infinite variance), the CLT cannot hold. Thus, the CLT is replaced with the Generalized CLT (GCLT). In the GCLT, the Gaussian distribution as a *domain-of-attraction* is replaced with the so-called *stable distribution*. The GCLT states that a sum of independent random variables from the same distribution, when properly centered and scaled, belongs to the domain-of-attraction of a stable distribution. Further, the only distributions that arise as limits from suitably scaled and centered sums of random variables are the stable distributions [13, 34]. Of interest in nonlinear signal processing are the stable Paretian distributions which are strictly non-Gaussian. Note that statistical distributions motivated by the CLT theorem can be viewed as a special case of the GCLT theorem.

Case (Sect. 4.3.1.3) motivates the whole research on nonlinear signal processing. The reasoning here is that if one forces a signal sampled from a population which possesses an infinite variance to be modeled, or more generally processed, using a linear technique, one simply ignores some valuable information which can only be exploited through utilizing nonlinear signal processing methods [13]. A practical example is the statistical model often used in the front-end stage (i.e., target detection) of an automatic target recognition (ATR) system. Other examples are the features generated from the target chips for training and testing the intermediate (i.e., low-level classifier) and the back-end (i.e., high-level classifier) stages of the ATR system. The empirical applicability of Case (Sect. 4.3.1.3) to high-resolution SAR imagery is discussed in detail in Sect. 4.8.1.

4.4. Nonlinearity Detection in SAR Imagery

Under this section, the topic of nonlinearity detection in SAR imagery is presented. Testing for nonlinearity through resampling is described in Sect. 4.4.1. Then, relevant test statistics for linearity and nonlinearity, used in this chapter, are presented in Sect. 4.4.2. Finally, pertinent parametric and nonparametric tests for statistical significance are introduced in Sect. 4.4.3.

4.4.1. Testing for Nonlinearity through Resampling

The most common method for nonlinearity detection in a 1-D signal is that based on the so-called surrogate data test. In this method, a surrogate signal $\{\mathbf{z}_t\}_{t=1}^{n}$ is resampled from an original signal $\{\mathbf{x}_t\}_{t=1}^{n}$ to be tested. The resampled signal should fulfill the following two conditions: (1) it should preserve the linear correlation of the original signal, and (2) it should retain the marginal distribution pertinent to the original signal [35–37]. Thus, $\{\mathbf{x}_t\}_{t=1}^{n}$ is resampled in accordance with a null hypothesis $\mathcal{H}_0$ (for linearity) such that a surrogate signal $\{\mathbf{z}_t\}_{t=1}^{n}$ is generated as follows

$$\mathcal{H}_0 : \mathbf{z}_t = \underline{h}\left(\mathbf{s}_t\right), \;\; \{\mathbf{s}_t\} \sim \mathcal{N}\left(0, 1, \rho_s\right), \tag{4.1}$$

where $\mathcal{H}_0$ is a stochastic linear process, $\{\mathbf{s}_t\}$ is a standard Gaussian process, ρ_s is the autocorrelation of $\mathbf{s}_t$, and $\underline{h}$ is a static instantaneous transform which can be linear/nonlinear/monotonic/nonmonotonic. Note that $\mathcal{N}\left(0, 1, \rho_s\right)$ accounts for the linear dynamics in the input signal and $\underline{h}$ allows for deviations from the marginal Gaussian distribution. Various relevant resampling methods are reported in the literature. Of interest to this study is the iterative amplitude adjusted Fourier transform (iAAFT) method [38, 39], which is chosen mainly because it is found to give acceptable results [40]. The iAAFT method approximates the sample power spectrum, $S_z(f) \approx S_x(f)$, where $S_x(f)$ is the periodogram of $\{\mathbf{x}_t\}_{t=1}^{n}$. Further, the iAAFT follows the constrained realization approach in a direct attempt to generate surrogate data that fulfill the abovementioned two conditions. Hence, the iAAFT is designed to be used for testing $\mathcal{H}_0$ of a Gaussian process undergoing a static transform (i.e., not only the monotonic, Case (Sect. 4.3.1.2) as discussed earlier). The iAAFT surrogate approximates the orig-

inal autocorrelation (i.e., linear correlation) and possesses the exact original marginal distribution of the input signal [38, 40, 41].

4.4.2. Measures for Linearity and Nonlinearity

In this study, two kinds of correlation measures are used to account for the linear and nonlinear statistics, respectively. Firstly, for capturing the linear correlation statistics in the SAR chip, we use the Pearson product-moment correlation (PPMC) given in [39, 42] as

$$r(\tau) = \frac{\sum_{t=1}^{n-\tau} (y_t - \bar{y})(y_{t+\tau} - \bar{y})}{\sum_{t=1}^{n-\tau} (y_t - \bar{y})^2}, \tag{4.2}$$

where τ is a lag and $\bar{y}$ is the mean of $\{y_t\}_{t=1}^{n}$. Secondly, for capturing the nonlinear correlation statistics, we use the mutual information (MI) defined as [43]

$$I(\tau) = I(Y_t, Y_{t-\tau}) = \sum_{Y_t} \sum_{Y_{t+\tau}} p_{Y_t Y_{t-\tau}}(y_t, y_{t-\tau}) \times \log \frac{p_{Y_t Y_{t-\tau}}(y_t, y_{t-\tau})}{p_{Y_t}(y_t)\, p_{Y_{t-\tau}}(y_{t-\tau})}, \tag{4.3}$$

where $p_{Y_t Y_{t-\tau}}(y_t, y_{t-\tau})$ is the joint probability mass function (PMF), and $p_{Y_t}(y_t)$ and $p_{Y_{t-\tau}}(y_{t-\tau})$ are the marginal PMFs for y_t and $y_{t-\tau}$, respectively. MI is known to be a powerful test statistic for nonlinearity, accounting for both linear and nonlinear behaviors [44–46]. To estimate the joint and marginal PMFs of Eq. 4.3 we use the equiprobable bin histogram (EBH) procedure which partitions the domain of Y_t and $Y_{t-\tau}$ into b intervals of similar occupancy and different width [44, 47, 48]. The histogram bins are chosen to have equal probability rather than equal width as is the usual case. Thus, the width of the bins is allowed to vary while the height of each bin is constrained so that the area under the PMF approximation is equal to one. The main advantage of EBH over the traditional equidistant histogram (EDH) is that it provides improved resolution in regions where there is a large number of samples. Further, the number

of bins b for each histogram considered in this study is set, as suggested in [44], to

$$b = \sqrt{\frac{n}{5}}, \tag{4.4}$$

where n is the total length of the 1-D vector.

4.4.3. Testing for Statistical Significance in the Linear/Nonlinear Measures

Testing for the statistical significance is of paramount importance in two scenarios pertaining to this study. Firstly, this test is required to examine the validity of the surrogates for nonlinearity testing (i.e., conformity of the surrogates with $\mathcal{H}_0$). This is achieved through examining the statistical significance of the linearity in the surrogates. If the surrogates are confirmed linear, they are deemed suitable for nonlinearity analysis. Secondly, the statistical significance of the nonlinearity in the original SAR data (i.e., deviation of the original SAR data from $\mathcal{H}_0$) must be tested.

The procedure for testing the significance of the statistic $\mathbb{Q}_S$ is formed by values of $\mathbb{Q}_S$ computed on an ensemble of N surrogates $\{\mathbb{Q}_1, \mathbb{Q}_2, ..., \mathbb{Q}_N\}$. Then, if the statistic computed on the original signal, denoted $\mathbb{Q}_0$, is found to be in the tails of the empirical null distribution, $\mathcal{H}_0$ is rejected. This test may be implemented using parametric and nonparametric methods. Both methods are considered in this study to confirm the significance of the results. The parametric test for linearity/nonlinearity is provided in Sect. 4.4.3.1, and the nonparametric test for Gaussianity, required to validate the parametric test, is given in Sect. 4.4.3.2. Finally, the nonparametric test for linearity/nonlinearity is described in Sect. 4.4.3.3.

4.4.3.1. Parametric Test for Linearity/Nonlinearity

Let $\mathbb{Q}_0$ denote the test statistic generated from the original signal to be tested, $\mathbb{Q}_\mathrm{i}$ denote the test statistic for the i^{th} surrogate under $\mathcal{H}_0$, and μ_S and σ_S denote the sample mean and standard deviation, respectively, of the test statistic pertaining to $\mathbb{Q}_S \sim \{\mathbb{Q}_1, \mathbb{Q}_2, ..., \mathbb{Q}_N\}$. The parametric measure of statistical significance is defined

as

$$\mathcal{L} = \frac{|\mathbb{Q}_0 - \mu_{\mathcal{S}}|}{\sigma_{\mathcal{S}}}. \tag{4.5}$$

If the distribution of $\mathcal{L}$ is Gaussian, then the P-Value is given by [49, 50] as

$$P = 1 - \operatorname{erf}\left(\frac{\mathcal{L}}{\sqrt{2}}\right) = \int_{\frac{\mathcal{L}}{\sqrt{2}}}^{\infty} \exp\left(-u^2\right) \mathrm{du}. \tag{4.6}$$

The P-Value represents the probability of observing a significance $\mathcal{L}$ or larger if $\mathcal{H}_0$ is true. Hence, $\mathcal{H}_0$ is rejected if the P-Value is less than or equal to a significance level α (i.e., the alternative hypothesis $\mathcal{H}_1$ is favored). Typically, α is chosen to be either 0.01 or 0.05 [49, 50].

4.4.3.2. Nonparametric Test for Gaussianity

In order for the parametric test of Sect. 4.4.3.1 to be valid, the measure values from the surrogates are assumed to follow the Gaussian distribution. Thus, the parametric test is rendered invalid (or at least inaccurate) if the measure values from the surrogates deviate from the Gaussian distribution. The nonparametric Kolmogorov-Smirnov (KS) test for Gaussianity is considered in this study to examine the conformity of the surrogate statistic ensemble $\{\mathbb{Q}_1, \mathbb{Q}_2, ..., \mathbb{Q}_N\}$ with the Gaussian distribution for a significance level α. The KS test achieves this through quantifying the largest vertical distance between the empirical distribution function (EDF) denoted by $\hat{F}(x)$ of the sample and an estimate of the cumulative distribution function (CDF) of the Gaussian distribution denoted by $G(x)$. The KS statistic is given in [51, 52] as

$$\mathcal{K} = \sup_x \left|\hat{F}(x) - G(x)\right|, \tag{4.7}$$

where $\sup_x$ is the supremum of the set of distances. An approximation for the critical

value pertaining to this test is given by [39, 53]

$$C_\alpha = \frac{K_\alpha}{\sqrt{N} + 0.12 + \frac{0.11}{\sqrt{N}}}, \tag{4.8}$$

where $K_\alpha = 1.358$ and $K_\alpha = 1.628$ for a significance level $\alpha = 0.05$ and $\alpha = 0.01$, respectively [39, 53]. For a significance level α, Gaussianity is accepted if $\mathcal{K} < C_\alpha$, and the parametric test in Sect. 4.4.3.1 is deemed valid. Otherwise, Gaussianity is rejected and the parametric test in Sect. 4.4.3.1 is deemed invalid.

4.4.3.3. Nonparametric Test for Linearity/Nonlinearity

Being distribution-free, the nonparametric approach offers a more robust way to define the statistical significance for linearity/nonlinearity. In this work, a two-sided test is used where $\mathcal{H}_0$ is rejected if $\mathbb{Q}_0$ is smaller than the $\frac{\alpha}{2}$ quantile or larger than the $1 - \frac{\alpha}{2}$ quantile of the surrogate statistic ensemble $\{\mathbb{Q}_1, \mathbb{Q}_2, ..., \mathbb{Q}_N\}$. For example, if $N = 1000$ and $\alpha = 0.05$, $\mathcal{H}_0$ is rejected if $\mathbb{Q}_0$ is in the first or last 25 positions of the rank ordered sequence $\{\mathbb{Q}_1, \mathbb{Q}_2, ..., \mathbb{Q}_N\}$.

4.5. Linear Transformation of SAR Chips from 2-D to 1-D Space

While the linear and nonlinear measures described in Sect. 4.4 may be applied to a particular direction in the SAR chip (e.g., vertical, horizontal, diagonal, etc.), it is desired that such measures be designed to account for the neighborhoods of each pixel. Under this section, we propose a method to transform the 2-D SAR chip into an abstract 1-D vector that accounts for the pixel neighborhoods. The method is inspired by the Radon transform. One main advantage of the Radon transform is that, being a linear transform in the spatial-domain, it preserves the original statistics present in the SAR image without introducing any nonlinear artifacts. A succinct description for the forward Radon transform is given in Sect. 4.5.1. Then, a novel method for linear transformation of the real-valued 2-D SAR chip into a 1-D vector is presented in Sect. 4.5.2. This is followed, in Sect. 4.5.3, by a novel method for linear transformation

of the bivariate 2-D SAR chip into a 1-D vector. Finally, Sect. 4.5.4 describes a method for linear transformation of the complex-valued 2-D SAR chip into a 1-D vector.

4.5.1. The Forward Radon Transform

The Radon transform $R_\theta(x')$ for a 2-D function $f(x, y)$ is the line integral of f parallel to the y' axis defined, for example in [21], as

$$R_\theta(x') = \int_{-\infty}^{\infty} f(x' \cos\theta - y' \sin\theta, x' \sin\theta + y' \cos\theta)\, dy', \tag{4.9}$$

where θ is the projection angle, and (x', y') are the projection coordinates which are related to the projection angle by

$$\begin{bmatrix} x' \\ y' \end{bmatrix} = \begin{bmatrix} \cos\theta & \sin\theta \\ -\sin\theta & \cos\theta \end{bmatrix} \begin{bmatrix} x \\ y \end{bmatrix}. \tag{4.10}$$

The geometry of the Radon transform is illustrated in Fig. 4.1.

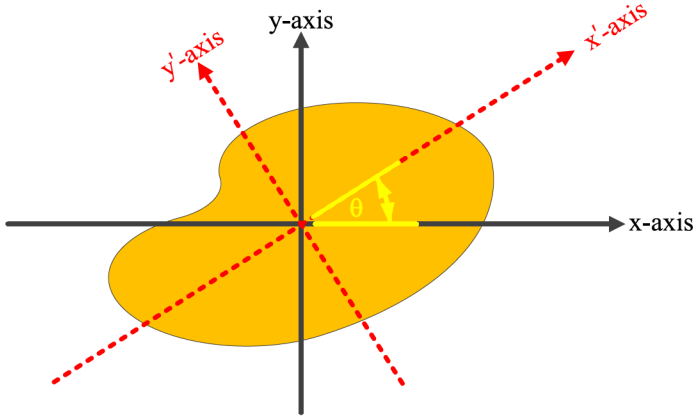

Figure 4.1: Illustration of the Radon transform for a projection angle θ. The random shape provided represents the 2-D function $f(x, y)$.

Note that the (x', y') coordinate is rotated (in the spatial-domain) about the center of the image as shown in Fig. 4.1. An important property of the Radon transform, which is of interest to the study presented in this chapter, is linearity [21]. This implies that the Radon transform is both additive and homogeneous. This guarantees that the Radon-transformed signal retains the statistics of the original 2-D SAR chip and does not include nonlinear artifacts due to the transformation process.

4.5.2. A Method for Linear Transformation of the Real-Valued 2-D SAR Chip into a 1-D Vector

Under this section, a procedure for transforming the real-valued 2-D SAR chip $f(x, y)$ into a 1-D vector, utilizing the Radon transform, is proposed. The proposed procedure is illustrated in Fig. 4.2. First, the Radon transform of the real-valued input SAR chip is computed for the angles in the interval $[0, \pi)$ as

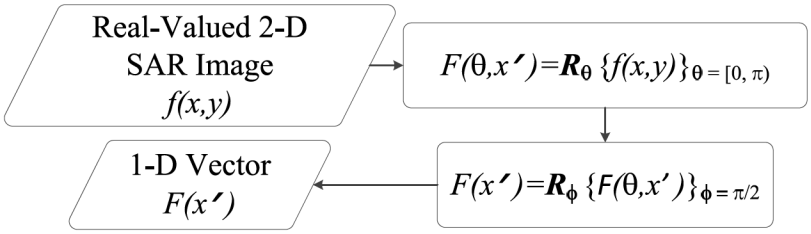

Figure 4.2: Proposed procedure for transforming a real-valued 2-D SAR chip into a 1-D vector.

$$F(\theta, x') = R_\theta \{f(x, y)\}|_{\theta=[0,\pi)}, \tag{4.11}$$

a representation known also as a *sinogram*. Note that angles in the range $[\pi, 2\pi]$ are omitted because their corresponding Radon transform provides identical values to the angles in the range $[0, \pi)$, and this redundancy is of no interest to this study. This

is followed by integrating out the projection angles $\theta = [0, \pi)$ through applying the Radon transform to the sinogram output at a projection angle $\phi = \frac{\pi}{2}$ to obtain

$$F(x') = R_{\phi}\{F(\theta, x')\}|_{\phi=\frac{\pi}{2}}. \tag{4.12}$$

The output given by Eq. 4.12 is an abstract 1-D vector representative of the input 2-D SAR chip. The procedure shown in Fig. 4.2 can be applied to any real-valued SAR chip, including the detected SAR chips (i.e., the power and the magnitude-detected chips) as well as the real and the imaginary parts of the complex-valued SAR chip.

4.5.3. A Method for Linear Transformation of the Bivariate 2-D SAR Chip into a 1-D Vector

Under this section, a procedure for transforming the bivariate SAR chip into a real-valued 1-D vector is proposed. The term bivariate is used here to denote that the real and the imaginary parts of the complex-valued SAR chip are treated as two separate real-valued chips. This is in analogy to the bivariate distribution (e.g., bivariate Gaussian) which is used to model the complex-valued data in such a manner (see page 20 in [54]). The procedure proposed here is meant to account for the bivariate statistics between the real and the imaginary parts of the complex-valued SAR chip. Fig. 4.3 depicts the proposed procedure.

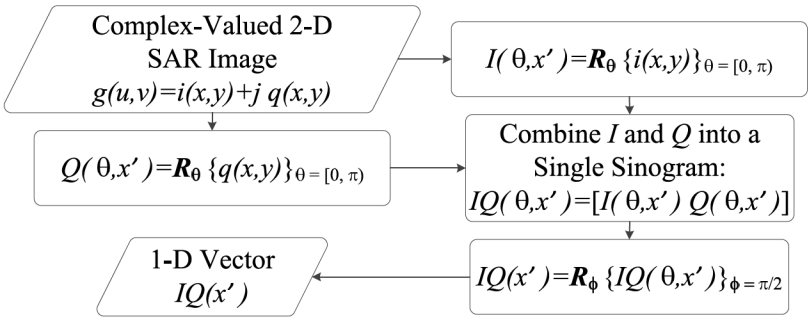

Figure 4.3: Proposed procedure for transforming a bivariate complex-valued SAR chip into a 1-D vector.

The complex-valued SAR chip is available in the form

$$g\left(u,v\right)=i\left(x,y\right)+j\,q\left(x,y\right), \tag{4.13}$$

where $i\left(x,y\right)$ and $q\left(x,y\right)$ are the real and the imaginary parts, respectively, of the complex-valued SAR chip; and $j=\sqrt{-1}$. Note that (x,y) represent the 2-D Cartesian coordinates of the real-valued plane, while (u,v) represent the 2-D Cartesian coordinates in the complex-valued plane.

The Radon transform is applied separately to the real and the imaginary parts of the complex-valued SAR chip as

$$I\left(\theta,x'\right)=R_{\theta}\left\{i\left(x,y\right)\right\}|_{\theta=[0,\pi)}, \tag{4.14}$$

$$Q\left(\theta,x'\right)=R_{\theta}\left\{q\left(x,y\right)\right\}|_{\theta=[0,\pi)}. \tag{4.15}$$

Then, the two sinograms output from Eq. 4.14 and Eq. 4.15, respectively, are combined together into a single sinogram as

$$IQ\left(\theta,x'\right)=\left[I\left(\theta,x'\right)\;Q\left(\theta,x'\right)\right]. \tag{4.16}$$

Note that Matlab notation is used in Eq. 4.16 to denote that the two sinograms are concatenated horizontally, along the second dimension. Thus, the resultant sinogram has the same number of rows as in the original sinogram (i.e., $I\left(\theta,x'\right)$ and $Q\left(\theta,x'\right)$ have the same size), and the number of columns is doubled. Following this, the projection angles $\theta=[0,\pi)$ are integrated-out. This is achieved through applying the Radon transform to the combined sinogram output from Eq. 4.16 at a projection angle $\phi=\frac{\pi}{2}$

as follows

$$IQ\left(x'\right) = R_{\phi}\left\{IQ\left(\theta, x'\right)\right\}\big|_{\phi=\frac{\pi}{2}} . \tag{4.17}$$

The output given by Eq. 4.17 is an abstract 1-D vector representative of the bivariate statistics in the input 2-D complex-valued SAR chip.

4.5.4. A Method for Linear Transformation of the Complex-Valued 2-D SAR Chip into a 1-D Vector

The procedure described in Sect. 4.5.3 accounts for the bivariate statistics between the real and the imaginary parts of the complex-valued SAR chip. However, the complex-valued statistics [54] are not meant to be accounted for by this procedure. Here, to account for such complex-valued statistics, a simple procedure is proposed. First, the real and the imaginary parts of the complex-valued SAR chip are suitably amalgamated in the spatial-domain according to

$$fu_{iq}\left(x, y\right) = \text{furud}\left(i\left(x, y\right), q\left(x, y\right)\right) . \tag{4.18}$$

This specific form of interleaving is referred to as *furud'ing*, inspired by the spectroscopic binary in the constellation Canis Major known by the traditional name Furud [55–58]. Fig. 4.4 illustrates our proposed furud'ing procedure.

In the next step, the real-valued furud chip is transformed to a 1-D vector through inputting it to the algorithm introduced in Fig. 4.2, with the final output being given by

$$Fu_{iq}\left(x'\right) = R_{\phi}\left\{R_{\theta}\left\{fu_{iq}\left(x, y\right)\right\}\big|_{\theta=[0,\pi)}\right\}\Big|_{\phi=\frac{\pi}{2}} . \tag{4.19}$$

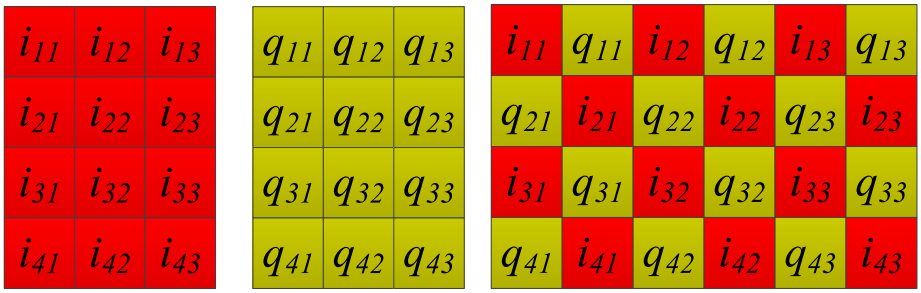

(a) Real-part of the complex-valued SAR chip, $i\,(x, y)$.

(b) Imaginary-part of the complex-valued SAR chip, $q\,(x, y)$.

(c) Furud'ed chip, $fu_{iq}\,(x, y)$.

Figure 4.4: Our proposed furud'ing procedure.

4.6. Proposed Procedure for Nonlinearity Testing in SAR Imagery

Our proposed procedure for nonlinearity testing in SAR imagery is depicted in Fig. 4.5. Firstly, the 2-D SAR chip is transformed into an abstract 1-D vector, to be used for all subsequent operations, following the procedure described in Sect. 4.5. Next, an N number of iAAFT surrogates is generated from the abstract 1-D SAR data based on the iAAFT method described in Sect. 4.4.1. Then, the surrogates are tested for linearity. This step is crucial as it guarantees the validity of the iAAFT surrogates for nonlinearity testing in the subsequent stage. The test for linearity commences with computing the PPMC coefficients, at a particular lag τ, for both the input 1-D SAR data as well as for each surrogate, as described by Eq. 4.2.

Following this, to determine the statistical significance of linearity in the resampled surrogates, the parametric and the nonparametric tests are conducted following the methods described in Sect. 4.4.3.1 and Sect. 4.4.3.3. Furthermore, in order to validate the parametric test for linearity, the PPMC measure values for the surrogates are also

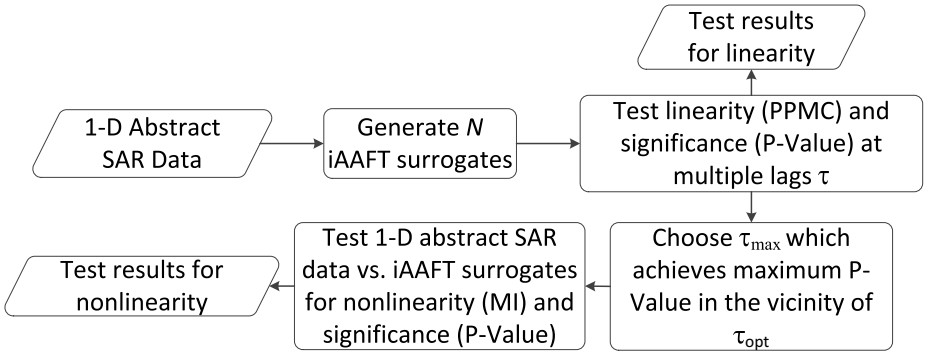

Figure 4.5: Proposed testing procedure for nonlinearity/linearity proposed in this chapter.

tested for Gaussianity following the KS test described in Sect. 4.4.3.2. If the measure values for the surrogates are found to be not strictly Gaussian, the parametric test for linearity is deemed invalid and only the nonparametric test is considered in this case. Otherwise, the P-Values for both the parametric and the non-parametric tests are considered. This procedure is repeated for different lags τ. It is reported in the literature that an approximate optimal value, τ_{opt}, for τ can be chosen such that it corresponds to the first local minimum of the mutual information given by Eq. 4.3 [43]. However, it should be noted that this value of τ_{opt} is not guaranteed to maximize the linearity in the surrogates. Thus, we choose a value of τ, in the vicinity of τ_{opt}, such that the P-Value for the linearity measures of the N surrogates is maximized and refer to this lag as τ_{max}. This validates the significance for the statistical conformity of the surrogates with $\mathcal{H}_0$. The chosen lag τ_{max} is used in the next stage for testing the nonlinearity.

Finally, to test for the nonlinearity, the MI coefficients, described in Eq. 4.3, are computed both for the input abstract 1-D SAR data and for the N iAAFT surrogates at lag τ_{max}. Further, both the parametric and the nonparametric tests are conducted to characterize the statistical significance of nonlinearity/linearity (i.e., whichever the test finds to be applicable) in the input abstract 1-D SAR data. The statistical significance for all the results is presented in terms of P-Values. The KS test is applied to the MI coefficients to validate the parametric test as described above.

4.7. Real-World SAR Chips for Nonlinearity Analysis

Multiple single-channel SAR chips are utilized in this study. These SAR chips come from four different SAR sensors. Radarsat-2 (RS-2) datasets are introduced in Sect. 4.7.1. Relevant chips from the MSTAR dataset are provided in Sect. 4.7.2. A SAR chip from our own SAR sensor is provided under Sect. 4.7.3.1. Finally, two additional SAR chips from a very high-resolution SAR sensor are presented in Sect. 4.7.3.2.

4.7.1. SAR Chips from Radarsat-2 Datasets

RS-2 is a spaceborne C-band radar. Two single-channel (HH) single-look complex-valued (SLC) datasets from RS-2 are considered in this study. SLC is the lowest-level product commercially available from MDA Corporation. In the first dataset, the imaging mode is Spotlight. In this mode, RS-2 allows for improved spatial resolution in the azimuth direction in which it delivers the highest nominal spatial resolution of 1.6×0.8 m in range and azimuth, respectively [59]. The targets of interest considered in this dataset are six construction vehicles (shown in red circles in Fig. 4.6a, and counted from left to right) and two corner reflectors (trihedrals, shown in red trapezoids in Fig. 4.6a, and counted from left to right) imaged in a site located in the former Naval Station Argentia in Newfoundland, Canada [60]. The phase image for this scene is provided in Fig. 4.6b. Ground-truthing is conducted by C-CORE (see Fig. 4.6c). Note that the size of these targets is comparable to the nominal spatial resolution of the RS-2 sensor (i.e., these targets can be considered as point targets).

In the second dataset, two single-channel SLC SAR chips were extracted from a public-domain RS-2 scene, i.e., Vancouver dataset in [61]. The imaging mode is 'Polarimetric Fine'. Only the HH channel is utilized. The nominal spatial resolution for this imaging mode is 5.2×7.7 m in range and azimuth, respectively [59]. In the first chip, the target is a ship occupying a rectangular area of size 72×34 m in range and azimuth, respectively. Note that this is an extended target. The magnitude-detected chip and the phase chip for this target are provided in Fig. 4.7. The second chip is pertinent to a target-free sea clutter. The magnitude-detected chip and the phase chip are shown in Fig. 4.8.

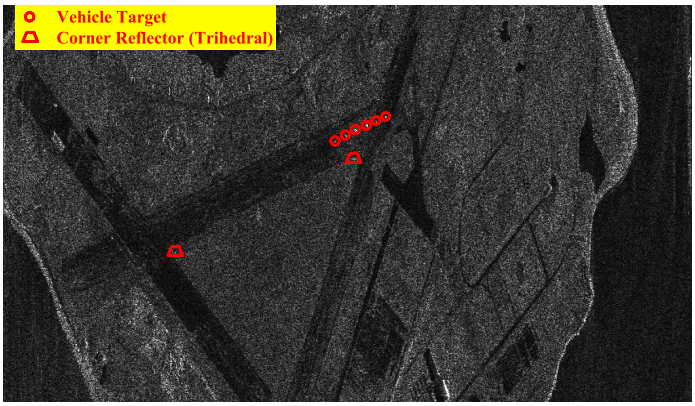

(a) Contrast-enhanced magnitude-detected RS-2 image. Vehicle targets are numbered 1 to 6, respectively, from left to right, Corner reflectors are numbered CR1 and CR2, respectively, from left to right.

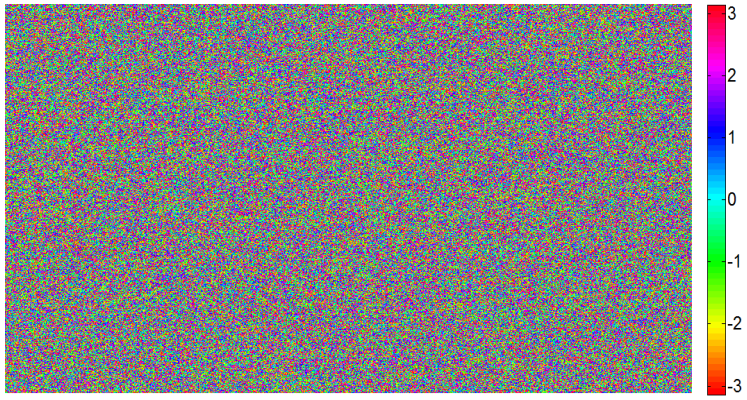

(b) Phase image.

(c) Ground-truth image (left to right: 1 dump truck, 1 loader, 2 dump trucks, 2 pickup trucks).

Figure 4.6: Spotlight RS-2 SLC image for a site in the former Naval Station Argentia [60] in Newfoundland, Canada. Ground-truth image is provided by C-CORE. RADARSAT-2 Data and Products © MacDonald, Dettwiler and Associates Ltd. (2011)

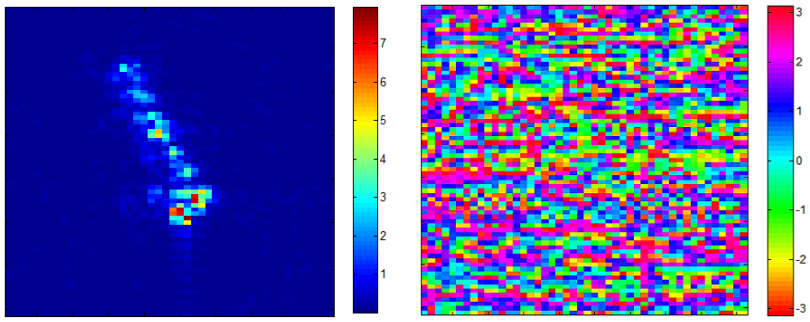

(a) Magnitude-detected chip. **(b)** Phase chip.

Figure 4.7: RS-2 chip for ocean-based extended (ship) target (ET). RADARSAT-2 Data and Products © MacDonald, Dettwiler and Associates Ltd. (2008)

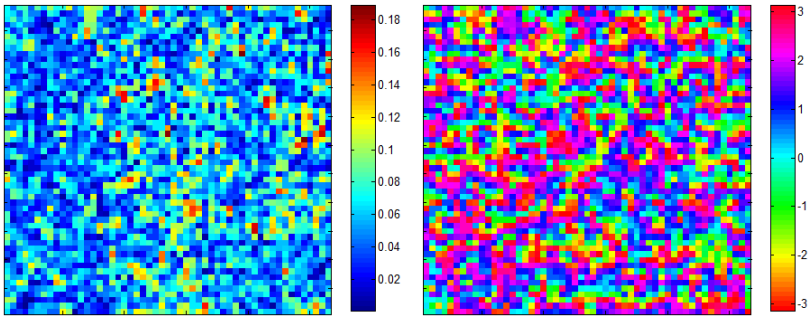

(a) Magnitude-detected chip. **(b)** Phase chip.

Figure 4.8: RS-2 chip for ocean clutter (*i.e.*, target-free (TF) chip). RADARSAT-2 Data and Products © MacDonald, Dettwiler and Associates Ltd. (2008)

4.7.2. SAR Chips from the MSTAR Dataset

MSTAR is a public-domain single-channel (HH) and ground-truthed dataset acquired by an airborne SAR sensor. MSTAR offers X-band SLC Spotlight chips for multiple types of military targets (mostly vehicles) imaged under various amounts of articulation, obscuration and camouflage. The MSTAR dataset provides a nominal spatial

resolution of 0.3047×0.3047 m in range and azimuth [62]. A set of MSTAR chips pertaining to extended target D7 (bulldozer) is arbitrarily chosen for this study. The chosen set is representative of different azimuth angles for this target. Table 4.1 provides a list of the chosen MSTAR chip IDs along with relevant azimuth angles. A ground-truth image for the target is shown in Fig. 4.9. The magnitude-detected chips considered in this chapter for all the MSTAR chips of target D7, are provided in Fig. 4.10. The corresponding phase chips are depicted in Fig. 4.11. The numbers shown on the chips represent the chip number provided in Table 4.1.

Table 4.1: List of the MSTAR chips of target D7 used in this chapter.

No.	MSTAR ID	Azimuth Angle
1	HB15056.005	13.307442°
2	HB15256.005	36.307442°
3	HB15132.005	94.307442°
4	HB14931.005	97.307442°
5	HB15006.005	113.307442°
6	HB15206.005	121.307442°
7	HB15082.005	144.307434°
8	HB15148.005	180.307434°
9	HB15156.005	220.307434°
10	HB14956.005	222.307434°
11	HB15031.005	243.307434°
12	HB15231.005	261.307434°
13	HB15106.005	274.307434°
14	HB14981.005	347.307434°
15	HB15181.005	350.307434°

Figure 4.9: Ground-truth image for target D7.

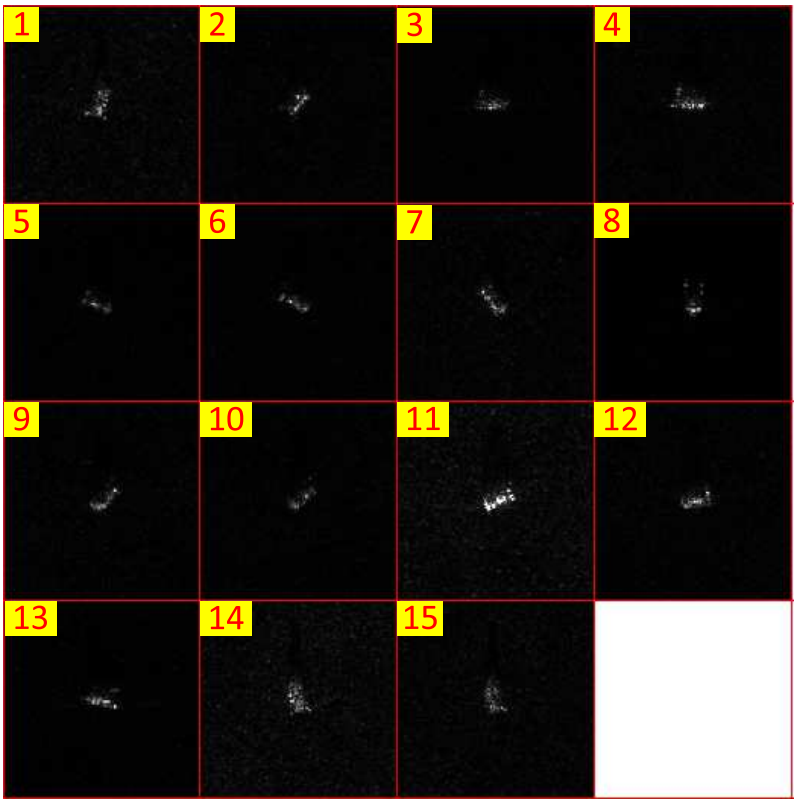

Figure 4.10: Magnitude-detected chips for a selected set from MSTAR target D7.

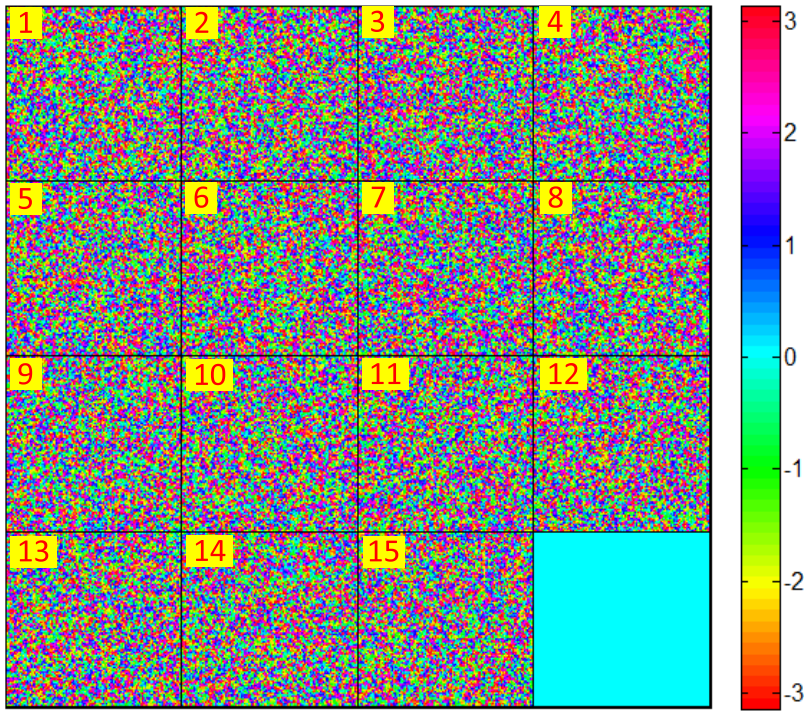

Figure 4.11: Phase chips for a selected set from MSTAR target D7.

4.7.3. SAR Chips from Miscellaneous Sensors

Three additional SAR chips are utilized in this study, the first being a ground-truthed chip from our own SAR sensor as described in Sect. 4.7.3.1. Finally, two ground-truthed chips, from a very high-resolution SAR sensor, are provided under Sect. 4.7.3.2.

4.7.3.1. A Chip from our Own SAR Sensor

A SAR chip for a vehicle target (i.e., extended target) from our self-designed S-band SAR sensor is utilized. Our SAR sensor offers single-channel SLC SAR data [63]. The antenna polarization is HH. The imaging mode is 'Stripmap'. The nominal spatial resolution of our SAR sensor is 0.67873×0.15 m in range and azimuth, respectively. A ground-truth photo for the imaged target is provided in Fig. 4.12. The magnitude-detected and phase chips are depicted in Fig. 4.13.

Figure 4.12: Ground-truth photo with magnitude-detected SAR chip superimposed.

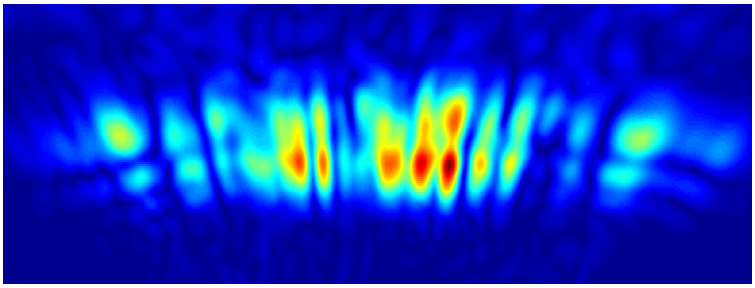

(a) Magnitude-detected SAR chip.

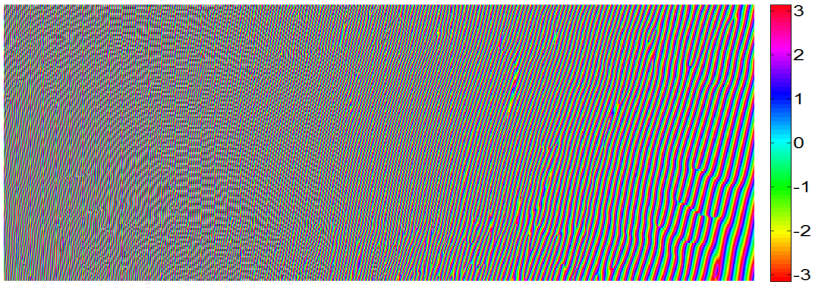

(b) Phase SAR chip.

Figure 4.13: SAR chip from our own SAR sensor.

4.7.3.2. Two SAR Chips from a Very High-Resolution SAR Sensor

The final two SAR chips considered in this study are from a very high-resolution single-channel X-band SAR system, obtained from [64, 65]. The imaging mode is 'Stripmap'.

The nominal spatial resolution of the SAR sensor is 0.03×0.012 m in range and azimuth, respectively. The first target is a bike. The magnitude-detected and phase chips for this target are shown in Fig. 4.14. The second target is the phrase GO STATE which is formed through using a group of tiny pushpins. The magnitude-detected and phase chips for this target are depicted in Fig. 4.15.

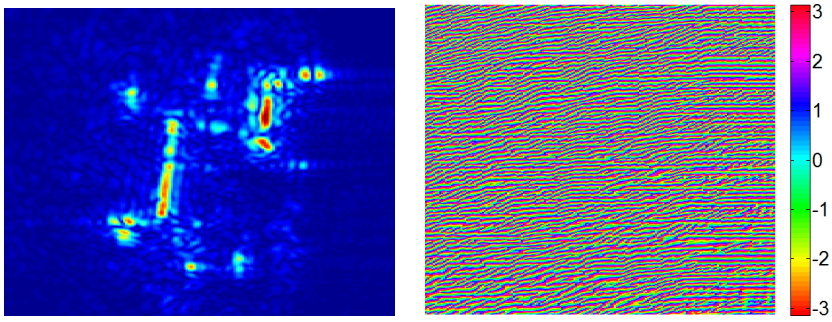

(a) Magnitude-detected chip. **(b)** Phase chip.

Figure 4.14: SAR chip for a bike from a very high-resolution X-band radar.

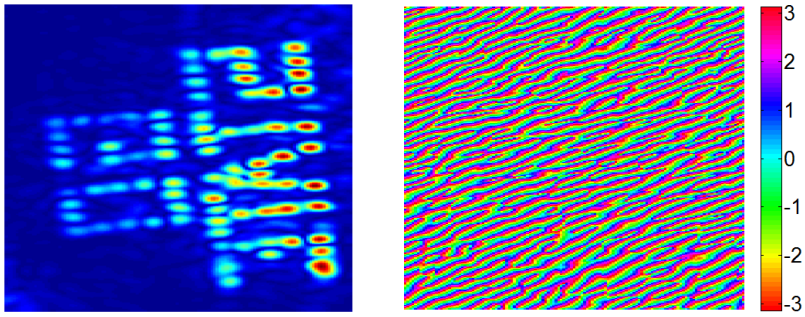

(a) Magnitude-detected chip. **(b)** Phase chip.

Figure 4.15: SAR chip for GO STATE in pushpins from a very high-resolution X-band radar.

4.8. Results and Comments

This section is comprised of three parts. The applicability of the GCLT theorem to the extended targets in SAR imagery is presented in Sect. 4.8.1. Results for the statistical significance of the nonlinear dynamics in the SAR datasets considered in this study are provided in Sect. 4.8.2. Finally, relevant comments are introduced under Sect. 4.8.3.

4.8.1. Applicability of the GCLT Theorem to SAR Imagery, and the Interrelationship with the Spatial Resolution

This section aims at empirically demonstrating the inapplicability of the CLT theorem to the extended targets in SAR imagery. Further, the effect of the spatial resolution for the SAR sensor is also examined. Five complex-valued SAR chips containing a variety of target types and having differing spatial resolutions are chosen. The first chip is for target-free (i.e., TF) ocean clutter taken from the RS-2 dataset introduced in Sect. 4.7.1. The second chip containing target #1 and representing the case of a point target, is taken from the RS-2 dataset introduced in Sect. 4.7.1. The third chip is for target ET taken from the RS-2 dataset introduced in Sect. 4.7.1. This chip represents the case of an extended target. The fourth chip is for target #11 taken from the MSTAR dataset presented under Sect. 4.7.2. This chip also represents an extended target. Finally, the fifth chip is for the phrase GO STATE in pushpins given under Sect. 4.7.3.2. This case also represents an extended target.

For each of these chips, the following procedure is applied. First, a normalized EDH histogram is computed for both the real-part and the imaginary-part, respectively. Then, the envelope of the resultant histogram is fitted to the Gaussian distribution and the GGD distribution, respectively. The Gaussian distribution serves to demonstrate the applicability/inapplicability of the CLT theorem. The GGD distribution is a non-Gaussian statistical model motivated by the GCLT theorem. GGD allows the rate of tail decay to be varied and it is known to offer a good model for some impulsive phenomena. The GGD family is general in that it encompasses a wide array of distributions with different tail characteristics from super-Gaussian to sub-Gaussian with specific densities such as Laplacian and Gaussian distributions [13, 66]. The GGD distribution is chosen in this study because it is found to closely fit our SAR data.

Fitting with the Gaussian distribution is performed using the minimum variance

unbiased estimator (MVUE) [67]. Fitting with the GGD distribution is done through minimizing the symmetrized relative entropy, known as the Jensen–Shannon (JS) divergence, between the envelope of the histogram and the GGD's PDF (see [17] and Eq. E.5 in Appendix E for details). Goodness-of-fit measures between the normalized histograms and both the Gaussian and the GGD PDFs are presented in terms of the JS divergence (see Eq. E.5 in Appendix E for details). Our results are presented in Fig. 4.16-Fig. 4.20, respectively. Goodness-of-fit measures are given in Table 4.2.

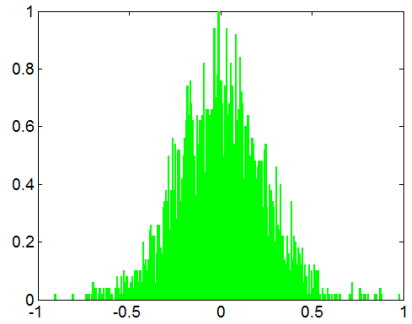

(a) Histogram for real-part.

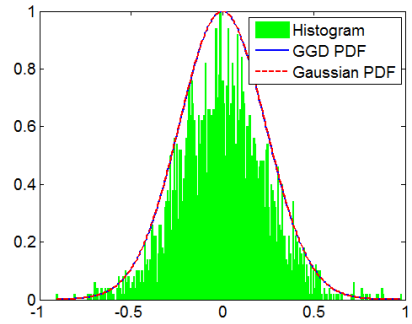

(b) GGD PDF and Gaussian PDF superimposed on histogram of real-part in Fig. 4.16a.

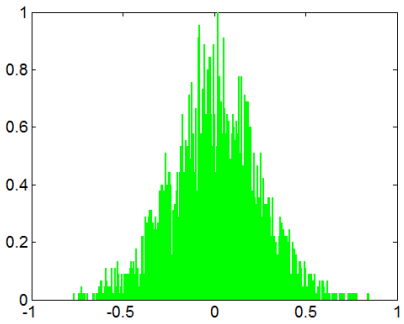

(c) Histogram for imaginary-part.

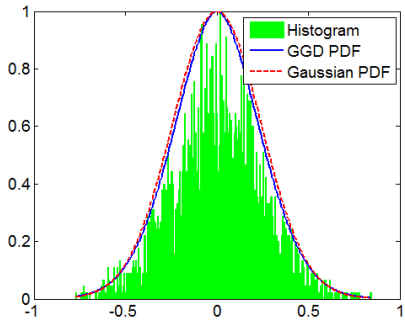

(d) GGD PDF and Gaussian PDF superimposed on histogram of imaginary-part in Fig. 4.16c.

Figure 4.16: Histogram and fitting with Gaussian and GGD distributions for ocean clutter (*i.e.*, target-free (TF) chip) .

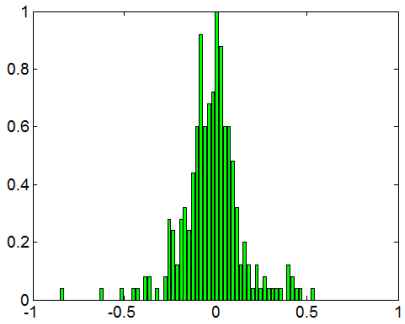

(a) Histogram for real-part.

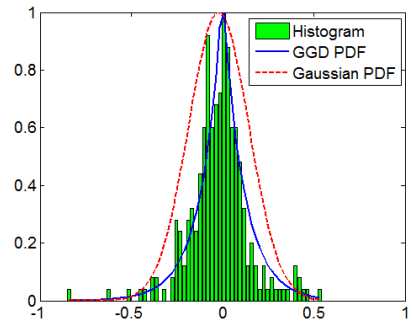

(b) GGD PDF and Gaussian PDF superimposed on histogram of real-part in Fig. 4.17a.

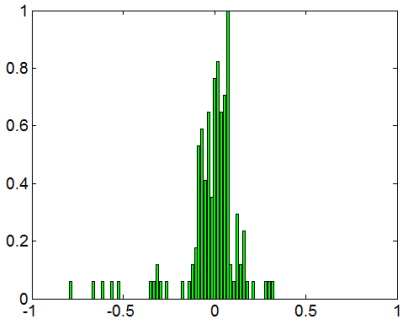

(c) Histogram for imaginary-part.

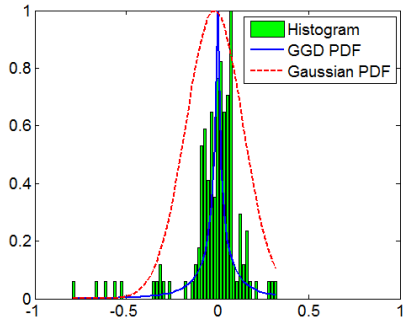

(d) GGD PDF and Gaussian PDF superimposed on histogram of imaginary-part in Fig. 4.17c.

Figure 4.17: Histogram and fitting with Gaussian and GGD distributions for RS-2 target #1.

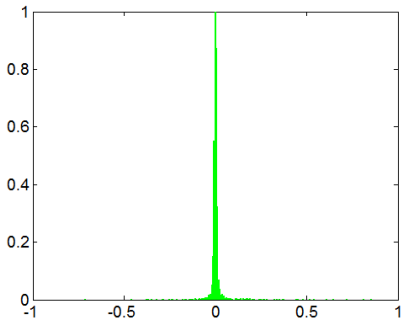

(a) Histogram for real-part.

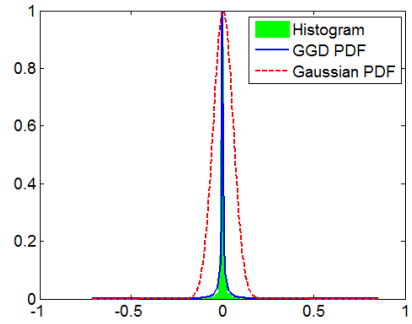

(b) GGD PDF and Gaussian PDF superimposed on histogram of real-part in Fig. 4.18a.

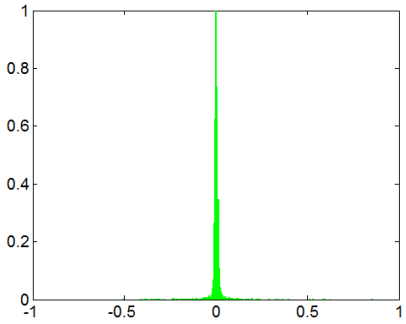

(c) Histogram for imaginary-part.

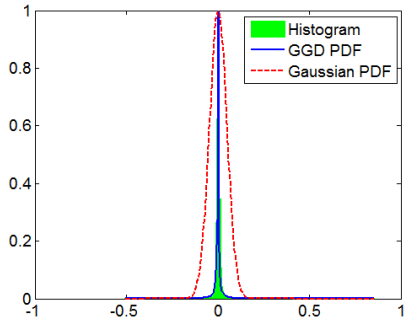

(d) GGD PDF and Gaussian PDF superimposed on histogram of imaginary-part in Fig. 4.18c.

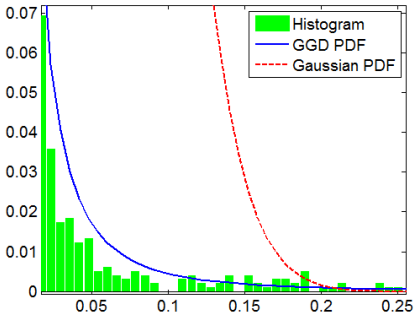

(e) Zoom-in into the right tail of Fig. 4.18b.

Figure 4.18: Histogram and fitting with Gaussian and GGD distributions for RS-2 extended (ship) target (ET).

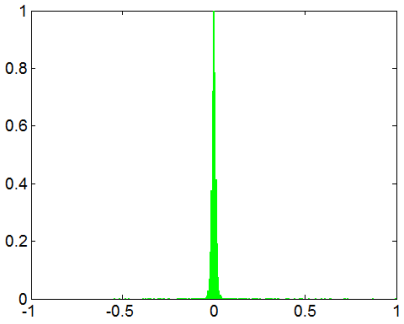

(a) Histogram for real-part.

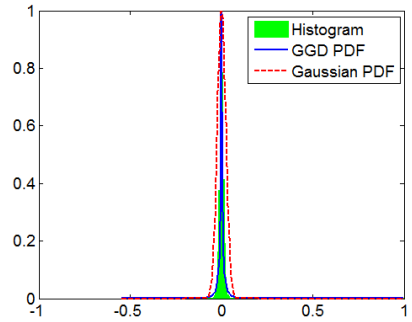

(b) GGD PDF and Gaussian PDF superimposed on histogram of real-part in Fig. 4.19a.

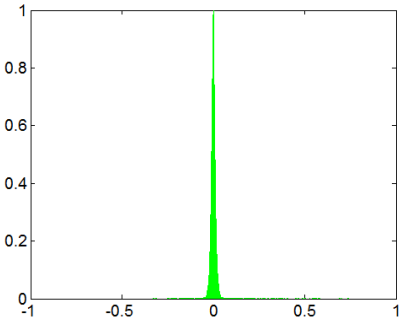

(c) Histogram for imaginary-part.

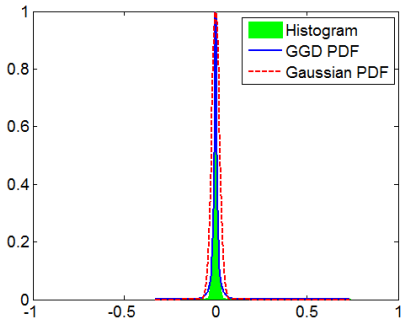

(d) GGD PDF and Gaussian PDF superimposed on histogram of imaginary-part in Fig. 4.19c.

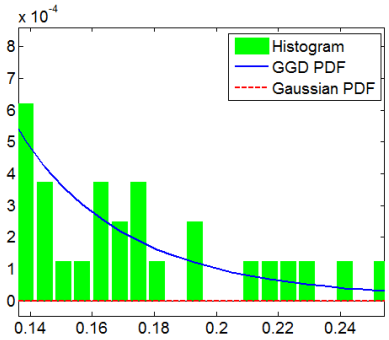

(e) Zoom-in into the right tail of Fig. 4.19b.

Figure 4.19: Histogram and fitting with Gaussian and GGD distributions for MSTAR target #11.

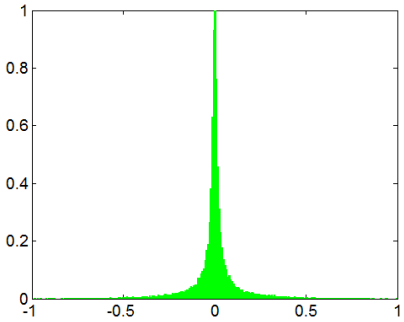

(a) Histogram for real-part.

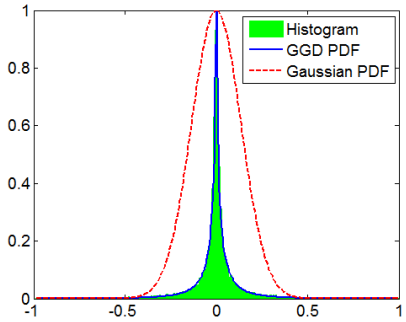

(b) GGD PDF and Gaussian PDF superimposed on histogram of real-part in Fig. 4.20a.

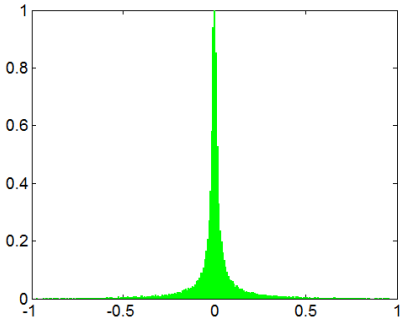

(c) Histogram for imaginary-part.

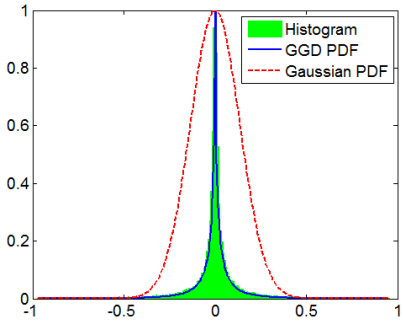

(d) GGD PDF and Gaussian PDF superimposed on histogram of imaginary-part in Fig. 4.20c.

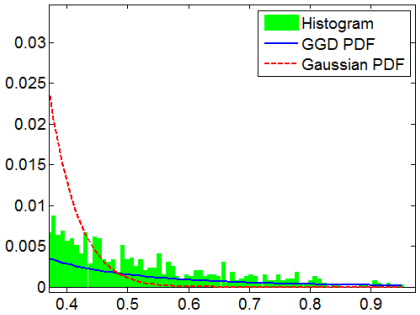

(e) Zoom-in into the right tail of Fig. 4.20b.

Figure 4.20: Histogram and fitting with Gaussian and GGD distributions for the SAR chip of GO STATE in pushpins.

Table 4.2: Goodness-of-fit measures for Fig. 4.16-Fig. 4.20, respectively.

Chip	Spatial Resolution [Range×Azimuth]	Target Type	Channel	JS Divergence	
				Gaussian PDF	GGD PDF
RS-2 TF	[0.3047 × 0.3047] m	Ocean Clutter	I	0.0592	0.0590
			Q	0.0625	0.0605
RS-2 #1	[1.6 × 0.8] m	Point Target	I	0.2204	0.1218
			Q	0.4678	0.3944
RS-2 ET	[5.2 × 7.7] m	Extended Target	I	2.0096	0.2277
			Q	1.8840	0.2839
MSTAR #11	[0.3047 × 0.3047] m	Extended Target	I	0.8886	0.2495
			Q	0.7589	0.1624
GO STATE	[0.03 × 0.012] m	Extended Target	I	0.7667	0.0353
			Q	0.7671	0.0384

The following conclusions are drawn based on the results obtained. First, for the target-free RS-2 chip considered, it is evident that the goodness-of-fit for both the Gaussian and the GGD PDFs are almost identical (see Fig. 4.16 and Table 4.2). It is thus concluded that nonlinearity is negligible in the absence of targets. Second, based on the fitting results for the case of point target considered (see Fig. 4.17 and Table 4.2), the Gaussian PDF and the GGD PDF are close to each other (i.e., in terms of the JS divergence), despite the relatively better fit achieved by the GGD PDF. It is observed that the GGD PDF gives more weight to the heavy tails and peakedness of the histogram while the Gaussian PDF is restricted by the sample variance. Note that the smaller the JS divergence measure is, the better the fit. Thus, it is evident that the point target considered also possesses minimum nonlinearity. Third, for all the other chips considered, the GGD distribution offers a much better fit than the Gaussian distribution. This is evident through visually inspecting the fitting results depicted in Fig. 4.18-Fig. 4.20, respectively. This is also confirmed from Table 4.2 for the JS divergence measures. It is clear that the Gaussian distribution cannot model pulsed phenomenon with heavy tails (i.e., super-Gaussian) similar to those obtained in the figures pertinent to the case of extended targets. However, the GGD distribution accounts for this behavior. Further, it is noted that the peakedness and the heavy tails get even more pronounced with the increase in the spatial resolution of the SAR sensor relative to the size of the imaged target. This is clearly observed through comparing

the histograms in Fig. 4.20 with Fig. 4.18 and Fig. 4.19, respectively. This behavior increases the goodness-of-fit between the histogram and the GGD PDF, in contrast to the Gaussian PDF. This is confirmed by examining the JS divergence measures provided in Table 4.2.

Since the Gaussian distribution is motivated by the CLT theorem, this demonstrates the inapplicability of the CLT theorem to the real-part and the imaginary-part of the SAR chips containing the extended targets. Similarly, since the GGD distribution is motivated by the GCLT theorem, it can be said that in the presence of extended targets, the SAR chips considered demonstrate some nonlinear behavior. This nonlinear behavior becomes even more pronounced with the increase in the spatial resolution of the SAR sensor, relative to the size of the imaged target. The statistical significance of the nonlinearity is investigated in the next section.

4.8.2. Statistical Analysis for Nonlinearity

This section presents the statistical analysis results for the nonlinear dynamics in the SAR datasets introduced under Sect. 4.7. This analysis follows the procedure described under Sect. 4.4.1. The analysis utilizes a number of 1024 iAAFT surrogates (i.e., $N = 1024$) for each 1-D vector representation. The number 1024 is chosen as a tradeoff between computational complexity and statistical significance. Once the iAAFT surrogates are calculated, the spatial lag τ_{max} is found for each 1-D vector representation as proposed in Sect. 4.6. Then, the nonlinear measures in terms of MI, are calculated at τ_{max} for each 1-D representation and its corresponding 1024 iAAFT surrogates. Parametric and nonparametric tests for the statistical significance pertinent to both the linearity of the surrogates (i.e., in terms of PPMC) and the nonlinearity of the 1-D representations (i.e., in terms of MI) are presented in terms of P-Values following the procedure outlined in Sect. 4.4.3.1 and Sect. 4.4.3.3, respectively. The applicability of the parametric test is validated following the procedure presented in Sect. 4.4.3.2.

The statistical analysis results for the SAR chips from the RS-2 dataset are presented in Table 4.3. The results pertaining to the SAR chips from the MSTAR dataset are provided in Table 4.4. Finally, Table 4.5 through Table 4.7 respectively present the statistical analysis results for the three chips from the miscellaneous SAR datasets.

Table 4.3: Nonlinearity analysis of the RS-2 chips.

No.	Type	τ_{max}	PPMC (P-Value)		MI (P-Value)	
			Parametric	Nonparametric	Parametric	Nonparametric
CR1	P	4	GR	0.9317	GR	0.3015
	M	12	GR	0.9902	GR	0.9278
	I	6	GR	0.9376	GR	0.7073
	Q	11	GR	0.7932	GR	0.1063
	IQ	19	GR	0.8595	GR	0.2234
	Fu_{iq}	15	GR	0.9473	GR	0.0634
CR2	P	18	GR	0.9785	GR	0.8907
	M	11	GR	0.9532	GR	0.9259
	I	6	GR	0.9220	GR	0.0010
	Q	2	GR	0.9629	GR	0.7424
	IQ	12	GR	0.9766	GR	0.0010
	Fu_{iq}	12	GR	0.9551	GR	0.0010
1	P	8	GR	0.9668	GR	0.9376
	M	13	GR	0.8966	GR	0.6527
	I	6	GR	0.2605	GR	0.9005
	Q	3	GR	0.6859	GR	0.3405
	IQ	20	GR	0.9220	GR	0.3990
	Fu_{iq}	7	GR	0.3600	GR	0.5141
2	P	7	GR	0.9863	GR	0.6273
	M	8	GR	0.9766	GR	0.9356
	I	3	GR	0.9590	GR	0.6898
	Q	2	GR	0.8263	GR	0.4693
	IQ	1	GR	0.9220	GR	0.2839
	Fu_{iq}	10	GR	0.6293	GR	0.6956
3	P	6	GR	0.9454	GR	0.5434
	M	9	GR	0.9356	GR	0.9434
	I	9	GR	0.8751	GR	0.9571
	Q	12	GR	0.7854	GR	0.3015
	IQ	6	GR	0.9649	GR	0.7873

	Fu_{iq}	20	GR	0.9629	GR	0.7229
4	P	6	GR	0.9688	GR	0.7483
	M	9	GR	0.8771	GR	0.8810
	I	9	GR	0.8927	GR	0.2078
	Q	6	GR	0.9863	GR	0.2878
	IQ	5	GR	0.9805	GR	0.3288
	Fu_{iq}	12	GR	0.8107	GR	0.4498
5	P	13	GR	0.8888	GR	0.8556
	M	13	GR	0.9649	GR	0.9902
	I	8	GR	0.9278	GR	0.7795
	Q	6	0.8092	0.8459	GR	0.0654
	IQ	10	GR	0.8595	GR	0.2898
	Fu_{iq}	2	GR	0.9317	GR	0.0927
6	P	12	GR	0.9395	GR	0.7854
	M	14	GR	0.9707	GR	0.9317
	I	18	GR	0.9766	GR	0.5805
	Q	6	GR	0.4400	GR	0.4985
	IQ	20	GR	0.9220	GR	0.5298
	Fu_{iq}	2	GR	0.7346	GR	0.9571
ET	P	4	GR	0.9707	0.0000	0.0010
	M	5	GR	0.7854	0.0216	0.0244
	I	5	GR	0.9044	0.0033	0.0049
	Q	9	GR	0.8576	GR	0.0556
	IQ	4	GR	0.7034	0.0014	0.0010
	Fu_{iq}	4	GR	0.4966	0.0000	0.0010
TF	P	6	GR	0.6468	GR	0.4322
	M	7	GR	0.5317	GR	0.2546
	I	5	GR	0.8439	GR	0.0088
	Q	5	GR	0.8673	0.1921	0.2098
	IQ	11	GR	0.7073	GR	0.8790
	Fu_{iq}	12	GR	0.7054	0.6191	0.6585

Table 4.4: Nonlinearity analysis of the MSTAR chips.

No.	Type	τ_{max}	PPMC (P-Value)		MI (P-Value)	
			Parametric	Nonparametric	Parametric	Nonparametric
1	P	5	GR	0.7268	GR	0.0010
	M	6	GR	0.7268	0.1406	0.1239
	I	8	GR	0.9239	GR	0.0127
	Q	9	GR	0.7678	GR	0.0283
	IQ	6	GR	0.6644	GR	0.0010
	Fu_{iq}	9	GR	0.9278	GR	0.0907
2	P	3	GR	0.8829	GR	0.0010
	M	12	GR	0.8498	0.1290	0.1063
	I	3	GR	0.9532	GR	0.0010
	Q	12	GR	0.5083	GR	0.0576
	IQ	4	GR	0.3015	GR	0.0302
	Fu_{iq}	10	GR	0.4810	GR	0.0088
3	P	1	GR	0.8732	GR	0.0010
	M	10	GR	0.8888	0.0581	0.0576
	I	3	GR	0.9707	GR	0.0029
	Q	7	GR	0.9941	0.0000	0.0010
	IQ	3	GR	0.9063	GR	0.0010
	Fu_{iq}	10	GR	0.7580	GR	0.0010
4	P	6	GR	0.9434	GR	0.0010
	M	12	GR	0.8498	0.0273	0.0302
	I	12	GR	0.8439	GR	0.1961
	Q	8	GR	0.6644	GR	0.0010
	IQ	14	GR	0.9063	GR	0.0068
	Fu_{iq}	12	GR	0.1220	GR	0.0029
5	P	5	GR	0.9766	GR	0.0010
	M	14	GR	0.9298	0.0148	0.0146
	I	17	GR	0.9337	0.1680	0.1571
	Q	7	GR	0.8166	GR	0.0010
	IQ	13	GR	0.7151	GR	0.0888

	Fu_{iq}	6	GR	0.7502	GR	0.0615
6	P	4	GR	0.9473	GR	0.0010
	M	9	GR	0.9844	0.0541	0.0380
	I	4	GR	0.4849	GR	0.0068
	Q	4	GR	0.4010	GR	0.0088
	IQ	4	GR	0.2117	GR	0.0010
	Fu_{iq}	3	GR	0.1298	GR	0.0010
7	P	6	GR	0.5063	0.0000	0.0010
	M	5	GR	0.7307	0.0413	0.0380
	I	4	GR	0.3307	GR	0.0537
	Q	7	GR	0.2702	GR	0.0029
	IQ	4	GR	0.6605	GR	0.0146
	Fu_{iq}	5	GR	0.3210	GR	0.0010
8	P	13	GR	0.8732	GR	0.0010
	M	3	GR	0.5044	GR	0.0010
	I	3	GR	0.9395	GR	0.0185
	Q	1	GR	0.8810	GR	0.0010
	IQ	2	GR	0.3249	GR	0.0029
	Fu_{iq}	4	GR	0.9024	GR	0.0010
9	P	6	GR	0.5161	GR	0.0010
	M	12	GR	0.9063	0.1155	0.0888
	I	7	GR	0.7463	GR	0.0010
	Q	10	GR	0.5922	GR	0.0049
	IQ	10	GR	0.8771	GR	0.0049
	Fu_{iq}	17	GR	0.8537	GR	0.0166
10	P	3	GR	0.9200	GR	0.0010
	M	12	GR	0.8341	0.0572	0.0634
	I	5	GR	0.3034	GR	0.0010
	Q	3	GR	0.8341	GR	0.0166
	IQ	4	GR	0.1688	GR	0.0166
	Fu_{iq}	6	GR	0.5688	GR	0.0010
	P	2	GR	0.9727	GR	0.0010
	M	11	GR	0.8732	0.0437	0.0556

11

	I	4	GR	0.5922	GR	0.0068
	Q	4	GR	0.8400	GR	0.0010
	IQ	6	GR	0.3951	GR	0.0010
	Fu_{iq}	8	GR	0.3268	GR	0.0029
12	P	7	GR	0.9278	0.0000	0.0010
	M	10	GR	0.8615	0.1059	0.1024
	I	10	GR	0.8478	GR	0.0810
	Q	8	GR	0.7951	GR	0.0010
	IQ	8	GR	0.6078	0.0000	0.0010
	Fu_{iq}	14	GR	0.5337	0.0000	0.0029
13	P	2	GR	0.9590	GR	0.0010
	M	9	GR	0.9180	0.0408	0.0459
	I	2	GR	0.9941	GR	0.0029
	Q	4	GR	0.7620	GR	0.0068
	IQ	2	GR	0.8556	GR	0.0010
	Fu_{iq}	5	GR	0.9434	GR	0.0127
14	P	4	GR	0.5220	GR	0.0010
	M	12	GR	0.7015	0.5185	0.5317
	I	8	GR	0.8556	GR	0.0010
	Q	17	GR	0.8537	GR	0.0068
	IQ	11	GR	0.8946	GR	0.0537
	Fu_{iq}	16	GR	0.9434	GR	0.0107
15	P	4	GR	0.9668	GR	0.0010
	M	5	GR	0.6351	0.0815	0.0654
	I	9	GR	0.9688	GR	0.0010
	Q	17	GR	0.9941	GR	0.5532
	IQ	13	GR	0.9844	GR	0.0634
	Fu_{iq}	12	GR	0.5668	GR	0.0049

Table 4.5: Nonlinearity analysis of the SAR chip from our own SAR sensor.

Type	τ_{max}	PPMC (P-Value)		MI (P-Value)	
		Parametric	Non-Parametric	Parametric	Non-Parametric
P	11	GR	0.5668	GR	0.0010
M	1	GR	0.3678	GR	0.0322
I	4	GR	0.8829	GR	0.0010
Q	4	GR	0.8517	GR	0.0010
IQ	4	GR	0.9571	GR	0.0010
Fu_{iq}	17	GR	0.8595	GR	0.0010

Table 4.6: Nonlinearity analysis of the SAR chip for a bike.

Type	τ_{max}	PPMC (P-Value)		MI (P-Value)	
		Parametric	Non-Parametric	Parametric	Non-Parametric
P	19	GR	0.9532	0.0000	0.0010
M	20	GR	0.4498	0.2070	0.2351
I	2	GR	0.7659	0.0000	0.0010
Q	2	GR	0.7971	0.0052	0.0068
IQ	2	GR	0.8185	0.0000	0.0010
Fu_{iq}	9	GR	0.9551	0.000	0.0010

Table 4.7: Nonlinearity analysis of the SAR chip for GO STATE in pushpins.

Type	τ_{max}	PPMC (P-Value)		MI (P-Value)	
		Parametric	Non-Parametric	Parametric	Non-Parametric
P	16	GR	0.9317	0.0795	0.0888
M	14	GR	0.6332	0.1156	0.1337
I	2	GR	0.5883	GR	0.0010
Q	2	GR	0.7307	GR	0.0010
IQ	2	GR	0.6351	GR	0.0010
Fu_{iq}	8	GR	0.8751	GR	0.0010

4.8.3. Comments

This section summarizes the main lessons learned from the statistical analysis for the nonlinearity in the datasets considered in this study. Firstly, through inspecting the results for the RS-2 dataset presented in Table 4.3, it is clear that the statistical significance for the nonlinearity is dependent on the target size relative to the spatial resolution of the SAR sensor. It is observed that the nonlinearity is negligible for all the point targets considered (i.e., construction vehicles and CR1) as well as for the target-free ocean clutter chip. This can be inferred through examining the P-Values under the MI measures. To reiterate,

$$\text{Linearity: } \mathcal{H}_0 \quad \in \quad \text{P-Value} > 0.01, \tag{4.20}$$

$$\text{Nonlinearity: } \mathcal{H}_1 \quad \in \quad \text{P-Value} \leq 0.01. \tag{4.21}$$

Further, CR2 has statistically significant nonlinear behavior. This nonlinear behavior originates from the real-part of this chip, and it is preserved in both the bivariate representation (i.e., IQ) and the furud'ed representation (i.e., $\mathrm{F}u_{iq}$). As this SAR chip is detected, the nonlinear behavior is obliterated in both the power and the magnitude chips. Note that there are no ground-truth images available for the corner reflectors. Thus, it is postulated that the positioning of CR1 and CR2, relative to the RS-2 sensor, are not identical. This explains the difference in the backscattering behavior of these two corner reflectors. Moreover, when an extended target for a ship of size of 72×34 m is considered, the nonlinear dynamics are found to become pronounced. This is expected since the ship size is orders of magnitude greater than the spatial resolution of the RS-2 sensor. For almost all the RS-2 target chips analyzed it is noted that the MI's P-Value pertaining to the power-detection is less than that of the magnitude-detection, and different from that of the real and the imaginary parts. This indicates that both the power and the magnitude detections alter the statistics in the original SAR image.

Next, from Table 4.4 it is evident that the nonlinearity behavior in the complex-valued MSTAR dataset is statistically significant. This is to be expected since the imaged objects are all extended targets. It can be seen that the smallest MI's P-Value alternates between the real and the imaginary parts which indicates that the

nonlinearity effect originates from both of these parts. A close look at the effect of detection in terms of P-Values reveals that magnitude-detection is worst when it comes to either greatly diminishing or obliterating the nonlinear dynamics originally present in the complex-valued SAR chip. This is in agreement with the results for the RS-2 dataset. The power-detected SAR chip retains some of the nonlinear characteristics present in the real and the imaginary parts. However, through visually comparing the 1-D representations for the undetected and the power-detected SAR chips, it is postulated that the nonlinear dynamics have been altered from their original form. Furthermore, it is also suggested that although the 1-D representation for the real-part, imaginary-part, bivariate and furud'ed representations, respectively, do possess some nonlinear behavior, the nonlinear dynamics in these different representations are not identical.

In addition to the foregoing observations, the results obtained from the miscellaneous SAR datasets given in Table 4.5 through Table 4.7, respectively, evidently reveal a significant nonlinear trend. This can be attributed to the fact that the imaged objects are extended targets. The nonlinear effect is clearly manifested through noting that all the MI's P-Values for the real-part, imaginary-part, bivariate and furud'ed representations, respectively, strongly favor $\mathcal{H}_1$ for the nonlinearity. Similarly, it is observed that the magnitude-detection greatly diminishes the nonlinear effects originally present in the complex-valued SAR chip. While the power-detection often retains some of the nonlinear characteristics in an altered form, it is noted that this may not be the case at very high resolution and for the relatively small targets such as that of GO STATE in pushpins (see Table 4.7).

Finally, several overall observations may be summarized. The nonlinear effects in complex-valued SAR chips are proportional to the spatial resolution and the size of the imaged target. Magnitude-detection greatly diminishes or obliterates the nonlinear effects. Power-detection either diminishes and/or alters the nonlinear effects. It is well-known that the power and the magnitude detections, respectively, degrade the spatial resolution originally present in the complex-valued SAR image by a factor of two or greater (see [68] and Sect. 2.8 in [4]). Hence, to take full advantage of the nonlinear statistics for the extended targets, it is advised to utilize the complex-valued SAR image rather than the detected one. To account for the different nonlinear dynamics, it may be useful to consider the real-part, imaginary-part, bivariate and furud'ed

representations as complementary to each other. The 1-D representations for the real and the imaginary parts capture the nonlinear dynamics in the 2-D counterparts. The bivariate representation captures the bivariate nonlinear dynamics between the real and the imaginary parts. The furud'ed representation accounts for the nonlinear dynamics both within and between the pixels of the real and the imaginary parts. From the perspective of the statistical significance for the nonlinear dynamics, this demonstrates the usefulness of the often discarded phase for the extended targets in high-resolution single-channel SAR imagery.

4.9. Conclusions

Nonlinear signal processing is motivated by the generalized central limit theorem (GCLT) which provides for capturing the peakedness and heavy tails, indicators of nonlinearity in the signal. In order to maximize the extraction of information from SAR imagery, it is important to approach it from this perspective. This allows for making informed decisions in the choice of suitable statistical models (e.g., for target detection) and signal processing methods (e.g., for feature generation) that exploit the inherent statistics embedded in the complex-valued SAR data. To provide for this, this chapter has introduced a systematic procedure to infer the statistical significance of the nonlinear dynamics in SAR imagery.

The applicability of our proposed procedure is demonstrated on various real-world chips from multiple SAR sensors having a variety of spatial resolutions. The analysis confirms the statistical significance of the nonlinear phenomenon, in the complex-valued chip, for the case of extended targets. Furthermore, as the SAR chip is magnitude-detected, the nonlinear effect is either obliterated or greatly diminished. The power-detected chip is found to retain some nonlinear statistics but it is postulated that such statistics are altered from their original form present in the complex-valued chip. Hence, for the case of extended targets, in order to utilize the 'nonlinear dynamics' in target recognition applications, it is recommended to use the complex-valued SAR image rather than the detected one. Ongoing investigation involves building a suitable classifier based on features generated from the complex-valued image. The usefulness of the 1-D representations, presented in this chapter, for harnesssing the nonlinear dynacmis from the complex-valued SAR chip will also be investigated.

Bibliography

[1] C. P. Silva, "Nonlinear dynamics and chaos: From concept to application," *Crosslink Magazine, Aerospace Corporation, Los Angeles, CA, Spring*, vol. 12, no. 1, pp. 40–51, 2011. [Online]. Available: http://www.aerospace.org/wp-content/uploads/crosslink/V12N1.pdf 69, 73

[2] SNDE. (2014) Society for nonlinear dynamics and econometrics. [Online]. Available: http://www.sndeecon.org

[3] S. Strogatz, *Nonlinear Dynamics And Chaos: With Applications To Physics, Biology, Chemistry, And Engineering (Studies in Nonlinearity)*. Reading, Massachusetts: Persues Books, 1994. 69, 73

[4] I. Cumming and F. Wong, *Digital signal processing of synthetic aperture radar data: algorithms and implementation*. Norwood, MA: Artech House, 2004. 69, 70, 72, 111

[5] A. Rihaczek and S. Hershkowitz, "Man-made target backscattering behavior: applicability of conventional radar resolution theory," *Aerospace and Electronic Systems, IEEE Transactions on*, vol. 32, no. 2, pp. 809–824, 1996. [Online]. Available: http://dx.doi.org/10.1109/7.489523 69, 70

[6] ——, *Radar resolution and complex-image analysis*. Norwood, MA: Artech House, 1996.

[7] ——, *Theory and practice of radar target identification*. Boston: Artech House, 2000. 69, 70

[8] D. P. Mandic and S. L. Goh, *Complex Valued Nonlinear Adaptive Filters: Noncircularity, Widely Linear and Neural Models*, ser. Wiley Series in Adaptive and Learning Systems for Signal Processing, Communications, and Control. West Sussex, UK: John Wiley & Sons, 2009. 69, 72

[9] T. Gautama, D. P. Mandic, and M. M. V. Hulle, "Signal nonlinearity in fMRI: A comparison between BOLD and MION," *IEEE Trans.*

Med. Imaging, vol. 22, no. 5, pp. 636–644, 2003. [Online]. Available: http://dx.doi.org/10.1109/TMI.2003.812248

[10] ——, "The delay vector variance method for detecting determinism and nonlinearity in time series," *Physica D: Nonlinear Phenomena*, vol. 190, no. 3-4, pp. 167–176, 2004. [Online]. Available: http://dx.doi.org/10.1016/j.physd.2003.11.001

[11] R. G. Andrzejak, K. Lehnertz, F. Mormann, C. Rieke, P. David, and C. E. Elger, "Indications of nonlinear deterministic and finite-dimensional structures in time series of brain electrical activity: Dependence on recording region and brain state," *Physical Review E - Statistical, Nonlinear, and Soft Matter Physics*, vol. 64, no. 6I, pp. 061 907/1–061 907/8, 2001. [Online]. Available: http://dx.doi.org/10.1103/PhysRevE.64.061907

[12] T. Schreiber and A. Schmitz, "Surrogate time series," *Physica D: Nonlinear Phenomena*, vol. 142, no. 3-4, pp. 346–382, 2000. [Online]. Available: http://dx.doi.org/10.1016/S0167-2789(00)00043-9 72

[13] G. R. Arce, *Nonlinear signal processing: a statistical approach*. Hoboken, NJ: Wiley-Interscience, 2004. 69, 70, 72, 75, 96

[14] K. El-Darymli, P. McGuire, D. Power, and C. Moloney, "Target detection in synthetic aperture radar imagery: a state-of-the-art survey," *J. Appl. Remote Sens*, vol. 7, no. 1, 2013. [Online]. Available: http://dx.doi.org/10.1117/1.JRS.7.071598 70, 74, 75

[15] M. Novey, T. Adali, and A. Roy, "Circularity and Gaussianity detection using the complex generalized Gaussian distribution," *Signal Processing Letters, IEEE*, vol. 16, no. 11, pp. 993–996, 2009. [Online]. Available: http://dx.doi.org/10.1109/LSP.2009.2028412 70, 72

[16] M. J. Wainwright, E. P. Simoncelli, and A. S. Willsky, "Random cascades on wavelet trees and their use in analyzing and modeling natural images," *Applied and Computational Harmonic Analysis*, vol. 11, no. 1, pp. 89–123, 2001. [Online]. Available: http://dx.doi.org/10.1006/acha.2000.0350 70

[17] K. El-Darymli, P. McGuire, E. W. Gill, D. Power, and C. Moloney, "Characterization and statistical modeling of phase in single-channel synthetic aperture radar imagery," *Aerospace and Electronic Systems, IEEE Transactions on [Accepted]*, 2015. 70, 97

[18] J. G. Proakis, *Digital Signal Processing: Principles, Algorithms, and Applications*, 4th ed. Upper Saddle RIver, New Jersey: Prentice Hall, 2006. 70, 73

[19] A. V. Oppenheim, *Discrete-Time Signal Processing*, 3rd ed. Upper Saddle River, NJ: Prentice-Hall, 2009. 70, 73

[20] J. P. Antoine, R. Murenzi, P. Vandergheynst, and S. T. Ali, *Two-dimensional wavelets and their relatives*. Cambridge, UK: Cambridge University Press, 2004. 70

[21] A. D. Poularikas, Ed., *Transforms and applications handbook*. Boca Raton, FL: CRC Press, 2010. 70, 81, 82

[22] R. Duda, P. Hart, and D. Stork, *Pattern classification*. New York, NY: John Wiley and Sons, 2001. 70

[23] N. E. Huang, Z. Shen, S. R. Long, M. C. Wu, H. H. Shih, Q. Zheng, N.-C. Yen, C. C. Tung, and H. H. Liu, "The empirical mode decomposition and the Hilbert spectrum for nonlinear and non-stationary time series analysis," *Royal Society of London. Series A: Mathematical, Physical and Engineering Sciences*, vol. 454, no. 1971, pp. 903–995, 1998. [Online]. Available: http://dx.doi.org/10.1098/rspa.1998.0193 70

[24] A.-O. Boudraa and J.-C. Cexus, "EMD-based signal filtering," *Instrumentation and Measurement, IEEE Transactions on*, vol. 56, no. 6, pp. 2196–2202, 2007. [Online]. Available: http://dx.doi.org/10.1109/TIM.2007.907967 70

[25] H. Huang and J. Pan, "Speech pitch determination based on Hilbert-Huang transform," *Signal Processing*, vol. 86, no. 4, pp. 792–803, 2006. [Online]. Available: http://dx.doi.org/10.1016/j.sigpro.2005.06.011 70

[26] Y. Chen and M. Q. Feng, "A technique to improve the empirical mode decomposition in the Hilbert-Huang transform," *Earthquake Engineering and Engineering Vibration*, vol. 2, no. 1, pp. 75–85, 2003. [Online]. Available: http://dx.doi.org/10.1007/BF02857540 70

[27] A. Singer and R. R. Coifman, "Non-linear independent component analysis with diffusion maps," *Applied and Computational Harmonic Analysis*, vol. 25, no. 2, pp. 226–239, 2008. [Online]. Available: http://dx.doi.org/10.1016/j.acha.2007.11.001 70

[28] K. El-Darymli, P. McGuire, E. W. Gill, D. Power, and C. Moloney,

"Understanding the significance of radiometric calibration for synthetic aperture radar imagery," in *Canadian conference on electrical and computer engineering (CCECE'14), IEEE*, Toronto, Canada, 2014. [Online]. Available: http://dx.doi.org/10.1109/CCECE.2014.6901104 71

[29] T. G. Leighton, P. R. White, and D. C. Finfer, "Contrast enhancement between linear and nonlinear scatterers," US Patent 11/917,990, 2010. [Online]. Available: http://www.google.ca/patents/US20100286514 73

[30] T. G. Leighton, G. H. Chua, and P. R. White, "Do dolphins benefit from nonlinear mathematics when processing their sonar returns?" *Royal Society A: Mathematical, Physical and Engineering Science*, vol. 468, no. 2147, pp. 3517–3532, 2012. [Online]. Available: http://dx.doi.org/10.1098/rspa.2012.0247 73

[31] T. G. Leighton, G. H. Chua, P. R. White, K. F. Tong, H. D. Griffiths, and D. J. Daniels, "Radar clutter suppression and target discrimination using twin inverted pulses," *Royal Society A: Mathematical, Physical and Engineering Science*, vol. 469, no. 2160, 2013. [Online]. Available: http://dx.doi.org/10.1098/rspa.2013.0512 73

[32] V. Illingworth, Ed., *The Penguin Dictionary of Physics*. London, UK: Penguin Books, 1991. 73

[33] J. Rice, *Mathematical Statistics and Data Analysis*. Belmont, CA: Duxbury Press, 1995. 73

[34] R. J. Brown and B. Rimmer. (2014) Generalized central limit theorem. Wolfram demonstration project. [Online]. Available: http://demonstrations.wolfram.com/GeneralizedCentralLimitTheorem/ 75

[35] T. Schreiber and A. Schmitz, "Improved surrogate data for nonlinearity tests," *Physical Review Letters*, vol. 77, no. 4, 1996. [Online]. Available: http://dx.doi.org/10.1103/PhysRevLett.77.635 76

[36] D. N. Politis, "The impact of bootstrap methods on time series analysis," *Statistical Science*, vol. 18, no. 2, pp. 219–230, 2003. [Online]. Available: http://dx.doi.org/10.1214/ss/1063994977

[37] D. Kugiumtzis, I. Vlachos, A. Papana, and P. G. Larsson, "Assessment of measures of scalar time series analysis in discriminating preictal states,"

International journal of Bioelectromagnetism, vol. 9, no. 3, pp. 134–145, 2007. [Online]. Available: http://www.ijbem.org/volume9/number3/090303.pdf 76

[38] J. Theiler, S. Eubank, A. Longtin, B. Galdrikian, and J. D. Farmer, "Testing for nonlinearity in time series: the method of surrogate data," *Physica D: Nonlinear Phenomena*, vol. 58, no. 1, pp. 77–94, 1992. [Online]. Available: http://dx.doi.org/10.1016/0167-2789(92)90102-S 76, 77

[39] D. S. Wilks, *Statistical methods in the atmospheric sciences*, 3rd ed. Waltham, MA: Academic Press, 2011, vol. 100. 76, 77, 80

[40] D. Kugiumtzis, "Evaluation of surrogate and bootstrap tests for nonlinearity in time series," *Studies in Nonlinear Dynamics and Econometrics*, vol. 12, no. 1, 2008. [Online]. Available: http://dx.doi.org/10.2202/1558-3708.1474 76, 77

[41] ——, "Statically transformed autoregressive process and surrogate data test for nonlinearity," *Physical Review E: Statistical, Nonlinear, and Soft Matter Physics*, vol. 66, no. 2, 2002. [Online]. Available: http://dx.doi.org/10.1103/PhysRevE.66.025201 77

[42] H. G. Schuster and W. Just, *Deterministic Chaos. An Introduction.* Weinheim: Wiley, 2006. 77

[43] A. M. Fraser and H. L. Swinney, "Independent coordinates for strange attractors from mutual information," *Physical review A: Atomic, Molecular, and Optical Physics*, vol. 33, no. 2, pp. 1134–1140, 1986. [Online]. Available: http://dx.doi.org/10.1103/PhysRevA.33.1134 77, 87

[44] C. J. Cellucci, A. M. Albano, and P. E. Rapp, "Statistical validation of mutual information calculations: Comparison of alternative numerical algorithms," *Physical Review E: Statistical, Nonlinear, and Soft Matter Physics*, vol. 71, no. 6, 2005. [Online]. Available: http://dx.doi.org/10.1103/PhysRevE.71.066208 77, 78

[45] M. Palus and D. Hoyer, "Detecting nonlinearity and phase synchronization with surrogate data," *Engineering in Medicine and Biology Magazine, IEEE*, vol. 17, no. 6, pp. 40–45, 1998. [Online]. Available: http://dx.doi.org/10.1109/51.731319

[46] K. Shi, X. Ma, and G. T. Zhou, "A mutual information based double-talk detector for nonlinear systems," in *Information Sciences and Systems (CISS 2008), 42nd IEEE Annual Conference*, 2008, pp. 356–360. [Online]. Available: http://dx.doi.org/10.1109/CISS.2008.4558551 77

[47] D. R. Ucci, W. Jacklin, and J. Grimm, "Investigation and simulation of nonlinear processors for spread spectrum receivers," Rome Laboratory, Air Forace Materical Command, Griffiss Air Force Base, New York, Tech. Rep. RL-TR-93-258, 1993. [Online]. Available: http://www.dtic.mil/cgi-bin/GetTRDoc?Location=U2&doc=GetTRDoc.pdf&AD=ADA278025 77

[48] M. Palus, "Testing for nonlinearity using redundancies: Quantitative and qualitative aspects," *Physica D: Nonlinear Phenomena*, vol. 80, no. 1, pp. 186–205, 1995. [Online]. Available: http://dx.doi.org/10.1016/0167-2789(95)90079-9 77

[49] D. S. Moore and D. K. Neal, *Introduction to the Practice of Statistics*. New York, NY: Macmillan, 2009. 79

[50] M. Abramowitz and I. A. Stegun, *Handbook of Mathematical Functions with Formulas, Graphs, and Mathematical Tables*, ser. 55. Washington, DC: National Bureau of Standards Applied Mathematics, Tenth Printing, 1972. 79

[51] F. J. Massey, "The Kolmogorov-Smirnov test for goodness of fit," *Journal of the American Statistical Association*, vol. 46, no. 253, pp. 68–78, 1951. [Online]. Available: http://www.jstor.org/stable/2280095 79

[52] G. Marsaglia, W. Tsang, and J. Wang, "Evaluating Kolmogorov's distribution," *Journal of Statistical Software*, vol. 8, no. 18, 2003. [Online]. Available: http://www.jstatsoft.org/v08/i18 79

[53] M. A. Stephens, "EDF statistics for goodness of fit and some comparisons," *Journal of the American statistical Association*, vol. 69, no. 347, pp. 730–737, 1974. [Online]. Available: http://dx.doi.org/10.1080/01621459.1974.10480196 80

[54] P. J. Schreier and L. L. Scharf, *Statistical signal processing of complex-valued data: the theory of improper and noncircular signals*. Cambridge, UK: Cambridge University Press, 2010. 83, 85

[55] R. H. Allen, *Star Names: Their Lore and Meaning*. New York, NY: Dover Publications Inc, 1963. [Online]. Available: http://penelope.uchicago.edu/Thayer/E/Gazetteer/Topics/astronomy/_Texts/secondary/ALLSTA/Canis_Major*.html 85

[56] J. G. A. Davis, "The pronunciations, derivations, and meanings of a selected

list of star names," *Popular Astronomy*, vol. 52, no. 3, 1944. [Online]. Available: http://tinyurl.com/mhr444u

[57] European Southern Observatory. (2014) Artist's impression of the evolution of a hot high-mass binary star (annotated version). [Online]. Available: http://www.eso.org/public/videos/eso1230b

[58] Wikipedia. Zeta canis majoris. [Online]. Available: http://en.wikipedia.org/wiki/Zeta_Canis_Majoris 85

[59] MacDonald, Dettwiler and Associates Ltd. (2011) Radarsat-2 product description. [Online]. Available: http://gs.mdacorporation.com/products/sensor/radarsat2/RS2_Product_Description.pdf 88

[60] Wikipedia. (2013) Naval station argentia. [Online]. Available: http://en.wikipedia.org/wiki/Naval_Station_Argentia xiv, 88, 89

[61] MacDonald, Detwiler and Associates Ltd. Radarsat-2 sample dataset. [Online]. Available: http://gs.mdacorporation.com/SatelliteData/Radarsat2/SampleDataset.aspx 88

[62] United States Air Force. (2013) MSTAR. [Online]. Available: https://www.sdms.afrl.af.mil/index.php?collection=mstar 91

[63] K. El-Darymli, C. Moloney, E. W. Gill, P. McGuire, and D. Power, "Design and implementation of a low-power synthetic aperture radar," in *International Geoscience and Remote Sensing Symposium (IGARSS'14), IEEE*, Quebec, Canada, 2014. [Online]. Available: http://dx.doi.org/10.1109/IGARSS.2014.6946618 93

[64] G. L. Charvat. (2013) Low-power X-band rail SAR. [Online]. Available: http://www.glcharvat.com/Dr._Gregory_L._Charvat_Projects/Low-Power_X-Band_Rail_SAR.html 94

[65] G. L. Charvat, L. Kempell, and C. Coleman, "A low-power high-sensitivity X-band rail SAR imaging system," *Antennas and Propagation Magazine, IEEE*, vol. 50, no. 3, pp. 108–115, 2008. [Online]. Available: http://dx.doi.org/10.1109/MAP.2008.4563576 94

[66] M. Novey, T. Adali, and A. Roy, "A complex generalized Gaussian distribution- characterization, generation, and estimation," *Signal Processing,*

IEEE Transactions on, vol. 58, no. 3, pp. 1427–1433, 2010. [Online]. Available: http://dx.doi.org/10.1109/TSP.2009.2036049 96

[67] Matlab. (2014b) Normal distribution. Mathworks R2013b documentation. [Online]. Available: http://www.mathworks.com/help/stats/normal-distribution.html 97

[68] K. El-Darymli, P. McGuire, E. W. Gill, D. Power, and C. Moloney, "Effect of detection on spatial-resolution in synthetic aperture radar imagery and mitigation through upsampling," *Journal of Applied Remote Sensing*, vol. 8, no. 1, 2014. [Online]. Available: http://dx.doi.org/10.1117/1.JRS.8.083601 111

5. Recognition of Nonlinear Dispersive Scattering in Synthetic Aperture Radar Imagery Imagery

5.1. Overview

This chapter presents a new insight into the nonlinear dynamics in SAR imagery. For extended targets, the conventional radar resolution theory is violated due to the nonlinear phase modulation induced by the dispersive scatterers. A novel algorithm motivated by the Hilbert view for the nonlinear phenomenon is introduced. Our algorithm may be used to not only detect the dispersive scatterers but also to estimate the nonlinear order of the phase modulation. Our results are demonstrated on a representative real-world target chip.

5.2. Introduction

Although our world is inherently nonlinear, conventional signal processing is built on a linear system theory that sees deviation from linearity as a noise that warrants removal. This is the Fourier view which assumes a first-order fundamental oscillation and bounding higher order harmonics. Despite its mathematical soundness, this view does not correspond to physical reality [1]. Nonlinear research migrates from the Fourier view, and it can be broadly classified into two branches: (1) development of methods that seek to exploit the nonlinear phenomenon and (2) development of techniques to harness the nonlinear dynamics embedded in the data generated by the linear signal processing methods. This chapter is concerned with the second branch,

as it is applied to the focused *single-channel* complex-valued (CV) synthetic aperture radar (SAR) image.

Following the conventional radar resolution theory, the focused SAR image is linear [2]. Thus, analysis of the SAR image has traditionally been based on linear techniques associated with the image intensity while the phase content is ignored. The inapplicability of the linear theory to extended targets has been reported in the literature [3–5], based on the empirical observation that man-made targets produce dispersive scattering. In effect, this induces a nonlinear phase modulation (PM) in the radar return signal which causes a mismatch in the correlator's output. This phenomenon is preserved in the CV image rather than the detected one.

The Hilbert Huang transform (HHT) represents an advancement in nonlinear and nonstationary signal processing [6]. First, it uses a technique known as empirical mode decomposition (EMD) to decompose the data, according to their characteristic scales, into a set of intrinsic mode functions (IMFs). Thus, unlike Fourier-based methods, the basis of the data comes from the data itself. Second, the IMFs are used to construct a time/space-frequency-energy distribution known as the Hilbert spectrum. Subsequently, the time/space localities of the events are preserved. Therefore, the frequency and energy defined by the Hilbert transform have intrinsic and instantaneous physical meaning. Although the term 'spectrum' and 'frequency' are traditionally associated with the Fourier-based analysis, the HHT provides a different interpretation for these terms. In doing so, the HHT avoids the Heisenberg principle, which is a serious setback to all Fourier-based time/space-frequency methods including the wavelet transform [6, 7].

In [3–5], a curve fitting algorithm is used to detect nonlinear scattering in SAR imagery. We pinpoint two issues with this approach. Firstly, it is non-adaptive due to its contingency on certain a priori assumptions. Secondly, while it identifies nonlinear scattering in general terms, it neither classifies it nor estimates its order. The algorithm presented in this chapter differs significantly. First, since our approach is motivated by the HHT transform, it is entirely data-driven. Second, our approach allows for classifying the dispersive scatterers as well as estimating their nonlinear order. To our knowledge, this capability has not been previously demonstrated in the SAR literature. A major advantage of the approach is the development of a new set of features which exploit the nonlinear dynamics for target recognition applications.

The remainder of this chapter is organized as follows. In Sect. 5.3, the origin of the nonlinear phenomenon in SAR imagery is elaborated. In Sect. 5.4, the proposed algorithm is introduced. In Sect. 5.5, an illustrative example is provided. Conclusions are provided in Sect. 5.6.

5.3. Origin of the Nonlinear Phenomenon

The baseband backscatter x_{BB} from a single point target, output from the quadrature demodulator and downlinked to the SAR processor [2], is known as the phase history or the raw data given by

$$\begin{aligned} x_{BB}(\tau,\eta) = A\exp(j\psi)\Bigg\{ & w_r\left(\tau - 2\frac{R(\eta)}{\underline{c}}\right) w_a(\eta-\eta_c) \\ & \exp\left(-j4\pi f_o\frac{R(\eta)}{\underline{c}}\right)\exp\left(j\pi K_r\left(\tau - 2\frac{R(\eta)}{\underline{c}}\right)^2\right)\Bigg\}, \end{aligned} \tag{5.1}$$

where A is the backscatter coefficient (i.e., σ_o), ψ is a phase change in the received pulse due to the scattering process from a surface, $j = \sqrt{-1}$, τ is the fast time, η is the slow time, $w_r(\tau) = rect(\tau/T_r)$ is the transmitted pulse envelope, T_r is the pulse duration, $R(\eta)$ is the distance between the radar and the point target, $\underline{c}$ is the speed of light in a vacuum, $w_a(\eta)$ is the two-way azimuth beam pattern, η_c is the beam center in the azimuth direction, f_o is the center frequency, and K_r is the FM rate of the range pulse. The SAR raw signal $x_{BB}(\tau,\eta)$ is conventionally modeled as

$$x_{BB}(\tau,\eta) = g(\tau,\eta) \otimes h(\tau,\eta) + n(\tau,\eta), \tag{5.2}$$

where $\otimes$ denotes convolution, $g(\tau,\eta)$ is the ground reflectivity, $h(\tau,\eta)$ is the impulse response of the SAR, and $n(\tau,\eta)$ is a noise component mainly due to the front-end receiver.

The SAR processor solves for $g(\tau,\eta)$. Following the conventional radar resolution theory, $h(\tau,\eta)$, bounded by the curly brackets in Eq. 5.1, is an impulse response of a point target. For a given reflector within the radar illumination time, ψ is assumed

to be constant [2]. For the case of an extended target, this assumption is adopted verbatim. Hence, such a target is modeled as the linear combination of its point reflectors. However, the assumption of constant ψ is violated in the presence of dispersive scattering from cavity-like reflectors, typical in stationary and moving man-made targets such as vehicles and airplanes. These reflectors trap the incident wave before it is backscattered, thus, inducing a PM. The problem arises when the PM is nonlinear. Besides the PM, this phenomenon also introduces amplitude modulation (AM) [3–5]. Thus, the backscatter term in Eq. 5.1 is rewritten

$$s\left(\tau\left(f_\tau\right),\eta\right) = A\left(\tau\left(f_\tau\right),\eta\right)\exp\left(j\psi\left(\tau\left(f_\tau\right),\eta\right)\right), \tag{5.3}$$

where $\tau\left(f_\tau\right)$ is the time delay due to the PM, and f_τ varies over the spectral width of the chirp, B. In Eq. 5.3, it is emphasized that the magnitude and phase of the backscatter is frequency dependent. While the AM is a linear process, this is often not the case for the PM. Indeed, based on the principle of stationary phase (POSP), the time delay induced by a dispersive scatterer is

$$\tau\left(f_\tau\right) \propto \frac{d}{df}\left(f_\tau\right)^n, \tag{5.4}$$

where n is the order induced by the dispersive scatterer. For $n \in \{0,1,2\}$, the PM is linear, and its effect is either translation or smearing of the response in the correlation filter. Another reason for the smearing of the response is the variable Doppler processing used for motion compensation. However, for $n \notin \{0,1,2\}$, the phase center possesses a nonlinear delay which introduces spurious effects in the correlator's output. This phenomenon is referred to as 'sideband responses', and the information about it is preserved in the CV image rather than the detected one. Further, in the presence of an extended target, it is empirically observed that this effect dominates the focused SAR imagery [3–5]. The sideband responses are radically different from the range and Doppler sidelobes. One of the reasons for this is that they are among the strongest responses. Secondly, unlike the range and the Doppler sidelobes, they are not restricted to the range and cross range gates. Thirdly, they are distributed over an area far larger than that occupied by the target. As stressed in [3–5], these

sideband responses cannot be suppressed by the weighting methods because they are target generated. Obviously, the nonlinear PM violates the resolution theory of point targets.

Although it is not common to exploit this phenomenon in radar applications, it is well-known in wave theory (see Ch. 14 and 15 in [8]). Indeed, Huang *et al.* [1] distinguish between two types of frequency modulation (FM): interwave and intrawave. The former implies that the frequency of oscillation gradually changes as do the waves in a dispersive system. The latter signifies that in dispersive waves, the frequency also changes within one wave. Before the advent of the HHT, this phenomenon was often treated as harmonic distortion [6]. In this study, we exploit this effect to detect and classify the dispersive scatterers in SAR imagery.

5.4. Our Proposed Algorithm

Our proposed algorithm is depicted in Fig. 5.1. Firstly, the CV SAR chip is available in the form

$$g\left(u,v\right)=i\left(\underline{x},\underline{y}\right)+j\,q\left(\underline{x},\underline{y}\right), \tag{5.5}$$

where $i\left(\underline{x},\underline{y}\right)$ and $q\left(\underline{x},\underline{y}\right)$ are the real and the imaginary parts of the SAR chip, respectively. To convert this chip to the 1-D space, the Radon transform is applied to each part separately as follows

$$F\left(\theta,x\right)=R_{\theta}\left\{f\left(\underline{x},\underline{y}\right)\right\}\Big|_{\theta=[0,\pi)}. \tag{5.6}$$

where $\theta\in[\pi,2\pi]$ is omitted because the corresponding Radon transform is redundant. $R_{\theta}\left(x\right)$ is the line integral of $f\left(\underline{x},\underline{y}\right)$ parallel to the y axis defined as [9]

$$R_{\theta}\left(x\right)=\int_{-\infty}^{\infty}f\left(x\cos\theta-y\sin\theta,x\sin\theta+y\cos\theta\right)dy, \tag{5.7}$$

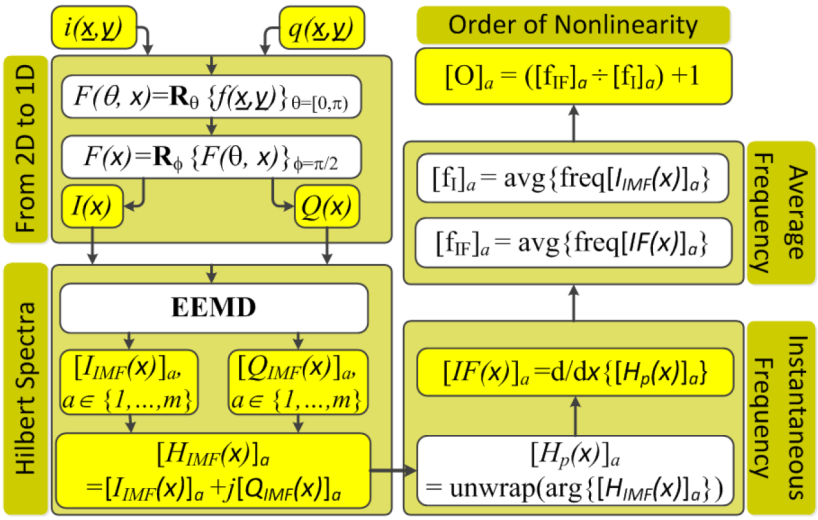

Figure 5.1: Our proposed algorithm for detection and classification of the nonlinear dispersive scatterers.

where θ is the projection angle, and (x, y) are coordinates related to θ by

$$\begin{bmatrix} x \\ y \end{bmatrix} = \begin{bmatrix} \cos\theta & \sin\theta \\ -\sin\theta & \cos\theta \end{bmatrix} \begin{bmatrix} \underline{x} \\ \underline{y} \end{bmatrix}. \tag{5.8}$$

and (x, y) is rotated about the center of the image. The Radon transform is linear which guarantees that it preserves the statistics of the original SAR chip. Then, the projection angles are integrated-out through applying the Radon transform to Eq. 5.6 at $\phi = \frac{\pi}{2}$ as follows

$$F(x) = R_{\phi}\{F(\theta, x)\}|_{\phi=\frac{\pi}{2}}. \tag{5.9}$$

The output given by Eq. 5.9 is a 1-D vector $I(x)$ and $Q(x)$, respectively, representative of $i\left(\underline{x}, \underline{y}\right)$ and $q\left(\underline{x}, \underline{y}\right)$. Secondly, the ensemble EMD (EEMD) is applied [10]. EEMD is a noise-assisted method which resolves the problem of mode mixing encountered in the traditional EMD [6]. Primarily, EEMD defines the true IMF as the mean value for an ensemble of trials. Each trial consists of the signal plus a white

noise of a finite amplitude. Hence, the EEMD decomposes the input data to a small number of IMFs based on the local characteristic time/space scale. An IMF represents a simple oscillatory mode as a counterpart to the harmonic function. By definition, an IMF is any function with the same number of extrema and zero crossings with its envelope symmetric with respect to zero. This definition guarantees a well-behaved Hilbert transform of the IMF. The procedure for extracting an IMF is referred to as sifting. In our subsequent analysis, we use a local stopping criterion for the sifting process as prescribed in [10]. Thus, a number $\underline{m}$ of IMFs are extracted from $I(x)$ and $Q(x)$ as

$$\begin{aligned} I(x) &= \sum_{a=1}^{\underline{m}} \left[I_{IMF}(x)\right]_a + r_I(x), \\ Q(x) &= \sum_{a=1}^{\underline{m}} \left[Q_{IMF}(x)\right]_a + r_Q(x). \end{aligned} \tag{5.10}$$

where $r_I(x)$ and $r_Q(x)$ are the residues.

Next, an analytic signal is formed from each IMF. Typically, the HHT achieves this through computing the Hilbert transform for the IMF, and the result is placed in the imaginary-part of the analytic signal. The real-part is the IMF signal itself. However, according to the Paley-Wiener theorem, the CV SAR data output from the quadrature demodulator is indeed an analytic signal whose imaginary-part is the Hilbert transform of its real-part [11]. Hence, we form the analytic signals based on a proper combination of the real-part and the imaginary-part for each IMF according to

$$\left[H_{IMF}(x)\right]_a = \left[I_{IMF}(x)\right]_a + j\ \left[Q_{IMF}(x)\right]_a, \tag{5.11}$$

where $a \in \{1, ..., \underline{m}\}$. This representation is known as the Hilbert spectrum. Then, the unwrapped instantaneous phase for the Hilbert spectrum is computed as

$$\left[H_p(x)\right]_a = \mathfrak{unwrap}\left(\arg\left\{\left[H_{IMF}(x)\right]_a\right\}\right), \tag{5.12}$$

where $\mathfrak{unwrap}$ denotes the addition of multiples of $\pm 2\pi$ when absolute jumps between consecutive elements of $[H_p(x)]_a$ are greater than or equal to the default jump tolerance of π radians.

Subsequently, the instantaneous frequency (IF) is computed following the definition of the POSP as

$$[IF(x)]_a = \frac{\mathrm{d}}{\mathrm{d}x}[H_p(x)]_a . \tag{5.13}$$

Then, the average frequency for the cycles of the IF and the real-part of each IMF is computed as

$$[f_{IF}]_a = f_{avg}\{[IF(x)]_a\}\ , [f_I]_a = f_{avg}\{[I_{IMF}(x)]_a\}\ . \tag{5.14}$$

Here, $[f_{IF}]_a$ is the intrawave frequency and $[f_I]_a$ is the corresponding oscillation frequency. Finally, we compute the nonlinear order for each IMF as [6, 12, 13]

$$[O]_a = \frac{[f_{IF}]_a}{[f_I]_a} + 1. \tag{5.15}$$

For $\frac{[f_{IF}]_a}{[f_I]_a} < 1$, $[f_{IF}]_a$ is undersampled, and should not be used for calculating $[O]_a$.

5.5. An Illustrative Example

A single-channel (i.e., with a horizontal-horizontal (HH) polarization) SAR chip for target D7 is arbitrarily chosen from the MSTAR dataset (see Fig. 5.2). MSTAR is a public-domain dataset that offers a nominal spatial resolution of 0.3047 m in both range and azimuth [14]. In Fig. 5.3, this chip is transformed to 1-D space using Eq. 5.9. Then, in Fig. 5.4, the EEMD is applied as described by Eq. 5.10. Based on [10], we used a number of 2000 ensembles with a ratio for the standard deviation of the added noise to the signal equal to 0.2. The power of the EEMD is obvious as it decomposes the SAR data into only four IMFs which are AM-FM signals. Note that the residues

are discarded.

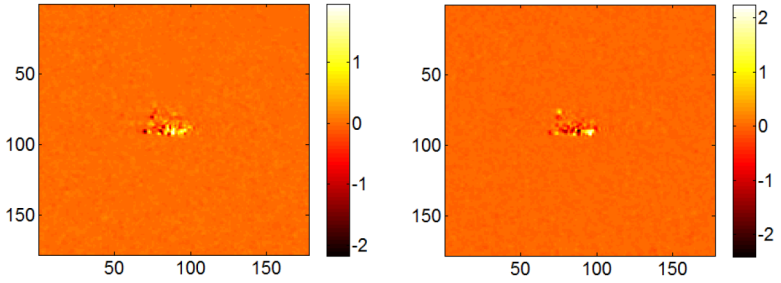

(a) Real-part, $i\left(\underline{x},\underline{y}\right)$. **(b)** Imaginary-part, $q\left(\underline{x},\underline{y}\right)$.

Figure 5.2: MSTAR chip for target D7: HB14931.005.

Table 5.1: Order of the nonlinear scatterers in Fig. 5.5.

a	$[f_I]_a$	$[f_{IF}]_a$	$O_a = \frac{[f_{IF}]_a}{[f_I]_a}+1$
1	0.2621 Hz	0.3414 Hz	2.3026
2	0.1364 Hz	0.2154 Hz	2.5792
3	0.0678 Hz	0.1076 Hz	2.5870
4	0.0256 Hz	0.0476 Hz	2.8594

Next, the IFs based on Eq. 5.13 are depicted in Fig. 5.5. Two types of modulation are noted: firstly, interwave modulation between the IMFs is a clear indicator for the presence of dispersive scatterers; secondly, intrawave modulation is evident within each $[IF\,(x)]_a$. In the case of linear dispersive scattering, one would expect the absence of oscillations in $[IF\,(x)]_a$. However, all $[IF\,(x)]_a$ have oscillations, a clear indicator for the nonlinear dispersive scattering [1, 6, 12]. In the final step, we compute the order of the nonlinear scattering for each $[IF\,(x)]_a$. This is achieved through applying Eq. 5.15. Our calculation for Eq. 5.14 is based on the distance between the peaks. The orders for the scatterers are provided in Table 5.1.

This result reveals four different nonlinear scatterers in the MSTAR chip considered. The capability of our proposed method to identify and classify these dispersive

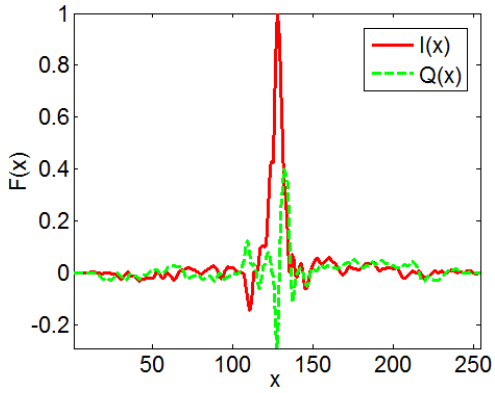

Figure 5.3: Normalized $I(x)$ and $Q(x)$.

scatterers is clear. This shows that the nonlinear effects in the CV SAR image can offer an important set of features for target recognition applications. These features are unique in that they accentuate the nonlinear dynamics of the scattering process.

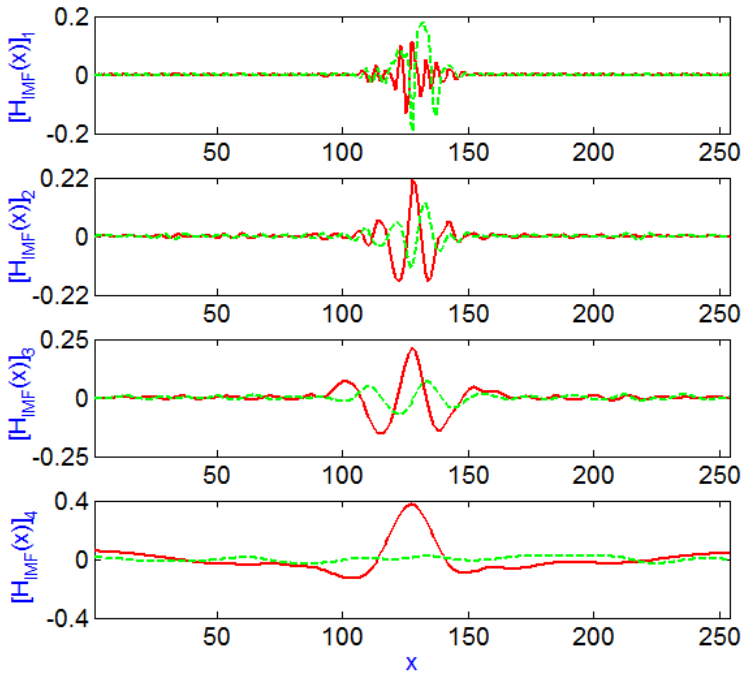

Figure 5.4: EEMD for Fig. 5.3. Red solid line is for $[I_{IMF}(x)]_a$. Dashed green line is for $[Q_{IMF}(x)]_a$.

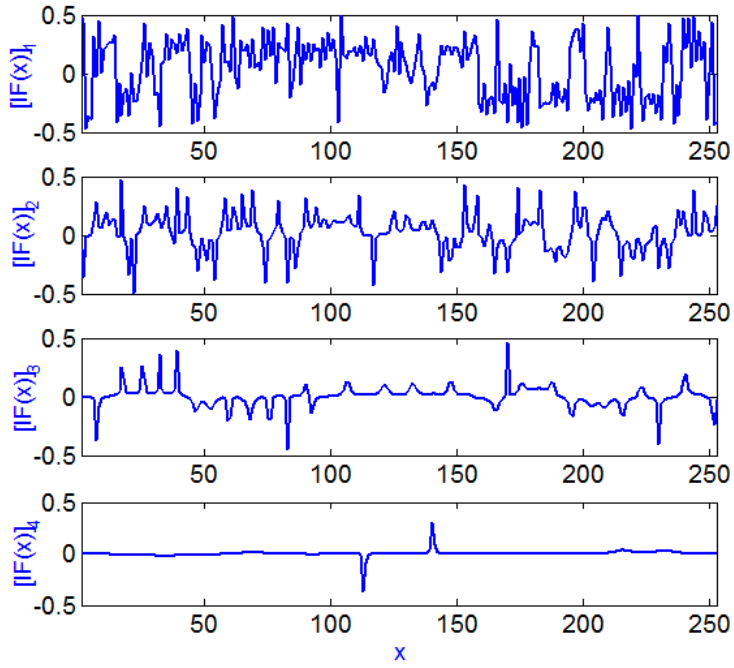

Figure 5.5: IF for Fig. 5.4. The ordinate is the normalized chirp bandwidth. For MSTAR, $B = 0.591$GHz.

5.6. Conclusions

Dispersive scatterers from man-made targets induce a predominant nonlinear phase modulation in the radar return signal. The conventional radar resolution theory views this phenomenon as distortions that warrant removal. Motivated by the Hilbert view, this chapter has presented a new insight into the nonlinear dynamics of the dispersive scatterers. A novel algorithm for recognizing the order of the nonlinear scatterers is introduced. The applicability of our algorithm is demonstrated on a real-world target chip from the MSTAR dataset. Ongoing research involves the development of a new set of features to harnesses this effect for target recognition applications in SAR imagery.

Bibliography

[1] N. Huang, Z. Shen, and S. Long, "A new view of nonlinear water waves: the hilbert spectrum," *Annual Review of Fluid Mechanics*, vol. 31, no. 1, pp. 417–457, 1999. [Online]. Available: http://dx.doi.org/10.1146/annurev.fluid.31.1.417 121, 125, 129

[2] I. Cumming and F. Wong, *Digital Processing of Synthetic Aperture Radar Data*. Norwood, MA: Artech House, 2005. 122, 123, 124

[3] A. Rihaczek and S. Hershkowitz, "Man-made target backscattering behavior: Applicability of conventional radarresolution theory," *IEEE Transactions on Aerospace and Electronic Systems*, vol. 32, no. 2, pp. 809–824, 1996. [Online]. Available: http://dx.doi.org/10.1109/7.489523 122, 124

[4] ——, *Radar Resolution and Complex-Image Analysis*. Norwood, MA: Artech House, 1996.

[5] ——, *Theory and Practice of Radar Target Identification*. Boston: Artech House, 2000. 122, 124

[6] N. Huang, Z. Shen, S. Long, M. Wu, H. Shih, Q. Zheng, N.-C. Yen, C. Tung, and H. Liu, "The empirical mode decomposition and the hilbert spectrum for nonlinear and non-stationary time series analysis," *Proceedings of the Royal Society of London. Series A: Mathematical, Physical and Engineering Sciences*, vol. 454, no. 1971, pp. 903–995, 1998. [Online]. Available: http://dx.doi.org/10.1098/rspa.1998.0193 122, 125, 126, 128, 129

[7] S. Mallat, *A Wavelet Tour of Signal Processing: the Sparse Way*. Burlington, MA: Elsevier, 2008. 122

[8] G. Whitham, *Linear and Nonlinear Waves*. New York, NY: John Wiley & Sons, 2011, vol. 42. 125

[9] A. Poularikas, Ed., *Transforms and Applications Handbook*. Boca Raton, FL: CRC Press, 2010. 125

[10] Z. Wu and N. Huang, "Ensemble empirical mode decomposition: A noise-assisted data analysis method," *Advances in Adaptive Data Analysis*, vol. 1, no. 1, pp. 1–41, 2009. [Online]. Available: http://dx.doi.org/10.1142/S1793536909000047 126, 127, 128

[11] M. Cheney and B. Borden, *Fundamentals of Radar Imaging*. Philadelphia: Society for Industrial and Applied Math, 2009. 127

[12] N. Huang, M. Lo, Z. WU, and X. Chen, "Method for quantifying and modeling degree of nonlinearity, combined nonlinearity, and nonstationarity," US Patent Patent App. 13/241,565, 2013. [Online]. Available: https://www.google.com/patents/US20130080378 128, 129

[13] Y. Yuan and N. Huang, "A reappraisal of ocean wave studies," *Journal of Geophysical Research: Oceans*, vol. 117, no. C11, pp. 1978–2012, 2012. [Online]. Available: http://dx.doi.org/10.1029/2011JC007768 128

[14] U. S. A. Force. MSTAR dataset. [Online]. Available: https://www.sdms.afrl.af.mil/index.php?collection=mstar 128

6. Characterization and Statistical Modeling of Phase in Single-Channel Synthetic Aperture Radar Imagery

6.1. Overview

Traditionally, the phase content in single-channel synthetic aperture radar (SAR) imagery is discarded. This practice is justified by the conventional radar resolution theory, which is a theory strictly relevant to point targets. The advent of high-resolution radars permits small targets previously considered to be points to be now treated as extended targets, in which case this theory is not strictly applicable. With this in mind, this chapter offers a new insight into the relevance of phase in single-channel SAR imagery. The proposed approach builds on techniques from the fields of complex-valued and directional statistics. In doing so, three main contributions are presented, the first being a novel method for characterizing the phase content. Secondly, a new statistical model for the phase is considered, and then a set of fifteen solely-phase-based features are discussed. Our results are demonstrated on real-world SAR datasets for ground-truthed targets. The statistical significance of the information carried in the phase is clearly demonstrated. Furthermore, if applied to a dataset with higher resolution, the proposed techniques are expected to achieve even higher performance.

6.2. Introduction

Synthetic aperture radar (SAR) is an active remote sensor that provides day-and-night and all-weather broad area imaging capabilities at high resolutions. These unique capabilities make SAR a distinctive sensor for both civilian and military applications. In most works published in the literature utilizing single look complex-valued (SLC) high-resolution SAR imagery, and particularly for single polarization (i.e., single-channel), the phase content is entirely discarded. Practitioners in the field usually comments that the phase is discarded because it is random and uniformly distributed (i.e., in the range $(-\pi, \pi]$) and, thus, useless. This statement bears some scrutiny. In order to trace the root of this common belief, it is best to approach the topic from the perspective of speckle. Indeed, the logic behind the discarding of the phase of a signal is based on the resolution theory of point targets [1], which in turn leads to the so-called fully-developed speckle model [2]. Among the main hypotheses motivating this model are [2, 3]: (1) the number of scatterers per resolution cell is large enough, (2) the magnitude and phase of a particular scatterer do not depend on those of other scatterers, (3) the magnitude and phase of any scatterer are independent of each other, and (4) the phases are uniformly distributed between $(-\pi, \pi]$ (i.e., in other words, the imaged surface is rough with respect to the wavelength of the radar). Clearly, with the advent of high-resolution radars, the foregoing assumptions may be no longer strictly applicable [1].

The main reason for violating the resolution theory of point targets is the introduction of nonlinear phase modulation into a signal due to dispersive scatterers [1]. This scattering behavior is due to the cavity-like reflectors in extended targets, and it dominates the focused SAR imagery [1]. Although the practice of using the complex-valued image is not common in the literature, in [1, 4, 5] a curve fitting algorithm is used to detect nonlinear scattering in single-channel SAR imagery. The output from this algorithm is used to generate features that take advantage of nonlinear scattering. These features are found to be useful for target recognition applications in SAR imagery. Another advantage of using the complex-valued SAR image is that it retains the full spatial resolution which is degraded by factors of two and greater for power and magnitude detections, respectively [1, 6, 7].

The study in this chapter builds on three previous investigations [8–10]. In [8, 9], an in-depth analysis for nonlinearity in single-channel SAR imagery was carried out.

The analysis demonstrated the statistical significance of the nonlinear phenomenon in high-resolution complex-valued SAR imagery. It was also shown that the nonlinear effect is either obliterated or altered/diminished for magnitude and power detections, respectively. In [10], an initial investigation into the effect of circularity/noncircularity (also known as propriety/impropriety) in complex-valued SAR imagery was conducted. It was demonstrated that, for the case of extended target, the complex-valued SAR chip is noncircular. Also, a proportional relationship between noncircularity and nonlinearity was noted.

This chapter offers a new approach for extracting useful information from the phase in single-channel SAR imagery. Primarily, the SAR image is considered from the perspectives of complex-valued [11–13] and directional [14–16] statistics, respectively. From the perspective of complex-valued statistics [11–13], the usefulness of the phase can be quantified using a measure called noncircularity. Noncircularity simply means that the complex-valued SAR image has a probability density function (PDF) that is variant under rotation in the complex plane. This present research has indicated that applying this measure directly to the phase image is misleading as it gives erroneous results for circularity (also known as propriety). Subsequently, it is important that each pixel in the phase image is properly referenced to its neighbors. This is achieved through borrowing relevant techniques from the field of directional statistics [14–16] which can easily handle the issue of phase wrapping. Once preprocessed, it transpires that in the presence of extended targets, the phase image is noncircular. Furthermore, relevant techniques from the field of directional statistics are applied to develop a suitable statistical model for the processed phase image. The following are main contributions presented in this chapter:

- A method for characterizing the phase content in SAR imagery (see Sect. 6.5),
- A statistical model for the characteristic phase in SAR imagery (see Sect. 6.6), and
- A set of fifteen solely-phase-based features for target classification in SAR imagery (see Sect. 6.7).

The ideas presented in this chapter are applicable to various kinds of stationary and moving extended targets including vehicles, ships, airplanes, icebergs, etc. Furthermore, the application of the methods proposed may be extended well beyond SAR to include various types of coherent sensors in general such as radar, sonar, syn-

thetic aperture sonar (SAS), ultrasound, and synthetic aperture ultrasound (SAU), etc. Throughout the chapter, the term *high-resolution* is used to nominally refer to a sensor with a spatial resolution finer than the size of the imaged target (i.e., an extended target [17]). Finally, the term *chip* is used to refer to a smaller image, for a particular target or clutter, extracted from a bigger scene.

The remainder of the chapter is organized as follows. In Sect. 6.3, the origin of the nonlinear phenomenon in SAR imagery is described. In Sect. 6.4, the SAR datasets utilized in this study are provided. In Sect. 6.5, the proposed method for phase characterization is introduced. In Sect. 6.6, the wrapped complex Gaussian scale mixture (WCGSM) for phase modeling is presented and compared with von Mises (vM) and wrapped Cauchy (WC) distributions. In Sect. 6.7, new fifteen phase-based features are developed and used to demonstrate the advantage of the proposed methods for target classification in SAR imagery. Finally, concluding remarks are given in Sect. 6.8.

6.3. On the Origin of the Nonlinear Phenomenon in SAR Imagery

The baseband backscatter x_{BB} from a single point target, output from the quadrature demodulator and downlinked to the SAR processor, is known as the phase history or the raw signal given by [6]

$$\begin{aligned} x_{BB}(\tau,\eta) = A\exp(j\psi)\Bigg\{ & w_r\left(\tau - 2\frac{R(\eta)}{\underline{c}}\right) w_a(\eta-\eta_c) \\ & \exp\left(-j4\pi f_o \frac{R(\eta)}{\underline{c}}\right)\exp\left(j\pi K_r\left(\tau - 2\frac{R(\eta)}{\underline{c}}\right)^2\right)\Bigg\}, \end{aligned} \tag{6.1}$$

where A is the backscatter coefficient (i.e., σ_o), ψ is a phase change in the received pulse due to the scattering process from a surface, $j=\sqrt{-1}$, τ is the fast time, η is the slow time, $w_r(\tau) = rect(\tau/T_r)$ is the transmitted pulse envelope, T_r is the pulse duration, $R(\eta)$ is the distance between the radar and the point target, $\underline{c}$ is the speed of light in a vacuum, $w_a(\eta)$ is the two-way azimuth beam pattern, η_c is the beam center in the azimuth direction, f_o is the center frequency, and K_r is the frequency modulation

(FM) rate of the range pulse. The SAR raw signal is conventionally modeled as

$$x_{BB}(\tau,\eta) = g(\tau,\eta) \otimes h(\tau,\eta) + n(\tau,\eta), \tag{6.2}$$

where $\otimes$ denotes convolution, $g(\tau,\eta)$ is the ground reflectivity, $h(\tau,\eta)$ is the impulse response of the SAR, and $n(\tau,\eta)$ is a noise component mainly due to the front-end receiver.

The SAR processor solves for $g(\tau,\eta)$. Following the conventional radar resolution theory, $h(\tau,\eta)$, bounded by the curly brackets in Eq. 6.1, is an impulse response of a point target. For a given reflector within the radar illumination time, ψ is assumed to be constant [6]. For the case of an extended target, this assumption is retained. Hence, such a target is modeled as the linear combination of its point reflectors. However, the assumption of constant ψ is violated in the presence of dispersive scattering from cavity-like reflectors, typical in stationary and moving man-made (extended) targets such as vehicles and airplanes. These reflectors trap the incident wave before it is backscattered, thus, inducing a phase modulation (PM). The problem arises when the PM is nonlinear. Besides the PM, this phenomenon also introduces amplitude modulation (AM) [1, 4, 5]. Thus, the backscatter term in Eq. 6.1 is rewritten as

$$s(\tau(f_\tau),\eta) = A(\tau(f_\tau),\eta)\exp(j\psi(\tau(f_\tau),\eta)), \tag{6.3}$$

where $\tau(f_\tau)$ is the time delay due to the PM, and f_τ varies over the spectral width of the chirp, B. In Eq. 6.3, it is emphasized that the magnitude and phase of the backscatter is frequency dependent. While AM is a linear process, this is often not the case for PM. Indeed, based on the principle of stationary phase (POSP), the time delay induced by a dispersive scatterer is

$$\tau(f_\tau) \propto \frac{d}{df}(f_\tau)^O, \tag{6.4}$$

where O is the order induced by the dispersive scatterer. For $O \in \{0,1,2\}$, the PM is linear, and its effect is either translation or smearing of the response in the correlation

filter[1]. However, for $O \notin \{0, 1, 2\}$, the phase center possesses a nonlinear delay which introduces spurious effects in the correlator's output. This phenomenon is referred to as 'sideband response', and the information about it is preserved in the complex-valued image rather than the detected one. Further, in the presence of an extended target, it is empirically observed that this effect dominates the focused SAR imagery [1, 4, 5]. The sideband responses are radically different from the range and Doppler sidelobes. One of the reasons for this is that they are among the strongest responses. Secondly, unlike the range and the Doppler sidelobes, they are not restricted to the range and cross-range gates. Thirdly, they are distributed over an area far larger than that occupied by the target. As stressed in [1, 4, 5], these sideband responses cannot be suppressed by the weighting methods because they are target generated. It is clear, as a result of the effect, the nonlinear PM violates the resolution theory of point targets.

It may be noted that target recognition in SAR imagery is an important application of the nonlinear phenomenon. Previous research has empirically observed that 'nonlinear dynamics' are dependent on the target type and the operating conditions at which the target is imaged [1, 4, 5, 8, 10, 18]. Accordingly, through developing suitable techniques to harness the 'nonlinear dynamics' in complex-valued SAR imagery, relevant target recognition applications are naturally expected to achieve improvement in target discrimination accuracy.

6.4. The SAR Datasets

This study utilizes two single-channel (i.e., HH) and SLC SAR datasets imaged in the Spotlight mode: (1) a ground-truthed scene from the C-band Radarsat-2 (RS-2) imaged in a site located in the former Naval Station Argentia of Newfoundland, Canada [19], and (2) a comprehensive public-domain dataset collected and distributed under the DARPA moving and stationary target recognition (MSTAR) program, and acquired by an X-band STARLOS sensor [20]. The RS-2 scene offers a nominal spatial resolution of 1.6×0.8 metres in range and azimuth, respectively [21]. The targets of interest considered in this study are six construction vehicles. Ground-truthing (see Fig. 6.1) was conducted by C-CORE[2]. The RS-2 scene is mainly used to demonstrate

[1]Note that smearing also occurs due to the variable Doppler processing used for motion compensation.

[2]http://www.c-core.ca/

the population distribution for the characterized phase image (i.e., in Sect. 6.5).

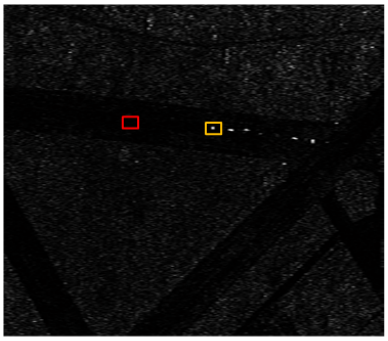

(a) Contrast-enhanced and magnitude-detected image. The red and orange rectangles respectively represent the target-free (RS-2 TF) and the target chip (RS-2 T1) utilized in Table 6.2 .

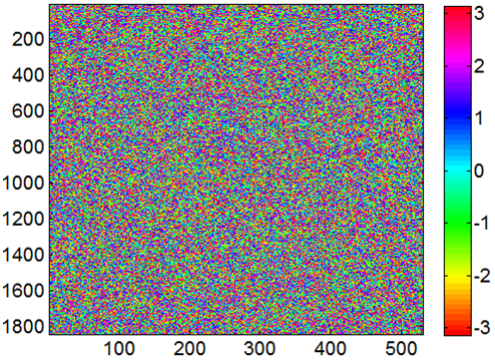

(b) Phase image.

(c) Ground-truth image (right to left: 2 pickup trucks, 2 dump trucks, 1 loader, 1 dump truck).

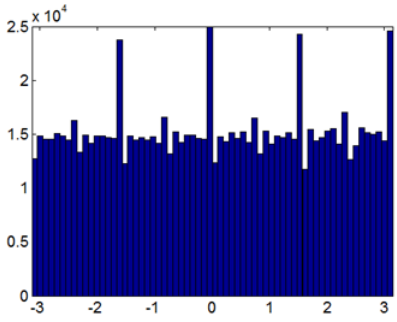

(d) Histogram for the phase image in (b).

Figure 6.1: Spotlight RS-2 SLC image for a site in the former Naval Station Argentia [19] in Newfoundland, Canada. Ground-truth image was provided by C-CORE. RS-2 Data and Products © MacDonald, Dettwiler and Associates Ltd. (2011)

The MSTAR dataset provides a nominal spatial resolution of 0.3047×0.3047 metres in range and azimuth. The dataset used in this study comes from two CDs available from the Sensor and Data Management System (SDMS) and entitled MSTAR/IU Mixed Targets CD1 and CD2. In total, for each CD there are eight different types of stationary (extended) targets imaged at azimuth angles covering the full span of

[0°, 360°). CD1 and CD2 include SAR data collected at 15° and 17° depression angles, respectively. In this chapter, the 17° and 15° datasets, respectively, are used for training and testing the classifier. A list for the target names and the overall number of the complex-valued chips used in this study is provided in Table 6.1. Ground-truth pictures for the eight MSTAR targets are depicted in Fig. 6.2. An example for a chip pertaining to target T-62 is provided in Fig. 6.3. Fig. 6.1d and Fig. 6.3c serve to demonstrate the shape of the histograms for the phase chip prior to characterization (see Sect. 6.5).

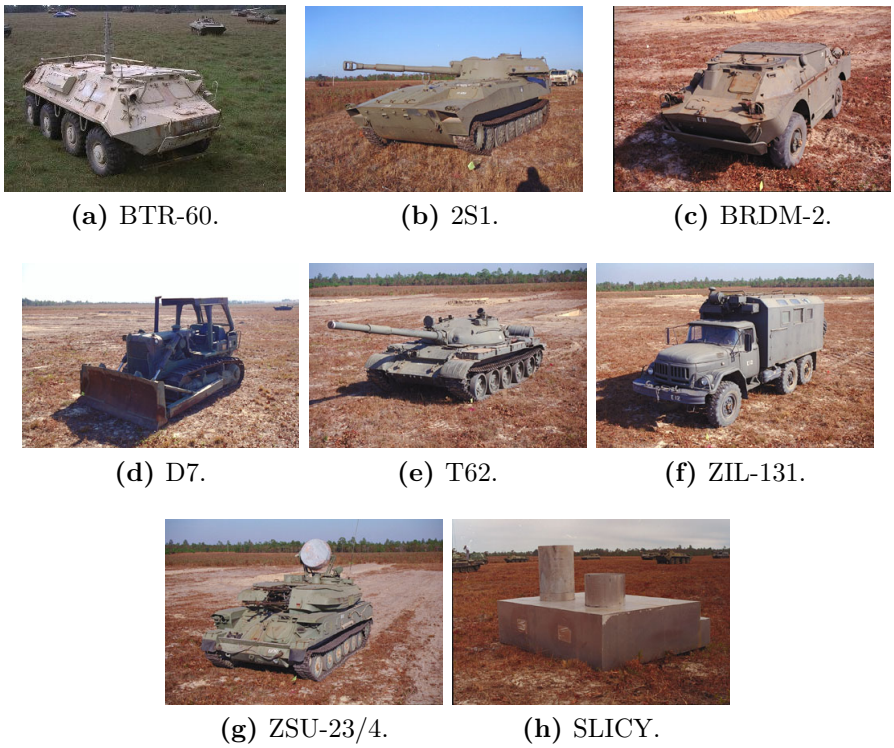

(a) BTR-60. **(b)** 2S1. **(c)** BRDM-2.

(d) D7. **(e)** T62. **(f)** ZIL-131.

(g) ZSU-23/4. **(h)** SLICY.

Figure 6.2: Ground-truth pictures for the MSTAR targets used in this study [20].

Table 6.1: List of the MSTAR targets used in this study.

Target Name	No. of Training Chips (17^o depression angle)	No. of Testing Chips (15^o depression angle)
BTR-60	256	195
2S1	299	274
BRDM-2	298	274
D7	299	274
T62	299	273
ZIL-131	299	274
ZSU-23/4	299	274
SLICY	298	274

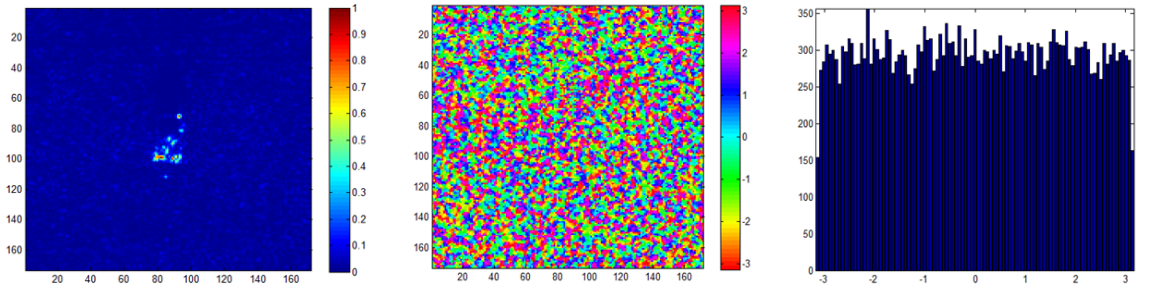

(a) Magnitude-detected chip. **(b)** Phase chip. **(c)** Histogram for the phase chip in (b).

Figure 6.3: Images for an MSTAR chip of target T-62 (Tank HB15206.016). Azimuth angle for this target is 5.515511^o. In this chapter, this chip is referred to as MSTAR T1.

6.5. Phase Characterization: Backscatter Relative Phase Image (BRPI)

This section is comprised of three parts. An algorithm for phase characterization in single-channel complex-valued SAR imagery is proposed in Sect. 6.5.1. Measures for circularity and noncircularity are introduced in Sect. 6.5.2. Illustrative results are provided in Sect. 6.5.3.

6.5.1. A Novel Algorithm for Phase Characterization

The complex-valued SAR chip is available in the form

$$c\left(u,v\right)=i\left(x,y\right)+j\,q\left(x,y\right), \tag{6.5}$$

where $i\left(x,y\right)$ and $q\left(x,y\right)$ are the real and imaginary parts of the complex-valued SAR chip, respectively. Note that (x,y) represent the 2-D Cartesian coordinates of the real-valued plane, while (u,v) represent the 2-D Cartesian coordinates in the complex-valued plane. Hence, the phase chip is given by

$$\Phi\left(x,y\right)=\arg\left\{c\left(u,v\right)\right\}. \tag{6.6}$$

The phase chip $\Phi\left(x,y\right)$ should be properly processed in order to make sense of the information content it carries. This is because, by definition, the phase is relative and it often appears meaningless if it is not appropriately characterized. Accordingly, a simple algorithm is proposed to compute the so-called backscatter relative phase image (BRPI). Then, a histogram can be produced based on the BRPI image. The proposed algorithm is depicted in Fig. 6.4.

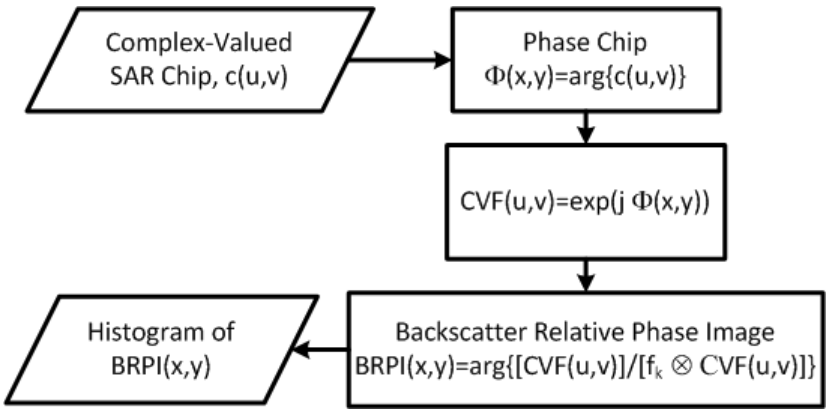

Figure 6.4: Proposed algorithm for phase characterization in single-channel complex-valued SAR imagery.

$$\begin{bmatrix} 1 & 1 & 1 \\ 1 & 0 & 1 \\ 1 & 1 & 1 \end{bmatrix}$$ **(a)** Kernel *a*.

$$\begin{bmatrix} 0 & 1 & 0 \\ 1 & 0 & 1 \\ 0 & 1 & 0 \end{bmatrix}$$ **(b)** Kernel *b*.

$$\begin{bmatrix} 0 & 0 & 0 \\ 1 & 0 & 1 \\ 0 & 0 & 0 \end{bmatrix}$$ **(c)** Kernel *c*.

$$\begin{bmatrix} 0 & 1 & 0 \\ 0 & 0 & 0 \\ 0 & 1 & 0 \end{bmatrix}$$ **(d)** Kernel *d*.

$$\begin{bmatrix} 1 & 0 & 1 \\ 0 & 0 & 0 \\ 1 & 0 & 1 \end{bmatrix}$$ **(e)** Kernel *e*.

$$\begin{bmatrix} 0 & 0 & 1 \\ 0 & 0 & 0 \\ 1 & 0 & 0 \end{bmatrix}$$ **(f)** Kernel *f*.

$$\begin{bmatrix} 1 & 0 & 0 \\ 0 & 0 & 0 \\ 0 & 0 & 1 \end{bmatrix}$$ **(g)** Kernel *g*.

$$\begin{bmatrix} 0 & 0 & 0 \\ 0 & 0 & 1 \\ 0 & 0 & 0 \end{bmatrix}$$ **(h)** Kernel *h*.

$$\begin{bmatrix} 0 & 0 & 0 \\ 1 & 0 & 0 \\ 0 & 0 & 0 \end{bmatrix}$$ **(i)** Kernel *i*.

$$\begin{bmatrix} 0 & 0 & 1 \\ 0 & 0 & 0 \\ 0 & 0 & 0 \end{bmatrix}$$ **(j)** Kernel *j*.

$$\begin{bmatrix} 0 & 0 & 0 \\ 0 & 0 & 0 \\ 0 & 1 & 0 \end{bmatrix}$$ **(k)** Kernel *k*.

$$\begin{bmatrix} 1 & 1 & 1 & 1 & 1 \\ 1 & 1 & 1 & 1 & 1 \\ 1 & 1 & 0 & 1 & 1 \\ 1 & 1 & 1 & 1 & 1 \\ 1 & 1 & 1 & 1 & 1 \end{bmatrix}$$ **(l)** Kernel *l*.

$$\begin{bmatrix} 1 & 1 & 1 & 1 & 1 & 1 & 1 \\ 1 & 1 & 1 & 1 & 1 & 1 & 1 \\ 1 & 1 & 1 & 1 & 1 & 1 & 1 \\ 1 & 1 & 1 & 0 & 1 & 1 & 1 \\ 1 & 1 & 1 & 1 & 1 & 1 & 1 \\ 1 & 1 & 1 & 1 & 1 & 1 & 1 \\ 1 & 1 & 1 & 1 & 1 & 1 & 1 \end{bmatrix}$$ **(m)** Kernel *m*.

Figure 6.5: Examples of the convolution kernel f_k tested in this chapter.

Phase values are in the range $(-\pi, \pi]$. The phase chip should be first converted to the polar form as

$$CVF(u,v) = \exp(j\Phi(x,y)) = \cos\{\Phi(x,y)\} + j\sin\{\Phi(x,y)\}. \tag{6.7}$$

The main advantage of the polar representation is that it offers a unique means for handling the phase wrapping typically encountered in linear statistics. This idea is borrowed from the field of directional statistics [3][14–16]. $CVF(u,v)$ has a size $M_c \times N_c$. The neighborhood-processed phase image is obtained through convolving $CVF(u,v)$ with a kernel f_k. The kernel should have a value of zero in the center and ones where desired. The kernel convolution operation produces an average phase image for the neighborhood of each pixel in the phase chip. Examples of selected kernels tested in

[3]Directional statistics are also known as circular statistics. The name circular stems from the fact that the phase values are on a circle where the angles π and $-\pi$ meet at the same point. In directional statistics, 'phase wrapping' is also called 'phase circularity'. This is not to be confused with circularity/noncircularity discussed later in this chapter.

this chapter are depicted in Fig. 6.5. The convolution kernel f_k has a size $M_k \times N_k$. M_k and N_k are typically chosen to be odd values to avoid ambiguity in defining the center pixel. Convolving $CVF\,(u,v)$ with the kernel f_k at a particular pixel location in the image (m_c, n_c) yields the following convolution image

$$CI\,(m_c,n_c) = f_k \otimes CVF\,(m_c,n_c) = \sum_{m_k=1}^{M_k}\sum_{n_k=1}^{N_k} f_k\,(m_k,n_k)\;CVF\,(m_c-m_k,n_c-n_k)\,, \tag{6.8}$$

where $m_c \in \{1,2,...,M_c\}$ and $n_c \in \{1,2,...,N_c\}$. The BRPI image is defined as

$$BRPI\,(x,y) = \arg\left\{\frac{CVF\,(u,v)}{CI\,(u,v)}\right\}. \tag{6.9}$$

The resultant BRPI image defines the characteristic phase of each pixel in the input phase image $\Phi\,(x,y)$ relative to its neighborhood, defined by the convolution kernel f_k.

6.5.2. Circularity vs. Noncircularity

From the perspective of complex-valued statistics, the practice of discarding the phase may be justified by the implicit assumption that the underlying random variables are second-order circular (also known as proper) in nature [11–13]. The assumption of circularity means that the complex-valued SAR chip has a PDF that is invariant under rotation in the complex plane. This also implies that the complex-valued SAR chip is uncorrelated with its complex-conjugate. Accordingly, discarding the phase content implicitly implies that the aforementioned assumptions are satisfied. Otherwise, valuable information about the targets in the complex-valued image is lost. This information is important for target recognition applications.

Formally, a zero-mean complex-valued random variable (i.e., $X = X_R + jX_I$) is said to be second-order circular, or proper, when its pseudo-covariance is zero [11]. That

is,

$$\Psi = E\left\{X^2\right\} = 0. \tag{6.10}$$

This means,

$$\sigma_{X_R} = \sigma_{X_I}, \text{ and } E\left\{X_R X_I\right\} = 0. \tag{6.11}$$

where σ_{X_R} and σ_{X_I} are the standard deviations of the real and imaginary parts of X, respectively.

For a random vector $\mathbf{X}$, circularity implies that [11, 12]

$$E\left\{\mathbf{X}_R \mathbf{X}_R^T\right\} = E\left\{\mathbf{X}_I \mathbf{X}_I^T\right\}, \tag{6.12}$$

and

$$E\left\{\mathbf{X}_R \mathbf{X}_I^T\right\} = -E\left\{\mathbf{X}_I \mathbf{X}_R^T\right\}, \tag{6.13}$$

where $\mathbf{X}_R$ and $\mathbf{X}_I$ are the real and imaginary parts of $\mathbf{X}$, respectively; $E\{\cdot\}$ is the expectation; and T denotes the transpose.

A stronger condition for circularity is based on the PDF of the random variable. A random variable X is circular if X and $X\exp(j\Phi)$ have the same PDF (i.e., the PDF is rotation invariant) [13]. This implicitly means that the phase of the complex-valued random variable is non-informative; hence, the PDF is a function of only the magnitude which implies that the PDF can be written as a function of XX^* rather than X and X^*, separately, where * denotes the complex conjugate. Since the phase is non-informative for a circular random variable, a real-valued approach and complex-valued approach for this case are equivalent [11, 12].

In this chapter, a combination of two methods [11, 12] is applied to detect and characterize the circularity/noncircularity in complex-valued single-channel SAR imagery. In the first method, a hypothesis test is adopted to examine the circularity/noncircularity (i.e., alternative hypothesis $\mathcal{H}_{1,NC}$ is for noncircularity) in the complex-valued SAR chip. This test employs a generalized likelihood ratio test (GLRT) based on the complex generalized Gaussian distribution (CGGD) at a specific detection threshold defined by the probability of false alarm (PFA) [12]. CGGD is a bivariate GGD model that utilizes the so-called augmented representation [13] of the complex-valued random variables, and it offers an excellent fit for the SAR data used in this study [9] (see Fig. 6.8).

In the second method, the strength of noncircularity in the complex-valued SAR chip is quantified using the modulus of the pseudo-covariance [11, 12]

$$|\Psi| = \left| E\left\{X^2\right\} \right|, \; 0 < |\Psi| < 1. \tag{6.14}$$

Note that the greater $|\Psi|$, the higher the noncircularity effect. Furthermore, the angle of Ψ is used in this study as a feature. It is defined by

$$\angle\Psi = \arg\left\{\Psi\right\}. \tag{6.15}$$

The foregoing two methods are applied to both the original phase chip (i.e., $\Phi\left(x, y\right)$) as well as to the BRPI image given by Eq. 6.9. Thus, the random variable X is substituted with the polar representations for the phase chip and the BRPI image, after they are converted to a 1-D vector.

6.5.3. Results

This subsection demonstrates the applicability of the proposed phase characterization method. Firstly, in order to gain an insight into the shape of the histograms produced by the different kernels in Fig. 6.5, the proposed method is applied to the whole phase image in Fig. 6.1b. The output result for the thirteen kernels considered is depicted in Fig. 6.6. This output represents the statistical distribution for the population. Next,

the phase characterization method is applied to the phase chip for target T-62 from the MSTAR dataset shown in Fig. 6.3b. The corresponding output result is given in Fig. 6.7.

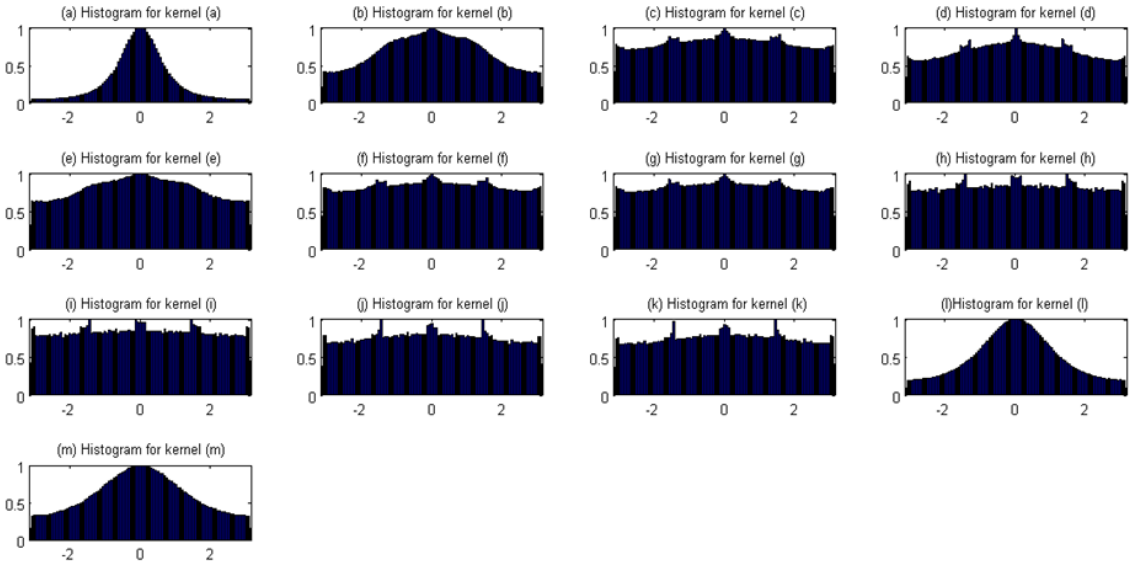

Figure 6.6: Normalized BRPI histograms (population distribution) pertaining to the RS-2 image in Fig. 6.1b, and for all the kernels in Fig. 6.5. The abscissa denotes the angles $[-\pi, \pi]$ in radians.

Based on these results, it is evident that the proposed method properly characterizes the phase content in SAR imagery. This can be easily inferred through comparing the output results in Fig. 6.6 and Fig. 6.7, respectively, with the original histograms in Fig. 6.1d and Fig. 6.3c. It is obvious that kernels a, l and m produce histograms that look consistent with typical statistical distributions. Hence, these three kernels are considered for all the subsequent analysis while the other kernels are discarded.

To further demonstrate the advantage of the proposed method, the two tests for circularity/noncircularity (see Sect. 6.5.2) are applied to a selection of three phase chips both before and after phase characterization. The first and second phase chips are for the target-free (TF) and the first target (T1) chips, respectively, taken from the RS-2 image in Fig. 6.1a and Fig. 6.1b. The third phase chip is for the MSTAR target T-62 (i.e., MSTAR T1) in Fig. 6.3b. The overall analysis results are given in Table 6.2.

These results suggest that the phase for extended targets in SAR imagery is noncircular in nature. However, in order to reveal the noncircularity, the phase chip should be

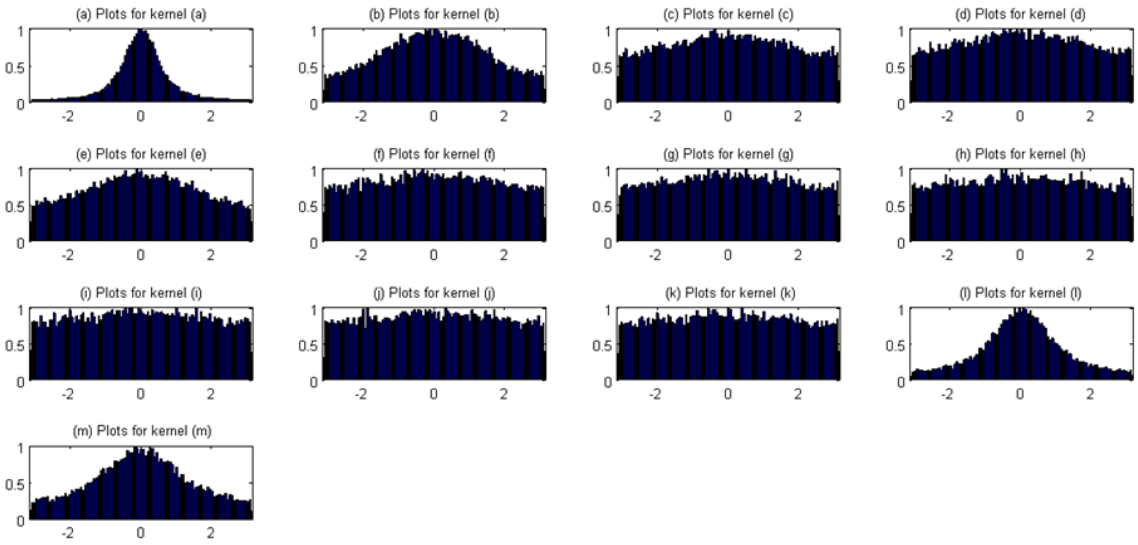

Figure 6.7: Normalized BRPI histograms pertaining to the MSTAR phase chip in Fig. 6.3b, for all the kernels in Fig. 6.5. The abscissa denotes the angles $[-\pi, \pi]$ in radians.

processed using the proposed method. Note that the RS-2 TF phase chip considered is circular (i.e., $|\Psi| \approx 0$ and $\mathcal{H}_{1,NC} = 0$). Furthermore, the RS-2 T1 phase chip possess minimum noncircularity as suggested by $|\Psi|$. This is expected since RS-2 T1 is closer to being a point-target. However, for the MSTAR T1 phase chip, the noncircularity is more pronounced. This implies that the noncircularity measure i.e., $|\Psi|$, may serve as a useful feature, for example, in target classification applications. The statistical significance of the noncircularity in the MSTAR dataset is investigated later in this chapter (see Sect. 6.7).

6.6. Statistical Phase Modeling

An important aspect of statistical analysis is probability modeling. If the BRPI histogram can be fit to a particular probability model through a suitable process of parameter estimation, then the phase information can be efficiently abstracted. In Sect. 6.6.1.1, a novel statistical model for the BRPI image is introduced. In Sect. 6.6.2, two relevant circular models, used for comparison purposes, are overviewed. Finally, the applicability of the proposed model is demonstrated in Sect. 6.6.3.

Table 6.2: Results for the investigation into circularity/noncircularity of the phase in single-channel SAR imagery. PFA=0.0001.

		RS-2 TF	RS-2 T1	MSTAR T1
Target Type		Target-Free	Point	Extended
Shape parameter for CGGD ($\hat{c}$)		1	1	0.2
Without preprocessing	Noncircularity $(\mathcal{H}_{1,NC})$	0	0	0
	$\lvert\Psi\rvert$	0.0054	0.0097	0.0129
Preprocessing with kernel a	Noncircularity $(\mathcal{H}_{1,NC})$	0	0	1
	$\lvert\Psi\rvert$	0.0055	0.0146	0.4683
Preprocessing with kernel l	Noncircularity $(\mathcal{H}_{1,NC})$	0	0	1
	$\lvert\Psi\rvert$	0.0022	0.0094	0.1908
Preprocessing with kernel m	Noncircularity $(\mathcal{H}_{1,NC})$	0	0	1
	$\lvert\Psi\rvert$	0.0043	0.0062	0.0817

6.6.1. A Novel Statistical Model for the BRPI Image

6.6.1.1. Motivations

Envelopes for the histograms of the real and the imaginary parts pertaining to the MSTAR chip in Fig. 6.3 are depicted by red dashed lines in Fig. 6.8. It is obvious that these histograms follow a peaky and heavy-tailed non-Gaussian distribution (see [8–10] for more details). These characteristics can be well-modeled using the generalized Gaussian distribution (GGD) [22]. The GGD distribution adapts to a large family of symmetric distributions, from super-Gaussian to sub-Gaussian with specific densities such as Laplacian and Gaussian distributions [23]. These histograms are fitted with the GGD PDF. Fitting was done using the maximum likelihood estimator (MLE) [24, 25]. The fitting results are superimposed on the histograms in Fig. 6.8.

The normalized Jensen-Shannon divergence (JSD_N) between the histogram and the GGD PDF (see Eq. E.6 in Appendix E) for the real and the imaginary parts, respectively, are 0.0059 and 0.0083. Note that the smaller the JSD_N measure is, the better the fit. This goodness-of-fit is confirmed for various examples extracted from the MSTAR dataset. It is well-known that the GGD distribution is a special case of the more generic Gaussian scale mixture (GSM) [26]. A major advantage of the GSM

model, besides its relative generality, is that it naturally accounts for correlations between the neighboring pixels which are not accounted for in the GGD model. Thus, the complex GSM (CGSM) distribution is proposed to model the BRPI histogram. The relevance of this choice is demonstrated below.

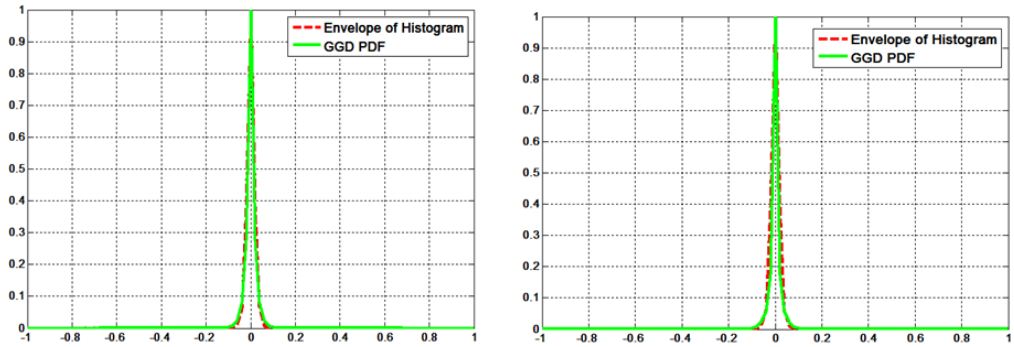

(a) Real-part. **(b)** Imaginary-part.

Figure 6.8: Normalized histograms and GGD PDFs for the real and imaginary parts of the MSTAR chip in Fig. 6.3.

6.6.1.2. Modeling the Complex-Valued SAR Image (i.e., $c(u, v)$) Using CGSM

Consider the complex-valued SAR image represented by a complex random vector $z_C = x_C + jy_C$ (i.e., this is the 1-D representation of $c(u, v)$ in Eq. 6.5). This vector can be characterized by a CGSM model. The CGSM model is the product of a complex Gaussian random vector (i.e., $u_C = u_{C,R} + ju_{C,I}$) and an independent hidden scalar multiplier (i.e., γ_C). The neighboring pixels in the complex-valued SAR image are indirectly linked by their shared dependency on the hidden multiplier. Hence, the CGSM model can efficiently account for the correlation between neighboring pixels in the complex-valued SAR image. Following the CGSM model, the real and imaginary parts of the complex valued random vector can be described as follows [26, 27]

$$z_C = x_C + jy_C = \sqrt{\gamma_C}u_{C,R} + j\sqrt{\gamma_C}u_{C,I} = \sqrt{\gamma_C}u_C. \tag{6.16}$$

Since the distribution of the real-part (i.e., x_C) is GSM, the conditional probability $p(x_C|\gamma_C)$ is Gaussian. Similarly, since the distribution of the imaginary-part (i.e., y_C) is

GSM, $p(y_C|\gamma_C)$ is also Gaussian. Accordingly, when it is conditioned on the multiplier γ_C, the distribution of the complex-valued random vector (i.e., z_C) is complex Gaussian and [26–28]

$$p\left(z_C|\gamma_C\right) = \frac{\exp\left(-z_C^H C_{z_C|\gamma_C}^{-1} z_C\right)}{\pi \det\left(C_{z_C|\gamma_C}\right)}, \tag{6.17}$$

where $C_{z_C|\gamma_C} = \gamma_C C_{u_C}$ is the complex covariance matrix for z_C, $C_{u_C} = E\left[u_C\, u_C^H\right]$ is the zero-mean (see Fig. 6.8) complex covariance matrix for u_C, and the dimensionality of z_C and u_C is $N = 1$ in this case; and H implies complex conjugate transposition. Based on the definition of the CGSM model, u_C is complex-Gaussian, and the scalar real parameter $\sqrt{\gamma_C}$ has some distribution on $(0, \infty)$ with a PDF $p(\gamma_C)$ where $\gamma_C > 0$ (see [28] for the PDF of γ_C). Subsequently, z_C can be modeled with CGSM as [27, 28]

$$p\left(z_C\right) = \int \frac{\exp\left(-z_C^H C_{z_C|\gamma_C}^{-1} z_C\right)}{\pi \det\left(C_{z_C|\gamma_C}\right)} p(\gamma_C)\, \mathrm{d}\gamma_C. \tag{6.18}$$

6.6.1.3. Modeling the Average Phase Image (i.e., $CI\,(u, v)$) using CGSM

Given the wide range of distribution families encompassed by the CGSM model, it is assumed that the complex-valued average phase image (i.e., $CI\,(u, v)$ in Eq. 6.8) can be modeled using the CGSM model. By analogy with the earlier description, the 1-D representation for $CI\,(u, v)$ is given by

$$z_{CI} = x_{CI} + j y_{CI} = \sqrt{\gamma_{CI}} u_{CI,R} + j\sqrt{\gamma_{CI}} u_{CI,I} = \sqrt{\gamma_{CI}} u_{CI}, \tag{6.19}$$

and,

$$p\left(z_{CI}\right) = \int \frac{\exp\left(-z_{CI}^H C_{z_{CI}|\gamma_{CI}}^{-1} z_{CI}\right)}{\pi \det\left(C_{z_{CI}|\gamma_{CI}}\right)} p(\gamma_{CI}) \mathrm{d}\gamma_{CI}. \tag{6.20}$$

Note that this model is assumed to hold for the three convolution kernels a, l and m of Fig. 6.5.

6.6.1.4. Joint Distribution of $c(u,v)$ and $CI(u,v)$

Given that z_C and z_{CI} are modeled using CGSM, it is assumed that their joint distribution is also CGSM (i.e., $BRPI\,(x,y)$ in Eq. 6.9). Accordingly, $z_{brpi} = [z_C\, z_{CI}]^T$ can be modeled as

$$p\left(z_C, z_{CI}|\gamma_{brpi}\right) = \frac{\exp\left(-z_{brpi}^H C_{z_{brpi}|\gamma_{brpi}}^{-1} z_{brpi}\right)}{\pi^2 \det\left(C_{z_{brpi}|\gamma_{brpi}}\right)}. \tag{6.21}$$

Note that the vector dimension, N is 2 in this case. Equivalently, this can be written in polar form as [29]

$$p\left(r_C, r_{CI}, \Phi_C, \Phi_{CI}|\gamma_{brpi}\right) = \pi^{-2} \det\left(C_{z_{brpi}|\gamma_{brpi}}^{-1}\right) r_C r_{CI} \exp\left(-z_{brpi}^H C_{z_{brpi}|\gamma_{brpi}}^{-1} z_{brpi}\right). \tag{6.22}$$

The complex-valued random variables in Eq. 6.22 have a zero-mean (see Fig. 6.8) and their joint covariance matrix is defined as

$$C_{z_{brpi}|\gamma_{brpi}} = E\left[z_{brpi}, z_{brpi}^H|\gamma_{brpi}\right] = \gamma_{brpi} \begin{bmatrix} \rho_{11} & \rho_{12} \\ \rho_{12}^* & \rho_{22} \end{bmatrix}. \tag{6.23}$$

This matrix is positive definite Hermitian which implies that its inverse exists as

$$C_{z_{brpi}|\gamma_{brpi}}^{-1} = \frac{1}{\gamma_{brpi}} \begin{bmatrix} \beta_{11} & \beta_{12} \\ \beta_{12}^* & \beta_{22} \end{bmatrix}, \tag{6.24}$$

where

$$\beta_{12} = |\beta_{12}| \exp\left(j\underline{\phi}_{12}\right). \tag{6.25}$$

Subsequently, it can be easily shown that (see [29])

$$\begin{aligned}
&z_{brpi}^{H} C_{z_{brpi}|\gamma_{brpi}}^{-1} z_{brpi} \\
&= \left[\begin{array}{cc} r_C \exp\left(-j\Phi_C\right) & r_{CI} \exp\left(-j\Phi_{CI}\right) \end{array}\right] \left[\begin{array}{cc} |\beta_{11}| & |\beta_{12}| \exp\left(j\underline{\phi}_{12}\right) \\ |\beta_{12}| \exp\left(-j\underline{\phi}_{12}\right) & |\beta_{22}| \end{array}\right] \times \\
&\left[\begin{array}{c} r_C \exp\left(j\Phi_C\right) \\ r_{CI} \exp\left(j\Phi_{CI}\right) \end{array}\right] = r_C^2 |\beta_{11}+| r_{CI}^2 |\beta_{22}| + 2 r_C r_{CI} |\beta_{12}| \cos\left(\Phi_C - \Phi_{CI} - \underline{\phi}_{12}\right).
\end{aligned} \tag{6.26}$$

Substituting Eq. 6.26 into Eq. 6.22 and integrating-out r_C and r_{CI} yields (see p. 557 in [29])

$$\begin{aligned}
&p\left(\Phi_C, \Phi_{CI} | \gamma_{brpi}\right) \\
&= \pi^{-2} \det\left(C_{z_{brpi}|\gamma_{brpi}}^{-1}\right) \int_{r_{CI}=0}^{\infty} \int_{r_C=0}^{\infty} r_C r_{CI} \exp(-r_C^2 |\beta_{11}-| r_{CI}^2 |\beta_{22}| \\
&- 2 r_C r_{CI} |\beta_{12}| \cos(\Phi_C - \Phi_{CI} - \underline{\phi}_{12})) \mathrm{d}r_C \mathrm{d}r_{CI} \\
&= \left(8\pi^2 |\beta_{11}| |\beta_{12}|\right)^{-1} \det\left(C_{z_{brpi}|\gamma_{brpi}}^{-1}\right) \frac{\partial^2}{\partial c^2} \arccos^2(\chi),
\end{aligned} \tag{6.27}$$

where

$$\frac{\det\left(C_{z_{brpi}|\gamma_{brpi}}^{-1}\right)}{|\beta_{11}| |\beta_{12}|} = 1 - \frac{|\beta_{12}|^2}{|\beta_{11}| |\beta_{22}|} = 1 - \lambda_{12}^2, \tag{6.28}$$

where λ_{12}^2 is the correlation coefficient which may be observed to be independent of

γ_{brpi} (see Eq. 6.23 and Eq. 6.24) since

$$\lambda_{12}^2 = \frac{\left|\frac{1}{\gamma_{brpi}}\beta_{12}\right|^2}{\left|\frac{1}{\gamma_{brpi}}\beta_{11}\right|\left|\frac{1}{\gamma_{brpi}}\beta_{22}\right|} = \frac{\left|\gamma_{brpi}\rho_{12}\right|^2}{\left|\gamma_{brpi}\rho_{11}\right|\left|\gamma_{brpi}\rho_{22}\right|} = \frac{\left|\rho_{12}\right|^2}{\left|\rho_{11}\right|\left|\rho_{22}\right|}. \tag{6.29}$$

Also, in Eq. 6.27 χ is given by

$$\chi = \lambda_{12}\cos\left(\Phi_C - \Phi_{CI} - \underline{\phi}_{12} + \pi\right). \tag{6.30}$$

Hence, Eq. 6.27 simplifies to

$$\begin{aligned} p\left(\Phi_C, \Phi_{CI}|\gamma_{brpi}\right) = \frac{1-\lambda_{12}^2}{8\pi^2}\frac{\partial^2}{\partial C^2}\arccos^2\left(\chi\right) = \frac{1-\lambda_{12}^2}{8\pi^2}\times 2\left(\frac{\chi\arccos\left(\chi\right)}{\left(1-\chi^2\right)^{1.5}} + \frac{1}{1-\chi^2}\right) \\ = \frac{1-\lambda_{12}^2}{4\pi^2\left(1-\chi^2\right)}\left(\frac{\chi\arccos\left(\chi\right)}{\left(1-\chi^2\right)^{0.5}} + 1\right). \end{aligned} \tag{6.31}$$

Noting that, according to Eq. 6.29 and Eq. 6.30, both λ_{12} and χ are independent on γ_{brpi},

$$p\left(\Phi_C, \Phi_{CI}|\gamma_{brpi}\right) \equiv \frac{p\left(\Phi_C, \Phi_{CI}\right)p\left(\gamma_{brpi}\right)}{p\left(\gamma_{brpi}\right)} = p\left(\Phi_C, \Phi_{CI}\right). \tag{6.32}$$

Thus, from Eq. 6.31 and Eq. 6.32,

$$p\left(\Phi_C, \Phi_{CI}\right) = \frac{1-\lambda_{12}^2}{4\pi^2\left(1-\chi^2\right)}\left(\frac{\chi\arccos\left(\chi\right)}{\left(1-\chi^2\right)^{0.5}} + 1\right). \tag{6.33}$$

The interest here is in modeling the distribution of the BRPI image (i.e., Φ_{brpi}) where

$$\Phi_{brpi} = \Phi_C - \Phi_{CI}. \tag{6.34}$$

Thus, from Eq. 6.30

$$c = \lambda_{12} \cos\left(\Phi_{brpi} - \underline{\phi}_{12} + \pi\right), \tag{6.35}$$

and, Eq. 6.33 becomes

$$p\left(\Phi_{brpi} + \Phi_{CI}, \Phi_{CI}\right) = \frac{1 - \lambda_{12}^2}{4\pi^2 \left(1 - \chi^2\right)} \left(\frac{\chi \arccos\left(\chi\right)}{\left(1 - \chi^2\right)^{0.5}} + 1\right). \tag{6.36}$$

Subsequently, Φ_{CI} can be integrated-out to obtain $p\left(\Phi_{brpi}\right)$ as follows

$$p\left(\Phi_{brpi}\right) = \int_{-\pi}^{\pi} \frac{1 - \lambda_{12}^2}{4\pi^2 \left(1 - \chi^2\right)} \left(\frac{\chi \arccos\left(\chi\right)}{\left(1 - \chi^2\right)^{0.5}} + 1\right) \mathrm{d}\Phi_{CI}. \tag{6.37}$$

Hence,

$$p\left(\Phi_{brpi}\right) = \frac{1 - \lambda_{12}^2}{2\pi \left(1 - \chi^2\right)} \left(\frac{\chi \arccos\left(\chi\right)}{\left(1 - \chi^2\right)^{0.5}} + 1\right). \tag{6.38}$$

The BRPI model derived in Eq. 6.38 is characterized by the location parameter $\underline{\phi} \in [-\pi, \pi]$ and the shape parameter $\lambda \in [0, 1)$ where the subscript 12 is dropped for notational simplicity. This model is referred to as the wrapped CGSM (i.e., $WCGSM\left(\underline{\phi}, \lambda\right)$). It is noted that this model resembles that reported in [30] which is used for modeling the 1-D complex-valued wavelet coefficients. Fig. 6.9 depicts the $WCGSM\left(\underline{\phi}, \lambda\right)$ PDF for two values of $\underline{\phi}$ and various values of λ. Given that this phase model is derived based on the CGSM distribution, it is straightforward to conclude that it encompasses multiple circular distributions such as the von Mises (vM) and wrapped Cauchy (WC) as special cases. This is explored in Sect. 6.6.3.

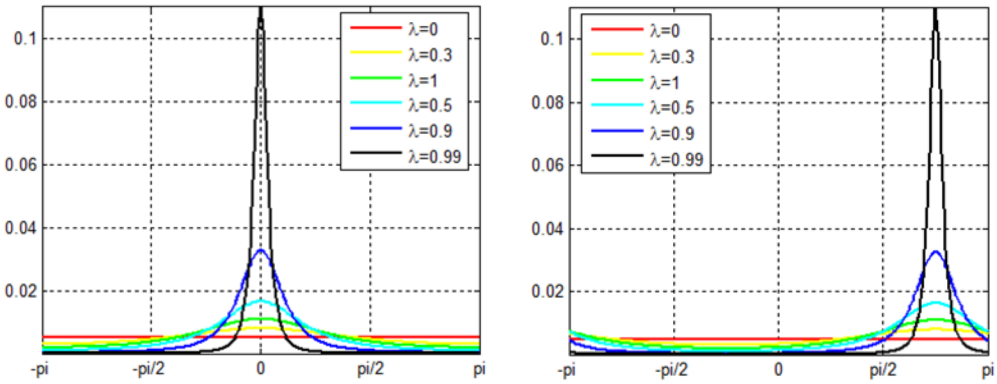

(a) WCGSM PDF for $\underline{\phi} = 0$. **(b)** WCGSM for $\underline{\phi} = 0.75\pi$.

Figure 6.9: PDFs for the WCGSM distribution at different values of λ.

6.6.1.5. Parameter Estimation for $WCGSM\left(\underline{\phi}, \lambda\right)$

The WCGSM distribution, characterized by two parameters, is given by

$$WCGSM\left(\underline{\phi}, \lambda\right) \equiv p\left(\Phi_{brpi}\right) = \frac{1-\lambda^2}{2\pi\left(1-\chi^2\right)}\left(\frac{\chi \arccos\left(\chi\right)}{\left(1-\chi^2\right)^{0.5}} + 1\right), \tag{6.39}$$

where,

$$\chi = \lambda \cos\left(\Phi_{brpi} - \underline{\phi} + \pi\right). \tag{6.40}$$

In [30], the MLE approach for estimating the parameters of a similar PDF was investigated, and it was concluded that no closed-form solution exists. Subsequently, an iterative procedure using the Newton-Raphson method was used. In this work, it is proposed to estimate the parameters of the WCGSM model as follows. Firstly, $\underline{\phi}$ is the location parameter, and it has been empirically observed that it can be accurately estimated using the circular mean of the BRPI image which is defined as [14]

$$\hat{\underline{\phi}} = \arg\left(\frac{1}{n}\sum_{i=1}^{n}\exp\left(j\Phi_{brpi,i}\right)\right), \tag{6.41}$$

where n is the total number of samples in the BRPI image. Secondly, it is proposed to utilize a simple numerical procedure based on the Jensen–Shannon divergence (JSD, see Appendix E) to estimate the shape parameter (i.e., λ) [31, 32]. This proposed procedure may be summarized as follows:

1. Convert the BRPI image (i.e., Φ_{brpi}) to a 1-D vector; this vector has a length of n.
2. Calculate $\hat{\underline{\phi}}$ based on Eq. 6.41.
3. Produce a histogram (i.e., h) based on the 1-D BRPI vector, and normalize it (i.e., $h_{Norm} = \frac{h}{\text{sum}(h)}$).
4. Define the desired range of λ (i.e., $lambdas \in [\lambda_{min}, \lambda_{max}] = [0, 1)$), and iterate as follows:
   - $i = 1$;
   - $lambdas\,(1) = 0$;
   - `while` $lambdas(i) < 1$
     - Produce the PDF for WCGSM model and normalize it as
       - $p\,(i) = \frac{WCGSM\left(\hat{\phi}, lambdas(i)\right)}{\text{sum}\left(WCGSM\left(\hat{\phi}, lambdas(i)\right)\right)}$;
     - Calculate the JS divergence between h_{Norm} and $p(i)$ as
       - $JS\,(i) = JSD\,(h_{Norm}, p\,(i))$; `%See JSD below`
     - $i = i + 1$;
     - Increment (inc) for iterations. The larger inc the faster will be the algorithm and the smaller inc, the more accurate the estimation result.
       - $inc = 0.00001$;
       - $lambdas(i) = lambdas(i-1) + inc$;
   - `end`
   - $\hat{\lambda} = lambdas(JS == min(JS))$; `%Find the best fit`
5. The JS divergence is calculated based on the following procedure (see Appendix E).

   `function` $JS = JSD(P, Q)$
   - $P = P./sum(P)$;
   - $Q = Q./sum(Q)$;
   - $KL1 = (P. * (log2(P) - log2(Q)))$;

- $KL2 = (Q. * (log2(Q) - log2(P)))$;
- $total = (KL1 + KL2)/2$;
- $total(isnan(total)) = 0$; `%resolving` $P(i) = Q(i) == 0$
- $JS = sum(total)$

`end`

As noted, for accurate estimation of λ, inc should be small, and, in this chapter $inc = 0.00001$ is used for all the calculations.

6.6.2. Relevant Circular Distributions

Two popular circular models, the von Mises (vM) and wrapped Cauchy (WC) are considered in this subsection. The PDFs pertaining to these two distributions are briefly introduced in Sect. 6.6.2.1 and Sect. 6.6.2.2, respectively.

6.6.2.1. von Mises Distribution, $vM\left(\mu_{vM}, \kappa\right)$

The vM distribution is the circular analogue of the Gaussian distribution. It is the most commonly used symmetric unimodal distribution for circular data. The vM distribution is a special case of the von Mises-Fisher distribution on the N-dimensional sphere. The vM PDF for the circular random variable (i.e., the phase, x) is given by [16, 33]

$$vM\left(\mu, \kappa\right) \equiv f\left(x|\mu_{vM}, \kappa\right) = \frac{\exp\left(\kappa \cos\left(x - \mu_{vM}\right)\right)}{2\pi I_o\left(\kappa\right)} \quad \text{where, } -\pi < \mu_{vM} \leq \pi,\ 0 \leq \kappa < \infty, \quad (6.42)$$

and

- $I_o\left(\kappa\right)$ is the modified Bessel function of order 0; $I_o\left(\kappa\right) = \frac{1}{\pi}\int_0^{\pi} \exp\left(\kappa \cos\left(x\right)\right) \mathrm{d}x$.
- μ_{vM} is the circular mean, which is a measure of location analogous to the mean in Gaussian distribution.
- κ is a measure of concentration. It is the reciprocal of dispersion. Note that $1/\kappa$ is analogous to σ^2 in the Gaussian distribution. As $\kappa \Rightarrow 0$, the vM distribution

converges to the uniform distribution. As κ becomes large, the vM distribution approaches the Gaussian distribution. As $\kappa \Rightarrow \infty$, the vM distribution tends to the point distribution concentrated in the direction μ.

The PDFs of the vM distribution for $\mu_{vM} = 0$ and $\mu_{vM} = 0.75\pi$ at different values of κ are depicted in Fig. 6.10a and Fig. 6.10b, respectively. These two parameters of the vM distribution can be estimated in a closed form based on an MLE procedure (see Sect. F.1).

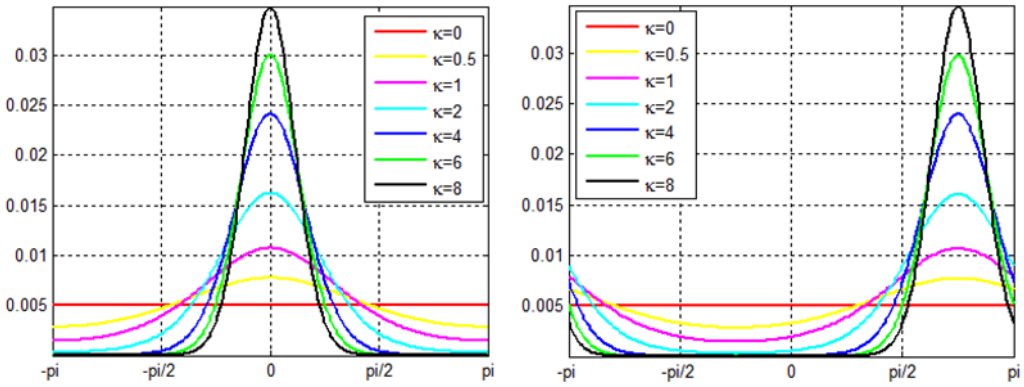

(a) vM PDF for $\mu_{vM} = 0$. **(b)** vM PDF for $\mu_{vM} = 0.75\pi$.

Figure 6.10: vM PDF for two values of μ_{vM} and different values of κ.

6.6.2.2. Wrapped Cauchy (also known as wrapped Lorentzian) Distribution, $WC(\mu_{wc}, \rho)$

The WC distribution is a symmetric unimodal distribution that can be obtained by wrapping the Cauchy distribution (on the line) around the circle. The PDF of the WC distribution is given by [34]

$$WC(\mu_{wc}, \rho) \equiv f(x|\mu, \rho) = \frac{1}{2\pi} \frac{1-\rho^2}{1+\rho^2-2\rho\cos(x-\mu_{wc})}, \quad \text{where } -\pi < \mu_{wc} \leq \pi,\ 0 \leq \rho \leq 1. \quad (6.43)$$

Note that μ_{wc} is the location parameter and ρ is the scale parameter. As $\rho \Rightarrow 0$ the WC distribution converges to the uniform distribution. As $\rho \Rightarrow 1$, the WC distribution tends to the point distribution concentrated in the direction μ_{wc}. The PDFs of the WC distribution for $\mu_{wc} = 0$ and $\mu_{wc} = 0.75\pi$ at different values of ρ are depicted in Fig. 6.11a and Fig. 6.11b, respectively. A summary of the estimation procedure for the two parameters of the WC distribution is provided in Sect. F.2.

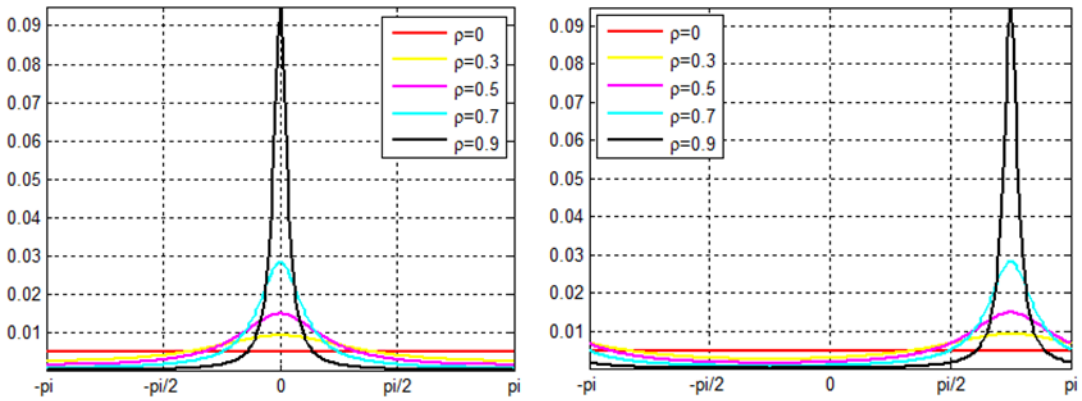

(a) WC PDF for $\mu_{wc} = 0$. **(b)** WC PDF for $\mu_{wc} = 0.75\pi$.

Figure 6.11: WC PDF for two values of μ_{wc} and different values of ρ.

6.6.3. Fitting Results

To demonstrate the applicability of the WCGSM PDF, two phase chips from the MSTAR dataset are considered. The first phase chip, referred to as MSTAR T1, is for target T-62 shown in Fig. 6.3b. The second phase chip, referred to as MSTAR T2, is for target BRDM-2 (see Fig. 6.2). The ID number for this chip is HB15156.001 and the azimuth angle is 103.325272°. For these two chips, the BRPI images for kernels a, l and m of Fig. 6.5 are obtained as described in Sect. 6.5.1. Then, for each BRPI image, the parameters of the WCGSM, vM and WC PDFs, respectively, are computed as described in Sect. 6.6.1 and Sect. 6.6.2. The fitting results pertaining to MSTAR T1 are depicted in Fig. 6.12. The overall fitting results for the two chips along with the goodness-of-fit in terms of JSD_N (see Eq. E.6 in Appendix E) are presented in Table 6.3.

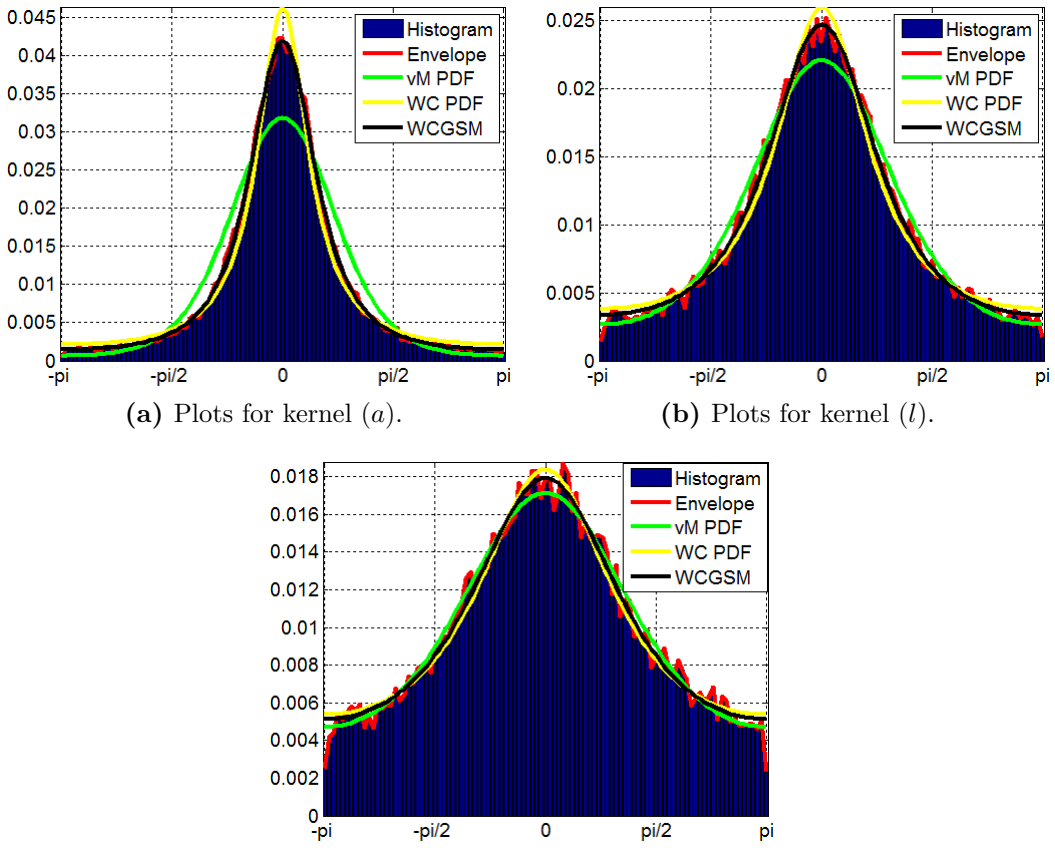

(a) Plots for kernel (a).

(b) Plots for kernel (l).

(c) Plots for kernel (m).

Figure 6.12: Plots for MSTAR T1. The vM, WC and WCGSM PDFs, respectively, are superimposed on the BRPI histograms for kernels a, l and m.

The following conclusions are drawn based on the results obtained. Firstly, comparing the vM, WC, and WCGSM PDFs it is apparent that the latter achieves the best fit for the three kernels. Secondly, as one moves from kernels a to m, the peakedness and heavy tails of the corresponding BRPI histograms become less pronounced. The WC PDF is more heavy-tailed and more peaked, which makes it a better model than the vM PDF for the BRPI histogram of kernel a. On the contrary, the vM PDF is less heavy-tailed and less peaked, which makes it a better model than the WC PDF for the BRPI histogram of kernel m. The peakedness and heavy tails pertaining to kernel

Table 6.3: Parameter estimates pertaining to kernels a, l and m for the vM, WC and WCGSM PDFs.

Kernel f_k	Chip	vM (μ_{vM}, κ)	JSD_N	WC (μ_{wc}, ρ)	JSD_N	$WCGSM$ $(\underline{\phi}, \lambda)$	JSD_N
a	T MSTAR #1	0.0053, 1.9418	0.0065	0.0048, 0.6458	0.0021	0.0053, 0.7919	**6.1331e-04**
	T MSTAR #2	0.0033, 1.8884	0.0061	-9.215e-04, 0.6398	0.0018	0.0033, 0.7846	**6.3857e-04**
l	T MSTAR #1	0.0081, 1.0561	0.0012	0.0061, 0.4457	0.0012	0.0081, 0.5641	**7.2833e-04**
	T MSTAR #2	-3.78e-04, 1.0237	0.0012	0.0021, 0.4373	0.0010	-3.78e-04, 0.5529	**6.2111e-04**
m	T MSTAR #1	0.0004, 0.6440	7.1752e-04	-0.003, 0.2983	8.4103e-04	0.0004, 0.3798	**7.1742e-04**
	T MSTAR #2	-0.002, 0.6466	6.6240e-04	7.1424e-04, 0.3013	6.8543e-04	-0.002, 0.3824	**5.9436e-04**

l is moderately situated between that of kernels a and m. This makes the fits of the vM and the WC PDFs relatively similar for this case. Finally, the results obtained demonstrate the general applicability of the WCGSM PDF and its adaptability to the BRPI histograms for the three kernels. It is evident that the vM and the WC PDFs can be viewed as special cases of the WCGSM PDF.

6.7. Classification Using Phase-Based Features

The purpose of this section is to demonstrate the advantage of the proposed methods for phase characterization and modeling in target classification in SAR imagery. First, baseline features extracted from the power-detected SAR chip are provided in Sect. 6.7.1. Then, a set of fifteen features based solely on the phase image are introduced in Sect. 6.7.2. Support vector machine (SVM) classifier design and feature ranking are described in Sect. 6.7.3 and Sect. 6.7.4, respectively. Finally, the overall results are presented in Sect. 6.7.5.

6.7.1. Baseline Features

Baseline features are solely based on the power-detected SAR chip. Nineteen baseline features are utilized in this study. The procedure for extracting the baseline features is summarized in Fig. 6.13. First, the complex-valued SAR chip is power-detected as

$$p(x,y) = [i(x,y)]^2 + [q(x,y)]^2 . \tag{6.44}$$

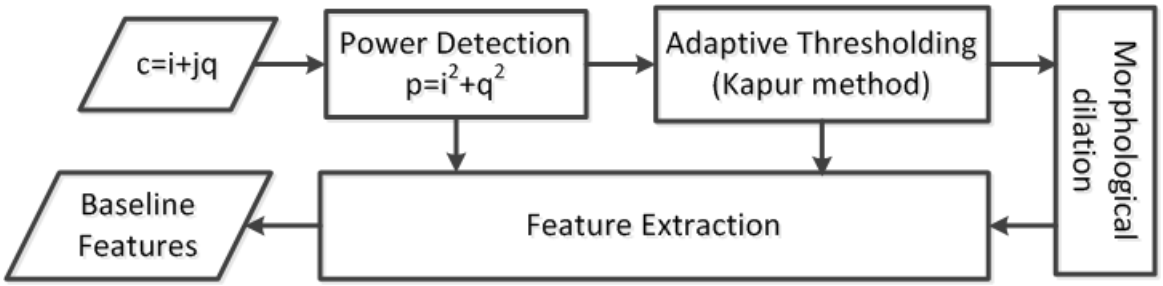

Figure 6.13: Procedure for extraction of the baseline features.

Then, the power-detected SAR chip is thresholded through an adaptive information theoretic approach based on the entropy of the histogram as originally proposed by Kapur *et al.* [35]. This method was chosen because it is found to offer excellent performance. Further, morphological dilation is applied to the thresholded image [36]. This operation is aimed at merging the relevant different connected regions in the thresholded image into one contiguous region representative of the target extent. In the next step, a set of features is extracted from the binary image, the dilated binary image, and the gray-level image. These extractions are meant to represent the power-based features commonly used in the literature, and they include the following [37]:

- Number of scattering centers (f_{BL1}): the number of connected regions in the binary image.
- Area (f_{BL2}): the total number of pixels with value of one in the binary image.
- Centroid (f_{BL3}, f_{BL4}): the 'center of mass' of the dilated binary image. Note that the first element (f_{BL3}) is the horizontal coordinate (or x-coordinate) of

the center of mass, and the second element (f_{BL4}) is the vertical coordinate (or y-coordinate).

- Major axis length (f_{BL5}): the length (in pixels) of the major axis of the ellipse that has the same normalized second central moments as the region. This measure is based on the dilated binary image.
- Minor axis length (f_{BL6}): the length (in pixels) of the minor axis of the ellipse that has the same normalized second central moments as the region. This measure is also based on the dilated binary image.
- Eccentricity (f_{BL7}): the eccentricity of the ellipse that has the same second-moments as the region. The eccentricity is the ratio of the distance between the foci of the ellipse and its major axis length. The value is between 0 and 1. This measure is also based on the dilated binary image.
- Orientation (f_{BL8}): the angle (in degrees ranging from -90^o to 90^o) between the x-axis and the major axis of the ellipse that has the same second-moments as the region. This measure is also based on the dilated binary image.
- Convex area (f_{BL9}): the number of pixels in the convex hull that specifies the smallest convex polygon that can contain the region. This measure is also based on the dilated binary image.
- Euler number (f_{BL10}): the number of objects in the region minus the number of holes in those objects. This measure is based on the binary image.
- Equivalent diameter (f_{BL11}): the diameter of a circle with the same area as the region. Computed as $\sqrt{\frac{4}{\pi} f_{BL2}}$. This measure is based on the dilated binary image.
- Solidity (f_{BL12}): the proportion of the pixels in the convex hull that are also in the region, computed as $\frac{f_{BL2}}{f_{BL9}}$. This measure is also based on the dilated binary image.
- Extent (f_{BL13}): the ratio of pixels in the region to pixels in the total bounding box. Computed as $\frac{f_{BL2}}{\text{Area of the Bounding Box}}$. This measure is also based on the dilated binary image.
- Perimeter (f_{BL14}): the distance between each adjoining pair of pixels around the border of the region. This measure is also based on the dilated binary image.
- Weighted centroid (f_{BL15}, f_{BL16}): the center of the region based on location and

intensity value. The first element (f_{BL15}) is the horizontal coordinate (or x-coordinate) of the weighted centroid. The second element (f_{BL16}) is the vertical coordinate (or y-coordinate). This measure is based on both the dilated binary image as well as the power-detected intensity image.

- Mean intensity (f_{BL17}): the mean of all the intensity values in the region of the power-detected image as defined by the dilated binary image.
- Minimum intensity (f_{BL18}): the value of the pixel with the lowest intensity in the region of the power-detected image as defined by the dilated binary image.
- Maximum intensity (f_{BL19}): the value of the pixel with the greatest intensity in the region of the power-detected image as defined by the dilated binary image.

6.7.2. Features Based Solely on the Phase Image

While various types of features can be extracted based on the BRPI image as well as the WCGSM model described in Sect. 6.5 and Sect. 6.6, for demonstration purposes the following set of fifteen features are considered in this study:

- The location parameter based on kernel a (f_{Ph1}): this is the location parameter $\hat{\underline{\phi}}$ of the WCGSM PDF for kernel a (see Fig. 6.5) estimated based on Eq. 6.41.
- The shape parameter based on kernel a (f_{Ph2}): this is the shape parameter $\hat{\lambda}$ of the WCGSM PDF for kernel a (see Fig. 6.5) estimated based on the JSD method presented in Sect. 6.6.1.5.
- Maximum peak value for kernel a (f_{Ph3}): this is the peak value for the WCGSM PDF based on kernel a. This is analogous to the peak value for the the normalized histogram defined by $h/\text{sum}(h)$ (see Fig. 6.12).
- The location parameter based on kernel l (f_{Ph4}): this is the location parameter $\hat{\underline{\phi}}$ of the WCGSM PDF for kernel l (see Fig. 6.5) estimated based on Eq. 6.41.
- The shape parameter based on kernel l (f_{Ph5}): this is the shape parameter $\hat{\lambda}$ of the WCGSM PDF for kernel l (see Fig. 6.5) estimated based on the JSD divergence method presented in Sect. 6.6.1.5.
- Maximum peak value for kernel l (f_{Ph6}): this is the peak value for the WCGSM PDF based on the kernel l.
- The location parameter based on kernel m (f_{Ph7}): this is the location parameter $\hat{\underline{\phi}}$ of the WCGSM PDF for the kernel m (see Fig. 6.5) estimated based on Eq. 6.41.

- The shape parameter based on kernel m (f_{Ph8}): this is the shape parameter $\hat{\lambda}$ of the WCGSM PDF for kernel m (see Fig. 6.5) estimated based on the JSD method presented in Sect. 6.6.1.5.
- Maximum peak value for kernel m (f_{Ph9}): this is the peak value for the WCGSM PDF based on kernel m.
- First pseudo-covariance measure (f_{Ph10}): this is the measure given in Eq. 6.15, and based on kernel a.
- Second pseudo-covariance measure (f_{Ph11}): this is the measure given in Eq. 6.15, and based on kernel l.
- Third pseudo-covariance measure (f_{Ph12}): this is the measure given in Eq. 6.15, and based on kernel m.
- First noncircularity measure (f_{Ph13}): this is the measure given in Eq. 6.14, and based on kernel a.
- Second noncircularity measure (f_{Ph14}): this is the measure given in Eq. 6.14, and based on kernel l.
- Third noncircularity measure (f_{Ph15}): this is the measure given in Eq. 6.14, and based on kernel m.

It may be noted that because the 'sideband responses' due to the nonlinear scattering are distributed over an area far larger than that physically occupied by the target [1], no segmentation should be utilized and the largest area possible around the target should be included. Hence, the entire MSTAR chip provided by SDMS is used in this study.

6.7.3. Classifier Design

The open source LIBSVM machine learning library [38] is used in this study to design an eight-class support vector machine (SVM) classifier. The kernel used in this work is the Gaussian radial basis function (RBF) [39, 40]. Two parameters (C, γ) play a crucial role in dictating the performance of the SVM classifier. $C > 0$ is the penalty or regularization parameter, and $\gamma > 0$ is the kernel parameter (see [38] for details). Following the guidelines in [38, 39, 41], a grid-search and a ν-fold cross-validation can be used to find the optimal values of these two parameters.

6.7.4. Feature Ranking

In this study, the Fisher score (F-Score) [42] is used to evaluate the statistical significance of the features. The F-Score is a technique for measuring the discrimination of two sets of real numbers. Given the training vectors x_k where $k = 1, ..., m$ and if the number of positive and negative instances are n_+ and n_-, respectively, then, the F-Score of the i^{th} feature is defined as [40, 42, 43]

$$F(i) = \frac{\left(\bar{\mathbf{x}}_i^{(+)} - \bar{\mathbf{x}}_i\right)^2 + \left(\bar{\mathbf{x}}_i^{(-)} - \bar{\mathbf{x}}_i\right)^2}{\frac{1}{n_+ - 1}\sum_{k=1}^{n_+}\left(x_{k,i}^{(+)} - \bar{\mathbf{x}}_i^{(+)}\right)^2 + \frac{1}{n_- - 1}\sum_{k=1}^{n_-}\left(x_{k,i}^{(-)} - \bar{\mathbf{x}}_i^{(-)}\right)^2}, \tag{6.45}$$

where $\bar{\mathbf{x}}_i$, $\bar{\mathbf{x}}_i^{(+)}$ and $\bar{\mathbf{x}}_i^{(-)}$, respectively, are the averages for the i^{th} feature of the whole, positive and negative datasets; $x_{k,i}^{(+)}$ is the i^{th} feature of the k^{th} positive instance; $x_{k,i}^{(-)}$ is the i^{th} feature of the k^{th} negative instance. The numerator indicates the discrimination between the positive and negative sets, and the denominator indicates that within each of the two sets. The larger the F-Score is, the more likely the feature is more discriminative [42, 43].

6.7.5. Results

Two different training and testing feature sets are extracted using the MSTAR datasets presented in Sect. 6.4. The first feature set contains the baseline features based on the power-detected SAR chips described in Sect. 7.8.1. In total, there are nineteen baseline features for each target chip. Hence, the size of the constructed baseline features matrix for training is 2347×19 and for testing is 2112×19. The second set is for the phase-based features presented in Sect. 6.7.2. Fifteen phase-based features are extracted from each target chip. The size of the phase-based features matrix for training is 2347×15 and for testing is 2112×15.

Following the steps outlined in Sect. 6.7.3, two different multi-class SVM classifiers are trained using the training baseline and phase-based feature sets. The grid search for the optimal values of (C, γ) pertaining to the two classifiers is depicted in Fig. 6.14. The accuracy depicted is based on a five-fold cross validation. Optimal values are found to be $(2^5, 2^{-1})$ and $(2, 2)$, respectively, for the baseline and phase-based feature

sets. Once the two classifiers are constructed based on the optimal parameters found, the classifiers are tested using the baseline and the phase-based testing feature sets, respectively. The confusion matrices for the baseline and phase-based classifiers are provided in Fig. 6.15 and Fig. 6.16, respectively. The overall classification accuracy (as well as the validation accuracy) is calculated based on [38] as

$$\text{Accuracy} = \frac{\text{No. of Correctly Predicted Data}}{\text{No. of Testing Data}} \times 100. \tag{6.46}$$

The classifier based on the baseline features achieves an overall classification accuracy of 73.6269%. Moreover, the results obtained for the phase-based features evidently demonstrate that the phase in single-channel SAR imagery is not useless as is often assumed in the literature. On the contrary, based only on fifteen phase-based features, an overall classification accuracy of 63.0208% is achieved. In comparison to the other targets, it is noted that SLICY, BTR-60, ZSU-23/4 and 2S1, respectively, scored an overall classification accuracy of 97.4453%, 87.6923%, 79.1971% and 71.5328% for the phase-based features, and an overall classification accuracy of 96.7153%, 73.3333%, 72.9927% and 64.2336% for the baseline features. This is a clear indication that the nonlinear dynamics possessed in the phase chips of these targets are relatively more pronounced, and they are captured by the proposed features. It is worth noting that SLICY achieved the highest classification accuracy for both the baseline and the phase-based classifiers. This is expected due to the unique phenomenology of SLICY in comparison to the other targets considered. It should also be noted that if a SAR dataset with higher resolution is used, one would expect an increase in the classification accuracy based solely on the phase features.

Next, the combinatorial effect of the baseline and the phase-based features is studied. This serves to illustrate the uniqueness of the information carried in the phase in comparison to the power-detected chip. The amalgamation of the baseline and the phase-based features is used to build a new SVM classifier following the procedure described in Sect. 6.7.3. Thus, the sizes of the new features matrices for training and testing, respectively, are $2347 \times (19 + 15)$ and $2112 \times (19 + 15)$. The optimal values for (C, γ) are obtained based on a grid search (see Fig. 6.17) and found to be $(2^5, 2^{-1})$. The confusion matrix and the classification accuracy for this classifier are provided in

Fig. 6.18.

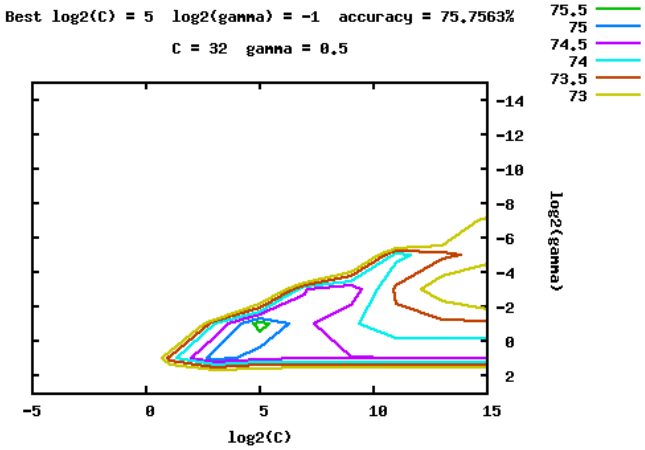

(a) Grid search for the baseline features.

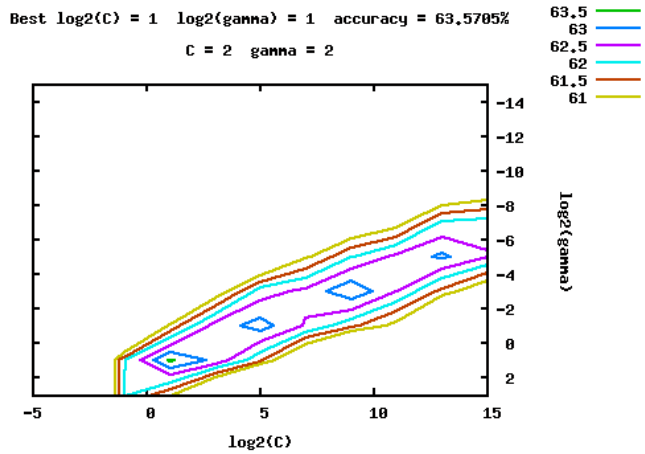

(b) Grid search for the phase-based features.

Figure 6.14: Grid search for optimal (C, γ) for the two set of features.

	BTR – 60	2S1	BRDM – 2	D7	T62	ZIL – 131	ZSU – 23/4	SLICY
BTR – 60	**73.3333**	3.0769	8.2051	2.0513	6.1538	3.0769	4.1026	0
2S1	5.8394	**64.2336**	6.9343	6.2044	8.7591	5.8394	1.0949	1.0949
BRDM – 2	9.4891	5.8394	**71.8978**	0.3650	3.6496	4.7445	4.0146	1.0949
D7	2.1898	5.1095	2.1898	**77.3723**	4.3796	3.2847	4.7445	0.7299
T62	6.2271	10.6227	5.4945	0.7326	**67.3993**	3.6630	5.4945	0.3663
ZIL – 131	6.2044	9.4891	5.1095	1.4599	9.4891	**64.9635**	1.0949	2.1898
ZSU – 23/4	6.5693	2.9197	4.0146	7.2993	4.3796	1.4599	**72.9927**	0.3650
SLICY	0.3650	1.4599	0	0.3650	0	1.0949	0	**96.7153**

Figure 6.15: Confusion matrix for the baseline classifier. Classification accuracy = 73.6269% (1555/2112).

	BTR – 60	2S1	BRDM – 2	D7	T62	ZIL – 131	ZSU – 23/4	SLICY
BTR – 60	**87.6923**	3.5897	1.0256	1.0256	0	0	3.0769	3.5897
2S1	6.9343	**71.5328**	1.8248	15.3285	0.7299	1.4599	1.8248	0.3650
BRDM – 2	0.7299	5.8394	**43.4307**	10.9489	19.3431	12.0438	7.2993	0.3650
D7	0	15.6934	6.2044	**44.8905**	9.1241	20.8029	3.2847	0
T62	0	0.7326	13.9194	8.0586	**43.5897**	20.5128	13.1868	0
ZIL – 131	0.3650	4.0146	6.2044	30.6569	10.9489	**43.4307**	4.3796	0
ZSU – 23/4	0	0	4.3796	0.3650	12.7737	1.0949	**79.1971**	2.1898
SLICY	0	0	1.0949	0	0	0	1.4599	**97.4453**

Figure 6.16: Confusion matrix for the classifier based solely on the phase features. Classification accuracy = 63.0208% (1331/2112).

These results demonstrate the uniqueness of the phase-based features. Particularly, upon combining the baseline and the phase-based features, the overall classification accuracy is increased by around 8%. Again, if a SAR dataset with higher resolution is used, one would expect even greater increase in accuracy. Next, the combination of the baseline and the phase-based features are ranked based on the procedure outlined in Sect. 6.7.4. F-Scores for the features are depicted in Fig. 6.19. The corresponding F-Score values are given in Table 6.5. Generally, the F-Score results convey that five of the phase-based features possess higher significance than the baseline features. Additionally, the F-Score of the phased-based features with indices of 22, 32 and 21, respectively, are around seven-fold of the maximum F-Score pertinent to the baseline features scored by the baseline feature with index number five. This shows the utility of the phase-based features.

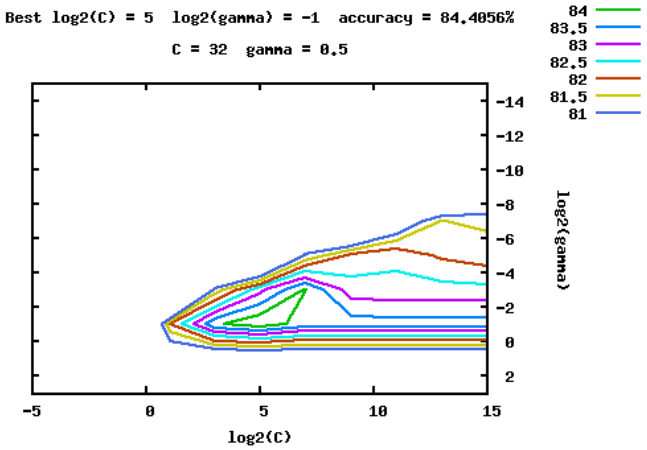

Figure 6.17: Grid search of optimal (C, γ) for combinations of the baseline + phase-based features.

	BTR – 60	2S1	BRDM – 2	D7	T62	ZIL – 131	ZSU – 23/4	SLICY
BTR – 60	**88.2051**	4.1026	1.0256	1.5385	0	1.0256	1.5385	2.5641
2S1	8.0292	**79.5620**	2.9197	5.4745	1.4599	2.1898	0.3650	0
BRDM – 2	0.3650	7.2993	**75.5474**	1.4599	5.8394	6.9343	2.5547	0
D7	1.4599	4.0146	3.2847	**84.6715**	2.1898	3.2847	1.0949	0
T62	0.7326	2.1978	10.2564	1.4652	**73.6264**	6.2271	5.4945	0
ZIL – 131	1.8248	8.0292	7.6642	3.6496	9.1241	**68.6131**	1.0949	0
ZSU – 23/4	0	1.4599	4.0146	2.1898	4.3796	1.4599	**85.4015**	1.0949
SLICY	0	0.3650	0.3650	0.3650	0	01.0949	0.3650	**97.4453**

Figure 6.18: Confusion matrix for the classifier based on baseline and phase-based features. Classification accuracy = 81.392% (1719/2112).

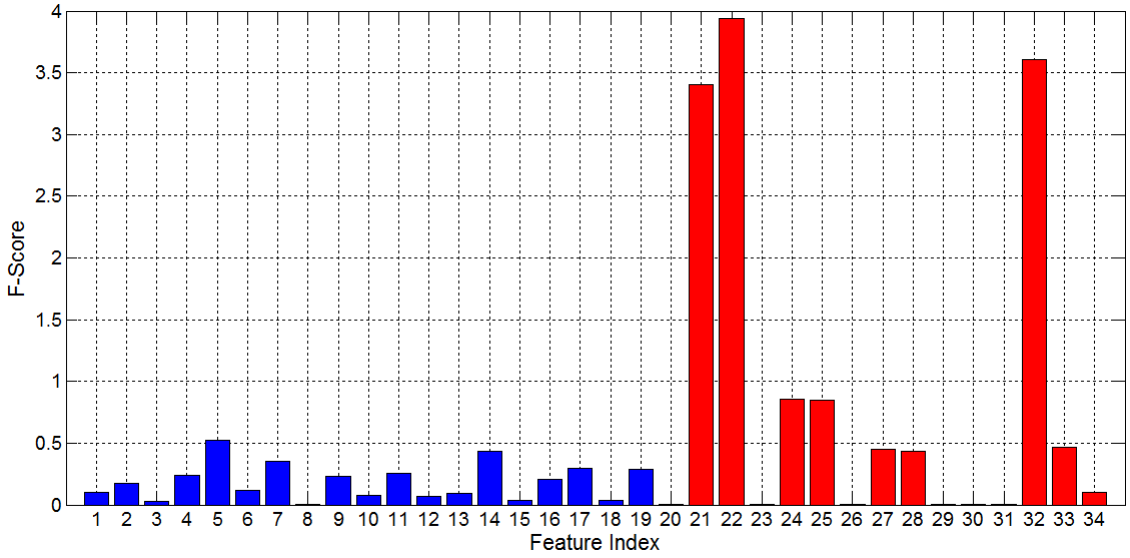

Figure 6.19: Significance in terms of the F-Score for all the features (baseline + phase-based) used in this study. Blue and red bars, respectively, represent the baseline and phase-based features. The feature index corresponds to the feature subscript provided in Table 6.4.

Table 6.4: F-Scores for the baseline features used in this study

Index	1	2	3	4	5	6	7	8
Type	$\mathbf{f}_{\text{BL1}}$	$\mathbf{f}_{\text{BL2}}$	$\mathbf{f}_{\text{BL3}}$	$\mathbf{f}_{\text{BL4}}$	$\mathbf{f}_{\text{BL5}}$	$\mathbf{f}_{\text{BL6}}$	$\mathbf{f}_{\text{BL7}}$	$\mathbf{f}_{\text{BL8}}$
F-Score	0.104282	0.174448	0.026250	0.240112	0.525163	0.116269	0.356272	0.007372
Index	9	10	11	12	13	14	15	16
Type	$\mathbf{f}_{\text{BL9}}$	$\mathbf{f}_{\text{BL10}}$	$\mathbf{f}_{\text{BL11}}$	$\mathbf{f}_{\text{BL12}}$	$\mathbf{f}_{\text{BL13}}$	$\mathbf{f}_{\text{BL14}}$	$\mathbf{f}_{\text{BL15}}$	$\mathbf{f}_{\text{BL16}}$
F-Score	0.234009	0.074707	0.252705	0.071361	0.090576	0.435705	0.037509	0.205777
Index	17	18	19					
Type	$\mathbf{f}_{\text{BL17}}$	$\mathbf{f}_{\text{BL18}}$	$\mathbf{f}_{\text{BL19}}$					
F-Score	0.296468	0.037128	0.290143					

Table 6.5: F-Scores for the phase-based features used in this study.

Index	20	21	22	23	24	25	26	27
Type	$\mathbf{f}_{\text{Ph1}}$	$\mathbf{f}_{\text{Ph2}}$	$\mathbf{f}_{\text{Ph3}}$	$\mathbf{f}_{\text{Ph4}}$	$\mathbf{f}_{\text{Ph5}}$	$\mathbf{f}_{\text{Ph6}}$	$\mathbf{f}_{\text{Ph7}}$	$\mathbf{f}_{\text{Ph8}}$
F-Score	0.002161	3.40389	3.93829	0.001028	0.852989	0.850224	0.000536	0.451283
Index	28	29	30	31	32	33	34	
Type	$\mathbf{f}_{\text{Ph9}}$	$\mathbf{f}_{\text{Ph10}}$	$\mathbf{f}_{\text{Ph11}}$	$\mathbf{f}_{\text{Ph12}}$	$\mathbf{f}_{\text{Ph13}}$	$\mathbf{f}_{\text{Ph14}}$	$\mathbf{f}_{\text{Ph15}}$	
F-Score	0.437565	0.003383	0.004468	0.001335	3.609093	0.466928	0.100274	

The following observations are based on the results obtained. First, unlike the common belief that the phase in single-channel complex-valued SAR imagery carries no useful information, the statistical significance of the information carried in the phase is clearly demonstrated. Second, the top ranked feature is that based on the peak value of the normalized WCGSM model. This is directly followed by the measure for noncircularity based on the absolute value for the pseudo-covariance of the BRPI image. Then, this is followed by the shape parameter of the WCGSM PDF. This demonstrates the advantage of the proposed method for phase characterization and modeling. Finally, it should be stressed that because we do not have access to a dataset with a greater resolution (i.e., typical of today's airborne SAR sensors), the MSTAR

dataset was utilized to illustrate the general advantages of our proposed methods. With the increase in the spatial resolution of the SAR sensor relative to the size of the imaged target, the nonlinear phenomenon is naturally expected to be more pronounced. Accordingly, the application of the proposed approach to this kind of SAR imagery should achieve higher classification accuracy.

6.8. Conclusions

Nonlinear phase modulation is a phenomenon of significance for extended targets in SAR imagery. Important information about this phenomenon is carried in the often discarded phase of the SAR image. This chapter presented a new insight into the phase in single-channel SAR imagery. A method for characterizing the phase content is presented. Additionally, a statistical model for the characteristic phase is derived. Furthermore, a set of fifteen phase-based features are introduced. The applicability of the proposed features is demonstrated on eight-class real-world phase chips from the MSTAR dataset. When a dataset with higher resolution is available, the techniques proposed in this chapter are expected to achieve superior classification accuracy. Ongoing research effort is focused on developing novel methods that take advantage of the nonlinear dynamics in the complex-valued SAR chip. The combinatorial effect for various types of features, including those considered in this study, will be examined.

Bibliography

[1] A. Rihaczek and S. Hershkowitz, "Man-made target backscattering behavior: Applicability of conventional radar resolution theory," *IEEE Transactions on Aerospace and Electronic Systems*, vol. 32, no. 2, pp. 809–824, 1996. [Online]. Available: http://dx.doi.org/10.1109/7.489523 135, 138, 139, 167

[2] J. C. Dainty, *Laser Speckle and Related Phenomena*. Springer-Verlag, 1984. 135

[3] H. Maitre, Ed., *Processing of Synthetic Aperture Radar Images*. Hoboken, NJ: ISTE and Wiley, 2008. 135

[4] A. Rihaczek and S. Hershkowitz, *Radar Resolution and Complex-Image Analysis*. Norwood, MA: Artech House, 1996. 135, 138, 139

[5] ——, *Theory and Practice of Radar Target Identification*. Norwood, MA: Artech House, 2000. 135, 138, 139

[6] I. Cumming and F. Wong, *Digital Processing of Synthetic Aperture Radar Data*. Norwood, MA: Artech House, 2005. 135, 137, 138

[7] K. El-Darymli, P. McGuire, E. W. Gill, D. Power, and C. Moloney, "Effect of detection on spatial resolution in synthetic aperture radar imagery and mitigation through upsampling," *Journal of Applied Remote Sensing*, vol. 8, no. 1, pp. 685–694, 2014. [Online]. Available: http://dx.doi.org/10.1117/1.JRS.8.083601 135

[8] K. El-Darymli, E. W. Gill, P. McGuire, D. Power, and C. Moloney, "Unscarmbling nonlinear dynamics in synthetic aperture radar imagery," *[Under Review]*, 2015. 135, 139, 150

[9] K. El-Darymli, C. Moloney, E. W. Gill, P. McGuire, and D. Power, "Nonlinearity and the effect of detection on signle-channel synthetic aperture radar imagery," in *Oceans'14 MTS/IEEE Taipei, Taiwan*, 2014. [Online]. Available: http://dx.doi.org/10.1109/OCEANS-TAIPEI.2014.6964493 135, 147

[10] ——, "On circularity/noncircularity in single-channel synthetic aperture radar imagery," in *OCEANS'14 MTS/IEEE, St. John's, Canada*, 2014. [Online]. Available: http://dx.doi.org/10.1109/OCEANS.2014.7003163 135, 136, 139, 150

[11] T. Adali and S. Haykin, *Adaptive Signal Processing*. Hoboken, NJ: Wiley, 2010. 136, 145, 146, 147

[12] M. Novey, T. Adali, and A. Roy, "Circularity and Gaussianity detection using the complex generalized Gaussian distribution," *Signal Processing Letters, IEEE*, vol. 16, no. 11, pp. 993–996, 2009. [Online]. Available: http://dx.doi.org/10.1109/LSP.2009.2028412 12, 146, 147

[13] P. J. Schreier and L. L. Scharf, *Statistical signal processing of complex-valued data the theory of improper and noncircular signals*. Cambridge, UK: Cambridge University Press, 2010. 136, 145, 146, 147

[14] K. V. Mardia and P. E. Jupp, *Directional statistics*, ser. Wiley Series in Probability and Statistics. London, UK: John Wiley and Sons, 2009, vol. 494. 136, 144, 157

[15] S. R. Jammalamadaka and A. Sengupta, *Topics in circular statistics*. River Edge, NJ: World Scientific, 2001.

[16] N. I. Fisher, *Statistical Analysis of Circular Data*. Cambridge, UK: Cambridge University Press, 1993. 136, 144, 159

[17] K. El-Darymli, P. McGuire, E. W. Gill, D. Power, and C. Moloney, "Understanding the significance of radiometric calibration for synthetic aperture radar imagery," in *Canadian conference on electrical and computer engineering (CCECE'14), IEEE*, Toronto, Canada, 2014. [Online]. Available: http://dx.doi.org/10.1109/CCECE.2014.6901104 137

[18] K. El-Darymli, C. Moloney, E. W. Gill, P. McGuire, and D. Power, "Recognition of nonlinear dispersive scattering in SAR imagery," in *IEEE IGARSS'14, Quebec, Canada*, 2014. [Online]. Available: http://dx.doi.org/10.1109/IGARSS.2014.6947548 139

[19] Wikipedia. (2012) Naval station argentia. [Online]. Available: http://en.wikipedia.org/wiki/Naval_Station_Argentia xv, 139, 140

[20] Sensor And Data Management System. (2014) MSTAR/IU mixed targets. US

Air Force. Airforce Research Lab. [Online]. Available: https://www.sdms.afrl.af.mil/index.php?collection=mstar&page=mixed xv, 139, 141

[21] D. MacDonald and A. Ltd. (2011) Radarsat-2 product description. [Online]. Available: http://gs.mdacorporation.com/includes/documents/RN-SP-52-1238_RS2_Product_Description_Iss1-9.pdf 139

[22] R. S. Nadarajah, "A generalized normal distribution," *Journal of Applied Statistics*, vol. 32, no. 7, pp. 685–694, 2005. [Online]. Available: http://dx.doi.org/10.1080/02664760500079464 150

[23] M. Novey, T. Adali, and A. Roy, "A complex generalized Gaussian distribution- characterization, generation, and estimation," *Signal Processing, IEEE Transactions on*, vol. 58, no. 3, pp. 1427–1433, 2010. [Online]. Available: http://dx.doi.org/10.1109/TSP.2009.2036049 150

[24] M. K. Varanasi and B. Aazhang, "Parametric generalized Gaussian density estimation," *The Journal of the Acoustical Society of America*, vol. 86, pp. 1404–1415, 1989. [Online]. Available: http://dx.doi.org/10.1121/1.398700 150

[25] M. N. Do and M. Vetterli, "Wavelet-based texture retrieval using generalized Gaussian density and Kullback-Leibler distance," *Image Processing, IEEE Transactions on*, vol. 11, pp. 146–158, 2002. [Online]. Available: http://dx.doi.org/10.1109/83.982822 150

[26] M. J. Wainwright, E. P. Simoncelli, and A. S. Willsky, "Random cascades on wavelet trees and their use in analyzing and modeling natural images," *Applied and Computational Harmonic Analysis*, vol. 11, no. 1, pp. 89–123, 2001. [Online]. Available: http://dx.doi.org/10.1006/acha.2000.0350 150, 151, 152

[27] D. F. Andrews and C. L. Mallows, "Scale mixtures of normal distributions," *Journal of the Royal Statistical Society Series B (Methodological)*, vol. 36, no. 1, pp. 99–102, 1974. [Online]. Available: http://www.jstor.org/stable/2984774 151, 152

[28] J. Portilla, V. Strela, M. J. Wainwright, and E. P. Simoncelli, "Image denoising using scale mixtures of gaussians in the wavelet domain," *Image Processing, IEEE Transactions on*, vol. 12, no. 11, pp. 1338–1351, 2003. [Online]. Available: http://dx.doi.org/10.1109/TIP.2003.818640 152

[29] K. S. Miller, "Complex gaussian processes," *SIAM Rev*, vol. 11, no. 4, pp.

544–567, 1969. [Online]. Available: http://www.jstor.org/stable/2029085 153, 154

[30] A. Vo, S. Oraintara, and N. Nguyen, "Vonn distribution of relative phase for statistical image modeling in complex wavelet domain," *Signal Processing*, vol. 91, no. 1, pp. 114–125, 2011. [Online]. Available: http://dx.doi.org/10.1016/j.sigpro.2010.06.014 156, 157

[31] C. D. Manning and H. Schütze, *Foundations of Statistical Natural Language Processing*. Cambridge, MA: MIT Press, 1999. 158

[32] D. M. Endres and J. E. Schindelin, "A new metric for probability distributions," *Information Theory, IEEE Transactions on*, vol. 49, no. 7, pp. 1858–1860, 2003. [Online]. Available: http://dx.doi.org/10.1109/TIT.2003.813506 158

[33] C. Forbes, M. Evans, N. Hastings, and B. Peacock, *Statistical Distributions*, 4th ed. Hoboken, NJ: Wiley, 2001. 159

[34] G. J. Borradaile, *Statistics of Earth Science Data: Their Distribution in Time, Space, and Orientation*. Berlin, Heidelberg: Springer, 2003. 160

[35] J. Kapur, P. Sahoo, and A. Wong, "A new method for gray-level picture thresholding using the entropy of the histogram," *Computer Vision, Graphics, and Image Processing*, vol. 29, no. 3, pp. 273–285, 1985. [Online]. Available: http://dx.doi.org/10.1016/0734-189X(85)90125-2 164

[36] Matlab 2014b documentation. (2014) Morphology fundamentals: dilation and erosion. Mathworks. [Online]. Available: http://tinyurl.com/q6zfwcp 164

[37] ——. (2014) Measure properties of image regions. Mathworks. [Online]. Available: http://tinyurl.com/k58dlqf 164

[38] C.-C. Chang and C.-J. Lin, "LIBSVM: A library for support vector machines," *ACM Transactions on Intelligent Systems and Technology*, vol. 2, no. 3, 2011. [Online]. Available: http://dx.doi.org/10.1145/1961189.1961199 167, 169

[39] C.-W. Hsu, C.-C. Chang, and C.-J. Lin, "A practical guide to support vector classification. technical report," Department of Computer Science and Information Engineering, National Taiwan University, Tech. Rep., 2010. [Online]. Available: http://www.csie.ntu.edu.tw/~cjlin/papers/guide/guide.pdf 167

[40] R. Duda, P. Hart, and D. Stork, *Pattern classification*. New York: John Wiley and Sons, 2001. 167, 168

[41] C.-C. Chang and C.-J. Lin, "LIBSVM: A library for support vector machines," Department of Computer Science National Taiwan University, Taipei, Taiwan, Tech. Rep., 2013. [Online]. Available: http://www.csie.ntu.edu.tw/~cjlin/papers/libsvm.pdf 167

[42] Y.-W. Chen and C.-J. Lin, *Feature Extraction: Foundations and Applications*. Berlin, Heidelberg: Springer, 2006, ch. Combining SVMs with Various Feature Selection, pp. 315–324. 168

[43] Y.-W. Chang and C.-J. Lin, "Feature ranking using linear SVM," in *Causation and Prediction Challenge Challenges in Machine Learning*, vol. 2, 2008, pp. 47–57. [Online]. Available: http://tinyurl.com/l97zpmm 168

7. Holism for Target Classification in Synthetic Aperture Radar Imagery

7.1. Overview

Reductionism and holism are two worldviews underlying the fields of linear and nonlinear signal processing, respectively. The conventional radar resolution theory is motivated by the former view, and it is violated due to nonlinear phase modulation induced by the dispersive scattering typically associated with extended targets. Motivated by the latter view, this chapter offers a new insight into the process of feature extraction for target recognition applications in single-channel SAR imagery. Two novel frameworks for feature extraction are presented. The first framework is based solely on the often-ignored phase chip. The second framework uses the complex-valued 2-D SAR chip after it is transformed into a 1-D vector. This transformation provides for the utilization of various nonlinear and nonstationary time series analysis methods. Some representative nonlinear features based on these two frameworks are introduced. Further, for comparison purposes, baseline features from the power-detected chip are also considered. Multiple instances of an eight-class support vector machine (SVM) classifier are designed based on combinations of feature sets extracted from the public-domain MSTAR dataset. A classification accuracy of 93.4186% is achieved for the combination of the phase and 1-D based nonlinear features. This is in comparison to 73.6269% for the baseline features. Because the nonlinear phenomenon is resolution-dependent, our proposed approach is expected to achieve even greater accuracy for SAR sensors with higher resolution.

7.2. Introduction

The underpinning philosophy for science in general, and the field of signal processing in particular, is based on either one of two multidisciplinary worldviews: reductionism (also known as Newtonianism) and holism [1–3]. In the reductionist worldview, a complex system is assumed to be simply the superposition of its parts, and its analysis is reduced to analysis of its individual components. Although this view may not seem to explicitly dismiss the existence of the so-called emergence phenomenon (i.e., multiplicity due to interactions between the individual components), it is implicit that the emergence phenomenon can be captured by the constituent processes. On the contrary, in the holistic worldview, the system is viewed as a whole that cannot be fully understood solely in terms of its constituent parts. This principle was succinctly summarized twenty-four centuries ago by Aristotle in Metaphysics: "The whole is greater than the sum of its parts" [3].

Reductionism and holism set the philosophical foundations of linear and nonlinear signal processing, respectively [1, 3]. In linear system theory [4], the reductionist view is applied, meaning that the signal is decomposed into fragments that are analyzed individually. The analysis result for the whole signal is obtained from proper scaling (i.e., homogeneity property) and addition of the fragments (i.e., superposition principle). For this process to be valid, the central limit theorem (CLT) is invoked; hence, it is implicitly assumed that the signal samples are drawn from a distribution possessing a finite variance [5]. Accordingly, the linear system theory treats deviation from linearity as noise that warrants removal. For example, the Fourier view, the heart of linear system theory, assumes a first-order fundamental oscillation and bounding higher order harmonics. Despite its mathematical soundness, this view does not correspond strictly to physical reality [6].

When the underlying random processes are nonlinear, advantages of the holistic approach become apparent. Statistically, nonlinear signal processing is motivated by the generalized central limit theorem (GCLT) which holds that the variance of the underlying random variables is infinite [7]. The Poincaré view [6, 8] is one such important view for nonlinear signal processing, which sets the foundations for chaos theory. The Hilbert view [6] is another important view which was popularized after the advent of the Hilbert-Huang transform (HHT) [9], an important advancement in adaptive nonlinear and nonstationary signal processing.

Conventional radar resolution theory, which is a resolution theory of point targets [10], represents a direct application of the reductionist worldview. Thus, analysis of the single-channel synthetic aperture radar (SAR) image has traditionally been based on linear techniques associated with the image intensity while the phase content is ignored. The insufficiency of the linear resolution theory to extended targets, based on the empirical observation that man-made targets produce dispersive scattering, has been reported in the literature [11–13]. In effect, this induces a nonlinear phase modulation (PM) in the radar return signal which causes a mismatch in the correlator's output. This phenomenon is preserved in the complex-valued image rather than the detected one.

In [11–13], a curve fitting algorithm is used to detect nonlinear scattering in SAR imagery. However, there are two possible drawbacks associated with this approach. Firstly, it is non-adaptive due to its contingency on certain a priori assumptions. Secondly, while it identifies nonlinear scattering in general terms, it neither classifies it nor estimates its order. The feature extraction approach presented in this chapter differs significantly in that it is entirely data driven without any a priori assumptions. Further, our approach is advantageous in that it allows for classifying the dispersive scatterers as well as estimating their nonlinear order. To our knowledge, this capability has not been previously demonstrated in the SAR literature. This provides for significantly utilizing nonlinear phenomena in target recognition applications.

The study in this chapter builds on six previous investigations [14–19]. In [14, 15], an in-depth analysis for nonlinearity in single-channel SAR imagery was conducted. The analysis demonstrated the statistical significance of the nonlinear phenomenon in high-resolution complex-valued SAR imagery. It was also shown that the nonlinear effect is either obliterated or altered/diminished for magnitude and power detections, respectively. In [16–18], a method for characterization and statistical modeling of the phase in single-channel SAR imagery was proposed. Also, the circularity (also known as propriety) in complex-valued SAR imagery was investigated. It was demonstrated that, for the case of extended target, the complex-valued SAR chip is noncircular. In [19], a method for estimating the order of nonlinear dispersive scattering in complex-valued SAR imagery was provided.

The main contributions presented in this study are:

- Development of a new feature set based solely on the phase in single-channel

SAR imagery,

- Development of three complementary 1-D representations for the 2-D real/imaginary parts, bivariate and complex-valued SAR chips. This allows for applying various nonlinear and nonstationary time series analysis methods for feature extraction,
- Development of a new set of features based on the HHT as well as methods motivated by chaos theory including permutation entropy (PE) and detrended fluctuation analysis (DFA), and
- A simple method for feature standardization based on the median and the interquartile range (IQR).

The topic addressed in this chapter is applicable to various kinds of stationary and moving targets including vehicles, ships, airplanes, icebergs, etc. Furthermore, the application of the methods proposed may be extended beyond SAR to include radar in general, sonar, synthetic aperture sonar (SAS), ultrasound, synthetic aperture ultrasound (SAU), etc.

The remainder of this chapter is organized as follows. Firstly, the origin of the nonlinear phenomenon in single-channel SAR imagery is approached in Sect. 7.3. Then, the proposed framework for nonlinear feature extraction based solely on the phase chip is described in Sect. 7.4. Thirdly, the three 1-D representations for the 2-D SAR chip are introduced in Sect. 7.5. Subsequently, methods used for nonlinear feature extraction based solely on the 1-D representations are proposed in Sect. 7.6, and this is followed in Sect. 7.7 by a discussion of the SAR dataset utilized in this study. The overall features used in the study, including the baseline features and the nonlinear features, as well as the proposed procedure for feature normalization, are defined in Sect. 7.8. The process of classifier design and feature selection are outlined in Sect. 7.9, and the overall results are elaborated upon in Sect. 7.10. Finally, conclusions are offered at the end of the chapter in Sect. 7.11.

7.3. Origin of the Nonlinear Phenomenon in SAR Imagery

The baseband backscatter x_{BB} from a single point target, output from the quadrature demodulator and downlinked to the SAR processor, is known as the phase history or

the raw data and is given by [10]

$$x_{BB}(\tau,\eta) = A\exp(j\psi)\left\{w_r\left(\tau - 2\frac{R(\eta)}{\underline{c}}\right)w_a(\eta-\eta_c)\right.$$
$$\left.\exp\left(-j4\pi f_o\frac{R(\eta)}{\underline{c}}\right)\exp\left(j\pi K_r\left(\tau - 2\frac{R(\eta)}{\underline{c}}\right)^2\right)\right\}, \tag{7.1}$$

where A is the backscatter coefficient (i.e., σ_o), ψ is a phase change in the received pulse due to the scattering process from a surface, $j = \sqrt{-1}$, τ is the fast time, η is the slow time, $w_r(\tau) = \text{rect}(\tau/T_r)$ is the transmitted pulse envelope, T_r is the pulse duration, $R(\eta)$ is the distance between the radar and the point target, $\underline{c}$ is the speed of light in a vacuum, $w_a(\eta)$ is the two-way azimuth beam pattern, η_c is the beam center in the azimuth direction, f_o is the center frequency, and K_r is the frequency modulation (FM) rate of the range pulse. The SAR raw signal $x_{BB}(\tau,\eta)$ is conventionally modeled as

$$x_{BB}(\tau,\eta) = g(\tau,\eta)\otimes h(\tau,\eta) + n(\tau,\eta), \tag{7.2}$$

where $\otimes$ denotes convolution, $g(\tau,\eta)$ is the ground reflectivity, $h(\tau,\eta)$ is the impulse response of the SAR, and $n(\tau,\eta)$ is a noise component mainly due to the front-end receiver.

The SAR processor solves for $g(\tau,\eta)$. Following the conventional radar resolution theory, $h(\tau,\eta)$, bounded by the curly brackets in Eq. 7.1, is an impulse response of a point target. For a given reflector within the radar illumination time, ψ is assumed to be constant [10]. For the case of an extended target, this assumption is adopted verbatim. Hence, such a target is modeled as the linear combination of its point reflectors. However, the assumption of constant ψ is violated in the presence of dispersive scattering from cavity-like reflectors, typical in stationary and moving man-made (extended) targets such as vehicles and airplanes. These reflectors trap the incident wave before it is backscattered, thus inducing a phase modulation (PM). The problem arises when the PM is nonlinear. Besides the PM, this phenomenon also introduces amplitude

modulation (AM) [11–13]. Therefore, the backscatter term in Eq. 7.1 is rewritten as

$$s\left(\tau\left(f_\tau\right),\eta\right) = A\left(\tau\left(f_\tau\right),\eta\right)\exp\left(j\psi\left(\tau\left(f_\tau\right),\eta\right)\right), \tag{7.3}$$

where $\tau\left(f_\tau\right)$ is the time delay due to the PM, and f_τ varies over the spectral width of the chirp, B. It should be emphasized that the magnitude and phase of the backscatter in Eq. 7.3 is frequency dependent. While the AM is a linear process, this is often not the case for the PM. Indeed, based on the principle of stationary phase (POSP), the time delay induced by a dispersive scatterer is

$$\tau\left(f_\tau\right) \propto \frac{\mathrm{d}}{\mathrm{d}f}\left(f_\tau\right)^O, \tag{7.4}$$

where O is the order of nonlinearity induced by the dispersive scatterer. For $O \in \{0,1,2\}$, the PM is linear, and its effect is either translation or smearing of the response in the correlation filter. Another reason for the smearing of the response is the variable Doppler processing used for motion compensation. However, for $O \notin \{0,1,2\}$, the phase center possesses a nonlinear delay which introduces spurious effects in the correlator's output. This phenomenon is referred to as 'sideband responses', and the information about it is preserved in the complex-valued image rather than the detected one. Further, in the presence of an extended target, it is empirically observed that this effect dominates the focused SAR imagery [11–13]. The sideband responses are radically different from the range and Doppler sidelobes. One of the reasons for this is that they are among the strongest responses. Secondly, unlike the range and the Doppler sidelobes, the sideband responses are not restricted to the range and cross-range gates. Thirdly, they are distributed over an area far larger than that occupied by the target. As stressed in [11–13], these sideband responses cannot be suppressed by the weighting methods because they are target generated. Obviously, the nonlinear PM violates the resolution theory of point targets.

7.4. Nonlinear Measures Based Solely on the Phase Chip

In a previous work [16, 18], it was demonstrated that the phase in single-channel complex-valued SAR imagery, particularly in the presence of extended target(s), can indeed be statistically well-modeled using the wrapped complex Gaussian scale mixture (WCGSM). A brief overview for our proposed algorithm for phase characterization is presented in Fig. 7.1. The complex-valued SAR chip is available in the form

$$c\left(u,v\right)=i\left(x,y\right)+j\,q\left(x,y\right), \tag{7.5}$$

where $i\left(x,y\right)$ and $q\left(x,y\right)$ are the real and imaginary parts of the complex-valued SAR chip, respectively. Note that (x,y) represent the 2-D Cartesian coordinates of the real-valued plane, while (u,v) represent the 2-D Cartesian coordinates in the complex-valued plane. Hence, the phase chip is given by

$$\Phi\left(x,y\right)=\arg\left\{c\left(u,v\right)\right\}. \tag{7.6}$$

The phase chip $\Phi\left(x,y\right)$ is processed in order to make sense of the information content it carries. This is because, by definition, the phase is always relative and it often appears meaningless if it is not appropriately characterized. Accordingly, the proposed algorithm simply produces the so-called backscatter relative phase image (BRPI). The main idea is that each pixel in the phase chip is characterized in relation to its neighbors. Then, a histogram can be computed based on the BRPI image.

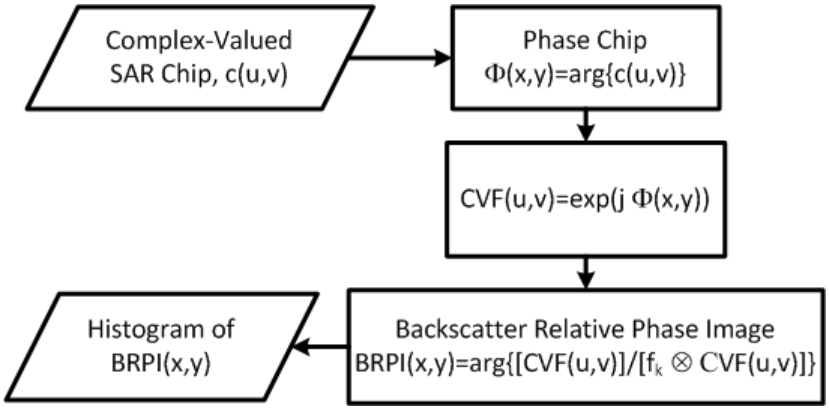

Figure 7.1: Proposed algorithm for phase characterization in SAR imagery.

The BRPI image is computed from the difference between the phase chip and the neighborhood-processed phase chip. The latter is obtained through convolving the phase chip with a kernel f_k. The kernel should have a value of zero in the center and ones where desired. The kernel convolution operation produces an average phase chip for the neighborhood of each pixel in the phase chip. In this study, three kernels are considered as shown in Fig. 7.2. As pointed-out in [16], these kernels were chosen because they are found to produce histograms consistent with typical statistical models.

$$\begin{bmatrix} 1 & 1 & 1 \\ 1 & 0 & 1 \\ 1 & 1 & 1 \end{bmatrix}$$

(a) First kernel.

$$\begin{bmatrix} 1 & 1 & 1 & 1 & 1 \\ 1 & 1 & 1 & 1 & 1 \\ 1 & 1 & 0 & 1 & 1 \\ 1 & 1 & 1 & 1 & 1 \\ 1 & 1 & 1 & 1 & 1 \end{bmatrix}$$

(b) Second kernel.

$$\begin{bmatrix} 1 & 1 & 1 & 1 & 1 & 1 & 1 \\ 1 & 1 & 1 & 1 & 1 & 1 & 1 \\ 1 & 1 & 1 & 1 & 1 & 1 & 1 \\ 1 & 1 & 1 & 0 & 1 & 1 & 1 \\ 1 & 1 & 1 & 1 & 1 & 1 & 1 \\ 1 & 1 & 1 & 1 & 1 & 1 & 1 \\ 1 & 1 & 1 & 1 & 1 & 1 & 1 \end{bmatrix}$$

(c) Third kernel.

Figure 7.2: The three convolution kernels (f_k) considered in this study.

Phase values are in the range $(-\pi, \pi]$ - i.e., the phase values are on a circle where the angles π and $-\pi$ meet at the same point. In order to account for the circularity of the

phase, the phase chip $\Phi(x,y)$ should be first converted to the polar form as follows [1]

$$CVF(u,v) = \exp(j\Phi(x,y)) = \cos\{\Phi(x,y)\} + j\sin\{\Phi(x,y)\}. \tag{7.7}$$

$CVF(u,v)$ has a size of $M_c \times N_c$. The convolution kernel f_k has a size of $M_k \times N_k$. M_k and N_k are typically chosen to be odd values to avoid ambiguity in defining the center pixel. Convolving $CVF(u,v)$ with the kernel f_k at a particular pixel location in the chip (m_c, n_c) yields the convolution image as

$$CI(m_c,n_c) = f_k \otimes CVF(m_c,n_c) = \sum_{m_k=1}^{M_k}\sum_{n_k=1}^{N_k} f_k(m_k,n_k)\, CVF(m_c-m_k, n_c-n_k), \tag{7.8}$$

where $\otimes$ denotes convolution, $m_c \in \{1,2,...,M_c\}$ and $n_c \in \{1,2,...,N_c\}$. The BRPI image is defined as the difference between the phase angles pertaining to the original phase chip and the convolution chip and may be expressed as

$$BRPI(x,y) = \arg\left\{\frac{CVF(u,v)}{CI(u,v)}\right\}. \tag{7.9}$$

The resultant BRPI image defines the characteristic phase of each pixel in the input phase chip $\Phi(x,y)$ relative to its neighborhood as defined by the convolution kernel f_k. The next step involves modeling the three resultant BRPI histograms using the WCGSM model described in [16]. The WCGSM distribution, characterized by two

[1] Processing the polar representation of the phase chip rather than the phase chip per se allows for easily accounting for phase wrapping. This idea is borrowed from the field of directional (also known as circular) statistics. See for example [20–22]. The term 'circular' stems from the fact that the phase values are on a circle where the angles π and $-\pi$ meet at the same point. In directional statistics, 'phase wrapping' is also called 'phase circularity'. This is not to be confused with circularity/noncircularity discussed later in this chapter.

parameters, is given by

$$WCGSM\left(\underline{\phi},\lambda\right)\equiv p\left(\Phi_{brpi}\right)=\frac{1-\lambda^{2}}{2\pi\left(1-\chi^{2}\right)}\left(\frac{\chi\,\arccos\left(\chi\right)}{\left(1-\chi^{2}\right)^{0.5}}+1\right), \tag{7.10}$$

where,

$$\chi=\lambda\,\cos\left(\Phi_{brpi}-\underline{\phi}+\pi\right). \tag{7.11}$$

The parameters of the WCGSM model are estimated as discussed below. First, it was empirically observed that the location parameter $\underline{\phi}$ can be accurately estimated using the circular mean of the BRPI image which is defined as

$$\hat{\underline{\phi}}=\arg\left(\frac{1}{n}\sum_{i=1}^{n}\exp\left(j\Phi_{brpi,i}\right)\right), \tag{7.12}$$

where n is the total number of samples in the BRPI image. The parameter λ is the shape parameter of the WCGSM distribution which is estimated based on a simple fitting procedure utilizing the the Jensen–Shannon (JS) divergence (see Sect. 6.6.1.5 for details). Once the three histograms pertaining to the three kernels are modeled using the three WCGSM models, features based on the WCGSM probability density function (PDF) can be extracted (see Sect. 7.8.2.1).

Besides the features based on the WCGSM model, it is possible to extract useful features directly from the BRPI image given in Eq. 7.9. One such important measure is the circularity/noncircularity which is also known as propriety/impropriety, respectively [23, 24]. Circularity means that the BRPI image has a PDF that is invariant under rotation in the complex plane. This also implies that the BRPI image is uncorrelated with its complex-conjugate. In [16, 18], it was shown that through utilizing the BRPI image, it is possible to characterize the noncircularity in the phase chip. This is achieved by using the modulus of the pseudo-covariance [23, 25, 26]

$$\left|\Psi\right|=\left|E\left\{\underline{\mathbf{BRPI}}\,\underline{\mathbf{BRPI}}^{T}\right\}\right|,\ 0<\left|\Psi\right|<1. \tag{7.13}$$

where $E\{.\}$ denotes the expectation, **BRPI** is the polar representation of $BRPI$ after conversion to a 1-D vector, and T denotes the transpose. Note that if $|\Psi| = 0$, then $BRPI$ is said to be second-order circular, or proper. Further, the angle of Ψ is also used in this study as

$$\angle\Psi = \arg\{\Psi\}. \tag{7.14}$$

7.5. Linear Transformation of 2-D SAR Chips to 1-D Space

This section presents three complementary algorithms to transform the 2-D SAR chip into an abstract 1-D vector that accounts for the pixel neighborhood. Our method is inspired by the Radon transform. The remainder of this section is organized as follows. First, a description for the forward Radon transform is given in Sect. 7.5.1. Second, a method for linear transformation of the real and the imaginary parts of the complex-valued 2-D SAR chip into a 1-D vector is presented in Sect. 7.5.2. Third, a method for linear transformation of the bivariate 2-D SAR chip into a 1-D vector is described in Sect. 7.5.3. Finally, Sect. 7.5.4 describes a method for linear transformation of the complex-valued 2-D SAR chip into a 1-D vector.

7.5.1. The Forward Radon Transform

The Radon transform $R_\theta(x')$ for a 2-D function $f(x, y)$ is the line integral of f parallel to the y' axis defined as [27]

$$R_\theta(x') = \int_{-\infty}^{\infty} f(x'\cos\theta - y'\sin\theta, x'\sin\theta + y'\cos\theta)\, dy', \tag{7.15}$$

where θ is the projection angle, and (x', y') are the projection coordinates which are related to the projection angle as

$$\begin{bmatrix} x' \\ y' \end{bmatrix} = \begin{bmatrix} \cos\theta & \sin\theta \\ -\sin\theta & \cos\theta \end{bmatrix} \begin{bmatrix} x \\ y \end{bmatrix}. \tag{7.16}$$

The geometry of the Radon transform is illustrated in Fig. 7.3. Note that the (x', y') coordinate is rotated about the center of the image as shown in Fig. 7.3. Among the main advantages of the Radon transform is that it is computed directly in the spatial domain, and it is a linear transform [27]. Hence, it preserves the statistics present in the original 2-D SAR chip without introducing any nonlinear artifacts.

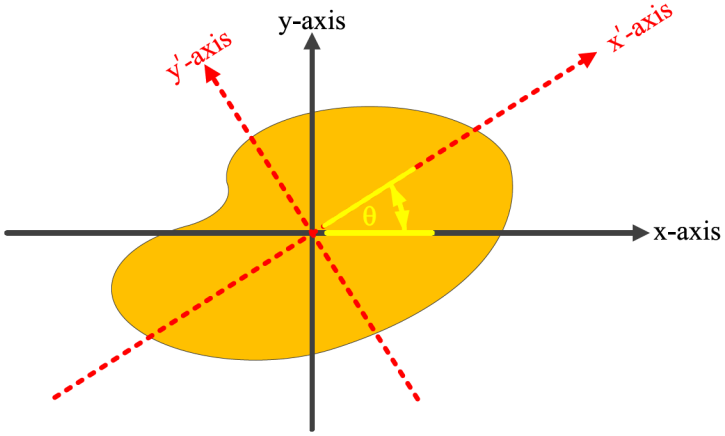

Figure 7.3: Illustration of the Radon transform for a projection angle θ. The random shape provided represents the 2-D function $f(x, y)$.

7.5.2. A Method for Linear Transformation of the Real and the Imaginary Parts of the 2-D SAR Chip into a 1-D Vector

Under this subsection, a procedure for transforming the real and the imaginary parts of the 2-D complex-valued SAR chip into a 1-D vector, utilizing the Radon transform, is proposed. Our proposed procedure is depicted in Fig. 7.4.

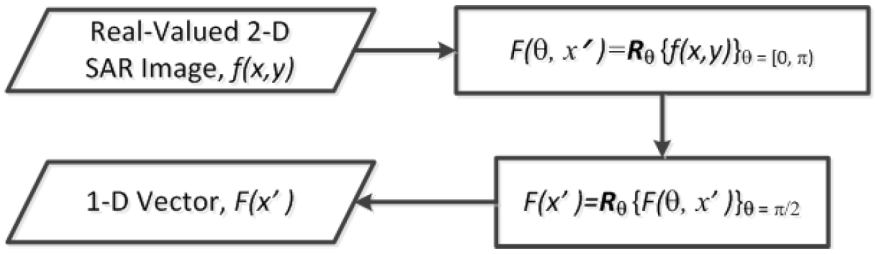

Figure 7.4: Proposed procedure for transforming the real and imaginary parts of the 2-D complex-valued SAR chip into a 1-D vector.

The Radon transform is applied separately to the real and imaginary parts of the complex-valued SAR chip (see Eq. 7.5) as

$$I\left(\theta, x'\right) = R_{\theta}\left\{i\left(x, y\right)\right\}\big|_{\theta=[0,\pi)}. \tag{7.17}$$

$$Q\left(\theta, x'\right) = R_{\theta}\left\{q\left(x, y\right)\right\}\big|_{\theta=[0,\pi)}. \tag{7.18}$$

Note that angles in the range $[\pi, 2\pi]$ are omitted because their corresponding Radon transform provides identical values to angles in the range $[0, \pi)$. This redundant information is of no interest in this study. Also, note that the Radon transform representation given by Eq. 7.17 and Eq. 7.18 is known as a *sinogram*. In the next step, the projection angles $\theta = [0, \pi)$ are integrated-out. This is achieved through applying the Radon transform to the sinograms at a projection angle $\phi = \frac{\pi}{2}$ as

$$I\left(x'\right) = R_{\phi}\left\{I\left(\theta, x'\right)\right\}\big|_{\phi=\frac{\pi}{2}}. \tag{7.19}$$

$$Q\left(x'\right) = R_{\phi}\left\{Q\left(\theta, x'\right)\right\}\big|_{\phi=\frac{\pi}{2}}. \tag{7.20}$$

The output given by Eq. 7.19 and Eq. 7.20 is an abstract 1-D vector representative of the real and imaginary parts of the complex-valued SAR chip.

7.5.3. A Method for Linear Transformation of the Bivariate 2-D SAR Chip into a 1-D Vector

Under this subsection, a procedure for transforming the bivariate SAR chip into a real-valued 1-D vector is proposed. The term bivariate is used here to denote that the real and imaginary parts of the complex-valued SAR chip are treated as two separate real-valued chips. This is in analogy to the bivariate distribution (e.g., bivariate Gaussian) which is used to model complex-valued data in such a manner (see page 20 in [24]). The procedure proposed here is meant to account for the bivariate statistics between the real and imaginary parts of the complex-valued SAR chip. Fig. 7.5 depicts our proposed procedure.

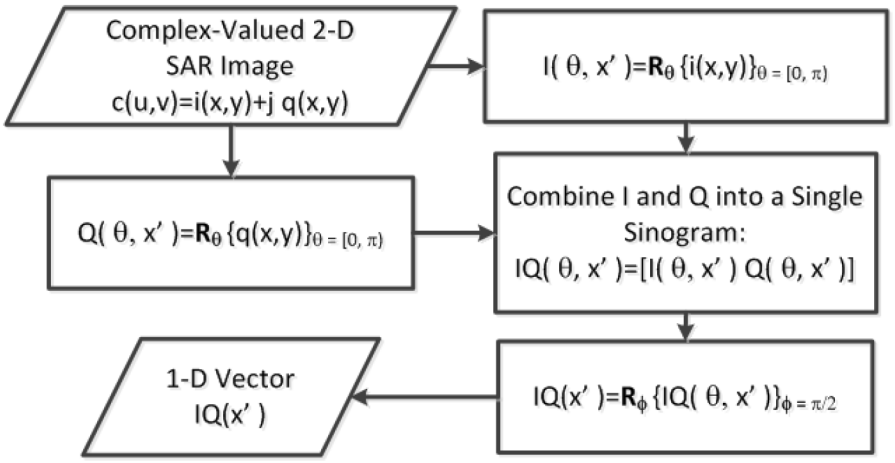

Figure 7.5: Proposed procedure for transforming the bivariate 2-D SAR chip into a 1-D vector.

The two sinograms output from Eq. 7.17 and Eq. 7.18, respectively, are combined together into a single sinogram as follows

$$IQ\left(\theta, x'\right) = \left[I\left(\theta, x'\right)\ Q\left(\theta, x'\right)\right]. \tag{7.21}$$

Note that Matlab notation is used in Eq. 7.21 to denote that the two sinograms are concatenated horizontally, along the second dimension. Thus, the resultant sinogram has the same number of rows as in the original sinogram (i.e., $I(\theta, x')$ and $Q(\theta, x')$ have similar dimensions), and the number of columns is doubled. In the next step, the projection angles $\theta = [0, \pi)$ are integrated-out. This is achieved through applying the Radon transform to the combined sinogram output from Eq. 7.21 at a projection angle $\phi = \frac{\pi}{2}$ as follows

$$IQ(x') = R_{\phi}\left\{IQ(\theta, x')\right\}|_{\phi=\frac{\pi}{2}}. \tag{7.22}$$

The output given by Eq. 7.22 is an abstract 1-D vector representative of the bivariate statistics in the input 2-D complex-valued SAR chip.

7.5.4. A Method for Linear Transformation of the Complex-Valued 2-D SAR Chip into a 1-D Vector

The procedure described in Sect. 7.5.3 accounts for the bivariate statistics between the real and imaginary parts of the complex-valued SAR chip. However, the complex-valued statistics [24] are not meant to be accounted for by this procedure. To account for these statistics, a simple procedure is proposed under this subsection. First, the real and the imaginary parts of the complex-valued SAR chip are suitably amalgamated in the spatial-domain as

$$fu_{iq}(x, y) = \text{furud}\left(i(x, y), q(x, y)\right). \tag{7.23}$$

This procedure, referred to as *furud'ing,* was inspired by the spectroscopic binary in the constellation Canis Major known with the traditional name Furud [28–31]. Fig. 7.6 demonstrates our proposed furud'ing procedure.

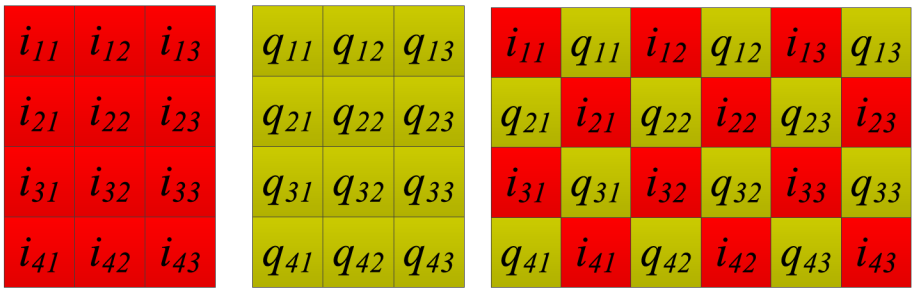

(a) Real-part of the complex-valued SAR chip, $i\,(x,y)$.

(b) Imaginary-part of the complex-valued SAR chip, $q\,(x,y)$.

(c) Furud'ed chip, $fu_{iq}\,(x,y)$.

Figure 7.6: Our proposed furud'ing procedure.

In the next step, the real-valued furud chip is transformed to a 1-D vector by inputting it to the proposed algorithm introduced in Fig. 7.4. The final output is given by

$$Fu_{iq}\,(x') = R_{\phi}\left\{R_{\theta}\left\{fu_{iq}\,(x,y)\right\}|_{\theta=[0,\pi)}\right\}\Big|_{\phi=\frac{\pi}{2}}. \tag{7.24}$$

7.6. Nonlinear Measures Based Solely on the 1-D Representation

In this section, the nonlinear measures considered in this study and based on the 1-D representation of the SAR chip are presented. Some of these measures are directly based on the 1-D Radon representations discussed earlier while some others are based on the Hilbert spectrum computed from the 1-D Radon representations. The remainder of this section is organized as follows. In Sect. 7.6.1, a brief overview for the Hilbert-Huang transform (HHT) [9] along with a few proposed modifications is presented. Further, in Sect. 7.6.2, a selection of relevant methods used in this study for quantifying the nonlinear dynamics is provided.

7.6.1. Hilbert-Huang Transform (HHT)

HHT represents an advancement in nonlinear and nonstationary signal processing [9]. Firstly, it uses a technique known as empirical mode decomposition (EMD) to decompose the data, according to their characteristic scales, into a set of intrinsic mode functions (IMFs). Thus, unlike Fourier-based methods, the basis of the data comes from the data itself. Secondly, the IMFs are used to construct a time/space-frequency-energy distribution known as the Hilbert spectrum. Subsequently, the time/space localities of the events are preserved. Therefore, the frequency and energy defined by the Hilbert transform have intrinsic and instantaneous physical meaning. Although the term 'spectrum' and 'frequency' are traditionally associated with the Fourier-based analysis, the HHT provides a different interpretation for these terms. In doing so, the HHT avoids the Heisenberg principle, which is a serious setback to all Fourier-based time/space-frequency methods including the Fourier-based wavelet transform [9, 32].

In this study, the ensemble EMD (EEMD) [33] is applied to the outputs given by Eq. 7.19 and Eq. 7.20 separately. EEMD is a noise-assisted method which resolves the problem of mode mixing encountered in the traditional EMD [9]. Primarily, EEMD decomposes the input data to a small number of IMFs based on the local characteristic time/space scale. An IMF represents a simple oscillatory mode as a counterpart to the harmonic function. By definition, an IMF is any function with the same number of extrema and zero-crossings, with its envelopes being symmetric with respect to zero. This definition guarantees a well-behaved Hilbert transform of the IMF. The procedure of extracting an IMF is called sifting. In our subsequent analysis, we use a local stopping criterion for the sifting process as prescribed in [33]. Thus, an $\underline{m}$ number of IMFs is extracted from $I(x')$ and $Q(x')$ as

$$\begin{aligned} I(x') &= \sum_{a=1}^{\underline{m}} \left[I_{IMF}(x')\right]_a + r_I(x'), \\ Q(x') &= \sum_{a=1}^{\underline{m}} \left[Q_{IMF}(x')\right]_a + r_Q(x'). \end{aligned} \tag{7.25}$$

where $r_I(x')$ and $r_Q(x')$ are the residues. The total number of IMFs is specified as [9]

$$\underline{m} = \log_2(\underline{n}) - 1, \tag{7.26}$$

where $\underline{n}$ is the length of the original 1-D signal. In order to calculate the Hilbert spectrum, two methods are used in this study [34, 35]: the direct quadrature (DQ) method and the generalized zero-crossing (GZC) method. The DQ method is based on the analytic signal for each IMF. Traditionally, the HHT transform achieves this through computing the Hilbert transform for the IMF, and the result is placed in the imaginary-part of the analytic signal. The real-part is the IMF signal itself. However, according to the Paley-Wiener theorem, the complex-valued signal output from the quadrature demodulator is indeed an analytic signal where its imaginary-part is simply the Hilbert transform of its real-part [36]. Hence, we form the analytic signals based on proper combination of the real and the imaginary parts for each IMF according to

$$[H_{DQ}(x')]_a = [I_{IMF}(x')]_a + j\ [Q_{IMF}(x')]_a\,, \tag{7.27}$$

where $a \in \{1, ..., \underline{m}\}$. Note that this representation is known as the Hilbert spectrum. Thus, the instantaneous magnitude of the Hilbert spectrum is given by

$$[b_{DQ}(x')]_a = \left([I_{IMF}(x')]_a^2 + [Q_{IMF}(x')]_a^2\right)^{0.5}. \tag{7.28}$$

Further, the unwrapped instantaneous phase for the Hilbert spectrum is computed as

$$[h_{DQ}(x')]_a = \mathfrak{unwrap}\left(\arg\left\{[H_{DQ}(x')]_a\right\}\right), \tag{7.29}$$

where $\mathfrak{unwrap}$ denotes the addition of multiples of $\pm 2\pi$ when absolute jumps between consecutive elements of $[h_{DQ}(x')]_a$ are greater than or equal to the default jump tolerance of π radians. Subsequently, the instantaneous frequency is computed following

the definition of POSP as

$$[IF_{DQ}(x')]_a = \frac{\mathrm{d}}{\mathrm{d}x'}[h_{DQ}(x')]_a . \tag{7.30}$$

In the GZC method, the instantaneous frequency $[IF_{GZC}(x')]_a$ is defined for the whole wave (i.e., based on the real-part of each IMF in our case), which includes the values from crest-to-crest, trough-to-trough and up (down) zero-crossing to up (down) zero-crossing. The corresponding $b_{GZC}(.)$ is denoted $[b_{GZC}(x')]_a$ (see [34, 35] for details).

7.6.2. Quantifying the Nonlinear Dynamics

Under this subsection, the nonlinear measures used in this study are presented. First, the order of nonlinearity is described in Sect. 7.6.2.1. Second, the degree of nonlinearity is elaborated on in Sect. 7.6.2.2. Third, the combined degree of nonlinearity is described in Sect. 7.6.2.3. Fourth, the permutation entropy (PE) is introduced in Sect. 7.6.2.4. Finally, the scaling exponent, based on detrended fluctuation analysis (DFA), is discussed in Sect. 7.6.2.5.

7.6.2.1. Order of Nonlinearity

The average frequency for the cycles of the instantaneous frequency and the real-part of each IMF, respectively, are computed from

$$[f_{IF}]_a = f_{avg}\left\{[IF_{DQ}(x')]_a\right\} , \tag{7.31}$$

$$[f_I]_a = f_{avg}\{[I_{IMF}(x')]_a\} . \tag{7.32}$$

Note that $[f_{IF}]_a$ is the intrawave frequency and $[f_I]_a$ is the corresponding oscillation

frequency. Thus, we compute the nonlinear order for each IMF as [9, 34, 37]

$$[O]_a = \frac{[f_{IF}]_a}{[f_I]_a} + 1. \tag{7.33}$$

$\frac{[f_{IF}]_a}{[f_I]_a} < 1$ implies that $[f_{IF}]_a$ is undersampled. This means that the estimate of $[O]_a$ based on such values is incorrect or at least inaccurate. Thus, we do not use the undersampled frequencies for order estimation in this study. Note that in Eq. 7.31, it is possible to replace the average with the median [38].

7.6.2.2. Degree of Nonlinearity

For each IMF, the degree of nonlinearity, DN_a, can be computed as [34]

$$DN_a = \text{std}\left\langle \left[\frac{[IF_{DQ}(x')]_a - [IF_{GZC}(x')]_a}{[IF_{GZC}(x')]_a} \right] \frac{[b_{GZC}(x')]_a}{[\bar{b}_{GZC}(x')]_a} \right\rangle, \tag{7.34}$$

where std denotes the standard deviation and $[\bar{b}_{GZC}(x')]_a$ is the mean value for $[b_{GZC}(x')]_a$. It is possible to replace std with the interquartile range (IQR) [39]. It is also possible to replace the mean value for $[b_{GZC}(x')]_a$ with the median.

7.6.2.3. Combined Degree of Nonlinearity

The combined degree of nonlinearity, CDN, weighs the degree of nonlinearity for each IMF by the energy in each IMF as [34]

$$CDN = \sum_{a=1}^{m} DN_a \frac{[E_{IMF}]_a^2}{\sum_{k=1}^{m} [E_{IMF}]_k^2}, \tag{7.35}$$

where $[E_{IMF}]_a^2$ is the energy in the real-part of the analytic signal pertaining to each IMF (i.e., $[I_{IMF}(x')]_a$).

7.6.2.4. Permutation Entropy

Permutation entropy (PE) [40] is a simple yet robust complexity measure for a time series based on its neighboring values. In analogy to relevant measures for chaotic dynamical systems, PE behaves similar to the Lyapunov exponent, and it is found to be useful, particularly in the presence of nonlinear dynamics in the signal. To take into account the causal information pertaining to any effects stemming from the temporal order of the successive elements of the time series, the time series is encoded first into sequences of symbols, based on the theory of symbolic dynamics. Then, the entropy is computed for the encoded sequence as follows [40]

$$H_{\underline{c}} = -\sum_{\underline{c}=1}^{l!} \grave{p}_{\underline{c}} \log_2 \left(\grave{p}_{\underline{c}} \right). \tag{7.36}$$

Here, $\grave{p}_{\underline{c}}$ represents the relative frequencies of the possible patterns of symbol sequences, termed permutations, and l is an important parameter for the number of possible permutation patterns. Also, note that in computing $\grave{p}_{\underline{c}}$ there is an important parameter called τ which describes the time delay between successive points in the symbol sequence. Detailed description for the PE algorithm as well as important practical recommendations for choosing the two parameters can be found in [41].

7.6.2.5. Scaling Exponent based on Detrended Fluctuation Analysis (DFA)

Detrended fluctuation analysis (DFA) is a simple technique for identifying the extent of fractal self-similarity in a nonstationary time series based on the calculation of a scaling exponent α. First, $x(\tilde{n})$ the time series to be analyzed is integrated to produce a self-similar random walk [42, 43]

$$y\left(\tilde{n}\right) = \sum_{\underline{\rho}=1}^{\tilde{n}} x\left(\underline{\rho}\right). \tag{7.37}$$

Then, $y(\tilde{n})$ is successively subdivided into windows of length L samples. For a time series of length M samples there will be the nearest integer to $\log_2 M$ scales. A least-

squares straight line local trend is calculated by analytically minimizing the squared error E^2 over the slope and intercept parameters a and b as [42, 43]

$$\arg\min_{a,\,b} E^2 = \sum_{\tilde{n}=1}^{L} \left(y\left(\tilde{n}\right) - a\tilde{n} - b\right)^2 . \tag{7.38}$$

Then, the fluctuation is calculated over all windows at each time scale as [42, 43]

$$F\left(L\right) = \left[\frac{1}{L}\sum_{\tilde{n}=1}^{L} \left(y\left(\tilde{n}\right) - a\tilde{n} - b\right)^2\right]^{0.5} . \tag{7.39}$$

On a log-log graph of L vs. $F(L)$, a straight line indicates self-similarity expressed as $F\left(L\right) \propto \alpha$. The scaling exponent α is calculated as the slope of a straight line fit to the log-log graph of L vs. $F(L)$ using least-squares as above (see [42, 43] for more details).

7.7. The SAR Dataset

This study utilizes a comprehensive public-domain single-channel (i.e., HH polarization) and single look complex-valued (SLC) SAR dataset collected and distributed under the DARPA moving and stationary target recognition (MSTAR) program [44]. Sandia National Laboratory used an X-band STARLOS sensor in Spotlight mode to collect the data. The MSTAR dataset provides a nominal spatial resolution of 0.3047×0.3047 metres in both range and azimuth. The data used in this study comes from two CDs available from the Sensor and Data Management System (SDMS) and entitled MSTAR/IU Mixed Targets CD1 and CD2. In total, for each CD there are eight different types of stationary targets imaged at azimuth angles covering the full span of [0°, 360°). CD1 and CD2 include SAR data collected at 15° and 17° depression angles, respectively. In this chapter, the 17° dataset is used for training the classifier while the 15° dataset is used for testing the classifier. A list for the target names and the overall number of the complex-valued SAR chips used in this study is provided in Table 7.1. Ground-truth pictures for the eight targets are depicted in Fig. 7.7.

Table 7.1: List of the MSTAR targets used in this study.

Target Name	No. of Training Chips (17^o depression angle)	No. of Testing Chips (15^o depression angle)
BTR-60	256	195
2S1	299	274
BRDM-2	298	274
D7	299	274
T62	299	273
ZIL-131	299	274
ZSU-23/4	299	274
SLICY	298	274

(a) BTR-60.

(b) 2S1.

(c) BRDM-2.

(d) D7.

(e) T62.

(f) ZIL-131.

(g) ZSU-23/4.

(h) SLICY.

Figure 7.7: Ground-truth pictures for the MSTAR targets used in this study [44].

7.8. Feature Extraction

This section presents the three feature sets utilized in this study. First, the baseline features extracted from the power-detected SAR chips are provided in Sect. 7.8.1. Then, features based on the nonlinear dynamics, extracted both from the phase chips and the 1-D representations, are introduced in Sect. 7.8.2. Finally, feature normalization is described in Sect. 7.8.3.

7.8.1. Baseline Features

Baseline features are solely based on the power-detected SAR chip. Nineteen baseline features are utilized in this study. The procedure for extracting the baseline features is summarized in Fig. 7.8. First, the complex-valued SAR chip is power-detected as

$$p\left(x,y\right) = \left[i\left(x,y\right)\right]^2 + \left[q\left(x,y\right)\right]^2 . \tag{7.40}$$

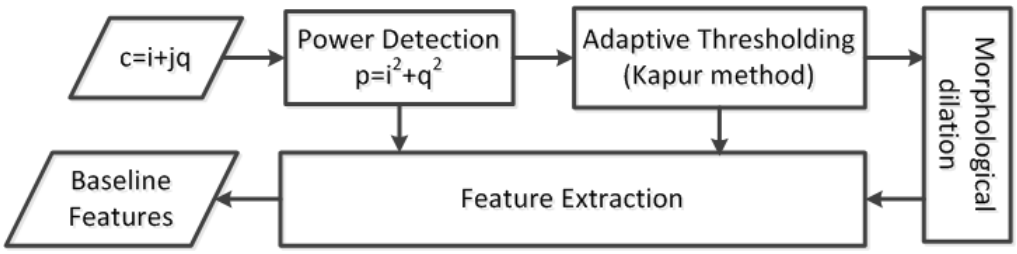

Figure 7.8: Procedure for extraction of the baseline features.

Then, the power-detected SAR chip is thresholded through an adaptive information theoretic approach based on the entropy of the histogram as originally proposed by Kapur *et al.* [45]. This method was chosen because it is found to offer excellent performance. Further, morphological dilation is applied to the thresholded image [46]. This operation is aimed at merging the relevant different connected regions in the thresholded image into one contiguous region representative of the target extent. In the next step, a set of features is extracted from the binary image, the dilated binary

image, and the gray-level image. These extractions are meant to represent the power-based features commonly used in the literature, and they include the following [47]:

- Number of scattering centers (f_{BL1}): the number of connected regions in the binary image.
- Area (f_{BL2}): the total number of pixels with value of one in the binary image.
- Centroid (f_{BL3}, f_{BL4}): the 'center of mass' of the dilated binary image. Note that the first element (f_{BL3}) is the horizontal coordinate (or x-coordinate) of the center of mass, and the second element (f_{BL4}) is the vertical coordinate (or y-coordinate).
- Major axis length (f_{BL5}): the length (in pixels) of the major axis of the ellipse that has the same normalized second central moments as the region. This measure is based on the dilated binary image.
- Minor axis length (f_{BL6}): the length (in pixels) of the minor axis of the ellipse that has the same normalized second central moments as the region. This measure is also based on the dilated binary image.
- Eccentricity (f_{BL7}): the eccentricity of the ellipse that has the same second-moments as the region. The eccentricity is the ratio of the distance between the foci of the ellipse and its major axis length. The value is between 0 and 1. This measure is also based on the dilated binary image.
- Orientation (f_{BL8}): the angle (in degrees ranging from -90^o to 90^o) between the x-axis and the major axis of the ellipse that has the same second-moments as the region. This measure is also based on the dilated binary image.
- Convex area (f_{BL9}): the number of pixels in the convex hull that specifies the smallest convex polygon that can contain the region. This measure is also based on the dilated binary image.
- Euler number (f_{BL10}): the number of objects in the region minus the number of holes in those objects. This measure is based on the binary image.
- Equivalent diameter (f_{BL11}): the diameter of a circle with the same area as the region. Computed as $\sqrt{\frac{4}{\pi} f_{BL2}}$. This measure is based on the dilated binary image.
- Solidity (f_{BL12}): the proportion of the pixels in the convex hull that are also in the region, computed as $\frac{f_{BL2}}{f_{BL9}}$. This measure is also based on the dilated binary

image.

- Extent (f_{BL13}): the ratio of pixels in the region to pixels in the total bounding box. Computed as $\frac{f_{BL2}}{\text{Area of the Bounding Box}}$. This measure is also based on the dilated binary image.
- Perimeter (f_{BL14}): the distance between each adjoining pair of pixels around the border of the region. This measure is also based on the dilated binary image.
- Weighted centroid (f_{BL15}, f_{BL16}): the center of the region based on location and intensity value. The first element (f_{BL15}) is the horizontal coordinate (or x-coordinate) of the weighted centroid. The second element (f_{BL16}) is the vertical coordinate (or y-coordinate). This measure is based on both the dilated binary image as well as the power-detected intensity image.
- Mean intensity (f_{BL17}): the mean of all the intensity values in the region of the power-detected image as defined by the dilated binary image.
- Minimum intensity (f_{BL18}): the value of the pixel with the lowest intensity in the region of the power-detected image as defined by the dilated binary image.
- Maximum intensity (f_{BL19}): the value of the pixel with the greatest intensity in the region of the power-detected image as defined by the dilated binary image.

7.8.2. Features Based on the Nonlinear Dynamics

In this study, there are two sets of features based on the nonlinear dynamics in the SAR chip. First, the nonlinear features based solely on the phase image are presented in Sect. 7.8.2.1. Then, the nonlinear features based solely on the 1-D representations of the SAR chip are described in Sect. 7.8.2.2.

7.8.2.1. Nonlinear Features Based Solely on the Phase Image

While various types of features can be extracted based on the BRPI image as well as the WCGSM model described in Sect. 7.4, a set of fifteen features are considered in this study for demonstration purposes as follows:

- The location parameter based on the first kernel (f_{Ph1}): this is the location parameter $\hat{\underline{\phi}}$ of the WCGSM PDF for the first kernel (see Fig. 7.2), estimated based on Eq. 7.12.

- The shape parameter based on the first kernel (f_{Ph2}): this is the shape parameter $\hat{\lambda}$ of the WCGSM PDF for the first kernel (see Fig. 7.2), estimated based on the JS divergence method (see [16]).
- Maximum peak value for the first kernel (f_{Ph3}): this is the peak value for the WCGSM PDF based on the first kernel.
- The location parameter based on the second kernel (f_{Ph4}): this is the location parameter $\hat{\underline{\phi}}$ of the WCGSM PDF for the second kernel (see Fig. 7.2), estimated based on Eq. 7.12.
- The shape parameter based on the second kernel (f_{Ph5}): this is the shape parameter $\hat{\lambda}$ of the WCGSM PDF for the second kernel (see Fig. 7.2), estimated based on the JS divergence method (see [16]).
- Maximum peak value for the second kernel (f_{Ph6}): this is the peak value for the WCGSM PDF based on the second kernel.
- The location parameter based on the third kernel (f_{Ph7}): this is the location parameter $\hat{\underline{\phi}}$ of the WCGSM PDF for the third kernel (see Fig. 7.2), estimated based on Eq. 7.12.
- The shape parameter based on the third kernel (f_{Ph8}): this is the shape parameter $\hat{\lambda}$ of the WCGSM PDF for the third kernel (see Fig. 7.2), estimated based on the JS divergence method (see [16]).
- Maximum peak value for the third kernel (f_{Ph9}): this is the peak value for the WCGSM PDF, based on the third kernel.
- First pseudo-covariance measure (f_{Ph10}): this is the measure given in Eq. 7.14 and based on the first kernel.
- Second pseudo-covariance measure (f_{Ph11}): this is the measure given in Eq. 7.14 and based on the second kernel.
- Third pseudo-covariance measure (f_{Ph12}): this is the measure given in Eq. 7.14 and based on the third kernel.
- First noncircularity measure (f_{Ph13}): this is the measure given in Eq. 7.13 and based on the first kernel.
- Second noncircularity measure (f_{Ph14}): this is the measure given in Eq. 7.13 and based on the second kernel.
- Third noncircularity measure (f_{Ph15}): this is the measure given in Eq. 7.13 and

based on the third kernel.

7.8.2.2. Nonlinear Features Based Solely on 1-D Representations

Prior to converting the SAR chips from 2-D to 1-D space (see Sect. 7.5), it is important that all the SAR chips are zero-padded to a standardized size. This guarantees the compatibility of similar feature measures extracted from different target chips. For the MSTAR dataset considered it is noted that the size of the SAR chips varies from 54×54 pixels (i.e., for SLICY) to 193×192 pixels (i.e., for ZIL-131). Hence, each SAR chip is zero-padded on all sides to yield a standardized size of 200×200 pixels. Then, the nonlinear measures presented in Sect. 7.6 are invoked. In total, ninety eight nonlinear features are extracted from the 1-D representations of the SAR chip. These features are described as follows:

- Features based on the IMFs (f_{NL1} to f_{NL32}): In this study, the 1-D representation of the real and imaginary parts of the complex-valued SAR chip are decomposed using EEMD into eight distinct IMFs pairs. For each pair of the IMFs, the average frequency is calculated based on the real-part (f_{NL1}) as described by Eq. 7.32, the average instantaneous frequency based on the real and imaginary parts (f_{NL2}) as described by Eq. 7.31, the order of nonlinearity (f_{NL3}) as estimated by Eq. 7.33, and the degree of nonlinearity (f_{NL4}) as shown in Eq. 7.34.
- Combined degree of nonlinearity (f_{NL33}): this is calculated based on Eq. 7.35.
- Features based on the PE for the combination of the IMF pairs (f_{NL34} to f_{NL41}): the real and imaginary parts of each IMF pair are combined into one vector (i.e., $[[I_{IMF}(x')]_a, [Q_{IMF}(x')]_a]$); then, the PE is computed for the combined vector as described in Sect. 7.6.2.4. Note that all the PE computations in this chapter are based on the order of appearance where first occurrence implies a lower rank (see [41] for details). The number of permutation patterns (l) is set to 3. The time delay (τ) between successive points in the symbol sequence is set to 1. These parameters are used in all subsequent computations of the PE, and they were chosen following the recommendations provided in [41].
- Features based on the PE of the instantaneous frequency of the Hilbert spectrum calculated based on the DQ method (f_{NL42} to f_{NL49}): these are the PEs of the eight vectors (i.e., $[IF_{QD}(x')]_a$) produced by Eq. 7.30.

- Features based on the PE of the magnitude of the Hilbert spectrum calculated based on the DQ method (f_{NL50} to f_{NL57}): these are the PEs of the eight vectors (i.e., $[b_{QD}(x')]_a$) produced by Eq. 7.28.
- Features based on the PE of the instantaneous frequency of the Hilbert spectrum calculated based on the GZC method (f_{NL58} to f_{NL65}): these are the PEs of the eight vectors produced from $[IF_{GZC}(x')]_a$ (see Sect. 7.6.1).
- Features based on the PE of the magnitude of the Hilbert spectrum calculated based on the GZC method (f_{NL66} to f_{NL73}): these are the PEs of the eight vectors produced from $[b_{GZC}(x')]_a$ (see Sect. 7.6.1).
- Features based on the PE of the instantaneous frequency of the Hilbert spectrum calculated based on combination of the DQ and GZC methods (f_{NL74} to f_{NL81}): these are the PEs of the eight vectors produced from the combination given by $\left[[IF_{QD}(x')]_a, [IF_{GZC}(x')]_a\right]$.
- Features based on the PE of the magnitude of the Hilbert spectrum calculated based on the combination of the DQ and GZC methods (f_{NL82} to f_{NL89}): these are the PEs of the eight vectors produced from the combination given by $\left[[b_{QD}(x')]_a, [b_{GZC}(x')]_a\right]$.
- Features based on the PE of the 1-D Radon signals (f_{NL90} to f_{NL94}): this set of features are directly extracted from the 1-D Radon representation for the real-part (f_{NL90}) described in Eq. 7.19, the imaginary-part (f_{NL91}) described in Eq. 7.20, the combination of the real and imaginary parts into a 1-D vector (f_{NL92}), the bivariate representation (f_{NL93}) described in Eq. 7.22, and finally, the furud'ed representation (f_{NL94}) described in Eq. 7.24.
- Fluctuation index features based on the 1-D Radon signals (f_{NL95} to f_{NL98}): this set of features are directly extracted from the 1-D Radon representation for the real-part (f_{NL95}), the imaginary-part (f_{NL96}), the bivariate representation (f_{NL97}), and the furud'ed representation (f_{NL98}).

7.8.3. Feature Normalization

Feature standardization and feature scaling are two important aspects pertaining to feature normalization in this study. In the machine learning literature (see, for example, [48]) and its applications to target detection and classification in SAR imagery

(see, for example, [49] and [50]), feature standardization makes the values of each feature in the dataset have zero-mean and unit-variance and is defined as

$$\mathbf{f}_Z = \frac{\mathbf{f} - \hat{\mu}}{\hat{\sigma}}, \tag{7.41}$$

where $\mathbf{f}$ is feature vector, $\hat{\mu}$ is the sample mean of $\mathbf{f}$, and $\hat{\sigma}$ is the sample standard deviation of $\mathbf{f}$. In statistics, this standardization procedure is known as the standard score or the z-score [51]. A major assumption in Eq. 7.41 is that the data in $\mathbf{f}$ follows the Gaussian distribution, and the sample $\hat{\mu}$ and $\hat{\sigma}$ are similar or at least close to the population's mean (μ) and standard deviation ($\underline{\sigma}$). The second assumption is often unrealistic. For the feature set considered in this study, we noted that the feature vectors are not Gaussian distributed, and we found that standardization following Eq. 7.41 degrades the classification accuracy of the classifier. Accordingly, $\hat{\mu}$ and $\hat{\sigma}$, respectively, are replaced with the median and the interquantile range (IQR) as follows

$$\mathbf{f}_R = \frac{\mathbf{f} - \text{median}}{\text{IQR}}, \tag{7.42}$$

These two measures are borrowed from the field of robust statistics [38]. Robust statistics seek to provide methods that emulate popular statistical methods, but which are not unduly affected by outliers or other small departures from model assumptions. The median, being the numerical value separating the higher and lower halves of a data sample, is a robust measure of central tendency, while $\hat{\mu}$ is not. IQR is a measure of statistical dispersion, being equal to the difference between the upper and lower quartiles. It is the most significant basic robust measure of scale. If there are outliers in the data, then the IQR is more representative than $\hat{\sigma}$ as an estimate of the spread of the body of the data. [39].

Once the feature vectors are standardized the next step involves feature scaling. Feature scaling is an important step that prevents attributes in greater numeric ranges from dominating those in smaller numeric ranges. Following the recommendations in [52], each training feature vector is scaled first in the range $[-1, 1]$; then, the corresponding testing feature vector is scaled based on the minimum and maximum values in the training feature vector and not based on the testing vector.

7.9. Classifier Design and Feature Selection

This section is comprised of two parts. Sect. 7.9.1 contains a description of the classification method used in this study, and the classifier design procedure is also briefly described. In Sect. 7.9.2, a method for feature ranking and selection is presented.

7.9.1. Classifier Design

Here, the LIBSVM software system [53] is used to design multi-class support vector machine (SVM) classifiers. SVM is a powerful supervised classification technique that takes advantage of the so-called kernel trick. The main idea of the SVM is that the feature data is mapped to a much higher dimension than the original space. In the high dimensional space, data from two classes can always be linearly separated by a hyper plane. After determining the linear decision boundary, the data are then projected back to the original dimension of the feature space. This procedure is motivated by Cover's theorem which states that, *"a complex pattern classification problem, cast in a high dimensional space nonlinearly, is more likely to be linearly separable than in a low dimensional space, provided that the space is not densely populated* [54] *"*.

Based on the training data, the SVM produces a model that allows prediction of the target values of the test data given only the test data attributes. The building block of the multi-class SVM is a binary classifier (also known as a dichotomizer). The multi-class classifier can be composed based on the one-against-one approach. For a number of classes K, the total number of dichotomizers needed is given by [48]

$$\text{Number of dichotomizers} = \frac{K(K-1)}{2}. \tag{7.43}$$

For example, in the SAR dataset considered in this study there are eight target classes. Hence, 28 dichotomizers are required. Each dichotomizer should be trained on the combination of two classes. Thus, for a particular dichotomizer, given a training set of instance-label pairs $(\mathbf{x}_q, y_q)$ where $q = \{1, ..., l\}$, $\mathbf{x}_q \in \mathbb{R}^n$ and $y_q \in \{\omega_i, \omega_j\}^l$, the SVM

requires solving the following optimization problem [52, 53, 55, 56]

$$\begin{aligned}
&\min_{\mathbf{W}^{\omega_i\omega_j}, b^{\omega_i\omega_j}, \xi^{\omega_i\omega_j}} \left[\frac{1}{2}\left(\mathbf{W}^{\omega_i\omega_j}\right)^T\left(\mathbf{W}^{\omega_i\omega_j}\right) + C\sum_q \left(\xi^{\omega_i\omega_j}\right)\right], \\
&\qquad\qquad\qquad\qquad\qquad\qquad \text{subject to:} \\
&\left[\left(\mathbf{W}^{\omega_i\omega_j}\right)^{\mathrm{T}}\phi\left(\mathbf{x}_q\right) + b^{\omega_i\omega_j} \geq 1 - \left(\xi^{\omega_i\omega_j}\right)_q\right], \text{ if } \mathbf{x}_q \in \omega_i, \\
&\left[\left(\mathbf{W}^{\omega_i\omega_j}\right)^{\mathrm{T}}\phi\left(\mathbf{x}_q\right) + b^{\omega_i\omega_j} \leq -1 + \left(\xi^{\omega_i\omega_j}\right)_q\right], \text{ if } \mathbf{x}_q \in \omega_j, \\
&\qquad\qquad\qquad\qquad\qquad\qquad \xi_i \geq 0.
\end{aligned} \tag{7.44}$$

Here, $\mathbf{W}$ is the (not necessarily normalized) normal vector to the hyperplane, $\frac{b}{\|\mathbf{W}\|}$ determines the offset of the hyperplane from the origin along the normal vector $\mathbf{W}$, $\xi^{\omega_i\omega_j}$ is a non-negative slack variable which measures the degree of misclassification of the data, $C > 0$ is the penalty or regularization parameter for the error term and $\phi\left(.\right)$ is a higher dimensional space function that defines the kernel function as

$$K\left(\mathbf{x}_i, \mathbf{x}_j\right) \equiv \phi(\mathbf{x}_i)^T\phi(\mathbf{x}_j). \tag{7.45}$$

The kernel used in this work is the Gaussian radial basis function (RBF) defined as [48, 52]

$$K\left(\mathbf{x}_i, \mathbf{x}_j\right) = \exp\left(-\gamma\left\|\mathbf{x}_i - \mathbf{x}_j\right\|^2\right). \tag{7.46}$$

where $\gamma > 0$ is the kernel parameter. This kernel is chosen because it is found to give excellent performance for our feature set. The two parameters (C, γ) play a crucial role in dictating the performance of the SVM classifier. Following the guidelines in [52, 53, 57], we adopt a grid-search and a ν-fold cross-validation to find the optimal values of these parameters.

For each dichotomizer, given a testing instance $\mathbf{x}_{test}$, the decision function (predictor)

is [53]

$$g^{\omega_i\omega_j}\left(\mathbf{x}_{test}\right) = \operatorname{sgn}\left(\left(\mathbf{W}^{\omega_i\omega_j}\right)^T \phi\left(\mathbf{x}_{test}\right) + b^{\omega_i\omega_j}\right). \tag{7.47}$$

In the classification stage, a voting strategy is deployed based on the votes cast by each dichotomizer for all data points $\mathbf{x}_{test}$. Hence, a point with the maximum number of votes is designated to be in the class [53, 57, 58].

7.9.2. Feature Ranking and Selection

In this study, a method for feature ranking is used to evaluate the statistical significance of the features. Further, the ranked features are examined to determine the best sub-set of features for classifier construction. The strategy utilized is adopted from [59]. Primarily, a combination of the Fisher score (F-Score) and SVM multi-class classification is used. The F-Score is a technique for measuring the discrimination of two sets of real numbers. Given the training vectors x_k where $k = 1, ..., m$, and if the number of positive and negative instances are n_+ and n_-, respectively, then, the F-Score of the i^{th} feature is defined as [48, 59, 60]

$$F\left(i\right) = \frac{\left(\bar{\mathbf{x}}_i^{(+)} - \bar{\mathbf{x}}_i\right)^2 + \left(\bar{\mathbf{x}}_i^{(-)} - \bar{\mathbf{x}}_i\right)^2}{\frac{1}{n_+-1}\sum_{k=1}^{n_+}\left(x_{k,i}^{(+)} - \bar{\mathbf{x}}_i^{(+)}\right)^2 + \frac{1}{n_--1}\sum_{k=1}^{n_-}\left(x_{k,i}^{(-)} - \bar{\mathbf{x}}_i^{(-)}\right)^2}, \tag{7.48}$$

where $\bar{\mathbf{x}}_i$, $\bar{\mathbf{x}}_i^{(+)}$ and $\bar{\mathbf{x}}_i^{(-)}$, respectively, are the averages for the i^{th} feature of the whole, positive and negative datasets; $x_{k,i}^{(+)}$ is the i^{th} feature of the k^{th} positive instance; $x_{k,i}^{(-)}$ is the i^{th} feature of the k^{th} negative instance. The numerator indicates the discrimination between the positive and negative sets, and the denominator indicates the one within each of the two sets. The larger the F-Score, the more likely the feature is to be more discriminative. Once the F-Score is computed for each feature vector, the features are sorted based on their significance as defined by the F-Score. Then, the high F-Score features are added gradually and used to train the multi-class SVM classifier. This process is continued until the validation accuracy of the classifier decreases. The sub-set of features that achieves the highest validation accuracy is selected [59, 60].

7.10. Results

Using the training and testing datasets presented in Sect. 7.7, three different training and testing feature sets are extracted. The first feature set contains the baseline features based on the power-detected SAR chips described in Sect. 7.8.1. In total, there are nineteen baseline features for each target chip. Hence, the size of the constructed baseline features matrix for training is 2347×19 and for testing is 2112×19. The second set is for the phase-based features presented in Sect. 7.8.2.1. Fifteen phase-based features are extracted from each target chip. The size of the phase-based features matrix for training is 2347×15 and for testing is 2347×15. The third set is solely based on the nonlinear features from the 1-D representations, introduced in Sect. 7.6. A total of ninety eight features are extracted from each target chip. Accordingly, the size of the 1-D based features matrix for training is 2347×98 and for testing is 2112×98.

Each feature set is normalized following the procedure prescribed in Sect. 7.8.3. Then, following the steps outlined in Sect. 7.9.1, three different multi-class SVM classifiers are trained using the training feature sets. The grid search for the optimal values of (C, γ) pertaining to the three classifiers is depicted in Fig. 7.9. The accuracy depicted is based on a five-fold cross validation. Optimal values are found to be $(2^5, 2^{-1})$, $(2, 2)$ and $(2^{15}, 2^{-11})$, respectively, for the baseline, phase-based and 1-D based features. Once the three classifiers are constructed based on the optimal parameters found, the classifiers are tested using the testing feature set. The confusion matrices for the baseline, phase-based and nonlinear 1-D based classifiers are provided in Fig. 7.10, Fig. 7.11 and Fig. 7.12, respectively. The arrangement of the targets in the confusion matrices follows Table 7.1. The overall classification accuracy (as well as the validation accuracy), calculated based on [53], is

$$\text{Accuracy} = \frac{\text{No. of Correctly Predicted Data}}{\text{No. of Testing Data}} \times 100. \tag{7.49}$$

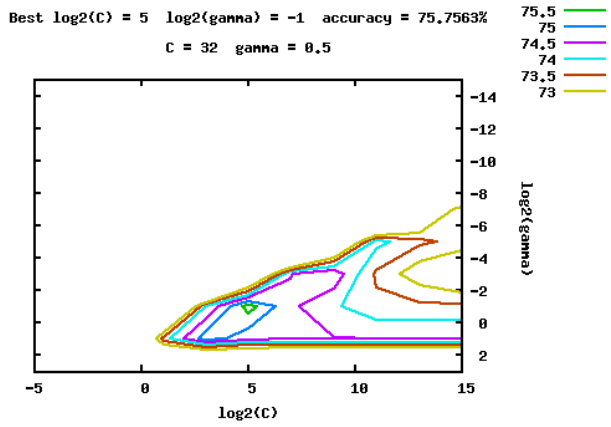

(a) Grid search for the baseline features.

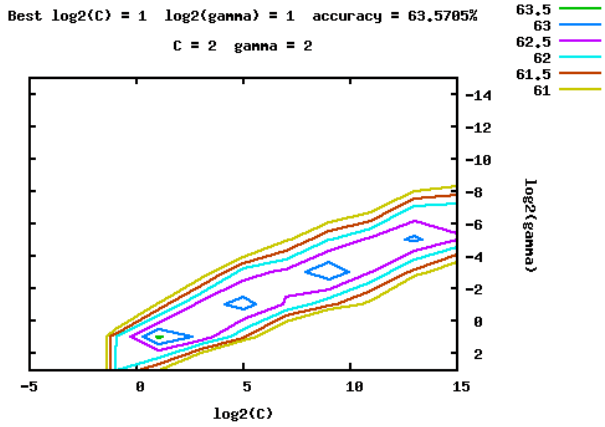

(b) Grid search for the nonlinear phase-based features.

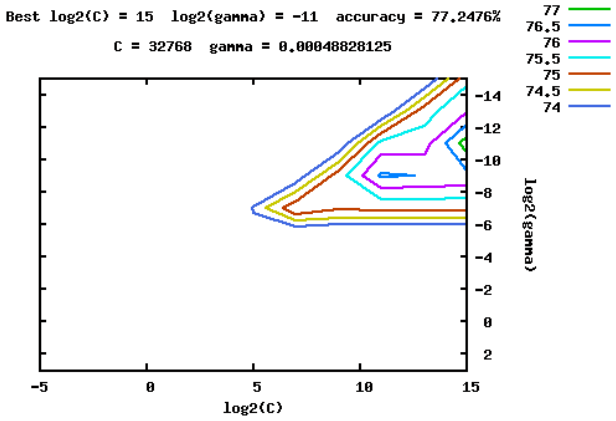

(c) Grid search for the nonlinear 1-D based features.

Figure 7.9: Grid search for optimal (C, γ) for the three set of features.

	BTR − 60	2S1	BRDM − 2	D7	T62	ZIL − 131	ZSU − 23/4	SLICY
BTR − 60	**73.3333**	3.0769	8.2051	2.0513	6.1538	3.0769	4.1026	0
2S1	5.8394	**64.2336**	6.9343	6.2044	8.7591	5.8394	1.0949	1.0949
BRDM − 2	9.4891	5.8394	**71.8978**	0.3650	3.6496	4.7445	4.0146	1.0949
D7	2.1898	5.1095	2.1898	**77.3723**	4.3796	3.2847	4.7445	0.7299
T62	6.2271	10.6227	5.4945	0.7326	**67.3993**	3.6630	5.4945	0.3663
ZIL − 131	6.2044	9.4891	5.1095	1.4599	9.4891	**64.9635**	1.0949	2.1898
ZSU − 23/4	6.5693	2.9197	4.0146	7.2993	4.3796	1.4599	**72.9927**	0.3650
SLICY	0.3650	1.4599	0	0.3650	0	1.0949	0	**96.7153**

Figure 7.10: Confusion matrix for the baseline classifier. Classification accuracy = 73.6269% (1555/2112).

	BTR − 60	2S1	BRDM − 2	D7	T62	ZIL − 131	ZSU − 23/4	SLICY
BTR − 60	**87.6923**	3.5897	1.0256	1.0256	0	0	3.0769	3.5897
2S1	6.9343	**71.5328**	1.8248	15.3285	0.7299	1.4599	1.8248	0.3650
BRDM − 2	0.7299	5.8394	**43.4307**	10.9489	19.3431	12.0438	7.2993	0.3650
D7	0	15.6934	6.2044	**44.8905**	9.1241	20.8029	3.2847	0
T62	0	0.7326	13.9194	8.0586	**43.5897**	20.5128	13.1868	0
ZIL − 131	0.3650	4.0146	6.2044	30.6569	10.9489	**43.4307**	4.3796	0
ZSU − 23/4	0	0	4.3796	0.3650	12.7737	1.0949	**79.1971**	2.1898
SLICY	0	0	1.0949	0	0	0	1.4599	**97.4453**

Figure 7.11: Confusion matrix for the classifier based solely on the phase features. Classification accuracy = 63.0208% (1331/2112).

	BTR − 60	2S1	BRDM − 2	D7	T62	ZIL − 131	ZSU − 23/4	SLICY
BTR − 60	**56.9231**	0	43.0769	0	0	0	0	0
2S1	0	**79.9270**	0	0	0.7299	0	19.3431	0
BRDM − 2	39.7810	0	**60.2190**	0	0	0	0	0
D7	0	0	0	**85.7664**	13.5036	0.3650	0.3650	0
T62	0	1.8315	0	26.3736	**70.3297**	0	1.4652	0
ZIL − 131	0	0	0	2.1898	0	**97.8102**	0	0
ZSU − 23/4	0	24.0876	0	0	0.3650	0	**75.5474**	0
SLICY	0	0	0	0	0	0	0	**100.0000**

Figure 7.12: Confusion matrix for the classifier based on nonlinear features extracted from 1-D representations. Classification accuracy = 79.1193% (1671/2112).

The results obtained based on the phase features evidently demonstrate that the phase in single-channel SAR imagery is not useless as is often assumed in the literature.

On the contrary, based only on fifteen features, an overall classification accuracy of 63.0208% is achieved. It is interesting to note that for four targets (i.e., BTR-60, 2S1, ZSU-23/4 and SLICY), higher classification accuracy was achieved in comparison to the baseline features. This implies that these targets possess greater nonlinear scattering effects manifested in their corresponding phase image. It should also be noted that if a SAR dataset with higher resolution is used, one would expect an increase in the classification accuracy based solely on the phase features. Based on the classification result given in Fig. 7.12, it is evident that the nonlinear features extracted based on the 1-D representations of the SAR chip provide for improvement in the classification accuracy. This clearly shows the importance of considering the often-ignored nonlinear dynamics in classification techniques associated with complex-valued SAR images.

Next, the three sets of features are ranked, and a search for the best sub-set of the features is conducted based on the procedure outlined in Sect. 7.9.2. F-Scores for the baseline, phase-based and nonlinear 1-D based features, respectively, are depicted in Fig. 7.13, Fig. 7.14 and Fig. 7.15. The F-Score values are given, respectively, in Table 7.2, Table 7.3 and Table 7.4. Generally, the F-Score results convey that the significance of the phase-based features for discrimination between the target classes is around seven-fold that of the baseline features. Furthermore, the significance of the 1-D based nonlinear features is around one-hundred-and-sixty-fold that of the baseline features. This shows the utility of the nonlinear approach. Further discussion on this appears later in this section. For each of the three sets of features, a search for the best sub-set led to the conclusion that all the features are important in attaining the classification accuracy achieved.

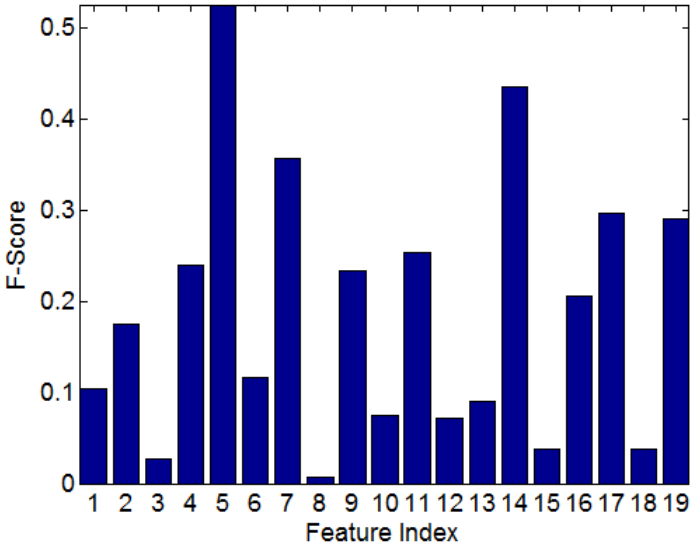

Figure 7.13: Significance of the baseline features. The feature index represents the feature subscripts provided in subsection Sect. 7.8.1.

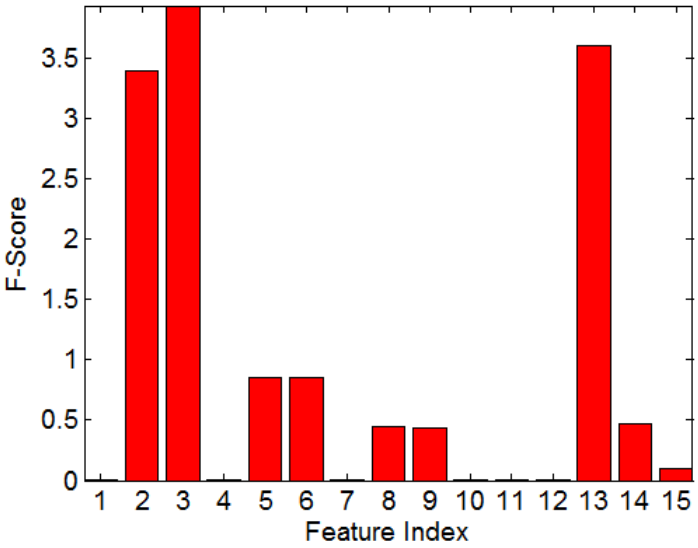

Figure 7.14: Significance of the phase features. The feature index represents the feature subscripts provided in Sect. 7.8.2.1.

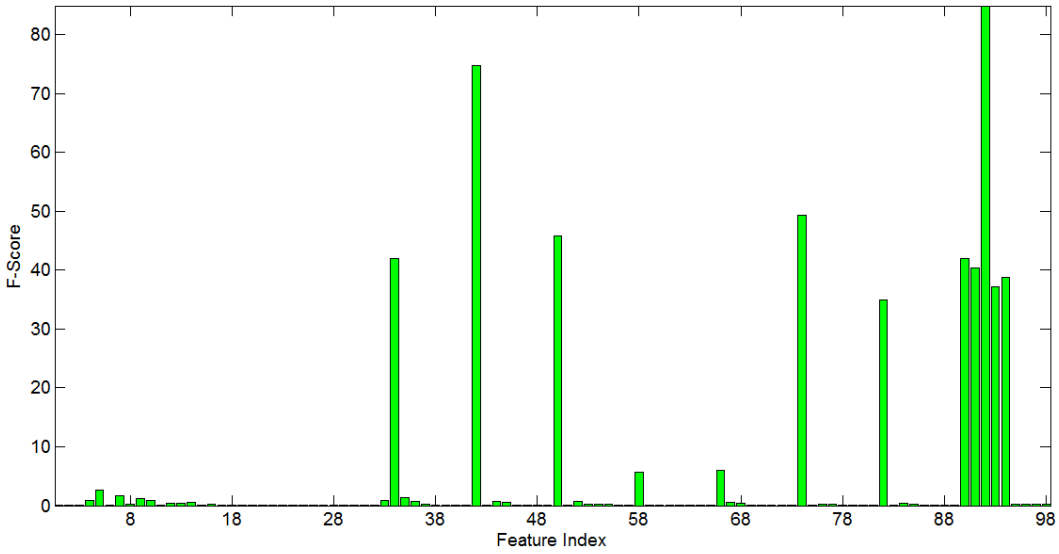

Figure 7.15: Significance of the nonlinear features without the phase. The feature index represents the feature subscripts provided in Sect. 7.8.2.2.

Next, the effect of different combinations for the three sets of features is studied. Three more classifiers are trained and tested following the procedure outlined earlier. The first classifier is based on the amalgamation of the baseline and the phase-based features, respectively. Thus, the sizes of the new features matrices for training and testing, respectively, are $2347 \times (19 + 15)$ and $2112 \times (19 + 15)$. The second classifier uses the amalgamation of the phase-based and the nonlinear 1-D based features, respectively. Hence, the size of the features matrix for training is $2347 \times (15 + 98)$ and for testing is $2112 \times (15 + 98)$. The third classifier utilizes the combination of the baseline, phase-based and nonlinear 1-D based features, respectively. Accordingly, the size of the features matrix for training is $2347 \times (19 + 15 + 98)$ and for testing is $2112 \times (19 + 15 + 98)$. The optimal values for (C, γ) are obtained based on a grid search (see Fig. 7.16) and found to be $(2^5, 2^{-1})$, $(2^9, 2^{-9})$ and $(2^5, 2^{-5})$ for the first, second and third classifiers, respectively. The confusion matrices and classification accuracy for the three classifiers are provided in Fig. 7.17, Fig. 7.18 and Fig. 7.19, respectively.

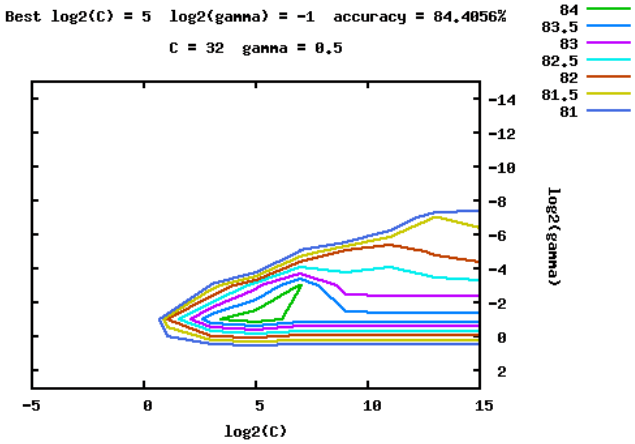

(a) Grid search for combination of baseline + phase-based features.

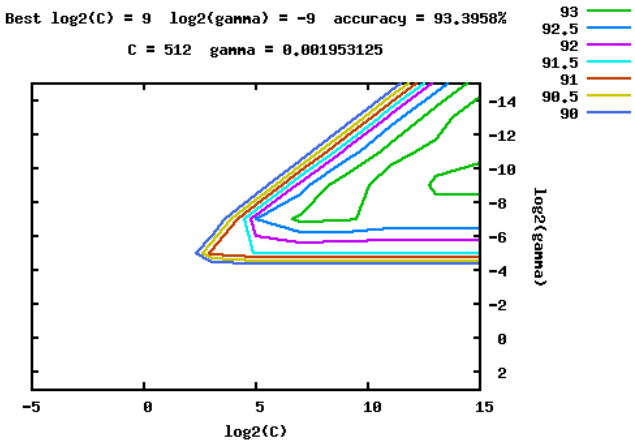

(b) Grid search for combination of the phase-based + nonlinear 1-D based features.

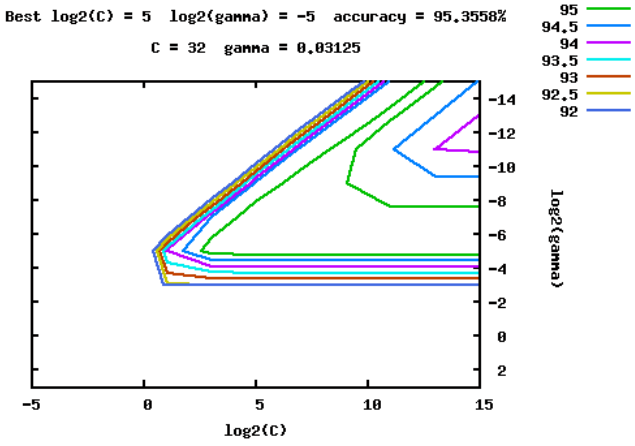

(c) Grid search for the baseline + phase-based + nonlinear 1-D based features.

Figure 7.16: Grid search for optimal (C, γ) for combinations of the three feature sets.

	BTR − 60	2S1	BRDM − 2	D7	T62	ZIL − 131	ZSU − 23/4	SLICY
BTR − 60	**88.2051**	4.1026	1.0256	1.5385	0	1.0256	1.5385	2.5641
2S1	8.0292	**79.5620**	2.9197	5.4745	1.4599	2.1898	0.3650	0
BRDM − 2	0.3650	7.2993	**75.5474**	1.4599	5.8394	6.9343	2.5547	0
D7	1.4599	4.0146	3.2847	**84.6715**	2.1898	3.2847	1.0949	0
T62	0.7326	2.1978	10.2564	1.4652	**73.6264**	6.2271	5.4945	0
ZIL − 131	1.8248	8.0292	7.6642	3.6496	9.1241	**68.6131**	1.0949	0
ZSU − 23/4	0	1.4599	4.0146	2.1898	4.3796	1.4599	**85.4015**	1.0949
SLICY	0	0.3650	0.3650	0.3650	0	01.0949	0.3650	**97.4453**

Figure 7.17: Confusion matrix for the classifier based on baseline + phase-based features. Classification accuracy = 81.392% (1719/2112).

	BTR − 60	2S1	BRDM − 2	D7	T62	ZIL − 131	ZSU − 23/4	SLICY
BTR − 60	**90.7692**	0	8.7179	0	0	0	0.5128	0
2S1	0	**96.3504**	0	0	0.3650	0	3.2847	0
BRDM − 2	4.3796	0	**95.6204**	0	0	0	0	0
D7	0	0.3650	0	**83.5766**	15.6934	0	0.3650	0
T62	0	0.7326	0	14.2857	**84.6154**	0	0.3663	0
ZIL − 131	0	0	0	2.1898	0.3650	**97.4453**	0	0
ZSU − 23/4	0	1.8248	0	0	0	0	**98.1752**	0
SLICY	0	0	0	0	0	0	0	**100.0000**

Figure 7.18: Confusion matrix for the classifier based on phase-based + nonlinear 1-D based features. Classification accuracy = 93.4186% (1973/2112).

	BTR − 60	2S1	BRDM − 2	D7	T62	ZIL − 131	ZSU − 23/4	SLICY
BTR − 60	**90.7692**	1.0256	7.6923	0	0	0	0.5128	0
2S1	0	**97.0803**	0	0	0.3650	0	02.5547	0
BRDM − 2	2.1898	0	**97.8102**	0	0	0	0	0
D7	0	0	0	**93.4307**	5.8394	0.3650	0.3650	0
T62	0	0.3663	0	4.7619	**93.4066**	0	1.4652	0
ZIL − 131	0	0	0	0	0.3650	**99.6350**	0	0
ZSU − 23/4	0	2.1898	0	0	0.7299	0	**97.0803**	0
SLICY	0	0	0	0	0	0	0	**100.0000**

Figure 7.19: Confusion matrix for the classifier based on baseline + phase-based + nonlinear 1-D based features. Classification accuracy = 96.3542% (2035/2112).

These results demonstrate the importance of the phase-based and nonlinear 1-D based features. Particularly, upon combining the baseline and phase-based features,

the classification accuracy is increased by around 8%. Furthermore, combination of the phase-based and nonlinear 1-D based features allows for an overall classification accuracy of 93.4186%. This significant improvement in the classification accuracy shows the importance of these two sets of features. Additionally, inclusion of the baseline features slightly increases the classification accuracy to 96.3542%.

Next, a search for the best sub-set of features from the combination of the three sets is conducted. First, significance in terms of the F-Scores for the three feature sets is depicted in Fig. 7.20. Note that the blue, red and green bars, respectively, represent the baseline, phase-based and nonlinear 1-D based features. Then, the overall features are sorted, and sub-set selection is conducted following the procedure outlined in Sect. 7.9.2. The top sixty-six features were selected as they are found to achieve the highest validation accuracy (i.e., 96.1653%). The overall F-Scores along with the selected sixty-six features are shown in Table 7.2- Table 7.4. It is worth noting that among the selected features, the top twenty-nine come from the nonlinear 1-D based and phase-based features, respectively.

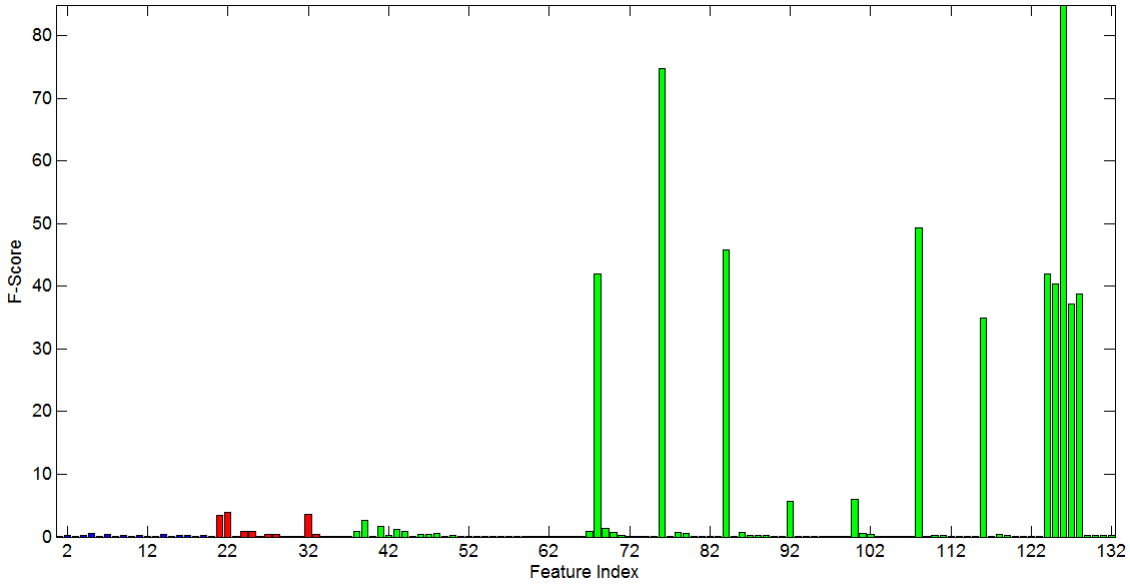

Figure 7.20: Significance for all the features (baseline + phase-based + nonlinear 1-D based) used in this study. Blue, red and green bars, respectively, represent baseline, phase-based and nonlinear 1-D based features.

Table 7.2: F-Scores for the baseline features used in this study. The bold numbers in brackets indicate the ranks for the top sixty-six features.

Index	1 **(64)**	2 **(59)**	3	4 **(51)**	5 **(30)**	6 **(63)**	7 **(39)**	8
Type	$\mathbf{f}_{\mathrm{BL1}}$	$\mathbf{f}_{\mathrm{BL2}}$	$\mathbf{f}_{\mathrm{BL3}}$	$\mathbf{f}_{\mathrm{BL4}}$	$\mathbf{f}_{\mathrm{BL5}}$	$\mathbf{f}_{\mathrm{BL6}}$	$\mathbf{f}_{\mathrm{BL7}}$	$\mathbf{f}_{\mathrm{BL8}}$
F-Score	0.104282	0.174448	0.026250	0.240112	0.525163	0.116269	0.356272	0.007372
Index	9 **(52)**	10	11 **(50)**	12	13	14 **(36)**	15	16 **(53)**
Type	$\mathbf{f}_{\mathrm{BL9}}$	$\mathbf{f}_{\mathrm{BL10}}$	$\mathbf{f}_{\mathrm{BL11}}$	$\mathbf{f}_{\mathrm{BL12}}$	$\mathbf{f}_{\mathrm{BL13}}$	$\mathbf{f}_{\mathrm{BL14}}$	$\mathbf{f}_{\mathrm{BL15}}$	$\mathbf{f}_{\mathrm{BL16}}$
F-Score	0.234009	0.074707	0.252705	0.071361	0.090576	0.435705	0.037509	0.205777
Index	17 **(42)**	18	19 **(44)**					
Type	$\mathbf{f}_{\mathrm{BL17}}$	$\mathbf{f}_{\mathrm{BL18}}$	$\mathbf{f}_{\mathrm{BL19}}$					
F-Score	0.296468	0.037128	0.290143					

Table 7.3: F-Scores for the nonlinear phase-based features used in this study. The bold numbers in brackets indicate the ranks for the top sixty-six features.

Index	20	21 **(15)**	22 **(13)**	23	24 **(21)**	25 **(22)**	26	27 **(34)**
Type	$\mathbf{f}_{\mathrm{Ph1}}$	$\mathbf{f}_{\mathrm{Ph2}}$	$\mathbf{f}_{\mathrm{Ph3}}$	$\mathbf{f}_{\mathrm{Ph4}}$	$\mathbf{f}_{\mathrm{Ph5}}$	$\mathbf{f}_{\mathrm{Ph6}}$	$\mathbf{f}_{\mathrm{Ph7}}$	$\mathbf{f}_{\mathrm{Ph8}}$
F-Score	0.002161	3.40389	3.93829	0.001028	0.852989	0.850224	0.000536	0.451283
Index	28 **(35)**	29	30	31	32 **(14)**	33 **(32)**	34 **(66)**	
Type	$\mathbf{f}_{\mathrm{Ph9}}$	$\mathbf{f}_{\mathrm{Ph10}}$	$\mathbf{f}_{\mathrm{Ph11}}$	$\mathbf{f}_{\mathrm{Ph12}}$	$\mathbf{f}_{\mathrm{Ph13}}$	$\mathbf{f}_{\mathrm{Ph14}}$	$\mathbf{f}_{\mathrm{Ph15}}$	
F-Score	0.437565	0.003383	0.004468	0.001335	3.609093	0.466928	0.100274	

Table 7.4: F-Scores for the nonlinear 1-D based features. The bold numbers in brackets indicate the ranks for the top sixty-six features.

Index	35	36	37	38 **(23)**	39 **(16)**	40	41 **(17)**	42 **(49)**
Type	$\mathbf{f}_{NL1}$	$\mathbf{f}_{NL2}$	$\mathbf{f}_{NL3}$	$\mathbf{f}_{NL4}$	$\mathbf{f}_{NL5}$	$\mathbf{f}_{NL6}$	$\mathbf{f}_{NL7}$	$\mathbf{f}_{NL8}$
F-Score	0.004376	0.043474	0.028188	0.837737	2.561608	0.083659	1.675789	0.255196
Index	43 **(19)**	44 **(24)**	45	46 **(38)**	47 **(37)**	48 **(28)**	49	50 **(55)**
Type	$\mathbf{f}_{NL9}$	$\mathbf{f}_{NL10}$	$\mathbf{f}_{NL11}$	$\mathbf{f}_{NL12}$	$\mathbf{f}_{NL13}$	$\mathbf{f}_{NL14}$	$\mathbf{f}_{NL15}$	$\mathbf{f}_{NL16}$
F-Score	1.151379	0.831957	0.048254	0.383011	0.402271	0.569529	0.003632	0.202775
Index	51	52	53	54 **(65)**	55	56	57	58
Type	$\mathbf{f}_{NL17}$	$\mathbf{f}_{NL18}$	$\mathbf{f}_{NL19}$	$\mathbf{f}_{NL20}$	$\mathbf{f}_{NL21}$	$\mathbf{f}_{NL22}$	$\mathbf{f}_{NL23}$	$\mathbf{f}_{NL24}$
F-Score	0.038605	0.043167	0.028673	0.101209	0.068022	0.032381	0.005276	0.044145
Index	59	60	61	62	63	64	65	66
Type	$\mathbf{f}_{NL25}$	$\mathbf{f}_{NL26}$	$\mathbf{f}_{NL27}$	$\mathbf{f}_{NL28}$	$\mathbf{f}_{NL29}$	$\mathbf{f}_{NL30}$	$\mathbf{f}_{NL31}$	$\mathbf{f}_{NL32}$
F-Score	0.006465	0.035941	0.025960	0.061196	0.011671	0.026343	0.004708	0.015550
Index	67 **(20)**	68 **(5)**	69 **(18)**	70 **(25)**	71 **(47)**	72	73	74
Type	$\mathbf{f}_{NL33}$	$\mathbf{f}_{NL34}$	$\mathbf{f}_{NL35}$	$\mathbf{f}_{NL36}$	$\mathbf{f}_{NL37}$	$\mathbf{f}_{NL38}$	$\mathbf{f}_{NL39}$	$\mathbf{f}_{NL40}$
F-Score	0.937748	41.99154	1.335222	0.737384	0.258012	0.021904	0.020498	0.008744
Index	75	76 **(2)**	77	78 **(27)**	79 **(31)**	80	81	82
Type	$\mathbf{f}_{NL41}$	$\mathbf{f}_{NL42}$	$\mathbf{f}_{NL43}$	$\mathbf{f}_{NL44}$	$\mathbf{f}_{NL45}$	$\mathbf{f}_{NL46}$	$\mathbf{f}_{NL47}$	$\mathbf{f}_{NL48}$
F-Score	0.005032	74.732794	0.012247	0.661262	0.521751	0.06181	0.094429	0.021047
Index	83	84 **(4)**	85	86 **(26)**	87 **(48)**	88 **(58)**	89 **(54)**	90
Type	$\mathbf{f}_{NL49}$	$\mathbf{f}_{NL50}$	$\mathbf{f}_{NL51}$	$\mathbf{f}_{NL52}$	$\mathbf{f}_{NL53}$	$\mathbf{f}_{NL54}$	$\mathbf{f}_{NL55}$	$\mathbf{f}_{NL56}$
F-Score	0.057071	45.77489	0.045835	0.698165	0.257581	0.191538	0.205569	0.035003
Index	91	92 **(12)**	93	94 **(62)**	95	96	97	98
Type	$\mathbf{f}_{NL57}$	$\mathbf{f}_{NL58}$	$\mathbf{f}_{NL59}$	$\mathbf{f}_{NL60}$	$\mathbf{f}_{NL61}$	$\mathbf{f}_{NL62}$	$\mathbf{f}_{NL63}$	$\mathbf{f}_{NL64}$
F-Score	0.031306	5.651479	0.092150	0.127972	0.026360	0.056588	0.087552	0.009154
Index	99	100 **(11)**	101 **(29)**	102 **(40)**	103 **(61)**	104	105	106
Type	$\mathbf{f}_{NL65}$	$\mathbf{f}_{NL66}$	$\mathbf{f}_{NL67}$	$\mathbf{f}_{NL68}$	$\mathbf{f}_{NL69}$	$\mathbf{f}_{NL70}$	$\mathbf{f}_{NL71}$	$\mathbf{f}_{NL72}$
F-Score	0.011370	5.932869	0.55627	0.348003	0.143246	0.035961	0.058544	0.003314
Index	107	108 **(3)**	109	110 **(46)**	111 **(56)**	112	113	114
Type	$\mathbf{f}_{NL73}$	$\mathbf{f}_{NL74}$	$\mathbf{f}_{NL75}$	$\mathbf{f}_{NL76}$	$\mathbf{f}_{NL77}$	$\mathbf{f}_{NL78}$	$\mathbf{f}_{NL79}$	$\mathbf{f}_{NL80}$
F-Score	0.005743	49.33849	0.029424	0.261102	0.202594	0.041158	0.067312	0.003950
Index	115	116 **(10)**	117	118 **(33)**	119 **(60)**	120	121	122
Type	$\mathbf{f}_{NL81}$	$\mathbf{f}_{NL82}$	$\mathbf{f}_{NL83}$	$\mathbf{f}_{NL84}$	$\mathbf{f}_{NL85}$	$\mathbf{f}_{NL86}$	$\mathbf{f}_{NL87}$	$\mathbf{f}_{NL88}$
F-Score	0.004851	34.94347	0.035165	0.452377	0.173644	0.090287	0.067904	0.003530
Index	123	124 **(6)**	125 **(7)**	126 **(1)**	127 **(9)**	128 **(8)**	129 **(43)**	130 **(41)**
Type	$\mathbf{f}_{NL89}$	$\mathbf{f}_{NL90}$	$\mathbf{f}_{NL91}$	$\mathbf{f}_{NL92}$	$\mathbf{f}_{NL93}$	$\mathbf{f}_{NL94}$	$\mathbf{f}_{NL95}$	$\mathbf{f}_{NL96}$
F-Score	0.006756	41.93384	40.41706	84.95294	37.15177	38.85961	0.296341	0.318477
Index	131 **(57)**	132 **(45)**						
Type	$\mathbf{f}_{NL97}$	$\mathbf{f}_{NL98}$						
F-Score	0.196293	0.261724						

Finally, the selected features are used to construct a new SVM classifier. A grid search is conducted (see Fig. 7.22) and the optimal values of (C, γ) are found to be $(2^5, 2^{-5})$, respectively. Once the classifier is constructed, it is tested using similar features extracted from the testing dataset. The confusion matrix for this classifier is provided in Fig. 7.21. Based on this result, it is clear that the classification accuracy for the classifier based on the selected sixty-six features is very close to that based on the whole set of one-hundred-and-thirty-two features.

	BTR – 60	2S1	BRDM – 2	D7	T62	ZIL – 131	ZSU – 23/4	SLICY
BTR – 60	**90.7692**	2.0513	6.1538	0	0	0	1.0256	0
2S1	0	**98.1752**	0	0	0.3650	0	1.4599	0
BRDM – 2	4.3796	0	**95.6204**	0	0	0	0	0
D7	0	0.3650	0	**94.1606**	4.0146	0.7299	0.7299	0
T62	0	1.0989	0	04.0293	**91.9414**	0.7326	2.1978	0
ZIL – 131	0	0	0	0.3650	0.7299	**98.9051**	0	0
ZSU – 23/4	0	1.0949	0	0	1.4599	0	**97.4453**	0
SLICY	0	0	0	0	0	0	0	**100.0000**

Figure 7.21: Confusion matrix for the classifier based on the selected sixty-six features.. Classification accuracy = 96.0701 % (2029/2112).

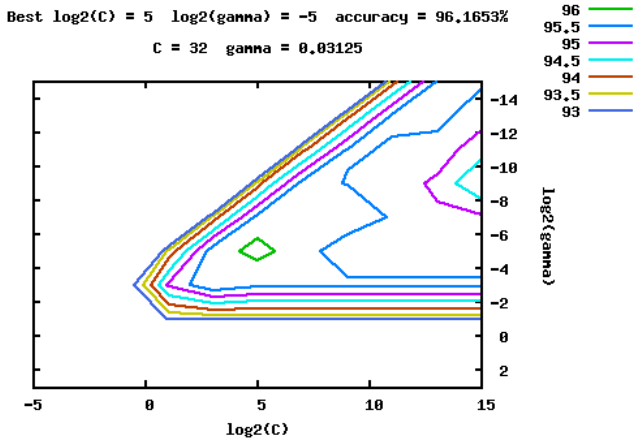

Figure 7.22: Grid search for optimal (C, γ) for the selected sixty-six features.

The most prominent lessons learned form this investigation are now highlighted. Firstly, contrary to the usual practice of discarding the phase in single-channel SAR imagery under the assumption that it carries no useful information, the statistical significance of the information carried in the phase in general, and the complex-valued chip in particular, is clearly demonstrated here. Secondly, a classification accuracy of 93.4186% is achieved based solely on the nonlinear features extracted from the combination of the phase-based and the nonlinear space 1-D based representations. This validates the superior performance of the proposed framework both for phase characterization and modeling and for transformation from 2-D to 1-D space. This also demonstrates that by using the correct set of features, it is possible to neglect features based on the detected SAR chips. Hence, through approaching the complex-valued SAR chip from the holistic perspective of nonlinearity, it is possible to gain a new insight into the process of feature extraction for target recognition in SAR imagery. Thirdly, it is interesting to note that among the most significant features are those based on the PE for the combination of the 1-D transformed real and imaginary parts, real-part, imaginary-part, furud'ed and bivariate representations, respectively. This validates the usefulness of the three radon-based 1-D representations proposed in this study. This also demonstrates the prominence of PE at capturing the nonlinear dynamics in the different representations. Additionally, among the top ranked features are those based on the Hilbert spectrum. This shows the superiority of the HHT transform at capturing the nonlinear dynamics. Next, it is important to note that the feature extraction methods presented in this study are by no means exhaustive. Rather, they serve to demonstrate the objective of the study and they open the door for more in-depth investigation into various nonlinear feature extraction methods. Finally, it should be stressed that with the increase in the spatial resolution of the SAR sensor relative to the size of the imaged target, the nonlinear phenomenon is naturally expected to be more pronounced. Thus, the application of our approach to this kind of SAR imagery should achieve even more prominent classification accuracy.

7.11. Conclusions

For the case of extended targets and due to the dispersive scatterers, phase change in the radar return signal is not linear as it is often assumed by the conventional res-

olution theory. In fact, nonlinear phase modulation is an intrinsic phenomenon for extended targets in SAR imagery. When the processed SAR image is approached from the reductionist perspective of linear signal processing, nonlinearity is often viewed as a noise that warrants removal. On the contrary, nonlinear signal processing methods are motivated by the holistic signal processing worldview which is designed to account for multiplicity due to interactions between the individual components in the radar returns. The advantage of holism for signal processing in SAR imagery is clearly demonstrated in this chapter. Two frameworks for feature extraction that take advantage of the nonlinear phenomenon are presented. The first framework is solely based on the phase chip of the extended target, and it allows for extracting unique features for target recognition applications. The second framework is based on 1-D representations for the complex-valued SAR chip. This provides for utilizing a wide array of methods for nonlinear and nonstationary time series analysis such as those associated with chaos theory and the Hilbert-Huang transform (HHT). Our proposed approach is demonstrated on the real-world MSTAR dataset. Comparison with baseline features from the power-detected chips is also considered. An overall improvement in the classification accuracy by around 20% is achieved due to the proposed approach. The higher the spatial resolution of the SAR sensor the more predominant the nonlinear dynamics in the processed image from the extended target. Hence, our proposed approach is expected to offer even greater gains for such sensors. The application of our approach extends well beyond SAR to include various kinds of relevant imagery such as that from radar, sonar and ultrasound.

Bibliography

[1] A. Scott, "Reductionism revisited," *Journal of Consciousness Studies*, vol. 11, no. 2, pp. 51–68, 2004. [Online]. Available: http://www.ingentaconnect.com/content/imp/jcs/2004/00000011/00000002/art00004 181

[2] S. Y. Auyang, *Foundations of complex-system theories: in economics, evolutionary biology, and statistical physics*. Cambridge: UK: Cambridge University Press, 1999.

[3] A. Scott, Ed., *Encyclopedia of nonlinear science*. New York, NY: Routledge, Taylor & Francis Group, 2005. 181

[4] A. V. Oppenheim, *Discrete-Time Signal Processing*, 3rd ed. Upper Saddle River: NJ: Prentice-Hall, 2009. 181

[5] J. Rice, *Mathematical Statistics and Data Analysis*. Belmont, CA: Duxbury Press, 1995. 181

[6] N. Huang, Z. Shen, and S. Long, "A new view of nonlinear water waves: the Hilbert spectrum," *Annual Review of Fluid Mechanics*, vol. 31, no. 1, pp. 417–457, 1999. [Online]. Available: http://dx.doi.org/10.1146/annurev.fluid.31.1.417 181

[7] G. R. Arce, *Nonlinear signal processing: a statistical approach*. Hoboken, NJ: Wiley-Interscience, 2004. 181

[8] S. H. Strogatz, *Nonlinear dynamics and chaos (with applications to physics, biology, chemistry and engineering*. New York, NY: Perseus Publishing, 1994. 181

[9] N. Huang, Z. Shen, S. Long, M. Wu, H. Shih, Q. Zheng, N.-C. Yen, C. Tung, and H. Liu, "The empirical mode decomposition and the Hilbert spectrum for nonlinear and non-stationary time series analysis," *Proceedings of the Royal Society of London. Series A: Mathematical, Physical and*

Engineering Sciences, vol. 454, no. 1971, pp. 903–995, 1998. [Online]. Available: http://dx.doi.org/10.1098/rspa.1998.0193 181, 195, 196, 197, 199

[10] I. Cumming and F. Wong, *Digital Processing of Synthetic Aperture Radar Data*. Norwood, MA: Artech House, 2005. 182, 184

[11] A. Rihaczek and S. Hershkowitz, "Man-made target backscattering behavior: Applicability of conventional radar resolution theory," *IEEE Transactions on Aerospace and Electronic Systems*, vol. 32, no. 2, pp. 809–824, 1996. [Online]. Available: http://dx.doi.org/10.1109/7.489523 182, 185

[12] ——, *Radar Resolution and Complex-Image Analysis*. Norwood, MA: Artech House, 1996.

[13] ——, *Theory and Practice of Radar Target Identification*. Norwood, MA: Artech House, 2000. 182, 185

[14] K. El-Darymli, E. W. Gill, P. McGuire, D. Power, and C. Moloney, "Unscarmbling nonlinear dynamics in synthetic aperture radar imagery," *[Under Review]*, 2015. 182

[15] K. El-Darymli, C. Moloney, E. W. Gill, P. McGuire, and D. Power, "Nonlinearity and the effect of detection on signle-channel synthetic aperture radar imagery," in *Oceans'14 MTS/IEEE Taipei, Taiwan*, 2014. [Online]. Available: http://dx.doi.org/10.1109/OCEANS-TAIPEI.2014.6964493 182

[16] K. El-Darymli, P. McGuire, E. W. Gill, D. Power, and C. Moloney, "Characterization and statistical modeling of phase in single-channel synthetic aperture radar imagery," *IEEE Transactions on Aerospace and Electronic Systems [Accepted]*, 2015. 182, 186, 187, 188, 189, 206

[17] K. El-Darymli, P. McGuire, D. Power, and C. Moloney, "Rethinking the phase in single-channel SAR imagery," in *Radar Symposium (IRS), 2013 14th International*, Dresden, Germany, June 2013, pp. 429–436. [Online]. Available: http://tinyurl.com/lb84t2y

[18] K. El-Darymli, C. Moloney, E. W. Gill, P. McGuire, and D. Power, "On circularity/noncircularity in single-channel synthetic aperture radar imagery," in *Oceans 14, MTS/IEEE, St. John's, Newfoundland*, 2014. [Online]. Available: http://dx.doi.org/10.1109/OCEANS.2014.7003163 182, 186, 189

[19] ——, "Recognition of nonlinear dispersive scattering in SAR imagery,"

in *IEEE IGARSS'14, Quebec, Canada*, 2014. [Online]. Available: http://dx.doi.org/10.1109/IGARSS.2014.6947548 182

[20] K. V. Mardia and P. E. Jupp, *Directional statistics*, ser. Wiley Series in Probability and Statistics. London, UK: John Wiley and Sons, 2009, vol. 494. 188

[21] S. R. Jammalamadaka and A. Sengupta, *Topics in circular statistics*. River Edge, NJ: World Scientific, 2001.

[22] N. I. Fisher, *Statistical Analysis of Circular Data*. Cambridge, UK: Cambridge University Press, 1993. 188

[23] T. Adali and S. Haykin, *Adaptive Signal Processing*. Hoboken, NJ: Wiley, 2010. 189

[24] P. J. Schreier and L. L. Scharf, *Statistical signal processing of complex-valued data: the theory of improper and noncircular signals*. Cambridge, UK: Cambridge University Press, 2010. 189, 193, 194

[25] M. Novey, T. Adali, and A. Roy, "A complex generalized Gaussian distribution- characterization, generation, and estimation," *Signal Processing, IEEE Transactions on*, vol. 58, no. 3, pp. 1427–1433, 2010. [Online]. Available: http://dx.doi.org/10.1109/TSP.2009.2036049 189

[26] ——, "Circularity and Gaussianity detection using the complex generalized Gaussian distribution," *Signal Processing Letters, IEEE*, vol. 16, no. 11, pp. 993–996, 2009. [Online]. Available: http://dx.doi.org/10.1109/LSP.2009.2028412 189

[27] A. D. Poularikas, Ed., *Transforms and applications handbook*. Boca Raton, FL: CRC Press, 2010. 190, 191

[28] R. H. Allen, *Star Names: Their Lore and Meaning*. New York: Dover Publications Inc, 1963. [Online]. Available: http://penelope.uchicago.edu/Thayer/E/Gazetteer/Topics/astronomy/_Texts/secondary/ALLSTA/Canis_Major*.html 194

[29] J. G. A. Davis, "The pronunciations, derivations, and meanings of a selected list of star names," *Popular Astronomy*, vol. 52, no. 3, 1944. [Online]. Available: http://tinyurl.com/mhr444u

[30] European Southern Observatory. (2014) Artist's impression of the evolution

of a hot high-mass binary star (annotated version). [Online]. Available: http://www.eso.org/public/videos/eso1230b

[31] Wikipedia. Zeta canis majoris. [Online]. Available: http://en.wikipedia.org/wiki/Zeta_Canis_Majoris 194

[32] S. Mallat, *A Wavelet Tour of Signal Processing: the Sparse Way*. Burlington, MA: Elsevier, 2008. 196

[33] Z. Wu and N. Huang, "Ensemble empirical mode decomposition: A noise-assisted data analysis method," *Advances in Adaptive Data Analysis*, vol. 1, no. 1, pp. 1–41, 2009. [Online]. Available: http://dx.doi.org/10.1142/S1793536909000047 196

[34] N. Huang, M. Lo, Z. WU, and X. Chen, "Method for quantifying and modeling degree of nonlinearity, combined nonlinearity, and nonstationarity," US Patent Patent App. 13/241,565, 2013. [Online]. Available: https://www.google.com/patents/US20130080378 197, 198, 199

[35] N. E. Huang, Z. Wu, S. R. Long, K. C. Arnold, X. Chen, and K. Blank, "On instantaneous frequency," *Advances in Adaptive Data Analysis*, vol. 1, no. 2, pp. 177–229, 2009. [Online]. Available: http://dx.doi.org/10.1142/S1793536909000096 197, 198

[36] M. Cheney and B. Borden, *Fundamentals of Radar Imaging*. Philadelphia: Society for Industrial and Applied Math, 2009. 197

[37] Y. Yuan and N. Huang, "A reappraisal of ocean wave studies," *Journal of Geophysical Research: Oceans*, vol. 117, no. C11, pp. 1978–2012, 2012. [Online]. Available: http://dx.doi.org/10.1029/2011JC007768 199

[38] P. J. Huber and E. M. Ronchetti, *Robust Statistics*, 2nd ed. Wiley, 2009. 199, 209

[39] G. Upton and I. Cook, *Understanding Statistics*. Oxford, UK: Oxford University Press, 1996. 199, 209

[40] C. Bandt and B. Pompe, "Permutation entropy: a natural complexity measure for time series," *Physical Review Letters, American Physical Society*, vol. 88, no. 17, p. 174102, 2002. [Online]. Available: http://dx.doi.org/10.1103/PhysRevLett.88.174102 200

[41] M. Riedl, A. Muller, and N. Wessel, "Practical considerations of permutation

entropy," *The European Physical Journal Special Topics*, vol. 222, no. 2, pp. 249–262, 2013. [Online]. Available: http://dx.doi.org/10.1140/epjst/e2013-01862-7 200, 207

[42] C. K. Peng, S. Havlin, H. E. Stanley, and A. L. Goldberger, "Quantification of scaling exponents and crossover phenomena in nonstationary heartbeat time series," *Chaos: An Interdisciplinary Journal of Nonlinear Science*, vol. 5, no. 1, pp. 82–87, 1995. [Online]. Available: http://scitation.aip.org/content/aip/journal/chaos/5/1/10.1063/1.166141 200, 201

[43] M. Little, P. McSharry, I. Moroz, and S. Roberts, "Nonlinear, biophysically-informed speech pathology detection," in *Acoustics, Speech and Signal Processing, 2006. ICASSP 2006 Proceedings. 2006 IEEE International Conference on*, vol. 2, 2006. [Online]. Available: http://dx.doi.org/10.1109/ICASSP.2006.1660534 200, 201

[44] Sensor And Data Management System. (2014) MSTAR/IU mixed targets. US Air Force. Airforce Research Lab. [Online]. Available: https://www.sdms.afrl.af.mil/index.php?collection=mstar&page=mixed xvi, 201, 202

[45] J. Kapur, P. Sahoo, and A. Wong, "A new method for gray-level picture thresholding using the entropy of the histogram," *Computer Vision, Graphics, and Image Processing*, vol. 29, no. 3, pp. 273–285, 1985. [Online]. Available: http://dx.doi.org/10.1016/0734-189X(85)90125-2 203

[46] Matlab 2014b documentation. (2014) Morphology fundamentals: dilation and erosion. Mathworks. [Online]. Available: http://tinyurl.com/q6zfwcp 203

[47] ——. (2014) Measure properties of image regions. Mathworks. [Online]. Available: http://tinyurl.com/k58dlqf 204

[48] R. Duda, P. Hart, and D. Stork, *Pattern classification*. New York: John Wiley and Sons, 2001. 208, 210, 211, 212

[49] K. El-Darymli, P. McGuire, D. Power, and C. Moloney, "Target detection in synthetic aperture radar imagery: a state-of-the-art survey," *J. Appl. Remote Sens*, vol. 7, no. 1, 2013. [Online]. Available: http://dx.doi.org/10.1117/1.JRS.7.071598 209

[50] K. El-Darymli, P. McGurie, E. W. Gill, D. Power, and C. Moloney, "Automatic target recognition in SAR imagery (SAR-ATR): A state-of-the-art review," *[To be submitted]*, 2015. 209

[51] E. Kreyszig, *Advanced Engineering Mathematics*, 10th ed. Hoboken, NJ: Wiley, 2011. 209

[52] C.-W. Hsu, C.-C. Chang, and C.-J. Lin, "A practical guide to support vector classification. technical report," Department of Computer Science and Information Engineering, National Taiwan University, Tech. Rep., 2010. [Online]. Available: http://www.csie.ntu.edu.tw/~cjlin/papers/guide/guide.pdf 209, 211

[53] C.-C. Chang and C.-J. Lin, "LIBSVM: A library for support vector machines," *ACM Transactions on Intelligent Systems and Technology*, vol. 2, no. 3, 2011. [Online]. Available: http://dx.doi.org/10.1145/1961189.1961199 210, 211, 212, 213

[54] T. Cover, "Geometrical and statistical properties of systems of linear inequalities with applications in pattern recognition," *Electronic Computers, IEEE Transactions on*, vol. 14, no. 3, pp. 326–334, 1965. [Online]. Available: http://dx.doi.org/10.1109/PGEC.1965.264137 210

[55] B. E. Boser, I. Guyon, and V. Vapnik., "A training algorithm for optimal margin classifiers," in *Proceedings of the Fifth Annual Workshop on Computational Learning Theory*. ACM Press, 1992, pp. 144–152. [Online]. Available: http://dx.doi.org/10.1145/130385.130401 211

[56] C. Cortes and V. Vapnik, "Support-vector networks," *Machine Learning*, vol. 20, no. 3, pp. 273–297, 1995. [Online]. Available: http://dx.doi.org/10.1023/A:1022627411411 211

[57] C.-C. Chang and C.-J. Lin, "Libsvm: A library for support vector machines," Department of Computer Science National Taiwan University, Taipei, Taiwan, Tech. Rep., 2013. [Online]. Available: http://www.csie.ntu.edu.tw/~cjlin/papers/libsvm.pdf 211, 212

[58] C.-W. Hsu and C.-J. Lin, "A comparison of methods for multiclass support vector machines," *Neural Networks, IEEE Transactions on*, vol. 13, no. 2, pp. 415–425, 2002. [Online]. Available: http://dx.doi.org/10.1109/72.991427 212

[59] Y.-W. Chen and C.-J. Lin, *Feature Extraction: Foundations and Applications*. Berlin, Heidelberg: Springer, 2006, ch. Combining SVMs with Various Feature Selection, pp. 315–324. 212

[60] Y.-W. Chang and C.-J. Lin, "Feature ranking using linear SVM," in *Causation*

and Prediction Challenge Challenges in Machine Learning, vol. 2, 2008, pp. 47–57. [Online]. Available: http://tinyurl.com/l97zpmm 212

8. Summary

8.1. Conclusions

The following thesis objectives were outlined in Sect. 1.4:

Primary objective

- To develop novel tools that take advantage of the nonlinear phenomenon in focused single-channel synthetic aperture radar (SAR) imagery; and
- To apply the developed tools to the problem of automatic target recognition in SAR (SAR-ATR).

Specific Objectives

- To comprehend the status quo in SAR-ATR;
- To develop a low-level understanding of the SAR data as well as the various factors that impact the SAR image; and
- To design novel features, inherently specific to SAR imagery, suitable for use in SAR-ATR.

The foregoing objectives have been successfully fulfilled, leading to the development of two new frameworks for feature extraction from complex-valued SAR imagery in Chapter 7. The methodology followed to resolve the objectives of this thesis is summarized below.

An in-depth review for the state-of-the-art in SAR-ATR has been conducted, and it is disseminated in two research articles [1, 2]. This review has offered an umbrella under which the various research activities in the field are broadly probed and taxonomized.

The underpinnings of the methods reviewed have been summarized, and advantages, shortcomings and challenges of the various SAR-ATR taxa have been pinpointed. A synopsis for this review work is presented in Chapter 2. For most works on single-channel SAR-ATR, the detected image (i.e., image intensity) is often utilized while the phase content is discarded. This is a result of the conventional radar resolution theory, a theory of point targets motivated by the linear system theory. At the heart of the linear system theory, the Fourier view assumes a first-order fundamental oscillation and bounding higher order harmonics. Subsequently, from the perspective of linear system theory, deviations from linearity are considered noise that warrants removal. Despite its mathematical soundness, this view does not correspond to physical reality.

The design and implementation of a low-power and high-resolution SAR system in Chapter 3 has provided for developing a low-level understanding of single-channel SAR imagery, and for comprehending the various factors that impact the focused complex-valued image. The developed system utilizes the linear frequency-modulated continuous wave (LFMCW) concept, and it operates in the S-band. The generic architecture for the system is presented along with a brief description for the concept of operation. The Omega-K algorithm (ωKA) is used to focus the phase history, and to produce a complex-valued SAR image for a ground-truthed target. Further, this image is utilized for nonlinearity analysis in Chapter 4.

In Chapter 4, a systematic procedure to infer the statistical significance of the nonlinear dynamics in SAR imagery has been introduced. A proper understanding of the inherent nature of the SAR data in terms of linearity and nonlinearity does not only allow for an informed choice pertaining to the most suitable statistical models and signal processing methods, but also it provides for the extraction of as much information as possible from the SAR data. The procedure utilizes hypothesis testing based on linear surrogates resampled from the original SAR data using a method known as the iterative amplitude adjusted Fourier transform (iAAFT). The statistical significance for the decision is provided in terms of both parametric and nonparametric P-Values. In order to apply the procedure, the SAR chips should be first transformed from the 2-D to the 1-D space. This is achieved through introducing three new methods. The first method is applicable to real-valued SAR chips including the detected, real and imaginary parts. The second method is meant to handle the bivariate interrelationship between the real and the imaginary parts. In the third method, a so-called furud'ing

operation is presented which allows for capturing the complex-valued statistics within and between the real and the imaginary parts. The applicability of the proposed procedure is demonstrated on various real-world target chips from multiple SAR sensors with different spatial resolutions. The analysis results confirm the statistical significance of the nonlinear phenomenon for the case of extended targets. Furthermore, as the complex-valued SAR chip is magnitude-detected, the nonlinear effect is either obliterated or greatly diminished. The power-detected chip is found to retain some nonlinear statistics but it is postulated that such statistics are altered from their original form present in the complex-valued chip. Subsequently, for the case of extended targets, it is recommended to utilize the complex-valued SAR image rather than the detected one. Furthermore, to exploit the embedded nonlinear statistics, it is advised to utilize relevant nonlinear signal analysis techniques.

Motivated by the Hilbert view for the nonlinear phenomenon, Chapter 5 has presented a new insight into the nonlinear dynamics of the dispersive scatterers in SAR imagery. It is demonstrated that dispersive scatterers from man-made targets induce a predominant nonlinear phase modulation in the radar return signal. The conventional radar resolution theory views this phenomenon as distortions that warrant removal. A novel algorithm for recognizing the order of the nonlinear scatterers is devised. The applicability of the proposed algorithm is demonstrated on a real-world target chip from the MSTAR dataset. This provides for developing a new set of features that take advantage of this effect for target recognition applications in SAR imagery. The approach described in this chapter is expanded upon in Chapter 7.

In Chapter 6, a new insight into the relevance of phase in single-channel SAR imagery is presented. Particularly, the SAR image is approached from the perspectives of complex-valued and directional statistics, respectively. From the perspective of complex-valued statistics, the usefulness of the phase is quantified using a measure called noncircularity (also known as impropriety). Noncircularity simply means that the complex-valued SAR image has a probability density function (PDF) that is variant under rotation in the complex plane. It is found that applying this measure directly to the phase image is misleading as it gives erroneous results for circularity (also known as propriety). Subsequently, it is important that each pixel in the phase image is properly referenced to its neighborhood. This is achieved through introducing a new algorithm for phase characterization which utilizes relevant techniques from

the field of directional statistics that can easily handle the issue of phase wrapping. The characterized phase image is called the backscatter relative phase image (BRPI). It transpires that in the presence of extended targets, the BRPI image is noncircular. Furthermore, relevant techniques from the field of directional statistics are also applied to derive a suitable statistical model for the processed phase image referred to as a wrapped complex Gaussian scale mixture (WCGSM). Accordingly, a new set of fifteen solely phase-based features for target classification in SAR imagery have been developed. An eight-class support vector machine (SVM) classifier utilizing the MSTAR dataset is used to examine the statistical significance of the information carried in the phase image. Unlike the common belief that the phase in single-channel SAR imagery carries no useful information, the statistical significance of the information carried in the phase is clearly demonstrated. With the increase in the spatial resolution of the SAR sensor relative to the size of the imaged target, the nonlinear phenomenon is naturally expected to be more pronounced. Accordingly, the application of the proposed approach to this kind of SAR imagery should achieve higher classification accuracy.

The objective of this research is culminated in Chapter 7. The worldviews of reductionism and holism, respectively, are shown to underlie the fields of linear and nonlinear signal processing. When the processed SAR image is approached from the reductionist perspective of linear signal processing, nonlinearity is often viewed as a noise that warrants removal. On the contrary, nonlinear signal processing methods are motivated by the holistic worldview which is designed to account for multiplicity due to interactions between the individual components in the radar returns. The advantage of holism for signal processing in SAR imagery is clearly demonstrated in this chapter. Two frameworks for feature extraction that take advantage of the nonlinear phenomenon are presented. The first framework is solely based on the phase chip of the extended target, and it allows for extracting unique features for target recognition applications. The second framework is based on 1-D representations for the complex-valued SAR chip. This provides for utilizing a wide array of methods for nonlinear and nonstationary time series analysis such as from chaos theory and the Hilbert-Huang transform (HHT). Comparison with conventional baseline features from the power-detected chips is also considered. Multiple instances of an eight-class SVM classifier are designed based on combinations of exemplary feature sets extracted from the MSTAR dataset. A superior classification accuracy of 93.4186% is achieved

for the combination of the phase and the 1-D based nonlinear features. This is in comparison to 73.6269% for the baseline features. Combining the baseline features with the proposed features increased the classification accuracy by less than 3%. Because the nonlinear phenomenon is resolution-dependent, the proposed approach is expected to achieve even greater accuracy for SAR sensors with higher spatial resolution.

8.2. Future Work

The focus of this research work has been on the development of techniques to extract useful information about the nonlinear dynamics embedded in the single-channel SAR data generated by conventional linear signal processing methods. Particularly, the advantage of the developed techniques is demonstrated on man-made vehicle targets from the public-domain MSTAR dataset. It should be stressed that besides stationary vehicle targets, this work is also applicable to various kinds of stationary and moving extended targets including vehicles, ships, airplanes, icebergs, oil slicks, etc. A future extension of this work is to examine the suitability of the developed techniques for recognition of natural extended targets in SAR imagery such as icebergs and oil slicks. Traditionally, in such cases, detected imagery is used, the phase content is discarded, and the nonlinear dynamics are often overlooked [3–5]. Similarly, another important application is the phenomenon of nonlinear internal water waves commonly referred to within the offshore oil and gas industry as solitons [6]. Solitons form large-amplitude solitary internal waves causing strong, rapidly varying currents within the water column that are a proven hazard to offshore oil and gas developments in several regions of the world [6]. Thus, there is a significant interest in studying this phenomenon, among others, from the oil and gas industry. Despite the numerous works on analyzing this phenomenon from single-channel SAR imagery [7, 8], the interest thus far has been focused on the detected imagery without considering the phase. It may be noted that solitary internal waves are also observed by high frequency (HF) radar [8]. Thus, subsequent application of the signal processing methods presented in this work may offer an important contribution to extracting new information about this phenomenon as observed by a variety of sensors.

Another important extension is to investigate the advantage of the developed techniques for dual, quad-polarimetric and compact-polarimetric SAR imagery [9, 10]. In

the literature, for multi-channel SAR imagery, the phase content is often utilized with the aim of extracting useful inter-channel information. Typical methods that take advantage of this phenomenon include [11–15] incoherent target decomposition (ITD), coherent target decomposition (CTD), complex Wishart distribution, and target coherency matrix (TCM), among others. Extension of the research work introduced in this thesis to multi-channel SAR imagery may offer new insights into extracting useful information specifically targeting the nonlinear phenomenon.

As alluded to above, the application of this research is extendable well beyond SAR to include various types of sensors such as radar, sonar, synthetic aperture sonar (SAS) [16], ultrasound, and synthetic aperture ultrasound (SAU) [17], etc. For example, it is demonstrated in the literature that backscatter from sea clutter imaged by an X-band radar possesses statistically significant nonlinear dynamics that are linked to the sea state [18]. Similar observations are noted for different kinds of targets imaged by radio frequency (e.g., HF radar [8, 19]), and ultrasound frequency (e.g., sonar [20] and medical ultrasound [21]). This demonstrates the potentiality of extending the frameworks for nonlinear feature extraction, presented in this thesis, to various kinds of remote sensing applications.

While the preceding discussion is concerned with harnessing the nonlinear effects embedded in the signals generated by conventional linear signal processing methods, a natural extension for this work is the development of methods that seek to explicitly exploit the nonlinear phenomenon. Indeed, there have been recent works in this direction where new techniques are deliberately designed to excite nonlinear scattering in the imaged object(s), and to properly harness it using suitable nonlinear signal processing methods [22]. One of the most interesting recent studies on the superiority of this approach for sonar is that reported in [22, 23]. In that study, it is empirically demonstrated that while conventional linear signal processing is not able to distinguish targets from bubble clutter, signal processing inspired by nonlinear dolphin-like sonar pulses can both detect and classify such targets. In [22, 24], the extension of this technique allowed the development of a new radar that relies on the excitation of nonlinearities in the imaged scene. Nonlinear signal processing was used to differentiate between linear and nonlinear scatterers, thus, improving the target recognition performance of the radar. Relevant work on the advantage of nonlinear signal processing for HF radar is available in [25]. Accordingly, an ambitious long-term goal for the research

presented in this thesis is to develop a new resolution theory for extended targets that is specifically tailored to handle nonlinear phenomena.

Bibliography

[1] K. El-Darymli, P. McGuire, D. Power, and C. Moloney, "Target detection in synthetic aperture radar imagery: a state-of-the-art survey," *J. Appl. Remote Sens*, vol. 7, no. 1, 2013. [Online]. Available: http://dx.doi.org/10.1117/1.JRS.7.071598 234

[2] K. El-Darymli, P. McGurie, E. W. Gill, D. Power, and C. Moloney, "Automatic target recognition in SAR imagery (SAR-ATR): A state-of-the-art review," *[To be submitted]*, 2015. 234

[3] C. Wesche and W. Dierking, "Iceberg signatures and detection in SAR images in two test regions of the Weddell Sea, Antarctica," *Journal of Glaciology*, vol. 58, no. 208, pp. 325–339, 2012-04-01T00:00:00. [Online]. Available: http://www.ingentaconnect.com/content/igsoc/jog/2012/00000058/00000208/art00012 238

[4] A. Solberg, "Remote sensing of ocean oil-spill pollution," *Proceedings of the IEEE*, vol. 100, no. 10, pp. 2931–2945, 2012. [Online]. Available: http://dx.doi.org/10.1109/JPROC.2012.2196250

[5] M. Fingas and C. Brown, "Review of oil spill remote sensing," *Marine pollution bulletin*, vol. 83, no. 1, pp. 9–23, 2014. [Online]. Available: http://dx.doi.org/10.1016/j.marpolbul.2014.03.059 238

[6] G. Jeans, M. Calverley, W. Jeffery, C. Jackson, V. Vlasenko, and A. Osborne. (2012, March) Worldwide internal soliton criteria. Paper presented at Oceanology International. London, UK. [Online]. Available: http://bit.ly/1lGstVP 238

[7] C. R. Jackson, J. C. B. da Silva, G. Jeans, W. Alpers, and M. Caruso, "Nonlinear internal waves in synthetic aperture radar imagery," *Oceanography*, vol. 26, no. 2, pp. 68–79, 2013. [Online]. Available: http://dx.doi.org/10.5670/oceanog.2013.32 238

[8] V. Klemas, "Remote sensing of ocean internal waves: An overview," *Journal*

of Coastal Research, vol. 28, no. 3, pp. 540–546, 2012. [Online]. Available: http://dx.doi.org/10.2112/JCOASTRES-D-11-00156.1 238, 239

[9] F. J. Charbonneau, B. Brisco, R. K. Raney, H. McNairn, C. Liu, P. W. Vachon, J. Shang, R. DeAbreu, C. Champagne, A. Merzouki, and T. Geldsetzer, "Compact polarimetry overview and applications assessment," *Canadian Journal of Remote Sensing*, vol. 36, no. 1, pp. S298–S315, 2010. [Online]. Available: http://dx.doi.org/10.5589/m10-062 238

[10] R. Shirvany, M. Chabert, and J.-Y.Tourneret, "Ship and oil-spill detection using the degree of polarization in linear and hybrid/compact dual-pol SAR," *Selected Topics in Applied Earth Observations and Remote Sensing, IEEE Journal of*, vol. 5, no. 3, pp. 885–892, 2012. [Online]. Available: http://dx.doi.org/10.1109/JSTARS.2012.2182760 238

[11] J. Lee and E. Pottier, *Polarimetric Radar Imaging From Basics to Applications*. Boca Raton, Florida: CRC Press, Taylor and Francis Group, 2009. 239

[12] R. Hansch and O. Hellwich, *Chapter 5, in Radar Remote Sensing of Urban Areas*. New York, NY: Springer, 2010.

[13] R. Touzi, W. M. Boerner, J. S. Lee, and E. Lueneburg, "A review of polarimetry in the context of synthetic aperture radar: concepts and information extraction," *Canadian Journal of Remote Sensing*, vol. 30, no. 3, pp. 380–407, 2004. [Online]. Available: http://dx.doi.org/10.5589/m04-013

[14] L. Zhang, "Comparison of methods for target detection and applications using polarimetric SAR image," *PIERS*, vol. 4, no. 1, pp. 140–145, 2008. [Online]. Available: http://www.piers.org/piersonline/pdf/Vol4No1Page140to145.pdf

[15] S. R. Cloude and E. Pottier, "A review of target decomposition theorems in radar polarimetry," *Geoscience and Remote Sensing, IEEE Transactions on*, vol. 34, no. 2, pp. 498–518, 1996. [Online]. Available: http://dx.doi.org/10.1109/36.485127 239

[16] M. Hayes and P. T. Gough, "Synthetic aperture sonar: A review of current status," *Oceanic Engineering, IEEE Journal of*, vol. 34, no. 3, pp. 207–224, July 2009. [Online]. Available: http://dx.doi.org/10.1109/JOE.2009.2020853 239

[17] J. Rasmussen, Y. Du, and J. A. Jensen, "Non-linear imaging using an experimental synthetic aperture real time ultrasound scanner," in *15th Nordic-Baltic Conference on Biomedical Engineering and Medical Physics (NBC*

2011), ser. IFMBE Proceedings, K. Dremstrup, S. Rees, and M. Jensen, Eds. Springer Berlin Heidelberg, 2011, vol. 34, pp. 101–104. [Online]. Available: http://dx.doi.org/10.1007/978-3-642-21683-1_25 239

[18] S. Haykin, R. Bakker, and B. Currie, "Uncovering nonlinear dynamics-the case study of sea clutter," *Proceedings of the IEEE*, vol. 90, no. 5, pp. 860–881, May 2002. [Online]. Available: http://dx.doi.org/10.1109/JPROC.2002.1015011 239

[19] L. Wyatt, "Non-linear effects in HF radar backscatter from the ocean," in *Electronic Engineering in Oceanography, 1997. Technology Transfer from Research to Industry., Seventh International Conference on*, Jun 1997, pp. 218–222. [Online]. Available: http://dx.doi.org/10.1049/cp:19970687 239

[20] F. P. J. Gabriel, S. P. Nasholm, A. Austeng, and S. Holm., "Exploiting nonlinear propagation in echo sounders and sonar," in *The 10th European Conference on Underwater Acoustics (ECUA)*, Istanbul, Turkey, 2010. [Online]. Available: http://urn.nb.no/URN:NBN:no-29563 239

[21] V. F. Humphrey, "Nonlinear propagation in ultrasonic fields: measurements, modelling and harmonic imaging," *Ultrasonics*, vol. 38, no. 1-8, pp. 267–272, 2000. [Online]. Available: http://dx.doi.org/10.1016/S0041-624X(99)00122-5 239

[22] T. G. Leighton, P. R. White, and D. C. Finfer, "Contrast enhancement between linear and nonlinear scatterers," US Patent 11/917,990, 2010. [Online]. Available: http://www.google.ca/patents/US20100286514 239

[23] T. G. Leighton, G. H. Chua, and P. R. White, "Do dolphins benefit from nonlinear mathematics when processing their sonar returns?" *Royal Society A: Mathematical, Physical and Engineering Science*, vol. 468, no. 2147, pp. 3517–3532, 2012. [Online]. Available: http://dx.doi.org/10.1098/rspa.2012.0247 239

[24] T. G. Leighton, G. H. Chua, P. R. White, K. F. Tong, H. D. Griffiths, and D. J. Daniels, "Radar clutter suppression and target discrimination using twin inverted pulses," *Royal Society A: Mathematical, Physical and Engineering Science*, vol. 469, no. 2160, 2013. [Online]. Available: http://dx.doi.org/10.1098/rspa.2013.0512 239

[25] S. J. Anderson, "Nonlinear scattering at HF: Prospects for exploitation in OTH radar systems," *Turkish Journal of Electrical Engineering and*

Computer Sciences, vol. 18, no. 3, pp. 439–456, 2010. [Online]. Available: http://dx.doi.org/10.3906/elk-1001-396 239

A. The SAR Datasets Avaliable for This Research

Three real-world, single-channel and single-look complex (SLC) SAR datasets are used throughout this thesis. Firstly, the Radarasat-2 dataset is described. Secondly, the public-domain MSTAR dataset is introduced. Finally, SAR chips from miscellaneous sensors are presented.

A.1. Radarsat-2 SAR Dataset

Radarsat-2 is Canada's next-generation commercial SAR satellite. The satellite was launched in December 14, 2007. Radarsat-2 is sponsored by Canada Space Agency (CSA) and operated by MacDonald Dettwiler and Associates (MDA) Corporation. Radarsat-2 carries a C-band SAR sensor whereby the finest spatial resolution commercially available is that of the single-channel Spotlight imaging mode. In this mode, Radarsat-2 offers a spatial resolution of 0.8×1.6 m in the azimuth and (slant) range, respectively [1]. The lowest-level product commercially available from Radarsat-2 is SLC [2]. This is the complex-valued and focused SAR image output from the SAR processor. No SAR phase history is available from Radarsat-2 as per the contract between CSA and MDA. The Radarsat-2 SLC dataset used in this thesis is originally due to the Virtual SAR Constellation (VSC) project [3] which utilizes a recent Spotlight mode dataset that comprises over 500 images of ground-truthed construction vehicles for scenes located in Long Harbour and Argentia, Newfoundland. Additionally, few single-channel SLC SAR chips were extracted from a public-domain Radarsat-2 scene, i.e., Vancouver dataset in [4]. The imaging mode is 'Polarimetric Fine'. Only the HH channel is utilized. The nominal spatial resolution for this imaging mode is 5.2×7.7 m in range and azimuth, respectively [1]. The targets of interest are ships.

A.2. MSTAR SAR Dataset

Moving and Stationary Target Acquisition and Recognition (MSTAR) is a predominantly Spotlight (except for few non-target clutter chips) real-world freely and publicly available X-band SAR dataset from the Sensor and Data Management System (SDMS) of the United States Air Force. The MSTAR dataset was originally collected in 1995 and 1996 at the Redstone Arsenal, Huntsville, AL by the airborne Sandia National Laboratory (SNL) SAR sensor platform and an X-band STARLOS sensor. The collection was jointly sponsored by DARPA and Air Force Research Laboratory. The MSTAR dataset offers a spatial resolution of 0.3047×0.3047 metres in both range and azimuth. Further, the MSTAR dataset is available in the form of SLC complex-valued chips. No SAR phase history pertaining to the MSTAR dataset is publicly available.

Under this dataset, two data collections are available. The first collection contains baseline X-band SAR imagery of 13 target types (20 actual targets) plus minor examples of articulation, obscuration and camouflage. Additional clutter imagery is also available. The second collection contains X-band SAR imagery of 15 target types (27 actual targets). Baseline data is available for 12 additional target types. Articulation and obscuration data is also available for numerous targets and their variants. Extensive research works based on this dataset are available in the literature [5]. The MSTAR dataset can be retrieved from this link [6]. The main advantage of using the MSTAR dataset in this thesis is its fine resolution relative to C-CORE's Radarsat-2 dataset.

A.3. SAR Chips from Miscellaneous Sensors

Three additional SAR chips are utilized in this study: (1) a ground-truthed chip from our own SAR sensor, and (2) two ground-truthed chips, from a very high-resolution SAR sensor.

A Chip from our Own SAR Sensor

A SAR chip for a vehicle target (i.e., extended target) from our self-designed S-band SAR sensor is utilized. Our SAR sensor offers single-channel SLC SAR data [7]. The

antenna polarization is HH. The imaging mode is 'Stripmap'. The nominal spatial resolution of our SAR sensor is 0.67873×0.15 m in range and azimuth, respectively.

Two SAR Chips from a Very High-Resolution SAR Sensor

The final two SAR chips considered in this study are from a very high-resolution single-channel X-band SAR system, obtained from [8, 9]. The imaging mode is 'Stripmap'. The nominal spatial resolution of the SAR sensor is 0.03×0.012 m in range and azimuth, respectively. The first target is a bike. The second target is the phrase GO STATE which is formed through using a group of tiny pushpins.

B. Reasons for Target Signature Variability in SAR Imagery

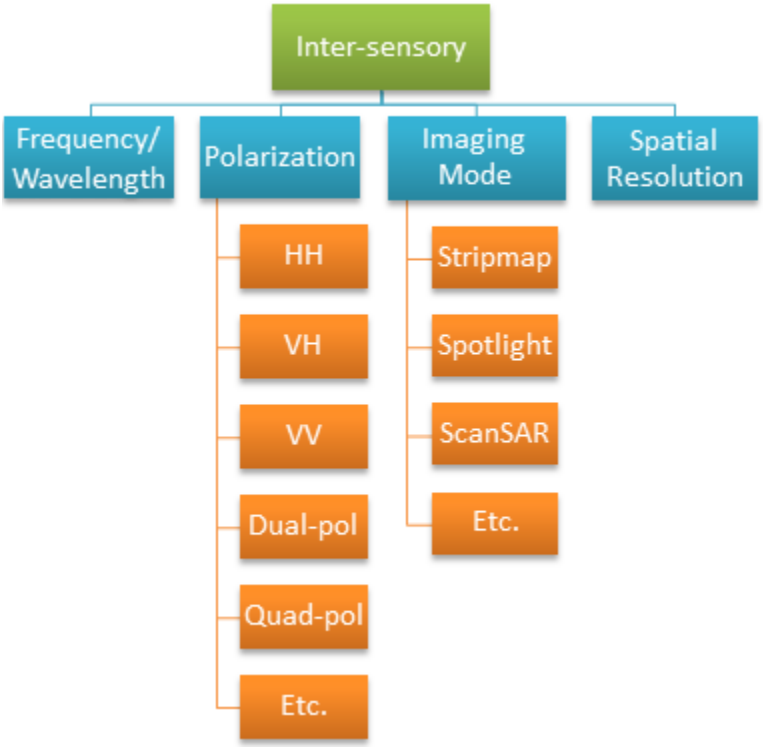

Figure B.1: Summary of the inter-sensory reasons for target-signature variability [5].

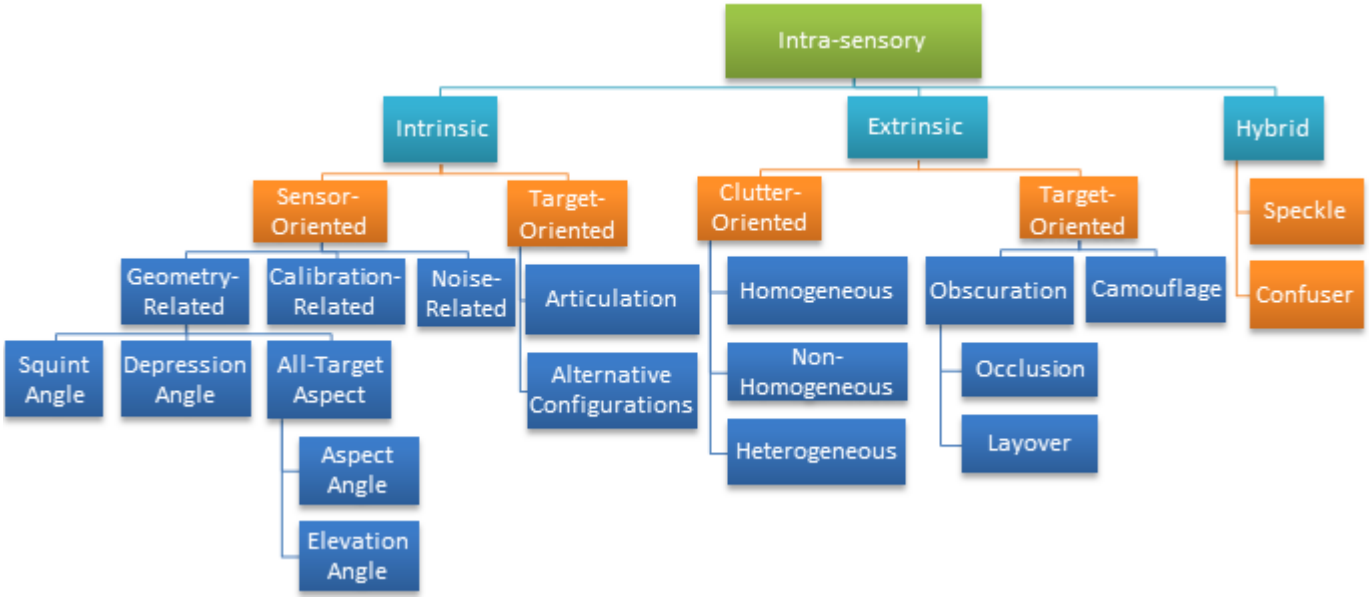

Figure B.2: Summary of the intra-sensory reasons for target-signature variability [5].

C. Data Acquisition Unit Used in the LFMCW SAR Radar

Figure C.1: The device used for data acquisition in the SAR radar. It is a high-quality sound recorder (H4N Handy Recorder) available from Zoom Corporation [10].

D. Transmit and Receive Antennas Used in the LFMCW SAR Radar

Figure D.1: Setup for the Tx and the Rx antennas.

E. Jensen–Shannon Divergence (JSD)

The Kullback–Leibler divergence (KLD, also known as the relative entropy) is an information-theoretic approach to measure the information lost when $q(x)$ is used to estimate $p(x)$. It is given by [11]

$$KLD\left(p||q\right) = \sum_{x \in X} p\left(x\right) \log_2 \left(\frac{p\left(x\right)}{q\left(x\right)}\right). \tag{E.1}$$

KLD provides a means for comparing the entropy of the two distributions over the same random variable. Intuitively, this allows for estimating the number of additional bits required when encoding a random variable X with a distribution $p(x)$ using the alternative distribution $q(x)$. The properties of interest for KLD are

$$KLD\left(p||q\right) \geq 0, \tag{E.2}$$

$$KLD\left(p||q\right) = 0 \,\text{iff}\, p\left(x\right) = q\left(x\right) \text{ for all } x \in X, \tag{E.3}$$

$$KLD\left(p||q\right) \neq KLD\left(q||p\right). \tag{E.4}$$

Jensen–Shannon divergence (JSD) is a symmetrized version of KLD. It is calculated

as [12, 13]

$$JSD = \frac{KLD\left(p||q\right) + KLD\left(q||p\right)}{2}. \tag{E.5}$$

In this study, in order to quantify the goodness-of-fit between the empirical BRPI histogram (i.e., p) and the PDF obtained based on the estimation of parameters (i.e., q), the following measure is considered

$$JSD_N = \frac{JSD}{H\left(p\right)} = \frac{JSD}{-\sum_{x \in X} p\left(x\right) \log_2 p\left(x\right)}, \tag{E.6}$$

where $H\left(p\right)$ is the histogram entropy.

F. Parameter Estimation for the vM and WC Distributions

F.1. Maximum Likelihood Parameter Estimation for the vM Distribution

The parameter μ is the circular mean of the vM distribution. The MLE estimate of this parameter is defined as follows [14, 15]

$$\hat{\mu} = \arg\left\{\frac{1}{n}\sum_{i=1}^{n}\exp\left(jx_i\right)\right\}, \tag{F.1}$$

where n is the total number of phase measurements, and x_i is the value of a particular phase measurement.

In order to estimate κ, it is important to calculate the $\bar{R}^2$ statistic which is the square of the length of the averaged vector given by [14, 15]

$$\bar{R}^2 = \bar{x}\,\overline{x^*} = \left(\frac{1}{n}\sum_{i=1}^{n}\cos x_i\right)^2 + \left(\frac{1}{n}\sum_{i=1}^{n}\sin x_i\right)^2 \tag{F.2}$$

The expectation value of the $\bar{R}^2$ statistic is given by [14, 15]

$$\left\langle \bar{R}^2 \right\rangle = \frac{1}{n} + \frac{n-1}{n}\frac{I_1\left(\kappa\right)^2}{I_0\left(\kappa\right)^2}, \tag{F.3}$$

Accordingly, the following statistic is the unbiased estimate for $\frac{I_1(\kappa)^2}{I_0(\kappa)^2}$

$$\left(\bar{R}_e\right)^2 = \frac{n}{n-1}\left(\bar{R}^2 - \frac{1}{n}\right). \tag{F.4}$$

Hence, solving the following equation for κ yields the MLE estimate in the limit of large n [14, 15]

$$\bar{R} = \frac{I_1(\kappa)}{I_0(\kappa)}, \tag{F.5}$$

where $I_m(\kappa)$ is the Bessel function defined as

$$I_m(\kappa) = \frac{1}{\pi}\int_0^{\pi} \exp(\kappa \cos x)\cos mx \, \mathrm{d}x. \tag{F.6}$$

F.2. Maximum Likelihood Parameter Estimation for the WC Distribution

The MLE estimates of μ_{wc} and ρ can be obtained by a recursive algorithm originally due to Kent and Tyler [16]. First, the PDF of the WC distribution needs to be parametrized by introducing the following two parameters [17]

$$\mu_1 = \frac{2\rho\cos\mu_{wc}}{1+\rho^2},\ \mu_2 = \frac{2\rho\sin\mu_{wc}}{1+\rho^2}, \tag{F.7}$$

Thus, Eq. 6.43 can be rewritten in terms of μ_1 and μ_2 as follows:

$$f(x;\mu_1,\mu_2) = \frac{1}{2\pi c_{wc}}\frac{1}{1-\mu_1\cos x - \mu_2\sin x}, \tag{F.8}$$

where,

$$c_{wc} = \frac{1}{1 - \mu_1^2 - \mu_2^2}, \tag{F.9}$$

Then, two other parameters η_1 and η_2 are introduced

$$\eta_1 = c_{wc}\,\mu_1,\ \eta_2 = c_{wc}\,\mu_2,\ c_{wc} = \sqrt{1 + \eta_1^2 + \eta_2^2}, \tag{F.10}$$

To obtain the MLE estimate $\hat{\mu}_1$ and $\hat{\mu}_2$, the log-likelihood function (i.e., logarithm of Eq. F.8) is differentiated with respect to η_1 and η_2 as follows

$$\frac{1}{c_{wc}} \sum_{i=1}^{n} w_i \left[\cos\theta_i - \mu_1\right] = 0, \tag{F.11}$$

$$\frac{1}{c_{wc}} \sum_{i=1}^{n} w_i \left[\sin\theta_i - \mu_2\right] = 0, \tag{F.12}$$

where,

$$w_i = \frac{1}{1 - \mu_1 \cos\theta_i - \mu_2 \sin\theta_i}, \tag{F.13}$$

where $i = 1, ..., n$. Accordingly, μ_1 and μ_2 can be expressed as adaptively weighted averages as

$$\mu_1 = \frac{\sum_{i=1}^{n} w_i \cos\theta_i}{\sum_{i=1}^{n} w_i}, \tag{F.14}$$

$$\mu_2 = \frac{\sum_{i=1}^{n} w_i \sin\theta_i}{\sum_{i=1}^{n} w_i}. \tag{F.15}$$

Thus, the MLE estimates $\hat{\mu}_1$ and $\hat{\mu}_2$, (and thus $\hat{\mu}_{wc}$ and $\hat{\rho}$) can be obtained through a reweighting iterative procedure as summarized in Fig. F.1 [17].

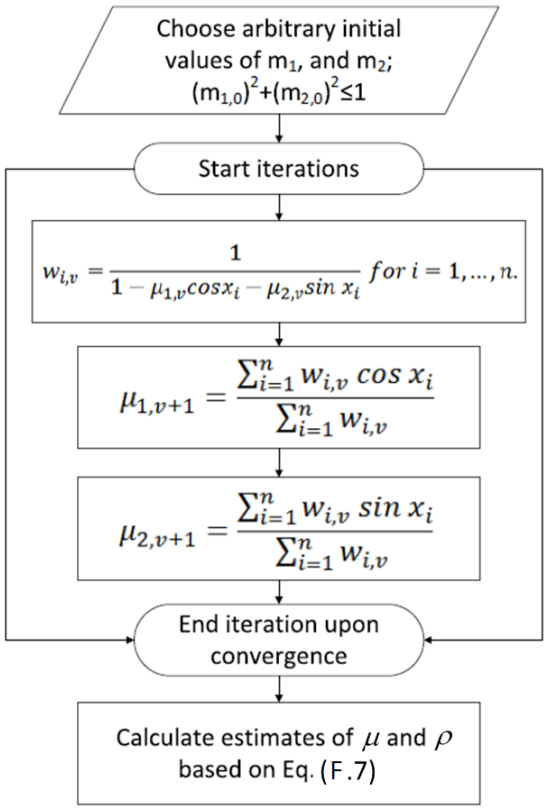

Figure F.1: Algorithm for MLE estimation of μ_{wc} and ρ.

Bibliography

[1] MacDonald, Dettwiler and Associates Ltd, "Radarsat-2 product description," MDA, Tech. Rep. RN-SP-52-1238, 2009. [Online]. Available: http://gs.mdacorporation.com/products/sensor/radarsat2/RS2_Product_Description.pdf 245

[2] MacDonald, Dettwiler and Associated Ltd. (2014) Radarsat-2 pricing information. MDA. [Online]. Available: http://gs.mdacorporation.com/SatelliteData/Radarsat2/Price.aspx 245

[3] C-CORE, "SAR constellation task 4 final report," C-CORE, Tech. Rep. R 09 086 700 v 2, 2010. 245

[4] MacDonald, Detwiler and Associates Ltd. Radarsat-2 sample dataset. [Online]. Available: http://gs.mdacorporation.com/SatelliteData/Radarsat2/SampleDataset.aspx 245

[5] K. El-Darymli, P. McGurie, E. W. Gill, D. Power, and C. Moloney, "Automatic target recognition in SAR imagery (SAR-ATR): A state-of-the-art review," *[To be submitted]*, 2015. xvii, 246, 248, 249

[6] United States Air Force. (2013) MSTAR. USAF. [Online]. Available: https://www.sdms.afrl.af.mil/index.php?collection=mstar 246

[7] K. El-Darymli, C. Moloney, E. W. Gill, P. McGuire, and D. Power, "Design and implementation of a low-power synthetic aperture radar," in *International Geoscience and Remote Sensing Symposium (IGARSS'14), IEEE*, Quebec, Canada, 2014. [Online]. Available: http://dx.doi.org/10.1109/IGARSS.2014.6946618 246

[8] G. L. Charvat. (2013) Low-power X-band rail SAR. [Online]. Available: http://www.glcharvat.com/Dr._Gregory_L._Charvat_Projects/Low-Power_X-Band_Rail_SAR.html 247

[9] G. L. Charvat, L. Kempell, and C. Coleman, "A low-power high-sensitivity X-band rail SAR imaging system," *Antennas and Propagation Magazine, IEEE*, vol. 50, no. 3, pp. 108–115, 2008. [Online]. Available: http://dx.doi.org/10.1109/MAP.2008.4563576 247

[10] Zoom Corporation. H4n handy recorder. [Online]. Available: http://www.zoom.co.jp/products/h4n xvii, 250

[11] K. P. Burnham and D. R. Anderson, *Model Selection and Multi-Model Inference: A Practical Information-Theoretic Approach*. New York, NY: Springer, 2010. 252

[12] D. M. Endres and J. E. Schindelin, "A new metric for probability distributions," *Information Theory, IEEE Transactions on*, vol. 49, no. 7, pp. 1858–1860, 2003. [Online]. Available: http://dx.doi.org/10.1109/TIT.2003.813506 253

[13] C. D. Manning and H. Schütze, *Foundations of Statistical Natural Language Processing*. Cambridge, MA: MIT Press, 1999. 253

[14] N. I. Fisher, *Statistical Analysis of Circular Data*. Cambridge, UK: Cambridge University Press, 1993. 254, 255

[15] G. J. Borradaile, *Statistics of Earth Science Data: Their Distribution in Time, Space, and Orientation*. Berlin, Heidelberg: Springer, 2003. 254, 255

[16] J. T. Kent and D. E. Tyler, "Maximum likelihood estimation for the wrapped cauchy distribution," *Journal of Applied Statistics Journal of Applied Statistics*, vol. 15, no. 2, pp. 247–254, 1988. [Online]. Available: http://dx.doi.org/10.1080/02664768800000029 255

[17] S. R. Jammalamadaka and A. Sengupta, *Topics in circular statistics*. River Edge, NJ: World Scientific, 2001. 255, 257